



CERN-THESIS-2011-283



*Thesis presented for the Ph.D degree (Doctor of Philosophy) in Physics*

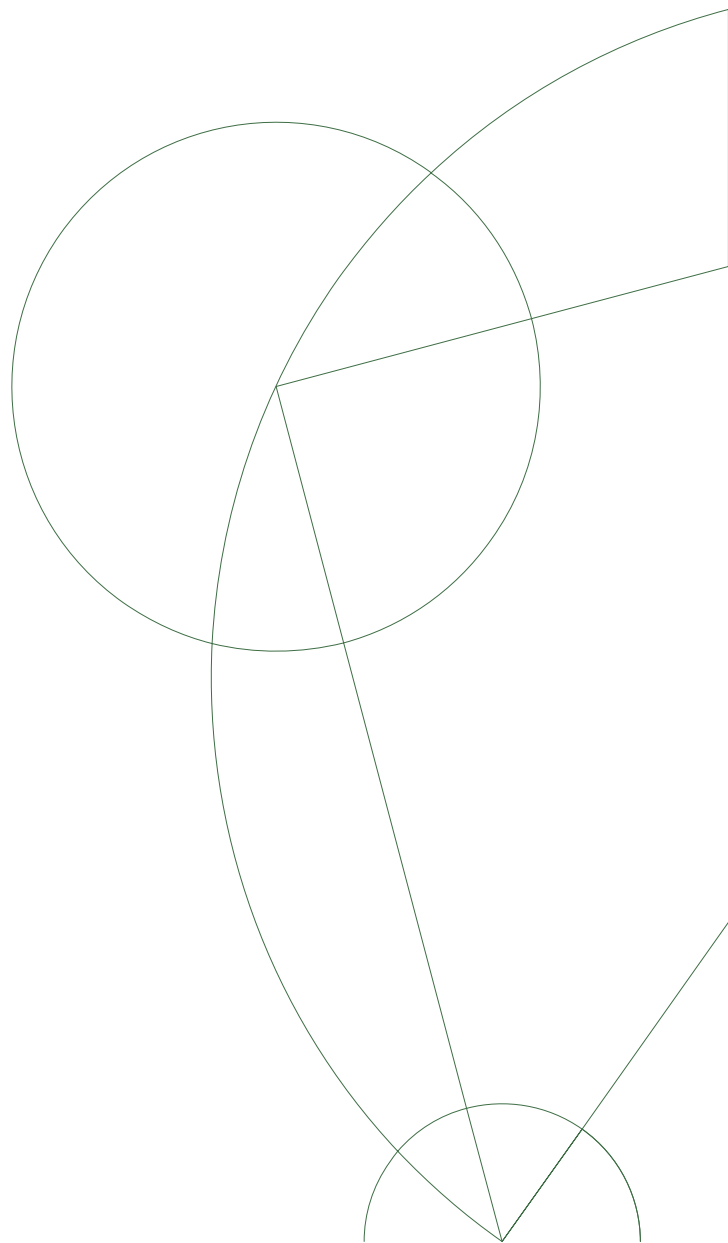
# Charged particle multiplicity distributions into forward pseudorapidities in pp and PbPb collisions at the LHC

Casper Nygaard

Niels Bohr Institute  
University of Copenhagen

Academic Advisor:  
Jens Jørgen Gaardhøje  
Niels Bohr Institute  
University of Copenhagen

*October, 2011*





# Contents

<b>Preface</b>	<b>1</b>
<b>1 The Standard Model of Particle Physics</b>	<b>5</b>
1.1 Quantum Chromo Dynamics . . . . .	7
1.2 Quark Gluon Plasma . . . . .	8
1.3 Kinematic Variables . . . . .	10
1.4 Relativistic Collisions . . . . .	12
1.4.1 Relativistic Heavy Ion Collisions . . . . .	12
1.4.2 Proton-Proton Collisions . . . . .	16
1.5 Previous Heavy Ion Results . . . . .	19
<b>2 Charged Particle Multiplicity</b>	<b>27</b>
2.1 Negative Binomial Distributions . . . . .	27
2.2 Koba–Nielsen–Olesen Scaling . . . . .	30
2.3 Previous Multiplicity Measurements . . . . .	33
2.3.1 Multiplicity Distributions . . . . .	33
2.3.2 $dN/d\eta$ measurements . . . . .	38
2.3.3 Mean Multiplicity Energy Dependence . . . . .	40
<b>3 Experimental Setup</b>	<b>43</b>
3.1 The Large Hadron Collider . . . . .	43
3.1.1 Colliding Protons . . . . .	43
3.1.2 Colliding Lead Ions . . . . .	44
3.2 The ALICE Experiment . . . . .	45
3.3 Central Barrel Detectors . . . . .	45
3.3.1 Inner Tracking System . . . . .	46
3.3.2 Time Projection Chamber . . . . .	47
3.3.3 Transition Radiation Detector . . . . .	48
3.3.4 Time Of Flight . . . . .	48
3.3.5 Photon Spectrometer . . . . .	48
3.3.6 Electro Magnetic Calorimeter . . . . .	49
3.3.7 High Momentum Particle Identification Detector . . . . .	49
3.4 Muon Spectrometer . . . . .	49
3.5 Forward detectors . . . . .	49
3.5.1 Photon Multiplicity Detector . . . . .	50
3.5.2 T0 . . . . .	50
3.5.3 V0 . . . . .	51
3.5.4 Zero Degree Calorimeter . . . . .	51
3.6 Data Acquisition System . . . . .	52

<b>4</b>	<b>The FMD and SPD</b>	<b>53</b>
4.1	Semi-conductor properties . . . . .	53
4.1.1	Doped Crystals . . . . .	54
4.2	Semi-conductor detectors . . . . .	55
4.2.1	n-p junctions . . . . .	55
4.3	Energy loss in Silicon . . . . .	56
4.4	Forward Multiplicity Detector . . . . .	60
4.4.1	Design and Motivation . . . . .	60
4.4.2	FMD Sensors and Electronics . . . . .	61
4.4.3	Pedestals and Gain . . . . .	65
4.5	Silicon Pixel Detector . . . . .	66
<b>5</b>	<b>Off-line Data Processing</b>	<b>69</b>
5.1	ROOT and AliROOT . . . . .	69
5.2	Simulations . . . . .	69
5.2.1	Digitisation . . . . .	70
5.3	Reconstruction . . . . .	71
5.4	Analysis Structure . . . . .	72
5.5	GRID and AliEn . . . . .	74
5.6	Data sets for analysis . . . . .	76
<b>6</b>	<b>Analysis</b>	<b>79</b>
6.1	Event Selection . . . . .	79
6.1.1	Trigger Selection . . . . .	79
6.1.2	Vertex Selection . . . . .	81
6.1.3	Centrality Selection . . . . .	83
6.2	FMD Particle Counting . . . . .	84
6.2.1	Energy distributions . . . . .	84
6.2.2	Hit Sharing . . . . .	87
6.2.3	Counting Methods . . . . .	94
6.2.4	FMD Acceptance . . . . .	97
6.3	SPD Particle Counting . . . . .	99
6.3.1	SPD Acceptance . . . . .	100
6.4	Secondary particles . . . . .	101
6.5	Strangeness Correction . . . . .	108
6.6	Unfolding . . . . .	109
6.6.1	Bayesian Iterative Unfolding . . . . .	110
6.6.2	Single Value Decomposition Unfolding . . . . .	112
6.6.3	Unfolding Quality Measure . . . . .	114
6.7	Trigger-Vertex Bias Correction . . . . .	118
6.8	Defining Analysis Parameters . . . . .	119
<b>7</b>	<b>Systematic Errors</b>	<b>125</b>
7.1	Uncertainty on event multiplicity . . . . .	125
7.2	Uncertainty on trigger-vertex bias correction and unfolding method . . . . .	129
7.3	Total systematic error . . . . .	131

<b>8</b>	<b>Results</b>	<b>133</b>
8.1	Multiplicity Distributions . . . . .	134
8.1.1	pp collisions . . . . .	134
8.1.2	PbPb collisions . . . . .	137
8.2	KNO . . . . .	139
8.2.1	pp collisions . . . . .	139
8.2.2	PbPb collisions . . . . .	143
8.3	$\frac{dN_{\text{ch}}}{d\eta}$ . . . . .	145
8.3.1	pp collisions . . . . .	145
8.3.2	PbPb collisions . . . . .	146
8.4	Mean Multiplicity Energy dependence . . . . .	147
8.5	Outlook . . . . .	148
<b>9</b>	<b>Conclusion</b>	<b>151</b>
<b>A</b>	<b>Lorentz Invariance of <math>dy</math></b>	<b>153</b>
<b>B</b>	<b>The Glauber Model</b>	<b>155</b>
<b>C</b>	<b>Sharing algorithm</b>	<b>157</b>
<b>D</b>	<b>Comparison between Poisson and Energy Fits counting</b>	<b>159</b>
<b>E</b>	<b><math>Q_1</math> in central <math>\eta</math>-interval</b>	<b>163</b>
<b>F</b>	<b>Detailed comparisons of multiplicity distributions</b>	<b>165</b>



# List of Figures

1.1	Quark Quark potential . . . . .	8
1.2	The formation of QGP through compression of matter. . . . .	8
1.3	QCD phase diagram. . . . .	9
1.4	ALICE coordinate system . . . . .	11
1.5	Schematic illustration of a relativistic heavy ion collision. . . . .	12
1.6	Proposed space-time evolution of a heavy ion collision. . . . .	14
1.7	Simplistic view of a collision in the transparent picture. . . . .	14
1.8	Simplistic view of a collision in the stopping picture. . . . .	15
1.9	Schematic of a $pp$ collision. . . . .	16
1.10	Chew-Frautschi plot . . . . .	17
1.11	Diffractive event class differences . . . . .	18
1.12	Nuclear modification factors from BRAHMS and ALICE. . . . .	19
1.13	Nuclear modification factors from CMS and PHENIX. . . . .	20
1.14	Jet Quenching . . . . .	21
1.15	Dijet imbalance . . . . .	22
1.16	The missing energy as a function of the dijet asymmetry from CMS . . . .	22
1.17	Flow measurements from ALICE. . . . .	23
1.18	Reaction plane and nuclei overlap. . . . .	24
1.19	Long range azimuthal correlation from ALICE . . . . .	25
2.1	Various Negative Binomial Distributions . . . . .	28
2.2	Split Field Magnet detector multiplicity measurements . . . . .	33
2.3	UA5 multiplicity measurements . . . . .	34
2.4	UA1 multiplicity measurements . . . . .	34
2.5	CDF multiplicity measurements. . . . .	35
2.6	ALICE and CMS multiplicity measurements at $\sqrt{s} = 900$ GeV, 2360 GeV, and 7000 GeV . . . . .	36
2.7	Multi-component NBD fits to UA5 data. . . . .	37
2.8	$\frac{dN_{ch}}{d\eta}$ measurements from pre-LHC experiments. . . . .	38
2.9	$\frac{dN_{ch}}{d\eta}$ measurements from ALICE and CMS. . . . .	39
2.10	Preliminary $\frac{dN_{ch}}{d\eta}$ measurements from ATLAS. . . . .	39
2.11	Unpublished $PbPb$ $\frac{dN_{ch}}{d\eta}$ measurements from ALICE. . . . .	40
2.12	Mean multiplicity collision energy scaling. . . . .	41
2.13	$\frac{dN_{ch}}{d\eta}$ predictions at mid-rapidity in $PbPb$ collisions at $\sqrt{s_{NN}} = 2760$ GeV . .	41
3.1	Schematic view of the CERN accelerator complex. . . . .	44
3.2	Overview of the ALICE detector . . . . .	45
3.3	Pseudorapidity coverage of ALICE . . . . .	46
3.4	ALICE central barrel detectors . . . . .	47
3.5	Muon Spectrometer . . . . .	50

3.6	Forward Detectors . . . . .	51
4.1	Band-gaps in insulators, semi-conductors and metals. . . . .	53
4.2	Semi-conductor bindings . . . . .	54
4.3	The stopper power for $\mu$ in Copper. . . . .	57
4.4	Landau distribution. . . . .	59
4.5	Overview of the FMD detector system . . . . .	60
4.6	Overview of FMD rings . . . . .	62
4.7	Schematic of the FMD electronics. . . . .	63
4.8	Capacitance and leakage current. . . . .	64
4.9	Depletion depth and leakage current stability. . . . .	64
4.10	Pedestal distribution and gain calibration. . . . .	65
4.11	Pedestal means. . . . .	66
4.12	Overview of the ITS detector system. . . . .	67
4.13	Close up view of the SPD. . . . .	67
5.1	Tracklet construction and vertex finding. . . . .	72
5.2	Schematic of analysis train structure. . . . .	73
5.3	Schematic of the analysis chain in ALICE. . . . .	74
5.4	Overview of the GRID computing centres in Europe and Egypt. . . . .	75
6.1	$v_z$ versus $\eta$ acceptance. . . . .	81
6.2	The measured $z$ -vertex distribution. . . . .	82
6.3	The measured $xy$ -vertex distribution . . . . .	83
6.4	An example of measured centrality classes by the $V0$ detector. . . . .	84
6.5	The measured energy distributions in FMD2I. . . . .	85
6.6	Energy distributions in the simulations. . . . .	86
6.7	Illustration of the concept of hit sharing. . . . .	87
6.8	Relation between the energy deposit in neighbouring strips. . . . .	88
6.9	Single, double and triple merged signals. . . . .	89
6.10	Simulated single, double and triple merged signals. . . . .	90
6.11	Sharing hit cut. . . . .	92
6.12	Example of the effect of merging shared signals on the energy distributions. . . . .	93
6.13	Example of a multiple (Gaussian convoluted) Landau fit. . . . .	94
6.14	The correction for high occupancy in the Poisson counting method. . . . .	95
6.15	Mean Occupancy . . . . .	97
6.16	Counting methods comparison in $pp$ collisions at $\sqrt{s} = 900\text{GeV}$ . . . . .	98
6.17	Inner ring $\phi$ -acceptance. . . . .	99
6.18	The frequency of various cluster patterns in the SPD. . . . .	100
6.19	The actual $\phi$ -acceptance of the SPD as a function of $\eta$ . . . . .	101
6.20	The origin of secondary particles within the central region of ALICE. . . . .	102
6.21	The origin of the secondary particles, which eventually hit the FMD system. . . . .	102
6.22	The origin of secondary particles hitting each individual FMD ring. . . . .	104
6.23	Origin of secondary particles hitting either the FMD or SPD inner layer. . . . .	105
6.24	Origin of secondary particles hitting the FMD rings and the SPD inner layer. . . . .	106
6.25	FMD3I secondary correction map. . . . .	107
6.26	SPD secondary correction map. . . . .	107
6.27	Strangeness correction factor . . . . .	108
6.28	Response matrix. . . . .	110
6.29	Number of iterations in Bayesian unfolding. . . . .	111

6.30	Over and under-regularisation . . . . .	113
6.31	Characteristic regions of multiplicity distributions. . . . .	114
6.32	$Q_1$ unfolding quality. . . . .	116
6.33	The best unfolding solutions for $ \eta  < 2.4$ . . . . .	117
6.34	Trigger–Vertex bias correction factor. . . . .	118
6.35	Secondary correction test. . . . .	119
6.36	Acceptance gaps test. . . . .	120
6.37	Event generator test. . . . .	122
6.38	Vertex range test. . . . .	123
7.1	Material density uncertainty. . . . .	125
7.2	Event generator uncertainty in the FMD. . . . .	126
7.3	Event generator uncertainty in the SPD. . . . .	127
7.4	Example of systematic errors on event multiplicity . . . . .	129
7.5	Example of total systematic error. . . . .	130
8.1	Multiplicity distributions for NSD $pp$ collisions at $\sqrt{s} = 900$ GeV. . . . .	133
8.2	Multiplicity distributions for NSD $pp$ collisions at $\sqrt{s} = 2760$ GeV. . . . .	134
8.3	Multiplicity distributions for NSD $pp$ collisions at $\sqrt{s} = 7000$ GeV. . . . .	135
8.4	$pp$ multiplicity distributions in $ \eta  < 0.5$ at $\sqrt{s} = 900$ GeV. . . . .	136
8.5	$pp$ multiplicity distributions in $ \eta  < 1.0$ at $\sqrt{s} = 7000$ GeV. . . . .	136
8.6	Multiplicity distribution for 0-5% $PbPb$ collisions . . . . .	137
8.7	Multiplicity distribution in $-3.4 < \eta < 5.1$ for $PbPb$ collisions . . . . .	138
8.8	$pp$ NSD collisions in KNO variables . . . . .	139
8.9	Detailed KNO scaling comparison . . . . .	140
8.10	Moments for $ \eta  < 0.5$ multiplicity distributions . . . . .	141
8.11	Moments for $ \eta  < 2.4$ multiplicity distributions . . . . .	142
8.12	KNO scaling in $PbPb$ collisions in various centrality classes. . . . .	143
8.13	KNO scaling in central $PbPb$ collisions in various $\eta$ -intervals . . . . .	144
8.14	$\frac{dN_{ch}}{d\eta}$ in $pp$ NSD collisions . . . . .	145
8.15	$\frac{dN_{ch}}{d\eta}$ in $PbPb$ collisions . . . . .	146
8.16	Mean multiplicity per participant pair scaling with collision energy. . . . .	147
8.17	Preliminary tuning of the simulated energy distributions. . . . .	149
B.1	$N_{part}$ versus impact parameter using the Glauber model. . . . .	155
C.1	Illustration of the concept of hit sharing. . . . .	157
C.2	Flow chart of the sharing algorithm. . . . .	158
D.1	Counting methods comparison in $pp$ collisions at $\sqrt{s} = 2760$ GeV . . . . .	159
D.2	Counting methods comparison in $pp$ collisions at $\sqrt{s} = 7000$ GeV . . . . .	160
D.3	Counting methods comparison in $PbPb$ collisions at $\sqrt{s_{NN}} = 2760$ GeV. . . . .	161
E.1	$Q_1$ parameter for the peak region in $ \eta  < 1.0$ . . . . .	163
E.2	$Q_1$ parameter for the peak region in $ \eta  < 1.0$ . . . . .	164
F.1	$pp$ multiplicity distributions in $ \eta  < 0.5$ at $\sqrt{s} = 900$ GeV. . . . .	165
F.2	$pp$ multiplicity distributions in $ \eta  < 1.0$ at $\sqrt{s} = 900$ GeV. . . . .	166
F.3	$pp$ multiplicity distributions in $ \eta  < 1.5$ at $\sqrt{s} = 900$ GeV. . . . .	166
F.4	$pp$ multiplicity distributions in $ \eta  < 2.0$ at $\sqrt{s} = 900$ GeV. . . . .	167
F.5	$pp$ multiplicity distributions in $ \eta  < 2.4$ at $\sqrt{s} = 900$ GeV. . . . .	167

## VIII

F.6	$pp$ multiplicity distributions in $ \eta  < 3.0$ at $\sqrt{s} = 900$ GeV. . . . .	168
F.7	$pp$ multiplicity distributions in $ \eta  < 0.5$ at $\sqrt{s} = 7000$ GeV. . . . .	168
F.8	$pp$ multiplicity distributions in $ \eta  < 1.0$ at $\sqrt{s} = 7000$ GeV. . . . .	169
F.9	$pp$ multiplicity distributions in $ \eta  < 1.5$ at $\sqrt{s} = 7000$ GeV. . . . .	169
F.10	$pp$ multiplicity distributions in $ \eta  < 2.0$ at $\sqrt{s} = 7000$ GeV. . . . .	170
F.11	$pp$ multiplicity distributions in $ \eta  < 2.4$ at $\sqrt{s} = 7000$ GeV. . . . .	170

# List of Tables

1.1	Overview of the fermions in the Standard Model . . . . .	5
1.2	Overview of the bosons in the Standard Model. . . . .	6
4.1	Overview of the segmentation and placement of the individual FMD rings.	61
5.1	Reconstruction in the FMD and SPD. The signal column show the various stored signals from the two detectors. The tracking column denotes the stored tracks, based on the measured signals. . . . .	72
5.2	Data samples used. . . . .	76
5.3	Flat multiplicity productions used. . . . .	77
5.4	Normal simulation productions used. . . . .	77
6.1	Overview of the trigger conditions used in this work. . . . .	80
6.2	Strangeness correction parametrisation. . . . .	108
7.1	Systematic uncertainty of the FMD and SPD measurements. . . . .	127
7.2	Event multiplicity systematic uncertainty. . . . .	128
C.1	Overview over the amount of single, double and triple signals. . . . .	158



# Preface

More than 10 years ago I was lured into the field of heavy ion physics as a young first year Astronomy student. This first endeavour resulted in a project for the High Energy Heavy Ion (HEHI) group, measuring the lifetime of the K-meson using the BRAHMS experiment at the Relativistic Heavy Ion Collider (RHIC). I continued in both the group and the BRAHMS collaboration, doing my bachelor's thesis on high  $p_T$  suppression at  $\sqrt{s_{NN}} = 200$  GeV, together with fellow students Signe Riemer Sørensen and Hans Hjersing Dalsgaard. After this, Hans and I measured the nuclear stopping in Au-Au collisions at  $\sqrt{s_{NN}} = 62.4$  GeV, a measurement which ultimately was accepted for publication in Physics Letters B [1].

In 2007 I turned in my Master's thesis, which revolved around the rapidity dependence of deuteron coalescence at  $\sqrt{s_{NN}} = 200$  GeV. This work was accepted for publication by Physical Review C [2]. My master's thesis marked the end of my involvement in the BRAHMS experiment.

When I started as a Ph.D. student I also started working on the ALICE experiment, located at the, at the time not operational, Large Hadron Collider (LHC). With the first collisions of the LHC on 23<sup>rd</sup> of November 2009, the entire field of high energy physics entered a new regime with collision energies potentially more than 20 times that of RHIC.

This thesis is the culmination of helping prepare the, locally built, Forward Multiplicity Detector (FMD) for first collisions, as well as studying the topic of charged particle multiplicities into forward pseudorapidities.

The thesis will start off with an introduction to the world of relativistic collisions, introducing both useful concepts as well as presenting some of the cutting edge results, that define the frontier of the field today. Following this is a chapter focusing on the theory behind the main topic of this work, the charged particle multiplicity distributions. This chapter also includes a review of previous multiplicity measurements, performed over the last decades. Chapter 3 focuses on introducing the LHC accelerator facility as well as the ALICE experiment. This leads directly to the next chapter, which zooms in on the specific ALICE detectors used for the measurements of this work; the Silicon Pixel Detector (SPD) and the FMD. Included in this chapter is also a review of relevant semi-conductor detector physics.

The next chapter functions as a transition towards the actual analysis done. It is devoted to discussing the analysis tools used, the initial reconstruction of data as well as the simulations, that are a crucial part of high energy physics. The analysis, the very heart of this work, follows in chapter 6. It presents all the analysis steps going from the initial energy depositions in the active detector elements to the fully corrected measurement results.

After presenting the analysis, the systematic uncertainties on the measurements are treated, before finally arriving at the presentation of the final measurement results. The results are split into four groups, namely measurements of charged particle multiplicity distributions, KNO scaling violation, pseudorapidity densities and finally the energy de-

pendence of the mean multiplicity.

Many people have helped in the process of creating this work. I would like to first thank my supervisor Professor Jens Jørgen Gaardhøje, for the opportunity to experience and participate at the frontier of scientific research, as well as guiding me in the right direction when needed. A special thanks goes to Post.Docs Christian Holm Christensen and Kristjan Gulbrandsen as well as fellow Ph.D. students Hans Hjersing Dalsgaard and Carsten Søgaard. Also a big thank to former Master student (and now Ph.D. student) Alexander Hansen. They have all been a joy to be around, and have contributed with invaluable inputs during countless fruitful discussions. I also wish to thank the rest of the HEHI group, Associate Professors Ian Bearden, Hans Bøggild and Børge Svane Nielsen for being ready with advice and letting me lean on their experiences when needed. Another one who deserves a thanks is Professor Jamie Nagle, who spend 6 months as a guest in the group. With his insights and energy, he managed to make a big impact in a short time.

Finally, I want to thank my family and friends for their love and support. In particular I want to thank my wife Yvonne for her love and patience with me. Without her support I would not be able to do the things I do.

When I entered the field of heavy ion physics as a new student 10 years ago, RHIC had recently started operations. Back then no-one could predict how the field would evolve. Quantities, which were deemed very important for understanding the dynamics of relativistic collisions, were suddenly seen as redundant, and new quantities took their place at the front row. Today, once more we find ourselves at the start of a new era and once again I am excited to see how deep the rabbit hole goes. Happy reading.

Casper Nygaard  
Copenhagen, October 2011

## Contact information:

Address Tøjmestervej 12, st.  
2400 Copenhagen NW, Denmark  
E-mail *cnygaard@nbi.dk*

Supervisor Professor Dr. Jens Jørgen Gaardhøje, Niels Bohr Institute  
E-mail *gardhoje@nbi.dk*

Chair of Opponents Associate Professor Stefania Xella, Niels Bohr Institute.  
Opponent Professor Torbjörn Sjöstrand, Lund University  
Opponent Professor Birger Bo Back, Argonne National Laboratory

*“...Thus the yeoman work<sup>1</sup> in any science, and especially in physics, is done by the experimentalist, who must keep the theoreticians honest.”*

**Michio Kaku**, co-founder of string field theory [3]

---

<sup>1</sup>Old English expression for regular hard, loyal and often great work.

# Chapter 1

## The Standard Model of Particle Physics

With the advent of the Large Hadron Collider, a new era of particle and nuclear physics is signalled. Never before have physicists had so much energy available to investigate the fundamental forces of nature, not least the elusive strong force. The Standard Model of particle physics is a quantum field gauge theory describing three of the four known fundamental interactions between the elementary particles that constitute all matter. It represents the current best knowledge we have obtained through decades of experiments.

The LHC also marks the beginning of investigations into physics that is beyond the Standard Model.

### Fermions

The building blocks of matter in the Standard Model are labelled fermions and comes in two subgroups; the quarks and leptons. There are six different quark flavours, namely the up (u), down (d), charm (c), strange (s), bottom (b) and top (t) quark respectively. Similarly six flavours of leptons exist, the electron (e), electron neutrino ( $\nu_e$ ), muon ( $\mu$ ), muon neutrino ( $\nu_\mu$ ), tau ( $\tau$ ) and the tau neutrino ( $\nu_\tau$ ). Each quark and lepton has a counterpart with identical mass but opposite charges. These are labelled anti-particles. The fermionic particles all have half-odd integer (e.g.  $\frac{1}{2}, \frac{3}{2}, \dots$ ) intrinsic spin and follow the Pauli exclusion principle. The fermionic matter is grouped in three generations; I, II and III. All observed matter in nature consists solely of the light generation I fermions, since the higher (and heavier) generations are unstable and decay into lighter fermions. The Large Electron Positron (LEP) collider has shown that precisely three generations of matter exist [4]. For an overview of the available fermions in the Standard Model see table 1. For more details consult [5].

Fermions			
Generation	I	II	III
Quarks	u	c	t
	d	s	b
Leptons	e	$\mu$	$\tau$
	$\nu_e$	$\nu_\mu$	$\nu_\tau$

Table 1.1: Overview of the fermions in the Standard Model. Each particle has an anti-particle associated with it.

Bosons			
Force	Electromagnetic	Weak nuclear	Strong Nuclear
Mediating boson	$\gamma$	$W^+, W^-, Z^0$	g

Table 1.2: Overview of the bosons in the Standard Model.

## Bosons

Besides the fermions the Standard Model includes bosons, which mediate the fundamental forces. All bosons have integer intrinsic spin, and thus do not follow the Pauli exclusion principle. Currently only three of the known four fundamental forces are described by the Standard Model<sup>2</sup>. These three are the weak nuclear interaction, the strong nuclear interaction and the electromagnetic interaction. The main purpose of particle physics is to study the fundamental interactions. The force mediating bosons are :

- **$W^+, W^-, Z^0$**  : These three bosons mediate the weak nuclear interaction between particles of different flavours. It has (as the only force) the ability to change a particle's flavour as seen in the  $\beta$ -decay, where a down quark in a neutron is transmuted to an up quark by emitting a W-boson.
- **Photon ( $\gamma$ )** : Photons mediate the electromagnetic force between electrically charged particles; i.e quarks, electrons, muons, tau,  $W^+$  and  $W^-$ . They are mass-less and are described by Quantum Electro-Dynamics (QED) [7]. In addition the photon and the three bosons of the weak interaction have been theoretically connected and can be treated as a single electroweak interaction.
- **Gluon (g)** : Gluons mediate the strong nuclear force between quarks of different colour charge, the interaction charge specific to the strong interaction. Gluons are mass-less and, contrary to the other force mediators, carry the interaction charge and can therefore interact with themselves. The strong interaction is described by the theory of Quantum Chromo Dynamics (QCD) [6].

In addition to the mentioned bosons, the inclusion of the so-called Higgs boson into the Standard Model, is needed. Without the Higgs boson the electroweak gauge bosons must be mass-less, which is inconsistent with experimental measurements (in the case of  $W^\pm$  and  $Z^0$ ).

This problem of apparent masses of the electroweak gauge bosons, is solved in the Standard Model, by introducing a Higgs mechanism, where the masses of the other gauge bosons are given by their ability to interact with a field of Higgs bosons. The higher interaction rate with this field, the higher mass. The Higgs mechanism thus can explain the current measured gauge boson masses. However it should be stressed that currently the Higgs boson has not been discovered. The potential discovery of it is one of the scientific cornerstones in the entire LHC physics program.

## Composite Particles

Composite particles made up from quarks and/or anti-quarks are designated as hadrons. The hadrons are composed of two subgroups, the baryons and the mesons:

---

<sup>2</sup>The fourth force, gravity, has not yet been incorporated successfully into the Standard Model, but a force carrier boson, the graviton, has been proposed [6], but has so far not been detected.

- **Baryons:** Baryons are made up of three quarks (or three anti-quarks). Since each quark has half-integer spin, the baryons are fermions themselves. The most well known baryons are the proton (uud) and the neutron (udd).
- **Mesons:** Mesons consists of a quark and an anti-quark, and are therefore bosons.

## 1.1 Quantum Chromo Dynamics

QCD is the theory describing the strong nuclear interaction. As briefly introduced previously, all strongly interacting particles carry colour charge. Colour charge is the strong interaction equivalent to electric charge in QED. There are three different colour charges for quarks, typically labelled red, green and blue. The colour charge have no real resemblance to macroscopic colours. The chosen labels merely utilise the analogy of three primary colours, adding up to be colour neutral<sup>3</sup>. Anti-quarks carry anti-colour charge, sometimes labelled anti-red, anti-green and anti-blue<sup>4</sup>. The gluons mediating the strong force carry both colour, and anti-colour. In total eight independent types of gluons exist [8].

Mathematically several approaches exist for working with QCD. One of these is perturbative QCD (pQCD), where the small coupling constant,  $\alpha_s$ , can be approximated as an expansion, and perturbation theory can be applied. pQCD is only applicable at very short distance scales or large momentum transfers.

Of the non-perturbative approaches the lattice QCD (lQCD) is the most established. lQCD describes space with a set of discrete points (the lattice), thus making it possible do QCD calculations on supercomputers.

## Confinement

The potential between two quarks have the following form [9]:

$$V(r) = -\frac{4\alpha_s(r)\hbar c}{3r} + k \cdot r \quad (1.1)$$

Here  $k$  is the colour string tension and  $\alpha_s(r)$  is the strong interaction coupling constant. Unlike in QED the coupling constant is however not really a constant in QCD. For small values of  $r$  it diminishes; a phenomenon known as asymptotic freedom. The quark-quark potential can be seen in figure 1.1.

The first part of (1.1) is reminiscent to the  $\frac{1}{r}$ -dependence of the electromagnetic potential in QED. However, in QCD the second linear term becomes dominant at large  $r$ . This term is a consequence of the gluon self-interaction [8]. Thus the gluons act like a rubber band, storing more and more energy when stretched further apart. This continues until sufficient energy is available to create new quark/anti-quark pairs.

Therefore it is always favourable entropy-wise to create a quark/anti-quark pair, instead of having the two individual quarks roam freely. This effectively confines all quarks inside colour neutral objects.

Scattering experiments, where one basically tries to separate the quarks by pulling them apart, confirms this, since only colour neutral objects has ever been measured [11].

<sup>3</sup>Analogous to white ‘neutral’ light being composed of the primary colours red, green and blue.

<sup>4</sup>and sometimes as complementary colours, cyan, magenta and yellow respectively.

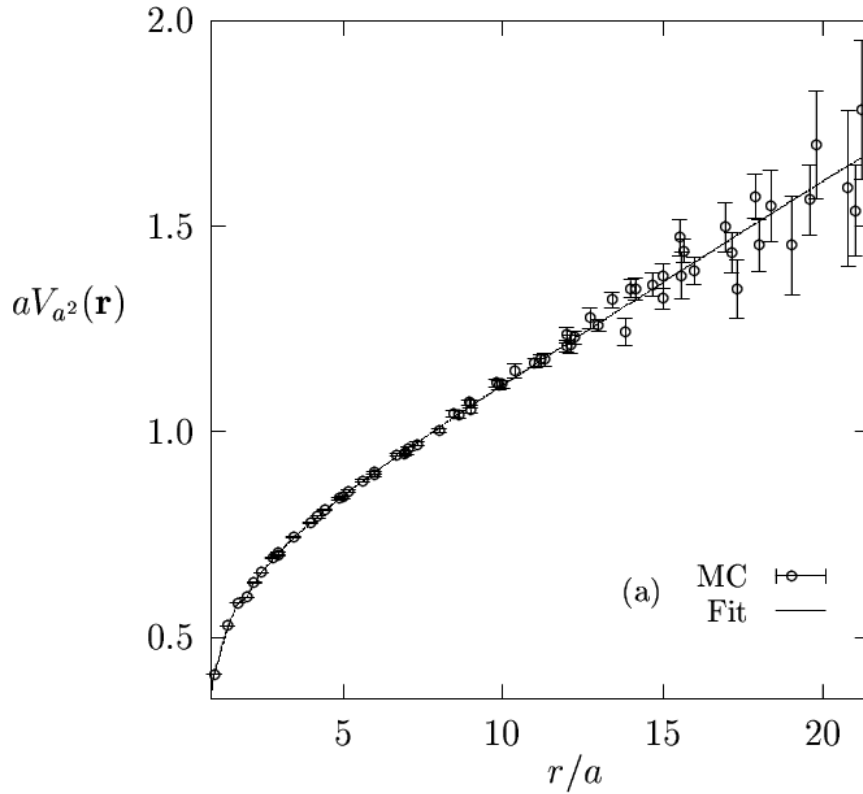


Figure 1.1: The quark-quark potential as a function of the distance between the quarks calculated from lQCD.  $a$  denotes the lattice constant i.e., the distance between individual lattice points. The points show Monte Carlo data, and the corresponding fit. Figure is taken from [10].

## 1.2 Quark Gluon Plasma

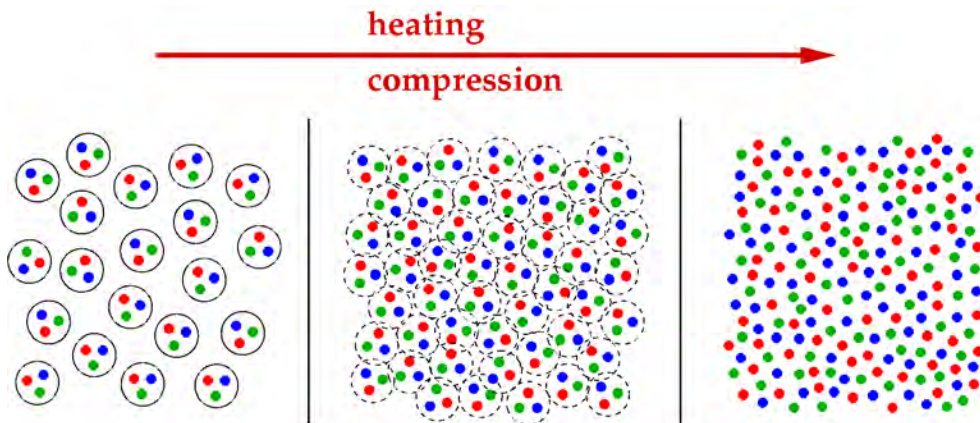


Figure 1.2: The formation of QGP through compression of matter. The hadronic structure breaks down and the quarks are deconfined inside a QGP. Figure taken from [12].

The concept of confinement holds true for normal temperatures and nuclear matter densities. QCD however, predicts a phase of matter in which the quarks are not confined inside hadrons, called a Quark Gluon Plasma (QGP).

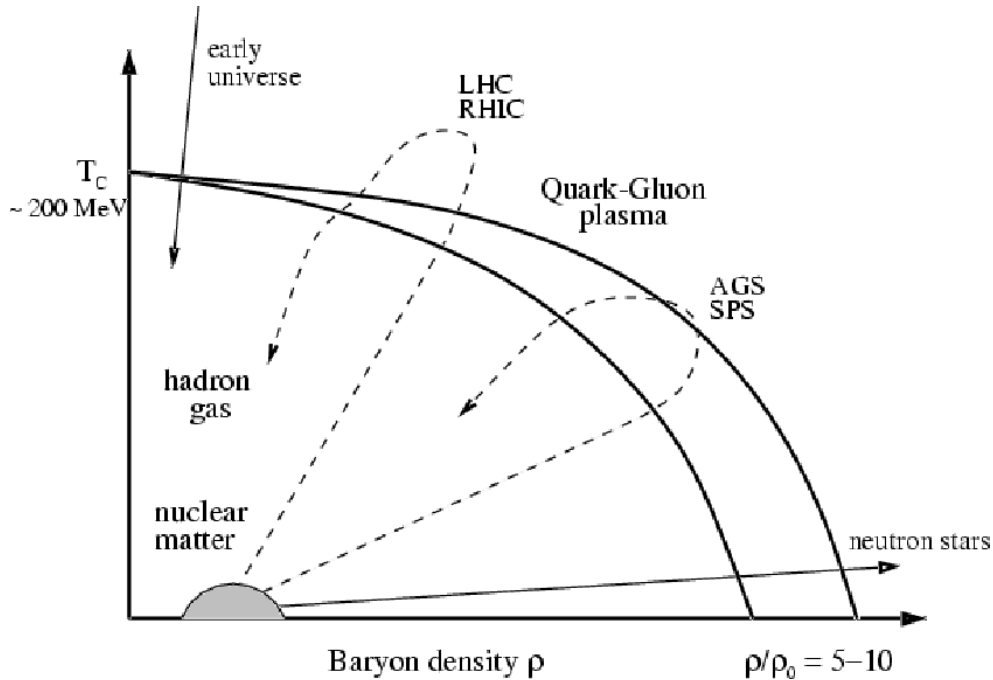


Figure 1.3: QCD Phase Diagram. The paths of several large experiments are shown. Furthermore the conditions in the early Universe, nuclear matter and neutron stars are indicated. It is worth mentioning that plotting the phase space as a function of baryon density or baryon-chemical potential (as used in the text) makes no conceptual difference, since the two are thermodynamically conjugate variables. Figure taken from [12].

The main idea of a heavy ion physics QGP, sketched in figure 1.2, is as follows. Consider a fixed volume, in which hadrons are filled. Since hadrons have a non-zero spatial volume [9], there exists a critical point where the hadrons completely fill out the volume. Adding even more hadrons (or decreasing the size of the volume) will thus cause the hadronic structure to break down, creating a plasma of ‘free’ quarks and gluons. It is worth mentioning that the quarks/gluons are still confined inside the plasma, but not inside hadrons.

The term plasma suggests a gas-like behaviour with few interactions. However the state of matter created at the Relativistic Heavy Ion Collider (RHIC) at centre-of-mass energy  $\sqrt{s_{NN}} = 200$  GeV and at the LHC at  $\sqrt{s_{NN}} = 2760$  GeV indicates a more strongly interacting QGP, with more interactions, thus behaving more like a perfect fluid [13].

The phase transition to QGP is predicted to happen at a critical temperature of  $T_C = 173 \pm 3$  MeV [14] for a chemical potential of  $\mu_B = 0$ . An illustration of the QCD phase diagram can be seen in figure 1.3.

It is obvious from figure 1.3 that there are essentially two ways of gauging the QGP phase; by raising either the temperature or by raising the chemical potential. At the Large Hadron Collider<sup>5</sup> the former approach is used.

<sup>5</sup>And the same is the case in previous experiments. The upcoming FAIR collider will follow the other approach.

## Cosmological Quark Gluon Plasma

Observational evidence in the field of cosmology coherently suggests that our Universe started as a mathematical singularity exploding spectacularly in the Big Bang. All the matter/energy of the Universe thus was concentrated in a volume of high density, temperature and pressure; the necessary conditions for a QGP to have formed. As a consequence of the rapid expansion, the Universe cooled down quickly. At approximately  $1 \mu\text{s}$  after the Big Bang the very hot Universe is believed to have been in a QGP phase, before hadronising.

The cosmological QGP and the QGP probably created in heavy ion collisions are not believed to be identical. Firstly the cosmological QGP is believed to have existed for a time scale of  $10^{-6}$  s whereas the observed heavy ion QGP has a lifetime of the order of  $10^{-23}$  s  $\sim 1$  fm/c [15]. Secondly, the baryon number densities of the early Universe is thought to be of the order  $N_b/N \sim 10^{-10}$  compared to the  $N_b/N \sim 10^{-1}$  in heavy ion collisions [15]. Here  $N$  refers to all particle types, i.e. hadrons, leptons, photons etc.

In the heavy ion collision QGP the baryonic density is sufficiently large, that strong interactions between quarks and gluons will happen regularly, and thus the medium can be said to be strongly interacting. This is believed to be in contrast to the situation in the early Universe where the scarcity of baryons makes strong interactions improbable. Furthermore the lifetime of the cosmological QGP certainly allows it to reach thermal equilibrium. For the heavy ion collision QGP this is still a topic of dispute. However recent theoretical calculations indicate that thermalisation might be possible as early as 0.35 fm/c after the collision [16].

## 1.3 Kinematic Variables

This section introduces kinematic variables and concepts which are fundamental to high energy/heavy ion physics in general.

The four-momentum of a particle of rest mass  $m_0$ , momentum  $\vec{p}$ , and energy  $E$  is given as:

$$P = (E, \vec{p}) = (E, p_x, p_y, p_z) \quad (1.2)$$

The traditional convention of setting  $\hbar = c = 1$  is utilised here. For  $2 \rightarrow 2$  particle reactions with four-momenta  $P_1$  and  $P_2$  before the reaction and four-momenta  $P'_1$  and  $P'_2$  after the reaction, the so-called Mandelstam variables are useful:

$$\begin{aligned} s &= (P_1 + P_2) = (P'_1 + P'_2) \\ t &= (P_1 - P'_1) = (P_2 - P'_2) \\ u &= (P_1 - P'_2) = (P_2 - P'_1) \end{aligned} \quad (1.3)$$

Thus  $\sqrt{s}$  is the collision energy in the centre-of-mass frame, and similarly  $\sqrt{t}$  is the momentum transfer. For heavy ion collisions, the collision energy is typically given per nucleon pair in the notation  $\sqrt{s_{NN}}$ .

Kinematic variables are expressed in terms of the ALICE global coordinate system, which is illustrated in figure 1.4.

The momenta of the created particles, are split into a longitudinal component,  $p_z$ , along the beam-line and a transverse momentum component,  $p_T$ , orthogonal to the beam. The

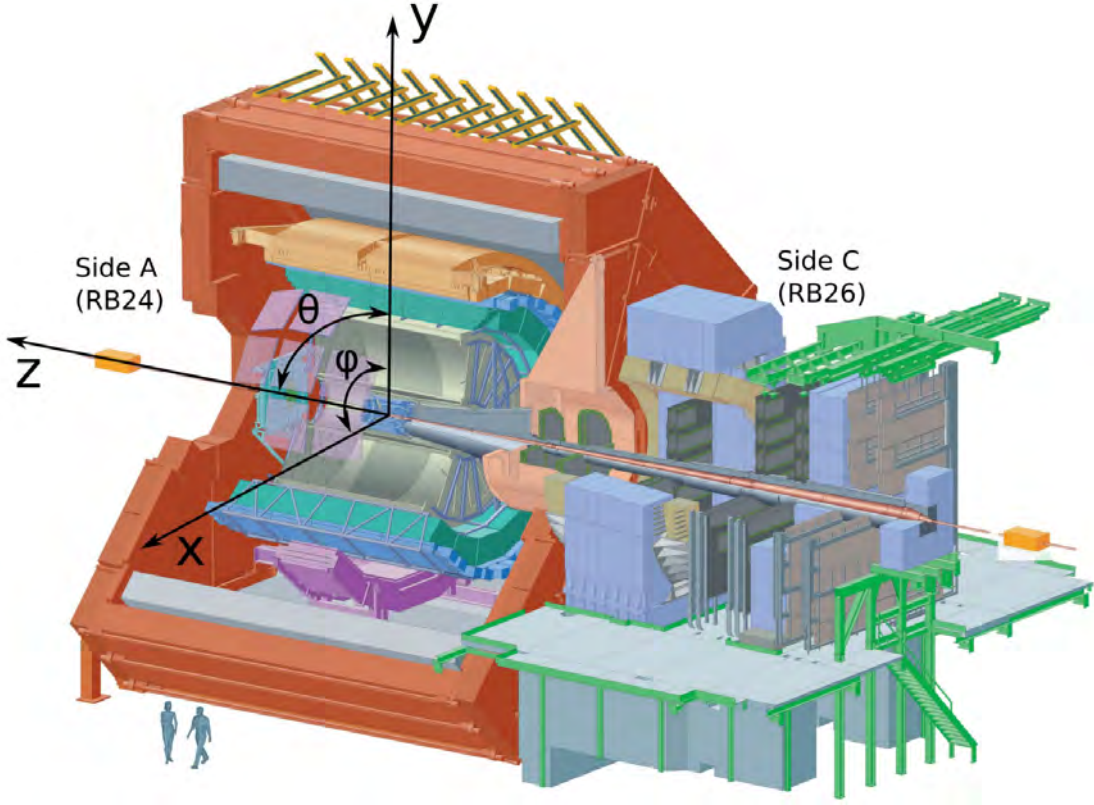


Figure 1.4: The ALICE global coordinate system. The z-axis always follow the beam direction, the x-axis points towards the accelerator centre, and the y-axis points upwards. Included is also the definitions of the angles  $\theta$  and  $\phi$ . The ALICE experiment itself will be treated in details in chapter 3.

transverse momentum and mass are given by:

$$p_T = \sqrt{p_x^2 + p_y^2} \quad \text{and} \quad m_T = \sqrt{m^2 + p_T^2} \quad (1.4)$$

Both the transverse mass and momentum are Lorentz invariant making them excellent variables in relativistic systems. Instead of using longitudinal momentum it is common practise to use the rapidity,  $y$ , which is defined as:

$$y = \frac{1}{2} \ln \left( \frac{E + p_z}{E - p_z} \right) \quad (1.5)$$

$E$  is the particle energy,  $E = p^2 + m^2$ . The rapidity is useful as a longitudinal variable compared to longitudinal momentum, since rapidity differences are Lorentz invariant (see Appendix A for more detail). In the case where one look at unidentified particles the pseudorapidity,  $\eta$ , replaces the rapidity as variable:

$$\eta = -\ln(\tan(\theta/2)) \quad (1.6)$$

$\theta$  denotes the polar angle between the momentum vector,  $p$ , and the beam axis. In the case where  $|p| \gg m$  the rapidity reduces to the pseudorapidity.

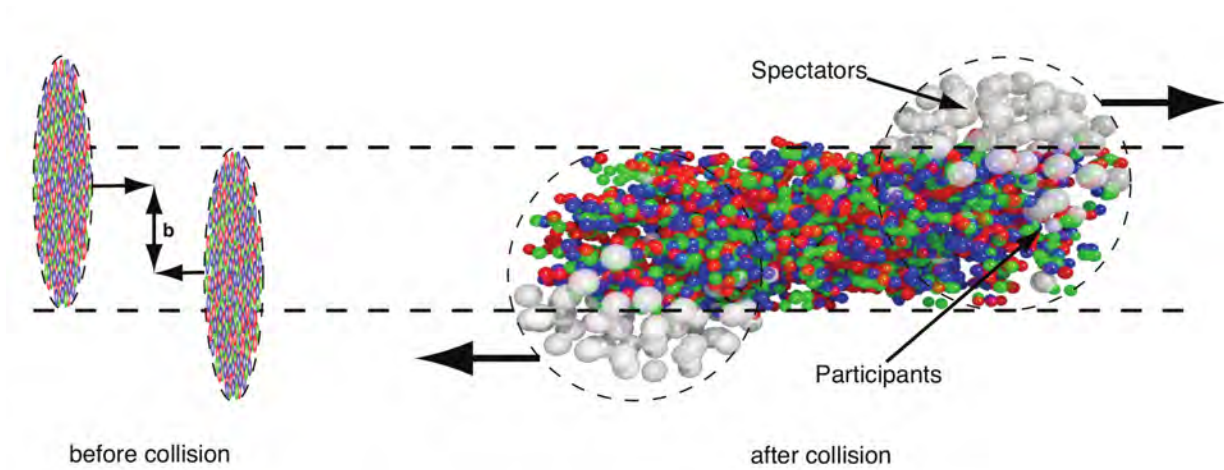


Figure 1.5: Schematic illustration of a relativistic heavy ion collision. The participant nucleons of the overlap region between the colliding nuclei form the high density fireball, whereas the rest of the nucleons continues unaffected as spectators. Picture taken from [17].

## 1.4 Relativistic Collisions

Relativistic collisions can be divided into three categories:

- AA** Collisions between heavy ions. Heavy nuclei are collided, creating thousands of final state particles in each collision. At the ALICE experiment, which is the foundation for this work, the main focus is on heavy ion  $PbPb$  collisions. Heavy ion collisions are expected to create a QGP, before cooling down.
- pp** Collisions between protons. The main focus on the LHC  $pp$  program (that take up the vast majority of beam time) is to discover the Higgs boson and possibly verifying the existence of Super SYmmetric (SUSY) particles. However since ALICE is a heavy ion detector, it does not have the trigger rate to gather enough statistics to be viable in those searches. Instead  $pp$  collisions at ALICE play another, but also important role in both looking for new physics, as well as a baseline measurement for  $PbPb$  collisions.
- pA** Collisions between protons and heavy ions. The LHC has not provided collisions between protons and lead-ions yet. For the heavy ion community this is a high priority, since these asymmetrical collisions, does not have a dense hot medium, and thus can yield important insights into the initial state of collisions. The LHC will attempt to deliver the first pA collisions at the end of 2011. The run plans for the following years will be heavily influenced depending on their success.

In the following an introduction to both proton-proton collisions and heavy ion collisions is given.

### 1.4.1 Relativistic Heavy Ion Collisions

While the majority of the results in this thesis are from  $pp$  collisions, one should keep in mind that due to the ALICE experiment being a heavy ion detector, the long range main focus is still on heavy ion physics. Furthermore the concepts from heavy ion physics might

prove more and more useful, since  $pp$  collisions at very high energies start to resemble heavy ion collisions more and more, with for instance collective effects appearing [18].

In Figure 1.5 an illustration of a relativistic collision is shown as seen from the laboratory frame of the nuclei. Each nucleus is highly Lorentz contracted along its direction of motion.

### Participants and Spectators

The nucleons directly involved in the collision, called participants, interact strongly giving rise to a high density volume, known as the fireball. Nucleons outside the overlapping region of the two nuclei are called spectators. They are unaffected by the collision except for Coulomb-interactions and they retain their initial momentum, flying away from the fireball.

Figure 1.5 also introduces the impact parameter,  $b$ , which is the transverse distance between the centres of the two nuclei. Hence a large impact parameter corresponds to a peripheral collision, where a small region of the nuclei overlap, whereas a small impact parameter gives a central collision with a large overlapping region. As it is practically impossible to measure the impact parameter directly, an experimental technique is used to connect impact parameter with centrality. The centrality can be measured using the total charged particle multiplicity of the events. This is discussed in section 6.1.3.

The impact parameter is through models connected to the centrality of the collision in the following way:

$$c = \frac{\int_0^{b_c} \frac{d\sigma_{in}(b')}{db'} db'}{\sigma_{in}} \quad (1.7)$$

Here  $\sigma_{in}$ ,  $\frac{d\sigma_{in}(b')}{db'}$  and  $b_c$  are the total inelastic nuclear reaction cross section, the differential cross section and a cut-off in the impact parameter respectively. Thus the centrality,  $c$ , denotes the probability that a collision occurs with a impact parameter of  $b \leq b_c$ . For a solid sphere  $\frac{d\sigma_{in}(b)}{db} = 2\pi b db$  and thereby under the assumption that nuclei are identical and spherical the centrality becomes:

$$\begin{aligned} c &= \frac{\int_0^{b_c} 2\pi b db}{\int_0^{2R} 2\pi b db} \\ &= \frac{b_c^2}{4R^2} \end{aligned} \quad (1.8)$$

Here  $R$  denotes the radius of the nuclei. The impact parameter and the number of participants in the collision are statistically related. Their relation can be estimated using the Glauber model [19]. A short introduction to it can be found in Appendix B.

### The Bjorken Picture

A very important contribution to heavy ion physics is a paper from 1983 by Bjorken [21], which uses a hydrodynamical description of the central rapidity region in heavy ion collisions. The description relies on four important assumptions on collisions between nuclei with nucleon number  $A$ :

- **Boost invariance** : The rapidity densities  $\frac{dN}{dy}$  are independent of rapidity for at least a few units of rapidity around mid-rapidity in  $pp$  and  $pA$  collisions. From this it is assumed that the same is true for  $AA$  collisions.

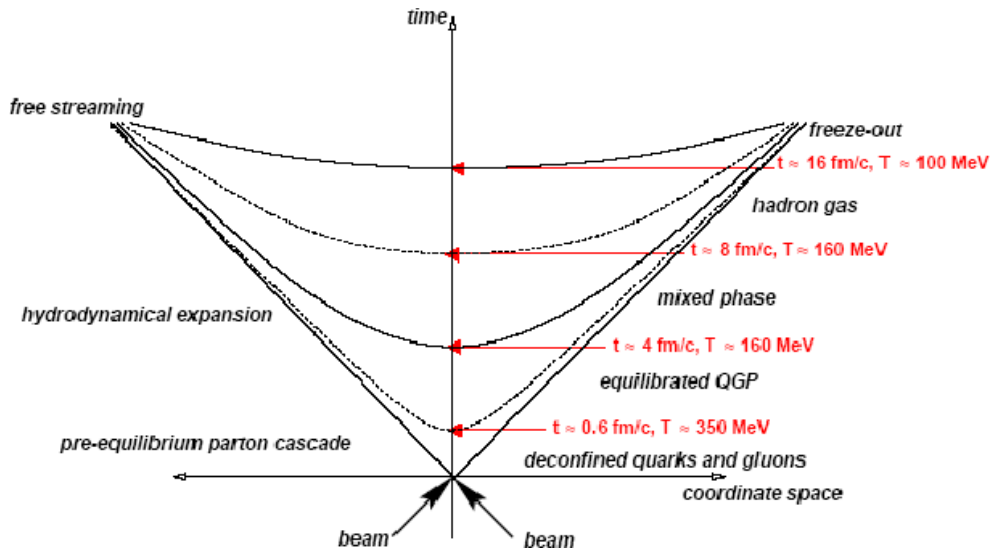


Figure 1.6: Proposed space-time evolution of a heavy ion collision. Quarks and gluons are at first deconfined in a QGP which thermalises; eventually the hadrons freeze out and streams away freely. Picture taken from [20].

- **Transparency :** The nuclei interpenetrates in the  $AA$  collision and the central plateau is formed through particle production from the breaking of colour strings. The fragments of the original nuclei end up some units of rapidity away from mid-rapidity. In Lorentz frames with velocities close to the mid-rapidity frame, the nuclei look like flat pancakes.
- **Transverse expansion :** The transverse expansion of the source can be ignored for most of the collisions because of the large initial transverse scale of the source compared to its longitudinal scale. This is only true for central collisions and reduces the problem to a 2-dimensional problem in the coordinates  $z$  and  $t$ .
- **Thermalisation :** At some early time, assumed to be of the order of the characteristic hadronic time scale  $t \sim 1$  fm/c, the system thermalises and hydrodynamics governs the evolution and expansion of the source.

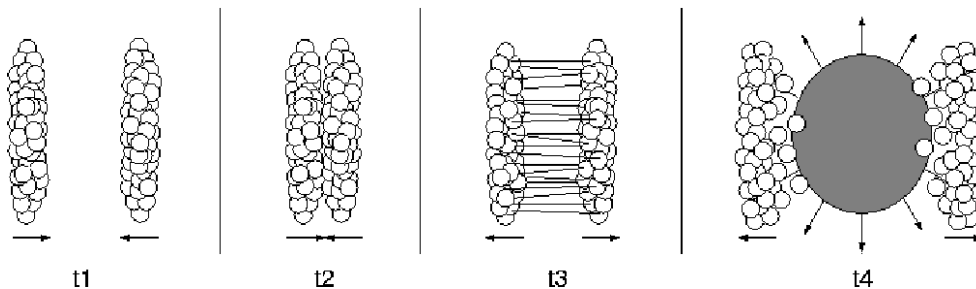


Figure 1.7: Simplistic view of a collision in the transparent Bjorken picture. Picture taken from [12].

If it is assumed that at  $t \sim 0$  the longitudinal extension,  $z$ , is negligible, and the proper time,  $\tau$ , is given by:

$$\begin{aligned} \tau \equiv \frac{t}{\gamma} &= \sqrt{t^2(1 - \frac{z^2}{t^2})} \\ &= \sqrt{t^2 - z^2} \end{aligned} \quad (1.9)$$

In a space-time diagram this yields hyperbolas of constant energy densities, which can be used to distinguish different evolutionary phases in heavy ion collisions. In figure 1.6 a sketch of the space-time evolution of a central collision is shown.

In the Bjorken picture the incoming nuclei are transparent to each other as mentioned, allowing them to interpenetrate without losing much of their initial kinetic energy. However, upon doing so they leave a highly excited colour field between them, in which particle production takes place due to the breaking of colour strings. The concept of transparency is illustrated in figure 1.7.

### The Landau Picture

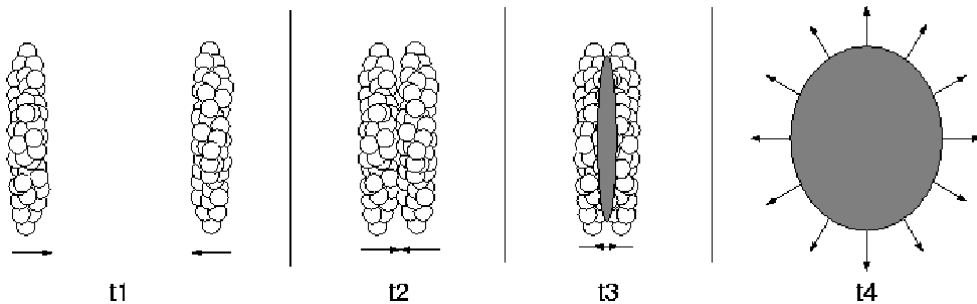


Figure 1.8: Simplistic view of a collision in the stopping picture. Picture taken from [12].

The opposite of the transparent Bjorken picture is a picture where full nuclear stopping is assumed. This picture was proposed by Landau in [22]. Landau argued that:

- **Full stopping** : The incoming nuclei are fully stopped when hitting each other. All their initial kinetic energy is deposited in the fireball.
- **Hydrodynamics** : Particles in the fireball have small mean free paths, so the fireball can be treated as an ideal fluid in the sense that it is non-viscous and non-heat conducting.
- **Adiabatic expansion** : The fluid expands adiabatically, i.e. the entropy is constant.

A collision in accordance with the Landau picture is illustrated in figure 1.8. These two extreme pictures correspond to very different macroscopic physical phenomena. The transparent Bjorken picture is reminiscent of the early Universe, with very high temperature and low baryo-chemical potential,  $\mu_B$ . In the other end of the scale, Landau's stopping picture is reminiscent of the conditions inside stellar objects like neutron stars, with large  $\mu_B$  and relatively low temperature. At RHIC it was found by nuclear stopping measurements, that the higher the collision energy is, the more transparent the collision is [1, 23].

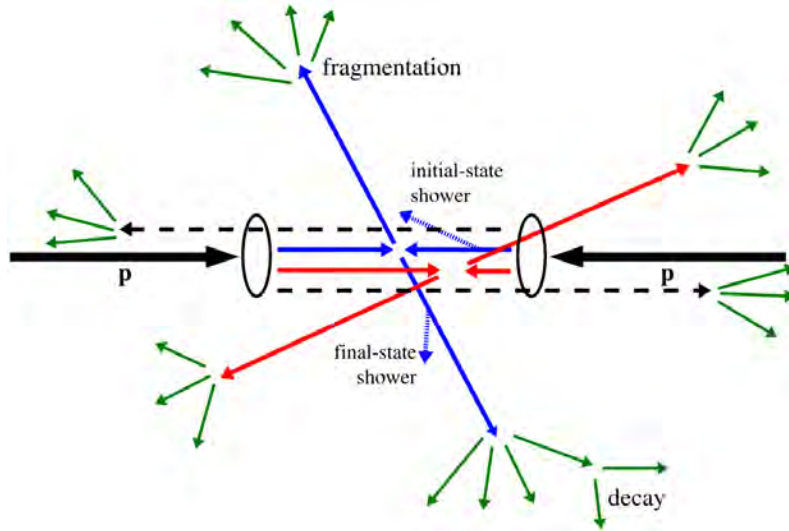


Figure 1.9: Schematic of a  $pp$  collision. Figure is from [24]. An incoming parton might branch ( $q \rightarrow qq$ ) before the collision in an initial-state shower. Similarly a parton branching after the collision is referred to as a final-state shower. After the collision colour string span between the outgoing quarks and gluons. These fragments into colourless hadrons, as described previously. The fragmented hadrons can be unstable, and further decay.

## 1.4.2 Proton-Proton Collisions

Initially, collisions between two protons might seem much simpler than collisions of ions, with hundreds of participants, but it is a truth with heavy modifications.

$pp$  collisions serve as a great reference measurement for heavy ion measurements due to a number of reasons. One of the main reasons is that  $pp$  collisions have not previously been believed to create a QGP. Thus deviations in measured quantities in  $pp$  and heavy ion collisions can serve as a probe of the differences between the two systems. And therefore, if no QGP is created in  $pp$  collisions, then differences between the two systems is useful for directly probing the characteristics of the QGP formed in  $PbPb$  collisions. However, it should be noted that it has been proposed that collective effects, and possibly even the formation of a QGP, could occur in very high energy  $pp$  collisions [18].

Regardless of whether or not such a QGP is formed in  $pp$  collisions,  $pp$  measurements does have a full physics motivation in its own right, with an important contribution being multiplicity results as presented in this work.

A schematic of a  $pp$  collisions is shown in figure 1.9.

### Diffraction

When dealing with inelastic  $pp$  collisions it is customary to distinguish between non-diffractive, single-diffractive and double diffractive events (ND, SD, and DD respectively).

The concept of diffraction in particle physics is analogous to diffraction in optics, where light beams scatter on obstacles.

A diffractive event is characterised by the colliding particle(s) being excited. This excitation creates a diffractive system, that carries the quantum number of the original particle, and subsequently fragments/decays into final state particles. For SD events only

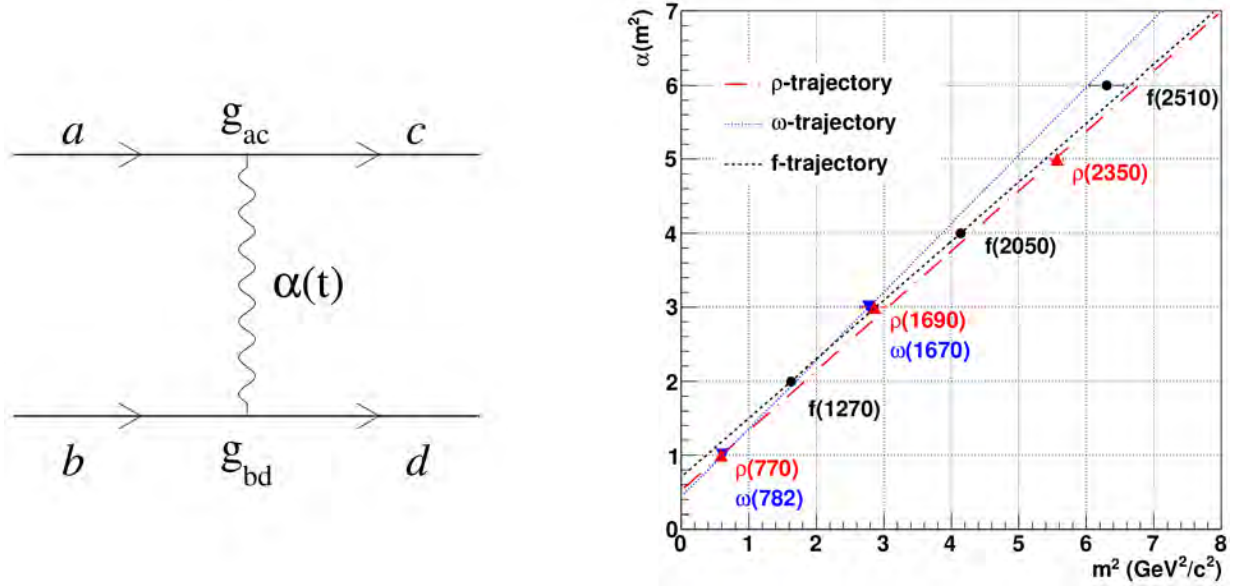


Figure 1.10: Left panel: Feynman diagram of a Regge Pole. The two gluons exchange a particle of spin  $J = \alpha(t)$ . Right panel: An example of a Chew-Frautschi plot, with the Regge trajectories for the  $\rho$ ,  $\omega$  and  $f$  mesons indicated.

one of the colliding particles becomes a diffractive system, whereas both of the particles become diffractive systems in the case of DD events. As the name implies no diffractive systems are created for ND events. The excitation of one or both of the incoming nucleons are thought to stem from gluons exchanging a so-called Pomeron. In this context the Pomeron is a strongly interacting colour singlet, which carry the quantum numbers of the vacuum [25]. However the exact nature and role of the pomeron in QCD is still not completely clear. [26]. In the following the theoretical motivation for the notion of pomeron exchange is briefly presented.

The introduction of the Pomeron stem from Regge Field Theory [26]. It describes the so-called Regge Pole, which corresponds to exchanging an object of spin  $J$  (which could be complex). A schematic Feynman diagram of the Regge Pole exchange is seen in the left panel of figure 1.10. A way to organise particles is to map them by plotting  $J$  as a function of mass squared,  $m_J$ . This plot is called a Chew-Frautschi plot, and is shown in the right panel of figure 1.10. Hadrons of the same type (in this context meaning same isospin, same parity etc.) can all be described by so-called Regge trajectories adhering to the linear form:

$$J = \alpha(t) = \alpha_0 + \alpha'(t)m_J^2 \quad (1.10)$$

For all hadrons the intersection value of  $J$  at  $m_J^2 = 0$ ,  $\alpha_0$ , is below unity. The first equality of (1.10) is due to the spin being dependent on the transferred momentum,  $t$ .

The contribution to the scattering amplitude in a Regge pole exchange at large energies  $s$  is given by [26]:

$$A(s, t) \propto s^{\alpha(t)} \quad (1.11)$$

Additionally the optical theorem for large  $s$ , can be rewritten, and yields the following

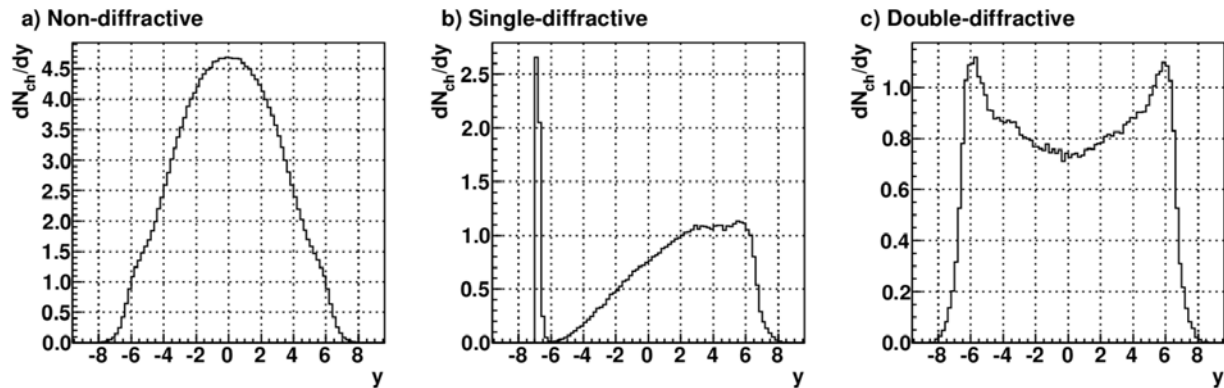


Figure 1.11: The difference in rapidity density shape for ND, SD, and DD events. Note that the scale is different.

contribution to the total cross section from the Regge Pole [25]:

$$\sigma_{tot} = \frac{1}{s} \Im(A(s, 0)) \propto s^{\alpha(0)} \quad (1.12)$$

Since all hadrons follow Regge trajectories with  $a_0 < 1$  this can not explain the experimental evidence that the total cross-section rises slightly with collision energy. For that a object with  $a_0 > 1$  is needed. This object is named the Pomeron, responsible for creating diffractive systems. Having a single Regge Pole Pomeron exchange would make the cross-section rise as a power law of  $s$ . This is in contradiction to the Froissart-Martin bound [27], which states that the cross-section can not increase faster than  $\ln^2 s$  for  $s \rightarrow \infty$ . The contradiction is resolved by including multiple Pomeron exchanges (referred to as eikonalisation), which in the end ensures that the cross-section increase is within the Froissart-Martin limit<sup>6</sup>.

Now turning back to the different types of diffractive events. The Pomeron exchange and excitation of the incoming nuclei heavily affect the distribution of final state particles observed. Figure 1.11 shows the pseudorapidity density of ND, SD, and DD events. For ND events the distribution is maximum around mid-rapidity and falls off steeply. For SD events one of the nuclei continues unaffected ending up at beam rapidity, whereas the other fragments (mostly) into forward rapidities. In DD events both nuclei fragment giving two peaks at forward rapidities and a minor dip in the central region.

Since the physics processes of collisions with diffraction and without can be significantly different one would ideally measure only ND events. However this is seldom possible. Historically, experiments have measured Non Single Diffractive events (i.e excluding the SD events). This is experimentally possible by discriminating the SD events due to their rapidity asymmetry. The DD events however are difficult to separate from the ND events, why the NSD event class is often used. Furthermore the cross-section of DD events compared to ND events are not too significant ( $\sigma_{DD}/\sigma_{INEL} \sim 0.1$  [28]), and thus the NSD event class is not too different from a pure inelastic event class.

In this work NSD events have been analysed for  $pp$  collisions, and Minimum Bias events have been analysed for  $PbPb$ -collisions.

<sup>6</sup>A closing historical remark on this is that the Regge trajectories can be explained by either the hadrons being composite objects, or if they are describable by elastic strings. This observation is among the influences that lead to the realisation by Gell-Mann that hadrons are indeed composite objects, composed of quarks. The other possibility of having elastic strings heavily influenced the eventual creation of the first string theories.

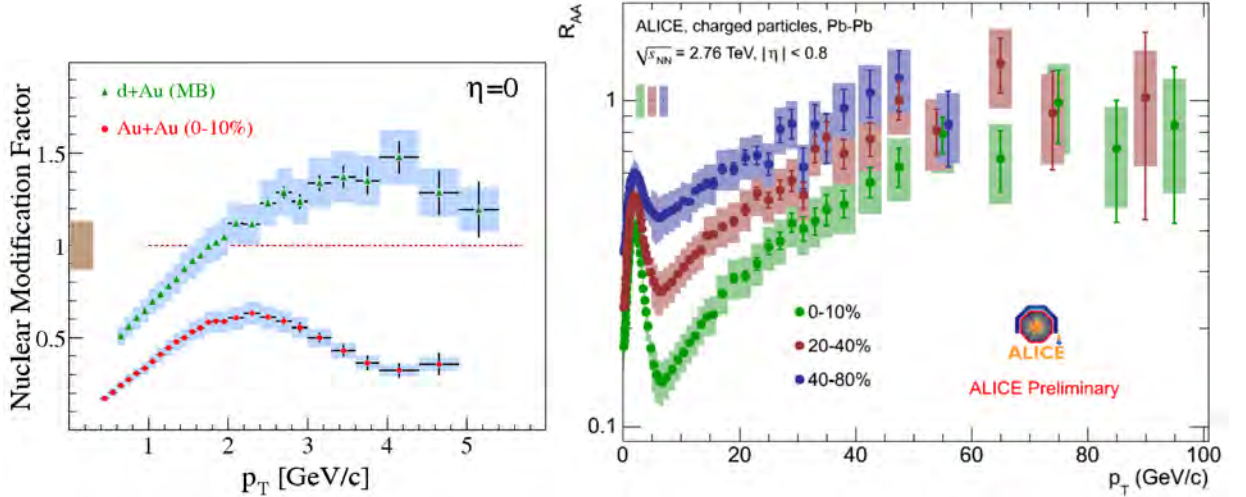


Figure 1.12: Left Panel: Nuclear modification factors measured by BRAHMS [29] in central  $AuAu$  and  $dAu$  collisions at  $\sqrt{s_{NN}} = 200$  GeV. Right panel: Nuclear modification factors measured in three centrality bins for  $PbPb$  collisions at  $\sqrt{s_{NN}} = 2760$  GeV by ALICE [30]. The suppression seen at RHIC is confirmed by ALICE. The nuclear modification factor rises slowly with  $p_T$  at very high  $p_T$ .

## 1.5 Previous Heavy Ion Results

This section is devoted to giving a brief overview of some of the experimental highlights of the recent years. It is an intriguing period with two strong experimental programs setting the stage; LHC gauging the highest energy possible, hoping to discover new physics and RHIC focused on scanning lower energies, in order to pin-point a possible QCD critical point<sup>7</sup>

Interesting results have already been published, and will continue to be so in the coming time. This chapter will only focus on briefly presenting three of the topics that have been instrumental in shaping the understanding of the medium created in heavy ion collisions over the past years. The next chapter is dedicated solely to multiplicity theory and previous multiplicity results.

### High $p_T$ Suppression

One of the first indications of a QGP at RHIC was the discovery that high  $p_T$  particles in central  $AuAu$  collisions at  $\sqrt{s_{NN}} = 200$  GeV were suppressed compared to  $pp$  collisions. Experimentally this is measured by the nuclear modification factor:

$$R_{AA} \equiv \frac{d^2N/dp_T d\eta_{AA}}{N_{bin} d^2N/dp_T d\eta_{pp}} \quad (1.13)$$

where  $R_{AA}$  is the transverse particle production of A+A collisions relative to a reference of  $pp$  collisions scaled by the number of binary collisions,  $N_{bin}$ .

The results from RHIC [31, 32] prompted the measurement of  $R_{AA}$  to be one of the top priorities at the LHC. The first LHC results confirms the suppression of high  $p_T$  par-

<sup>7</sup>QCD predicts a first order phase transition from hadronic matter to a QGP to have a minimum baryo-chemical potential. The onset of this 1<sup>st</sup> order transition is called the critical point. At lower potentials the phase transition is thought to be a smooth crossover.

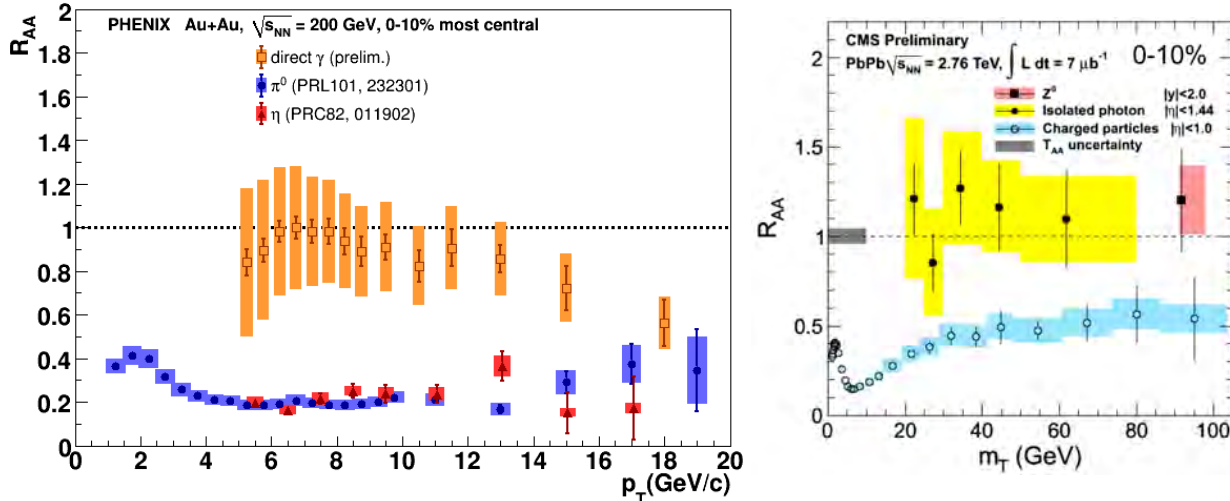


Figure 1.13: Nuclear modification factors for various particle species measured by PHENIX and CMS. Left panel shows PHENIX data [31, 32, 35] from RHIC for  $\pi^0$ ,  $\eta$  and direct photons at  $\sqrt{s_{NN}} = 200$  GeV. Right panel shows preliminary CMS data [33] for charged particles, isolated photons and  $Z^0$ . In both cases it is seen that the photons (and  $Z^0$ ), which do not interact strongly, are not suppressed.

ticles at LHC energies [30, 33]. Figure 1.12 shows the  $R_{AA}$  results for three centrality classes measured by ALICE in  $PbPb$  collisions at  $\sqrt{s_{NN}} = 2760$  GeV as well as  $R_{AA}$  results from BRAHMS at  $\sqrt{s_{NN}} = 200$  GeV. It is seen that there is heavy suppression over a very large  $p_T$ -range, especially for the most central collisions. The suppression is attributed to coloured objects interacting strongly with the medium, by emitting gluons as bremsstrahlung [13]. This is in contrast to  $dAu$  collisions, as measured by BRAHMS, where no suppression is seen, in accordance with expectations of no formed hot medium [29].

At very high  $p_T$  the nuclear modification factor starts rising gently, thus there is less suppression. The cause of this rise is not fully understood, but various models including Gyulassy-Levai-Vitev energy loss models predicts this behaviour [33, 34].

Direct photons, stemming from the initial interaction point/time, were however found not to be suppressed at RHIC [35]. Since they only couple to the electromagnetic force it is indicative that the medium suppressing high  $p_T$  particles is in fact strongly interacting, but not electromagnetically interacting. The nuclear modification factor of various particles including direct and isolated photons<sup>8</sup> from PHENIX and CMS respectively is shown in figure 1.13.

High  $p_T$  suppression is a clear indication of the formation of a strongly interacting QGP.

## Jet Quenching

Another of the early indications of the presence of a QGP at RHIC was the measurement of dihadron azimuthal correlations. The STAR experiment presented this in [36, 37], which is shown in the left panel of figure 1.14. Dihadron azimuthal correlation revolves around observing jets of high momentum particles near the fireball edge. One of the jets (the

<sup>8</sup>Direct and isolated photons are both probes of the very early phase, but the terms are not necessarily interchangeable. Direct photon analyses have decay photons statistically removed; isolated photon analyses try to eliminate these by requiring that the selected photon is spatially isolated. Thus there can be subtle differences between them. However, in the high  $p_T$  suppression physics perspective they are comparable.

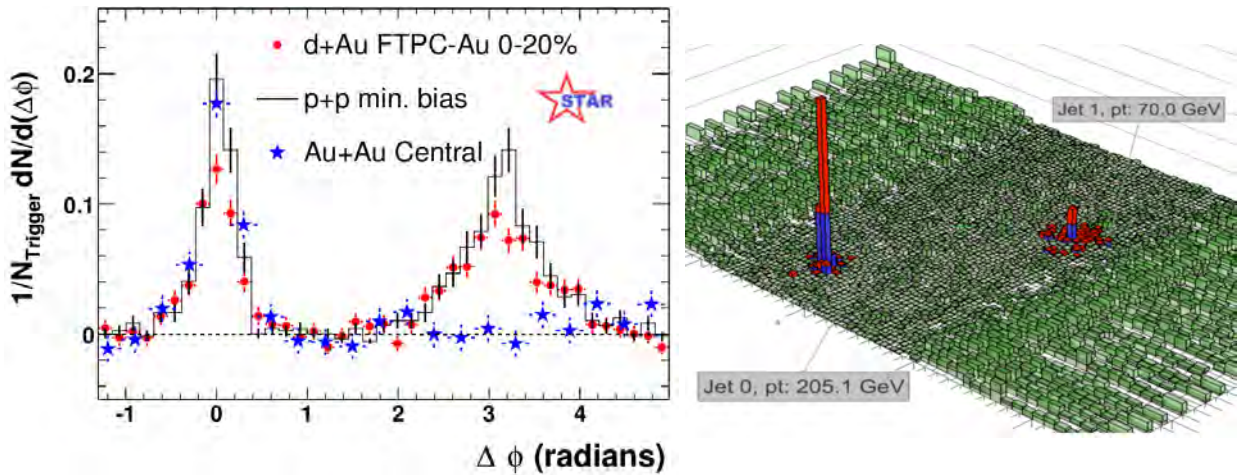


Figure 1.14: Left panel: Jet Quenching measured by STAR at  $\sqrt{s_{NN}} = 200$  GeV [36, 37]. The jet travelling the shortest path through the medium ( $\Delta\phi \sim 0$ ) is enhanced compared to the jet travelling through the longest path in the medium ( $\Delta\phi \sim \pi$ ). This is not seen in  $dAu$  and  $pp$  collisions, and is interpreted as the existence of a strongly interacting QGP at RHIC. Right panel: A concrete example of a jet reconstruction from CMS at  $\sqrt{s_{NN}} = 2760$  GeV [38]. The leading jet appears to be much more energetic than the away-side jet.

leading jet) is emitted away from the fireball, while the other is emitted in the opposite direction through the hot medium. In  $pp$  and  $dAu$  collisions the jets are measured at  $\Delta\phi \sim 0$  and  $\Delta\phi \sim \pi$ . However in  $AuAu$  collisions only the first jet is observed. The jet traversing the longest distance through the medium is not detected. This is due to it interacting strongly with the medium; it has been completely quenched by losing most of its energy to the medium.

Moving to LHC energies, significant jet quenching is also seen. However at the LHC the (weakened) away side jet escapes through the medium. This is shown by CMS [38] in the right panel of figure 1.14. However a lot of energy is missing. This dijet energy imbalance can be quantified by:

$$A_j = \frac{p_{T,1} - p_{T,2}}{p_{T,1} + p_{T,2}} \quad (1.14)$$

Here  $p_{T,i}$  is the transverse momentum of the  $i^{th}$  jet. Figure 1.15 shows the number of events as a function of  $A_j$  for various centralities at  $\sqrt{s_{NN}} = 2760$  GeV, measured by ATLAS [39, 40]. It is seen that for central collisions the jet events become increasingly imbalanced, a feature not seen in neither  $pp$  collisions or HIJING/PYTHIA simulations.

The energy and momentum balance can be recovered by considering the entire final state event. For central heavy ion collisions the jet energy lost in the medium is re-distributed over the full  $\phi$ -range. This is shown in figure 1.16. It shows (as a function of  $A_j$ ) the missing momentum by the quantity  $p_T^{\parallel}$ , which is the projection of  $p_T$  on the leading jet axis. Negative values show an excess towards the leading jet, and positive values show an excess away from the leading jet. Thus it is seen that the leading jet consists mainly of high  $p_T$  particles in the cone region. On the opposite side, the entire momentum of the away side jet is not found in the cone. Looking in the region outside the cone, it is seen that the remaining momentum of the away side jet has been redistributed to this region. Overall the momentum balance of the entire final state is conserved.

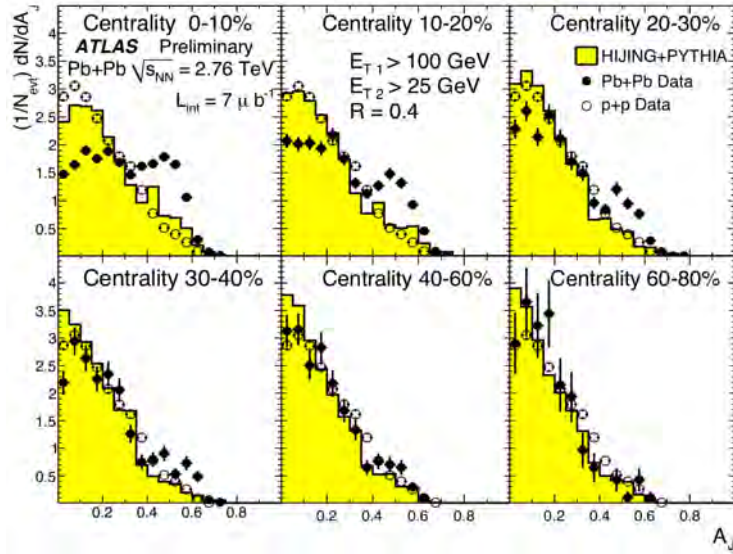


Figure 1.15: Dijet imbalance as a function of centrality for  $PbPb$  at  $\sqrt{s_{NN}} = 2760$  GeV [39, 40]. At peripheral collisions  $pp$  and  $PbPb$  collision behaves similarly (in accordance with simulations). However at central collisions significant imbalances occur for  $PbPb$  collisions.

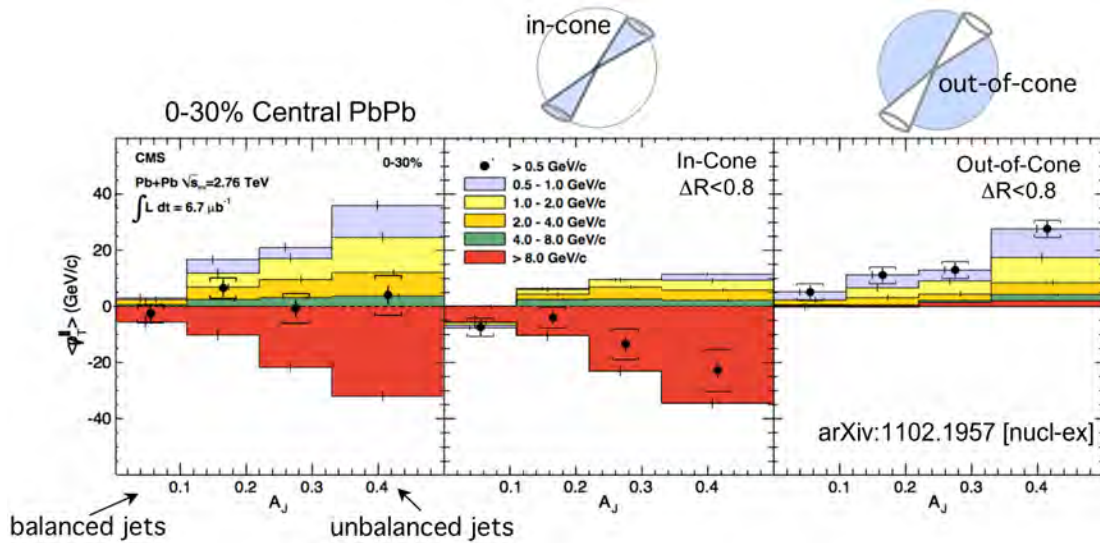


Figure 1.16: The missing energy as a function of the dijet asymmetry measured by CMS [38, 41]. Left panel shows the total energy balance. The red block is the leading jet, where as the other colours shows that the apparently missing energy can be found as low  $p_T$  particles. The black points shows that momentum is balanced over the entire event final state. Middle panel shows the same quantity looking only in the jet cone regions.  $\Delta R < 0.8$  denotes a characteristic size of the cone algorithm. Right panel: The momentum that appeared missing in the cone is found outside the cone. The conclusion is that the amount of energy, the away side jet loses in the medium, is distributed at very wide angles.

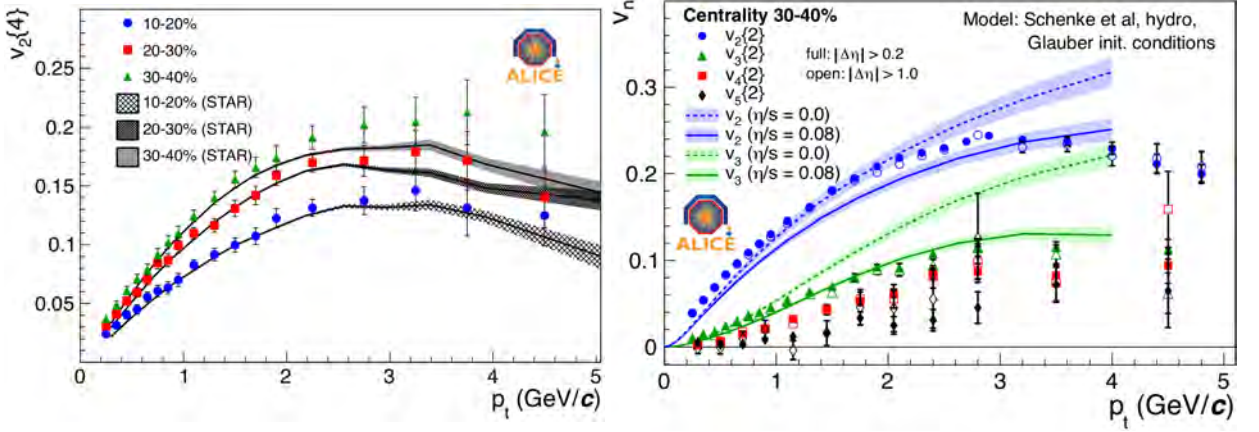


Figure 1.17: Measurements of flow from ALICE [42–44]. Left panel: The elliptic flow at various centralities, compared to the measurements from STAR at RHIC energies. It is seen that the elliptic flow is similar at both energies. Right panel: The flow components,  $v_2 - v_5$ . Comparisons with hydrodynamical calculations show agreement (to some extent). It indicates that the medium created flows perfectly (or close to).

## Flow

One of the collective dynamics of particles, which has garnered significant interest in recent years, is the concept of anisotropic transverse flow. Anisotropic transverse flow is caused by initial spatial asymmetries in the overlap region between the colliding nuclei. This spatial asymmetry give rise to pressure gradients, which causes a momentum asymmetry and thus asymmetry in the azimuthal distribution of particles. The distribution can be described by a Fourier expansion [45]:

$$r(\phi) = \frac{a_0}{2\pi} + \frac{1}{\pi} \sum_{n=1}^{\infty} (x_n \cos(n\phi) + y_n \sin(n\phi)) \quad (1.15)$$

Here  $a_0$  is a constant.  $x_n$  and  $y_n$  are the components of the expansion along the respective axis'. The Fourier transformation of (1.15) is used to quantise the flow [46]:

$$E \frac{d^3 N}{d^3 p} = \frac{1}{2\pi} \frac{d^2 N}{p_T dp_T dy} \left( 1 + \sum_{n=1}^{\infty} 2v_n \cos(n(\phi - \Psi_r)) \right) \quad (1.16)$$

Here  $\Psi_r$  is the azimuthal angle of the reaction plane to the  $xz$ -plane. The reaction plane is by definition spanned by the impact parameter vector and the  $z$ -axis. The harmonics coefficients  $v_n$  describes the various types of flow.  $v_1$  is called direct flow and  $v_2$  is called elliptic flow. Up until recently, especially the elliptic flow was deemed important in the description of heavy ion collisions. Now the consensus is that the higher harmonics play a large role as well.

In the left panel of figure 1.17 the newest measurement by ALICE [42,44] of the elliptic flow at different centralities can be seen. Comparisons to STAR measurements at RHIC energies show that the elliptic flow is comparable over the large range of energy.

Traditionally the overlap region between the colliding nuclei have been perceived as an almond shape. However recent calculations show that the fluctuations in the position of individual partons for each event causes the overlap to deviate significantly from almond shape. This can be seen in figure 1.18.

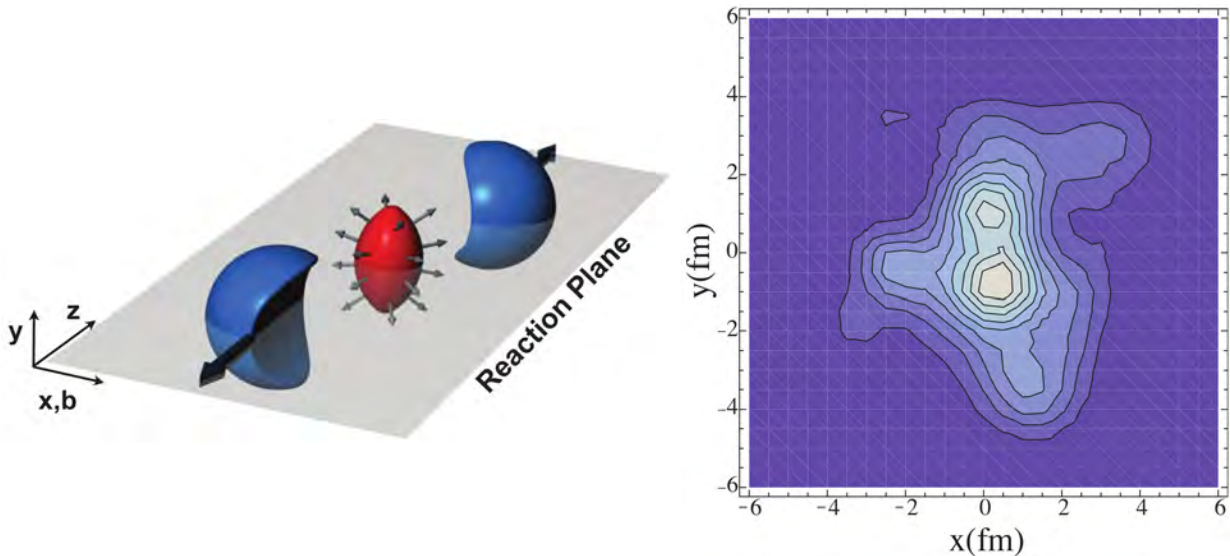


Figure 1.18: Left panel: An illustration of the concept of reaction plane. Figure is from [47]. Right panel: Detailed calculations of the overlap region between the nuclei, show that the shape can deviate significantly from almond shaped. This is due to fluctuations in the positions of the individual partons at the time of collisions. Figure is from [48].

In the right panel of figure 1.17 measurements from ALICE [43, 44] show the higher harmonics ( $v_2 - v_5$ ) for semi-peripheral collisions (30-40%). Also shown is the theoretical predictions from hydrodynamical calculations with the shear viscosity per entropy,  $\eta/s$ , being either 0 or 0.08 ( $\sim 1/(4\pi)$ ).

Anti de Sitter/Conformal Field Theory (AdS/CFT), a proposed duality between string theory and quantum field theory, predicts that the universally lowest possible value of  $\eta/s$  is  $1/(4\pi)$  [16]. This value corresponds to a perfect fluid. As can be seen there is reasonable agreement between the AdS/CFT calculations and the data, which is the main reason the QGP of heavy ion collisions is often termed a perfect fluid.

Another thing to note about the right panel of figure 1.17 is that it appears that  $v_2$  is clearly dominant over the higher order harmonics. However the strength of  $v_2$  is caused by the main pressure gradients of the almond shape, which is very prevalent in semi-peripheral collisions. Going to more and more central collisions will make the overlap region less and less almond shaped (for a full head on collision it is the shape of the nuclei). However fluctuations will create variances in each event. Thus for central collisions,  $v_2$  becomes less and less dominant compared to the higher order harmonics. At very central collisions  $v_2 \sim v_3 \sim v_4$ .

A clear example of the importance of higher harmonics comes from the measurements of azimuthal long range correlations i.e., taking one jet particle in a given  $p_T$  region and then comparing it to all particles some minimum  $\Delta\eta$  away at another  $p_T$  range. The measurement by ALICE [43, 44] of this correlation can be seen in figure 1.19. Included as the dashed lines are the contributions of the different flow types. The red line is the sum of the dashed lines i.e., it is not a fit to the data. The agreement is excellent. Thus fluctuations (and hence significant higher order flow) can completely account for the observed double hump structure of long range azimuthal correlations. Until quite recently this structure was attributed to a so-called Mach cone shock wave explanation. With the data presented here it is clear that the Mach cone idea is not needed for explaining the phenomenon. The other LHC experiments besides ALICE, as well as the PHENIX experiment, have also

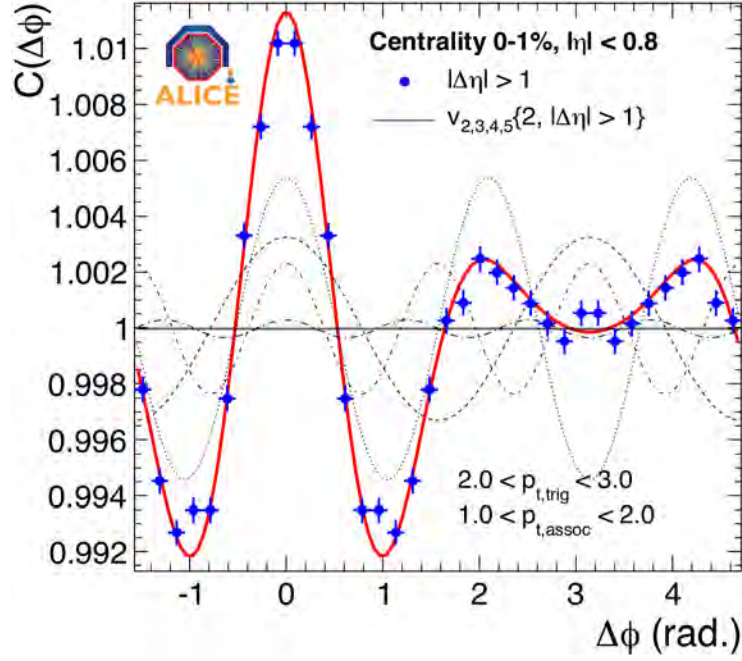


Figure 1.19: Measurement from ALICE [43, 44] of the long range azimuthal correlation for the most central collisions. The observed structure is explained by the flow fluctuations. The red line, which has excellent agreement with data, is the sum of the dashed contributions from the individual flow components.

presented similar recent flow measurements with the same conclusions [49–51].

On a last note it should be mentioned that large elliptic flow components requires a high number of interactions in the fireball region, since the asymmetry required for non-zero  $v_n$ 's would vanish for a non-interacting system [52]. On basis of the data it is concluded in [53] that the measured flow can only be explained if the system is thermalised in less than 1 fm/c; a time where the density of the fireball is at least an order of magnitude higher than the critical density for quark de-confinement. Thus it is concluded that a strongly interacting QGP is indeed formed.



# Chapter 2

## Charged Particle Multiplicity

Measuring the charged particle multiplicity of relativistic collisions, is one of the very fundamental measurements. For the same reason the first publications from a new experiment will often revolve around charged particle multiplicities. These topics will then usually be revisited later on with improved statistics and better detector understanding.

From this point on, the shorter term 'multiplicity' will denote 'charged particle multiplicity', where nothing else is specifically stated.

Multiplicity measurements typically fall into the following sub-groups:

**Pseudorapidity density**  $\frac{dN_{\text{ch}}}{d\eta}$ : Measurement of the average multiplicity as a function of  $\eta$ .

**Multiplicity distributions**  $P(N_{\text{ch}})$ : Measurement of the distribution of integrated multiplicities i.e., the total multiplicities of events in a given  $\eta$ -interval.

**KNO scaling**  $\langle N_{\text{ch}} \rangle P(\mathbf{z})$ : Derives from the multiplicity distribution, by plotting it in KNO-variables,  $P(N_{\text{ch}}) \langle N_{\text{ch}} \rangle$  as a function of  $z \equiv N_{\text{ch}} / \langle N_{\text{ch}} \rangle$ . This probes the energy scaling behaviour of multiplicity distributions.

**Energy scaling**: Derives from either  $\frac{dN_{\text{ch}}}{d\eta}$  or the multiplicity distributions by surveying the multiplicity at a given pseudorapidity as a function of energy.

Measurements of multiplicities yield some insight into the collisions themselves, but are also crucial as input parameters for a multitude of models, explaining various phenomena at later stages in the collisions.

The main goal of this work is to present multiplicity distributions and look for KNO scaling, but throughout this work, results will be presented on all four sub-groups. The remainder of this section is devoted to presenting some of the theoretical framework behind understanding charged particle multiplicity, followed by an overview of the measurements previously conducted on multiplicities.

### 2.1 Negative Binomial Distributions

It is found that a Negative Binomial Distribution (NBD) describe the observed multiplicity distributions at lower energies very well [24]. In general it is given by:

$$P(n; p; k) = \binom{n+k-1}{n} (1-p)^n p^k \quad (2.1)$$

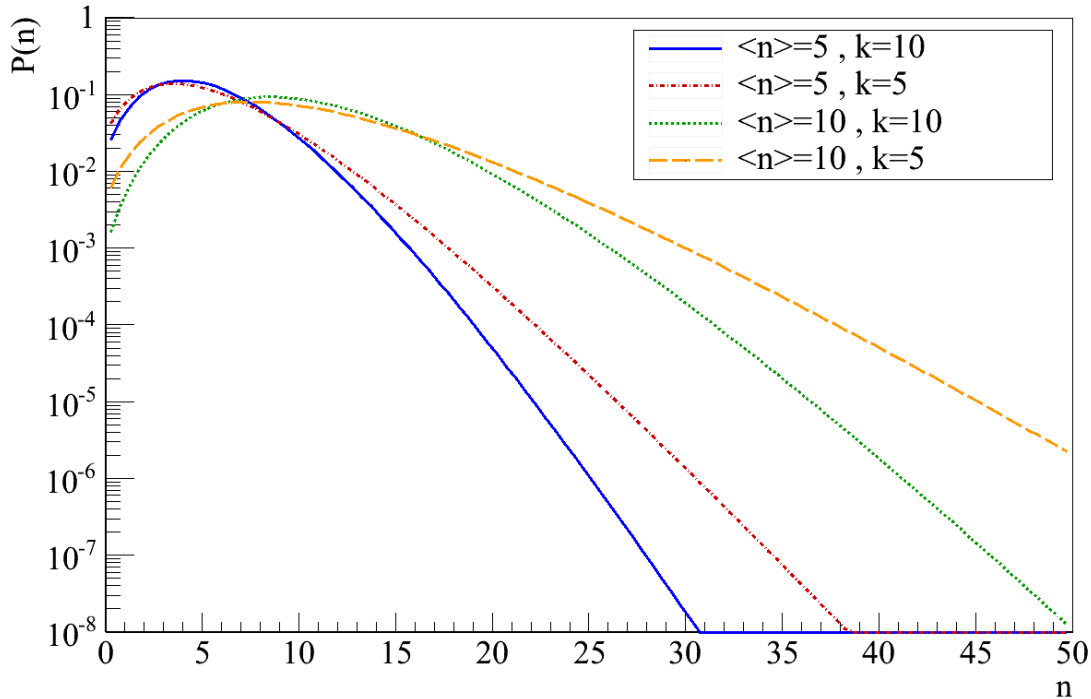


Figure 2.1: Examples of negative binomial distributions, with different parameter values. For NBDs with the same  $\langle n \rangle$ , the  $k$ -parameter determines the shape of the distribution. Lower  $k$ -values correspond to a flatter distribution.

To describe NBDs, consider a series of Bernoulli trials, each with two potential outcomes — ‘success’ or ‘failure’ — with the probabilities  $p$  and  $(1 - p)$  respectively. The NBD then describes the distribution of number of successes,  $n$ , observed before having the  $k^{\text{th}}$  failure. For  $k \rightarrow \infty$  the NBD reduces to the Poisson distribution, and for  $k = 1$  it is the geometric distribution.

Multiplicity distributions are described well using NBDs with  $p^{-1} = 1 + \langle n \rangle / k$ , where  $\langle n \rangle$  is the average multiplicity, thus yielding the following form [54]:

$$P(n; \langle n \rangle; k) = \binom{n+k-1}{n} \left( \frac{\langle n \rangle / k}{1 + \langle n \rangle / k} \right)^n \frac{1}{(1 + \langle n \rangle / k)^k} \quad (2.2)$$

Fig. 2.1 illustrates several NBDs, with different parameters.

Why multiplicity distributions are well described by NBDs are still not fully understood. Various attempts to theoretically generate negative binomially shaped multiplicity distributions from general particle production principles have been undertaken over the years [55]. The one most frequently used is referred to as the clan model [56, 57], and will be introduced in the following.

Multiplicity distributions can be characterized by a recurrence relation between collision with  $n + 1$  particles and  $n$  particles. While the individual particles can be of the same type, they are always distinguishable by their momenta. In general, a given collision of  $n + 1$  particles can be related to  $n + 1$  collisions each having  $n$  particles. These  $n + 1$  collisions (of  $n$  particles) are the ones left if any single one of the particles from the initial  $n + 1$  multiplicity collision were removed. Thus the simplest recurrence relation,  $g(n)$ , is given

by:

$$g(n) = \frac{(n+1)P(n+1)}{P(n)} \quad (2.3)$$

Inserting (2.2) into (2.3), and using  $\binom{i}{j} = i!/j!(i-j)!$  yields:

$$\begin{aligned} g(n) &= (n+k) \frac{\langle n \rangle / k}{(\langle n \rangle / k) + 1} \\ &= \frac{\langle n \rangle k}{\langle n \rangle + k} + n \frac{\langle n \rangle}{\langle n \rangle + k} \\ &= a + bn \quad \text{where } a = \frac{\langle n \rangle k}{\langle n \rangle + k} \text{ and } b = \frac{\langle n \rangle}{\langle n \rangle + k} \end{aligned} \quad (2.4)$$

Thus for a negative binomial distribution the recurrence relation gives that  $g(n)$  is linear in  $n$ .

The clan model describes particle multiplicity in terms of clusters (or clans). In this sense a cluster consists of all particles originating (directly or indirectly) from the originally produced particle, which is denoted the ancestor of the cluster. The additional cluster particles can come from various cascading processes such as decays and fragmentation. If an ancestor does not produce any other particle, it is considered a one-particle cluster, and is its own ancestor. In the clan model it is assumed that ancestors are created independently, i.e. with no regard to whether other ancestors exist.

Thus, the production of the  $(N+1)^{th}$  ancestor is independent of the existence of the other  $N$  ancestors. The production follows a Poisson distribution,  $P(n) = \gamma^n e^{-\gamma} / n!$  [58]. It is characterized by having  $g(n) = \gamma = \text{constant}$ , and thus the production of ancestors is represented by the constant term of (2.4). The linear term,  $bn$ , then represents the effect of the particles created within clusters. It is a reasonable assumption that this effect is proportional to the number of already present particles in the cluster, and thus the  $n$ -dependence.

As discussed the probability,  $P'(N)$ , to produce  $N$  clans is given by a Poisson distribution. The probability,  $P_c(n_c)$ , to produce  $n_c$  particles in the  $c^{th}$  clan is given by the requirement that a clan cannot be empty

$$P_c(0) = 0 \quad , \quad (2.5)$$

and the assumption that producing  $n_c + 1$  is proportional to  $n_c$  with the probability  $p$

$$\frac{(n_c + 1)P_c(n_c + 1)}{P_c(n_c)} = pn_c \quad . \quad (2.6)$$

By induction, it can be shown that

$$P_c(n_c) = P_c(1) \frac{p^{n_c-1}}{n_c} \quad . \quad (2.7)$$

The probability to produce a total of  $n$  particles is given by

$$P(n) = \sum_N \left[ P'(N) \left( \sum_{n_1+\dots+n_N=n} \prod_c P_c(n_c) \right) \right] \quad , \quad (2.8)$$

where  $n_c \in [1, n]$  is the number particles produced by the  $c^{th}$  clan. Using the definition of the Poisson distribution and inserting (2.7) into (2.8) yields:

$$P(n) \propto p^n \sum_N \left[ \frac{1}{N!} \left( \frac{\langle N \rangle P_c(1)}{p} \right)^N \left( \sum_{n_1+\dots+n_N=n} (n_1 \dots n_N)^{-1} \right) \right] \quad . \quad (2.9)$$

The expression in (2.9) can be identified as a NBD by Taylor expanding the relation  $(1 - z)^{-L} = \exp(-L \ln(1 - z))$ , and equating its coefficients [56]. This yields an identity of the form:

$$\sum_N \frac{k^N}{N!} \sum_{n_1 + \dots + n_N = n} (n_1 \dots n_N)^{-1} = k(k+1) \dots (k+n-1)/n! \quad (2.10)$$

where

$$k = \frac{\langle N \rangle P_c(1)}{p} \quad (2.11)$$

Thus we end up with the expression:

$$P(n) \propto p^n \frac{k(k+1) \dots (k+n-1)}{n!} = \binom{n+k-1}{n} p^n \quad (2.12)$$

which is recognized as the negative binomial form from (2.1) (without a factor of  $p^k$ ).

We end this section by summarising, that if the collision dynamics follows the clan model, the resulting multiplicity distributions will be well described by negative binomial distributions.

## 2.2 Koba–Nielsen–Olesen Scaling

In his 1969 paper [59], Feynman concludes that the mean total number of particles rises logarithmically with  $\sqrt{s}$ . He argues that the probability of finding a particle of type  $i$ , mass  $m$ , transverse momentum  $p_T$ , and longitudinal momentum  $p_z$  is of the form:

$$P_i(p_T, p_z, m) = f_i(p_T, p_z/W) \frac{dp_z d^2 p_T}{E} \quad (2.13)$$

where the energy of the particle  $E$ , and the parameter  $W$  is given by:

$$E = \sqrt{m^2 + p_T^2 + p_z^2} = \sqrt{m_T^2 + p_z^2} \quad \text{and} \quad W = \frac{\sqrt{s}}{2} \quad (2.14)$$

The function  $f_i(p_T, p_z/W)$  is a structure function and is known as the Feynman function. Feynman's assumption is that  $f_i$  is independent of  $W$ , which is called Feynman scaling. Furthermore the fractional longitudinal momentum in  $f_i$ ,  $x_F \equiv p_z/W$ , is often referred to as the Feynman- $x$ .

One can rewrite (2.13) using the invariant cross section,  $\sigma$ :

$$\frac{1}{\sigma} E \frac{d^3 \sigma}{dp_z d^2 p_T} = f_i(p_T, x_F) \quad (2.15)$$

Integrating (2.15) and using that  $f_i$  factorizes such that  $\int f_i(p_T, x_F) d^2 p_T = f_i(x_F)$  [24] gives the following expression for the mean multiplicity:

$$\langle N \rangle \equiv \int_{-\infty}^{\infty} \frac{1}{\sigma} E \frac{d^3 \sigma}{dp_z d^2 p_T} \frac{d^3 p}{E} = \int_{-\infty}^{\infty} f_i(p_T, x_F) \frac{d^3 p}{E} = \int_{-\infty}^{\infty} f_i(x_F) \frac{dp_z}{\sqrt{W^2 x_F^2 + m_T^2}} \quad (2.16)$$

which by changing integration variable through  $dp_z = W dx_F$  becomes:

$$\langle N \rangle = \int_{-1}^1 f_i(x_F) \frac{dx_F}{\sqrt{x_F^2 + \frac{m_T^2}{W^2}}} \quad (2.17)$$

For collisions of identical particles  $f_i(x_F)$  is symmetrical, and thus the integral is also symmetrical<sup>9</sup>. Integration by parts of (2.17) yields:

$$\langle N \rangle = \left[ 2f_i(x_F) \ln \left( x_F + \sqrt{x_F^2 + \frac{m_T^2}{W^2}} \right) \right]_0^1 - 2 \int_0^1 \frac{\partial f_i(x_F)}{\partial x_F} \ln \left( x_F + \sqrt{x_F^2 + \frac{m_T^2}{W^2}} \right) dx_F \quad (2.18)$$

The second term can be shown to converge to a constant for all  $W$  [24]. Thus, (2.18) then becomes:

$$\langle N \rangle = 2f_i(1) \ln \left( 1 + \sqrt{1 + \frac{m_T^2}{W^2}} \right) - 2f_i(0) \ln \left( \frac{m_T}{W} \right) + \text{constant} \quad (2.19)$$

In the limit of  $W \rightarrow \infty$ , (2.19) becomes:

$$\begin{aligned} \lim_{W \rightarrow \infty} \langle N \rangle &= \lim_{W \rightarrow \infty} 2f_i(1) \ln \left( 1 + \sqrt{1 + \frac{m_T^2}{W^2}} \right) - \lim_{W \rightarrow \infty} 2f_i(0) \ln(m_T) + \\ &\quad \lim_{W \rightarrow \infty} 2f_i(0) \ln(W) + \lim_{W \rightarrow \infty} \text{constant} \\ &= 2f_i(0) \ln(W) + \text{constants} \end{aligned} \quad (2.20)$$

The limit of the first, second and fourth term in (2.20) are all constants, and thus under the assumption Feynman made, that  $f_i(0) > 0$  it is clear that for large  $W$ :

$$\langle N \rangle \propto \ln(W) \propto \ln(\sqrt{s}) \quad (2.21)$$

The concept of Feynman scaling was the main assumption when Koba, Nielsen, and Olesen suggested a similar scaling in 1972 [60]. This scaling is now called KNO scaling. It is derived from generalising (2.17) to a  $q$ -dimensional Feynman scaling function,  $f^{(q)}$  i.e.,  $q$  particles with energy  $E_q$ , momenta  $p_{z,q}$  and  $p_{T,q}$  and Feynman-x  $x_{F,q}$ . Thus we have:

$$\langle n(n-1)\dots(n-q-1) \rangle = \int f^{(q)}((x_{F,1}, p_{T,1}); \dots; (x_{F,q}, p_{T,q})) \frac{dp_{z,1}}{E_1} dp_{T,1}^2 \dots \frac{dp_{z,q}}{E_q} dp_{T,q}^2 \quad (2.22)$$

As in the Feynman scaling case integration by parts is used for all  $x_{F,q}$  in (2.22) which ultimately (after a significant amount of calculations [60]) leads to:

$$\begin{aligned} \langle n(n-1)\dots(n-q-1) \rangle &= \int \left[ f^q((0, p_{T,1}); \dots; (0, p_{T,q})) + \mathcal{O} \left( \frac{1}{\ln(s)} \right) \right] \\ &\quad \times \prod_q \ln \left( \frac{s}{p_{T,q}^2 + m^2} \right) d^2 p_{T,1} \dots d^2 p_{T,q} \\ &= \tilde{f}^{(q)}(0, \dots, 0) (\ln(s))^q + \mathcal{O}((\ln(s))^{q-1}) \end{aligned} \quad (2.23)$$

$\mathcal{O}((\ln(s))^{q-1})$  refers to all terms which go at most like  $\ln(s)^{q-1}$  and  $\tilde{f}^{(q)}(x_{F,1}, \dots, x_{F,q}) = \int d^2 p_{T,1} \dots d^2 p_{T,q} f^{(q)}((x_{F,1}, p_{T,1}); \dots; (x_{F,q}, p_{T,q}))$ . It can be shown [60] that (2.23) can be rewritten in the form

$$\langle n^q \rangle \equiv \sum_n P_n(s) n^q \sim \int_0^\infty P_n(s) n^q dn = \tilde{f}^{(q)}(0, \dots, 0) (\ln(s))^q + \mathcal{O}((\ln(s))^{q-1}) \quad (2.24)$$

<sup>9</sup>For collision systems where the participants are not identical, the integral can be done separately for negative and positive  $x_F$ , yielding the same result as in the symmetric case [24].

By dividing both sides of (2.24) by  $(\ln(s))^q (\tilde{f}^{(1)}(0))^q$  it takes the form:

$$\int_0^\infty P_n(s) z^q \ln(s) \tilde{f}^{(1)}(0) dz = c^q + \mathcal{O}\left(\frac{1}{\ln(s)}\right) \quad (2.25)$$

where

$$z = \frac{n}{\ln(s) \tilde{f}^{(1)}(0)} \quad \text{and} \quad c^q = \frac{\tilde{f}^{(q)}(0, \dots, 0)}{(\tilde{f}^{(1)}(0))^q} \quad (2.26)$$

The moments  $c_q$ , which are independent of  $W$ , thus uniquely determines the multiplicity distribution:

$$P_n(s) = \frac{1}{\ln(s) \tilde{f}^{(1)}(0)} \Phi\left(\frac{n}{\ln(s) \tilde{f}^{(1)}(0)}\right) + \mathcal{O}\left(\frac{1}{\ln(s)^2}\right) \quad (2.27)$$

It can be shown that  $\langle n \rangle \sim \ln(s) \tilde{f}^{(1)}(0)$  [60], and thus  $z = n / \langle n \rangle$ , which yields the KNO scaling law in the following form:

$$P_n(s) = \frac{1}{\langle n \rangle} \Psi(z) + \mathcal{O}\left(\frac{1}{\langle n \rangle^2}\right) \quad (2.28)$$

The functional form of  $\Psi(z)$  is not known a priori, and in principle could be different for different collision systems, and dependent on which type of particle being measured.

Substituting  $z = n / \langle n \rangle$  into (2.25) yields the moments in the following form:

$$c_q = \frac{\langle n^q \rangle}{\langle n \rangle^q} \quad (2.29)$$

## 2.3 Previous Multiplicity Measurements

This section is devoted to presenting previous multiplicity measurements. Since multiplicity is one of the fundamental quantities it has been measured at various accelerator facilities around the world over many decades.

This section will first present measurements on multiplicity distributions (including in KNO variables), followed by measurements on  $\frac{dN_{\text{ch}}}{dn}$  and energy scaling.

### 2.3.1 Multiplicity Distributions

The very first hadron collider was the ISR (Intersecting Storage Ring). It was located at CERN, and was operated from 1971 to 1984. The ISR has collided  $pp$ ,  $p\bar{p}$ , and  $p\alpha$  at a top center of mass energy 63 GeV. At the ISR the Split Field Magnet detector [61] measured multiplicities at four energies;  $\sqrt{s} = 30.4, 44.5, 52.6$  and 62.2 GeV [62]. These can be seen in figure 2.2.

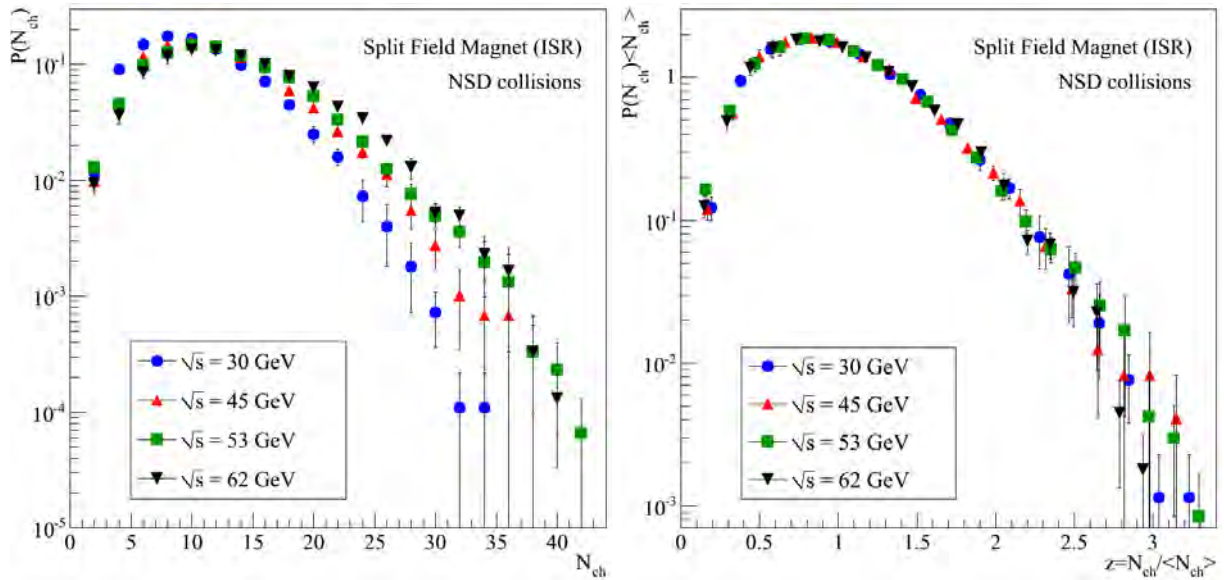


Figure 2.2: Charged particle multiplicity distributions from the Split Field Magnet detector at the ISR at four energies [62]. Left panel shows the normalised distributions and the right panel show them in KNO variables. It is clear that KNO scaling is valid at ISR energies.

In 1976 CERN started operating the SPS (Super Proton Synchrotron). Over the years the SPS has accelerated  $e^-$ ,  $e^+$ ,  $p$ ,  $\bar{p}$  and ions in various combinations. Later on, after modifications, the SPS collided  $p\bar{p}$  at the top energy  $\sqrt{s} = 900$  GeV<sup>10</sup>.

At the SPS two different experiments have published a variety of multiplicity measurements; UA1 [69] and UA5 [70] (Underground Area 1 & 5 respectively). Both published results at  $\sqrt{s} = 200, 540$  and 900 GeV [63–68]. Besides these common energies, UA1 also published multiplicities at  $\sqrt{s} = 500$  GeV [67].

Measurements from UA5 of multiplicity distributions with  $|\eta| < 1.5$  at their three energies can be seen in figure 2.3. Furthermore the UA1 results ( $|\eta| < 2.5$ ) can be seen in figure 2.4. Even though UA5 and UA5 published for different  $\eta$ -ranges it is interesting to compare the two. UA1 finds that KNO scaling holds up to and including 900 GeV,

<sup>10</sup>In this period it is sometimes referred to as  $Spp\bar{p}S$ . However throughout in this work it will still be referred to as SPS.

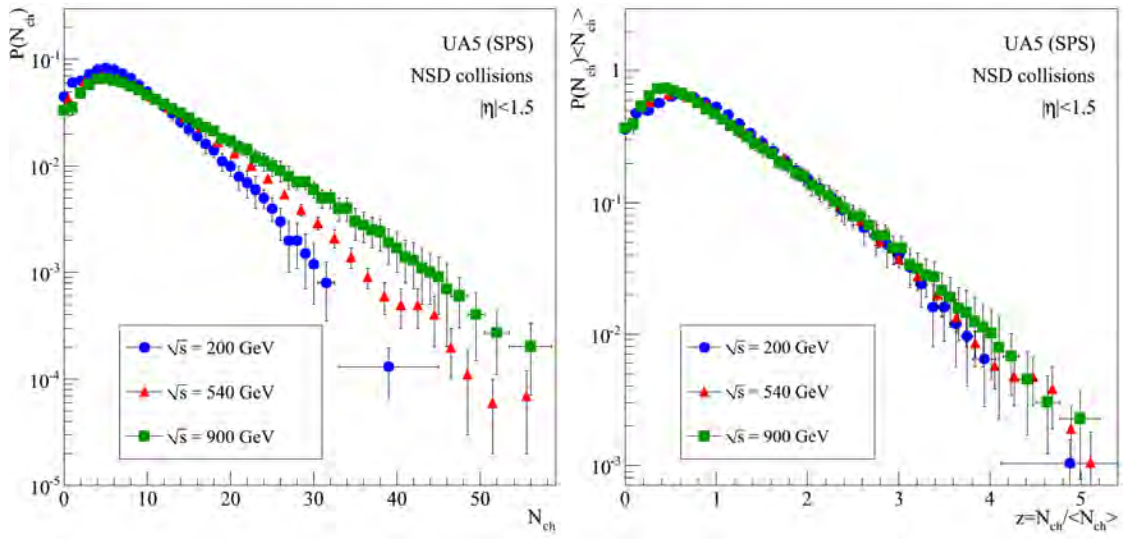


Figure 2.3: Charged particle multiplicity distributions for  $|\eta| < 1.5$ , measured by UA5 at three energies [63–66]. Left panel shows the normalised distributions and the right panel show them in KNO variables. UA5 concludes that KNO scaling is broken at  $\sqrt{s} = 900$  GeV.

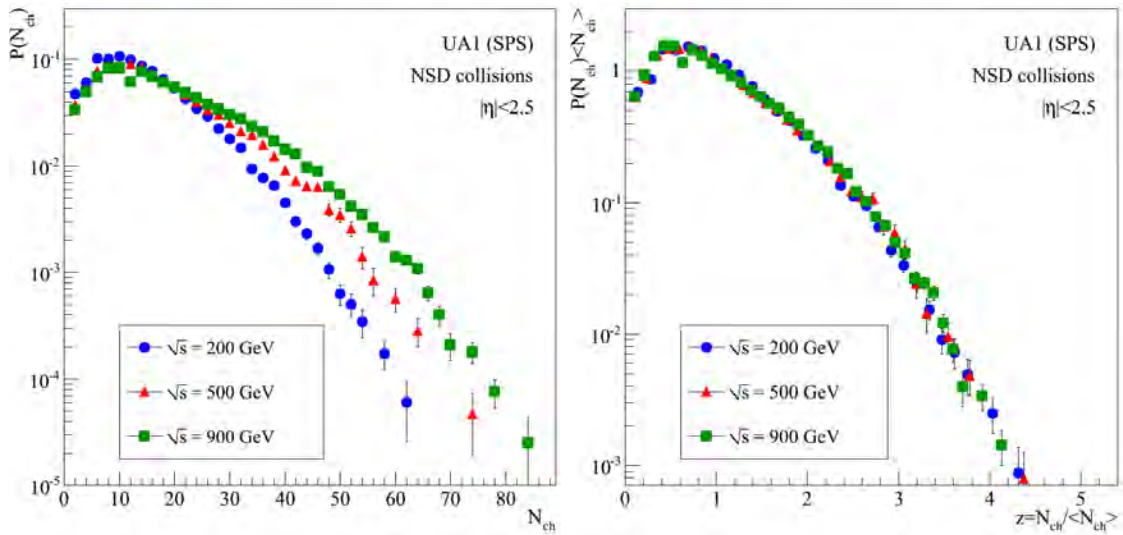


Figure 2.4: Charged particle multiplicity distributions for  $|\eta| < 2.5$ , measured by UA1 at three energies [67,68]. Left panel shows the normalised distributions and the right panel show them in KNO variables. Contrary to UA5, UA1 does not see the KNO scaling being broken at  $\sqrt{s} = 900$  GeV.

whereas UA5 concludes that it is broken at 900 GeV. Since the UA5 and UA1 results are at different  $\eta$  ranges their conclusions can differ and both still be valid. However it is an interesting fact that their conclusions are different. It is not addressed in the papers.

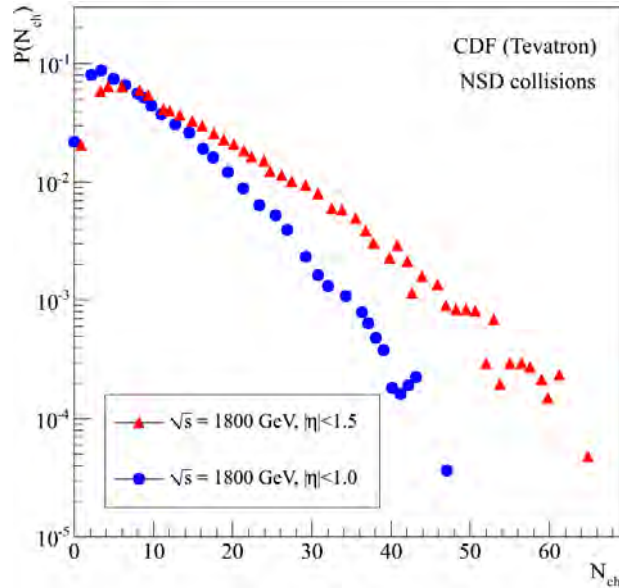


Figure 2.5: Charged particle multiplicity distributions at two  $\eta$ -intervals measured by CDF [71] at  $\sqrt{s} = 1800$  GeV.

In 1983 Fermi National Accelerator Laboratory started operating the Tevatron, which collides  $p\bar{p}$  at energies up to  $\sqrt{s} = 1960$  GeV. At the Tevatron the CDF (Collider Detector Fermilab) [72] has published multiplicity distributions at  $\sqrt{s} = 1800$  GeV. Their measurements are presented in figure 2.5.

Recently the LHC experiments have also presented multiplicity distributions. The CMS experiment has published data for  $\sqrt{s} = 900, 2360$  and  $7000$  GeV for a wide range of  $\eta$ -intervals [75]. ALICE has also published results at the same energies, however only for central  $\eta$  intervals. The measurements of ALICE and CMS are shown in figure 2.6.

Comparisons between the two experiments reveal good agreement. A more detailed comparison will be made in chapter 8.

As mentioned previously, the main ambition of this work is to extend the measurements already published by ALICE. This is done by using the forward detectors of ALICE, making it possible to measure multiplicity distributions over more than 8 units of  $\eta$ . This makes it possible to present both results for more  $\eta$ -intervals including very forward regions, as well as extending the multiplicity reach for existing measurements.

While lower energy multiplicity results are described well by a single NBD, this is not sufficient for the higher energies. Here a multi-component approach is needed, which is discussed in the following section.

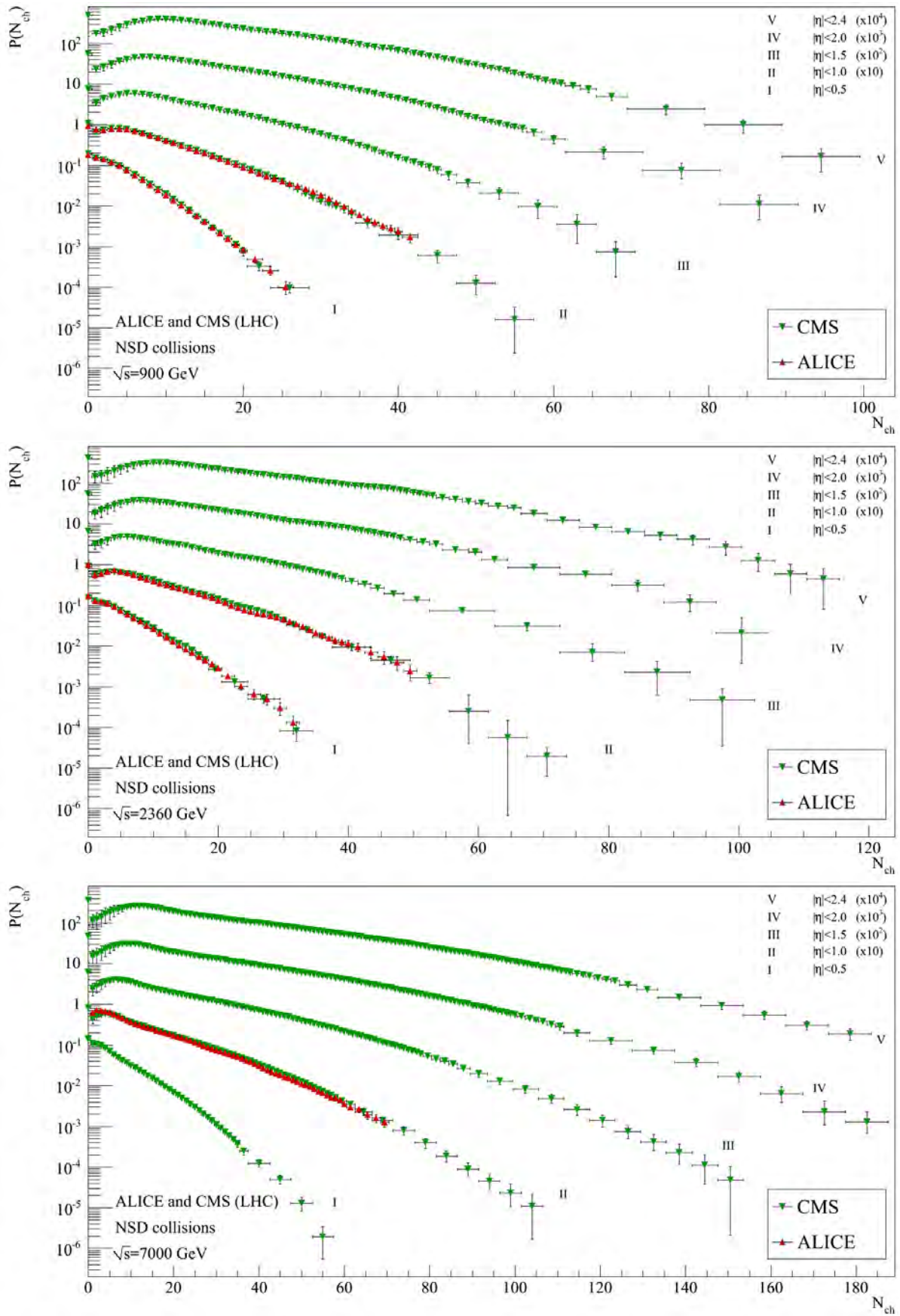


Figure 2.6: Charged particle multiplicity distributions at various  $\eta$ -intervals measured by ALICE [73, 74] and CMS [75] at  $\sqrt{s} = 900$  GeV, 2360 GeV, and 7000 GeV.

## Multiple Negative Binomial Distributions

Multiplicity distributions from UA5 is found to be best described by a sum of two NBDs [76]. An example of this is found in figure 2.7. The fit consists of five free parameters and are given by:

$$P(n) = \alpha_{soft} P(n; \langle n \rangle_{soft}; k_{soft}) + (1 - \alpha_{soft}) P(n; \langle n \rangle_{semi-hard}; k_{semi-hard}) \quad (2.30)$$

As the subscripts indicate, the two NBDs are found to correspond to a soft and semi-hard component respectively [77]. The semi-hard component is understood as being events where mini-jets are observed, and the soft component are the events where there are no mini-jets. The fraction of mini-jets events seen by UA1 is consistent with the value of  $\alpha_{semi-hard} = 1 - \alpha_{soft}$ , obtained by fitting the UA5 data.

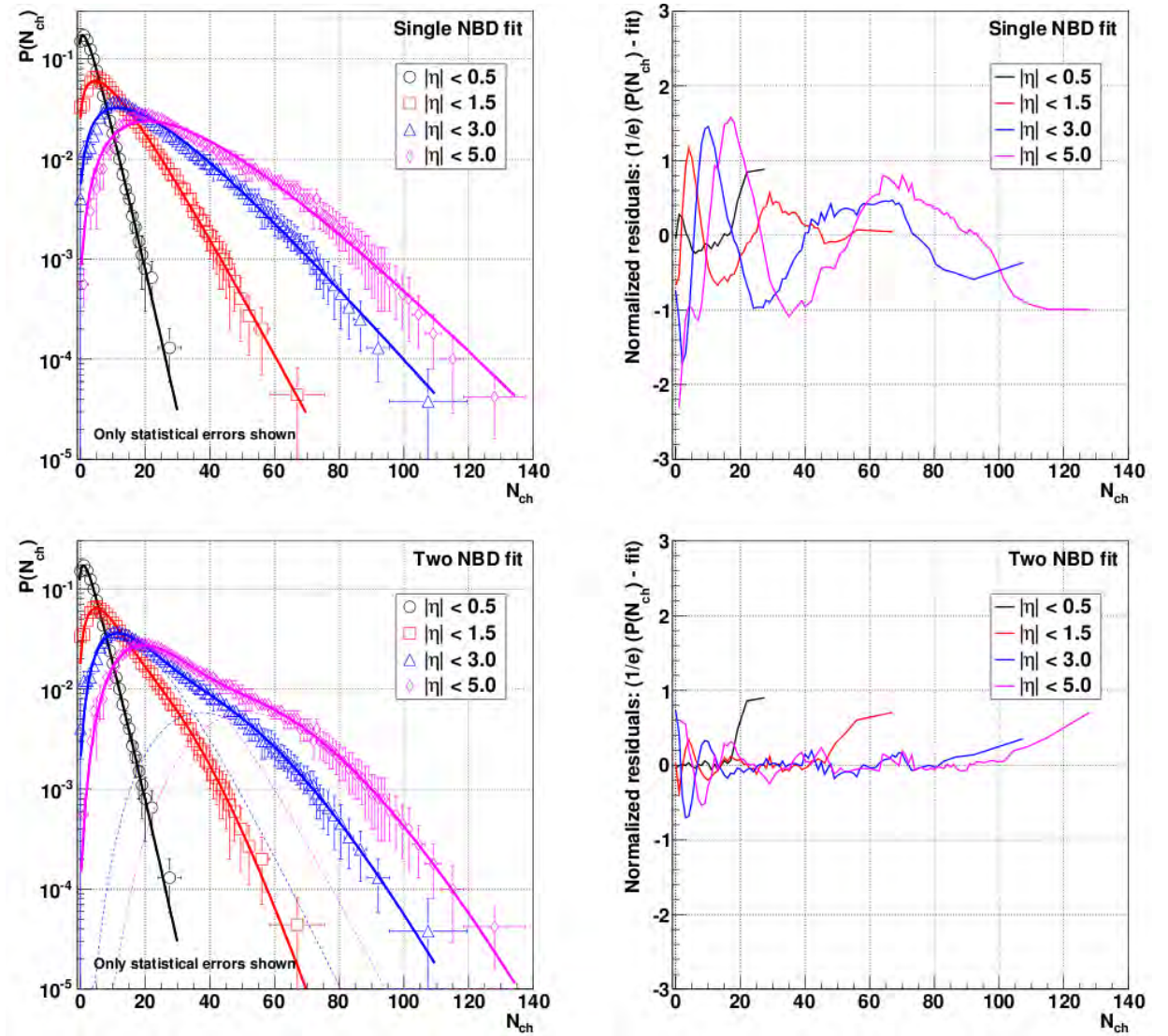


Figure 2.7: Single and two-component NBD fits to UA5 data at  $\sqrt{s} = 900$  GeV. The right panels show the residuals between the data and the fit. It is clear that the fits with two NBDs describe the data better. Figure is from [24].

By fitting UA5 energies at  $\sqrt{s} = 200$  GeV, 546 GeV and 900 GeV it is found [77] that the mean multiplicities of the two components depend on collision energy in the following

way:

$$\langle n \rangle_{soft} = -5.54 + 4.72 \ln(\sqrt{s}) \quad (2.31)$$

$$\langle n \rangle_{semi-hard} \sim 2 \langle n \rangle_{soft} \quad (2.32)$$

In [77] a correction of the order  $\langle n \rangle \ln^2(\sqrt{s})$  to (2.32) is also proposed. However, due to the quality of the fits to the data in [77], it is still debated if the correction is actually there, or (2.32) is valid.

On a similar note it should be mentioned that the fits to the UA5 data finds that the shape parameter of the soft component is energy independent ( $k_{soft} \sim 7$ ), which is equivalent to KNO scaling being valid. For the semi-hard component this is not true. At higher collision energies a third component has been proposed [78].

The authors of [79] and [80] conclude that the second and possibly third components are the results of multi-parton interactions. Multi-parton interactions denote having multiple independent parton-parton interactions within a single collision. In the context of this discussion the semi-hard and the third component are identified as double-parton and triple-parton interactions. Thus, said in a different way, the cause of mini-jet events might be double-parton interactions.

### 2.3.2 $dN/d\eta$ measurements

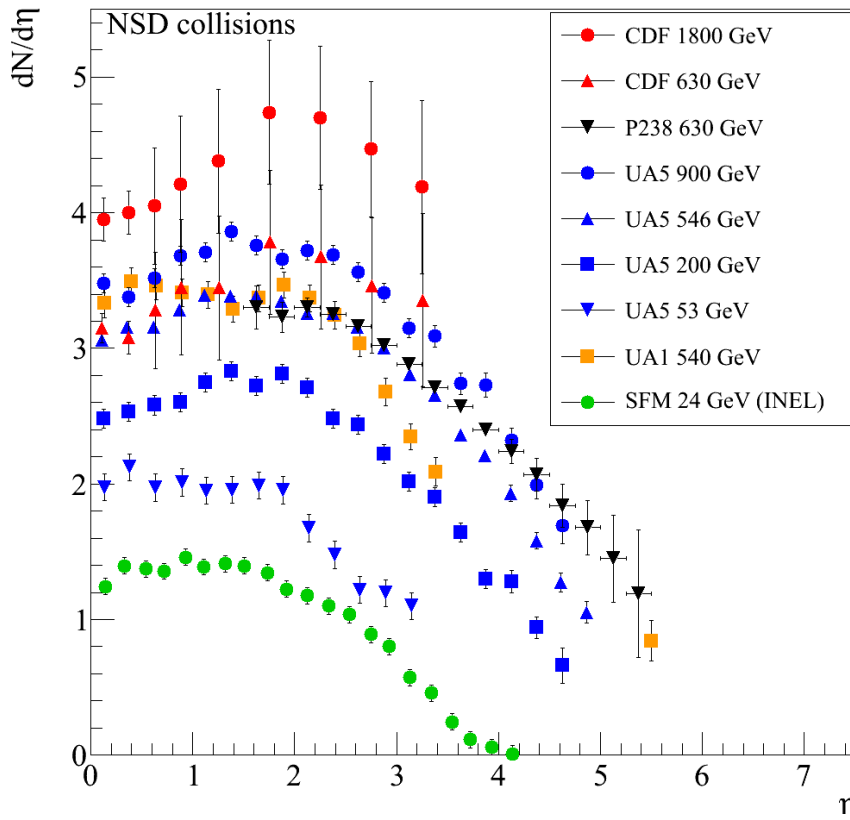


Figure 2.8:  $\frac{dN_{ch}}{d\eta}$  measurements from pre-LHC experiments [62, 63, 65, 68, 81–83]. Going up in collision energy increases and widens the distribution. All distributions are from NSD collisions except the lowest energy result from SFM, which are INEL.

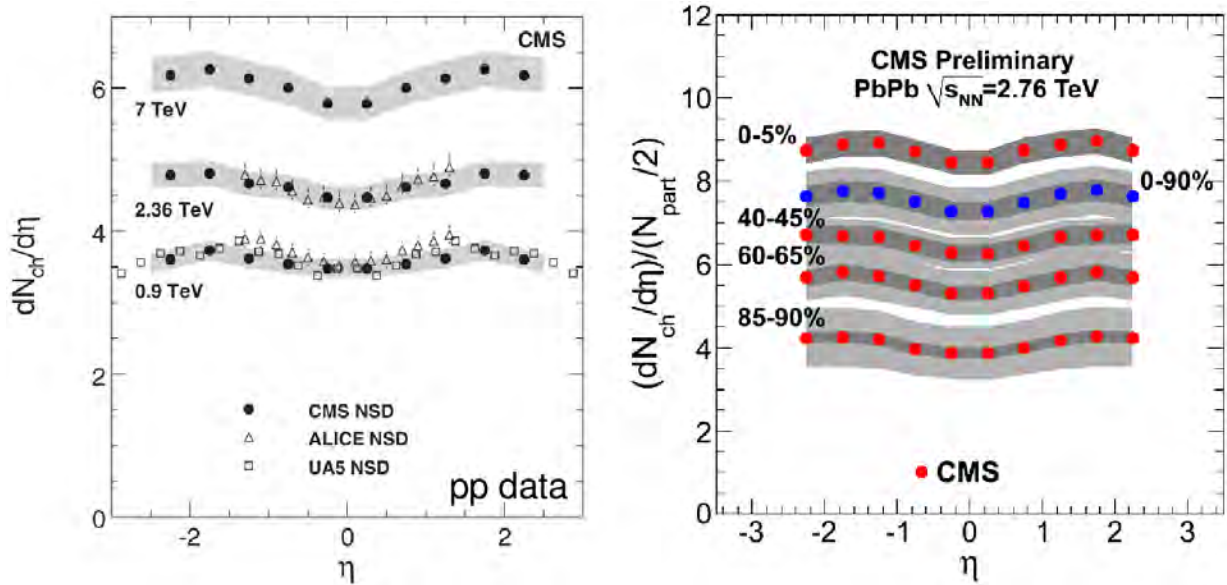


Figure 2.9: Left panel:  $\frac{dN_{ch}}{d\eta}$  measurements in  $pp$  collisions at  $\sqrt{s} = 900, 2360$  and  $7000$  GeV from CMS [84] and ALICE [73]. Right panel: Preliminary results from CMS on  $\frac{dN_{ch}}{d\eta}$  in PbPb collisions at  $\sqrt{s_{NN}} = 2760$  GeV [85].

The experiments introduced in the previous section not only published multiplicity distributions for  $pp$  ( $p\bar{p}$ ) collisions but also  $\frac{dN_{ch}}{d\eta}$  measurements. For the pre-LHC experiments these are presented in figure 2.8. Included in the figure is also  $\frac{dN_{ch}}{d\eta}$  at  $\sqrt{s} = 630$  GeV by the P238 (LHCb Test Beam) Experiment [81], located at the SPS. They did however never publish multiplicity distributions.

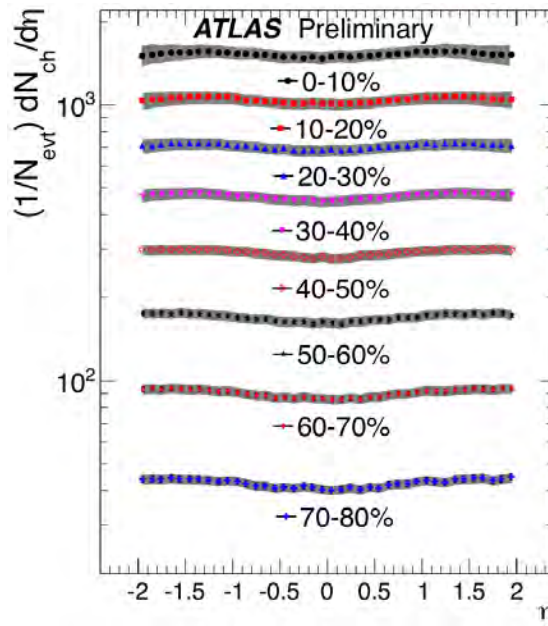


Figure 2.10: Preliminary results from ATLAS on  $\frac{dN_{ch}}{d\eta}$  in PbPb collisions at  $\sqrt{s_{NN}} = 2760$  GeV [86].

Left panel of 2.9 show the  $\frac{dN_{ch}}{d\eta}$  results at three energies from CMS and ALICE for  $pp$  collisions. One of the ambitions for ALICE is to extend these measurements to forward

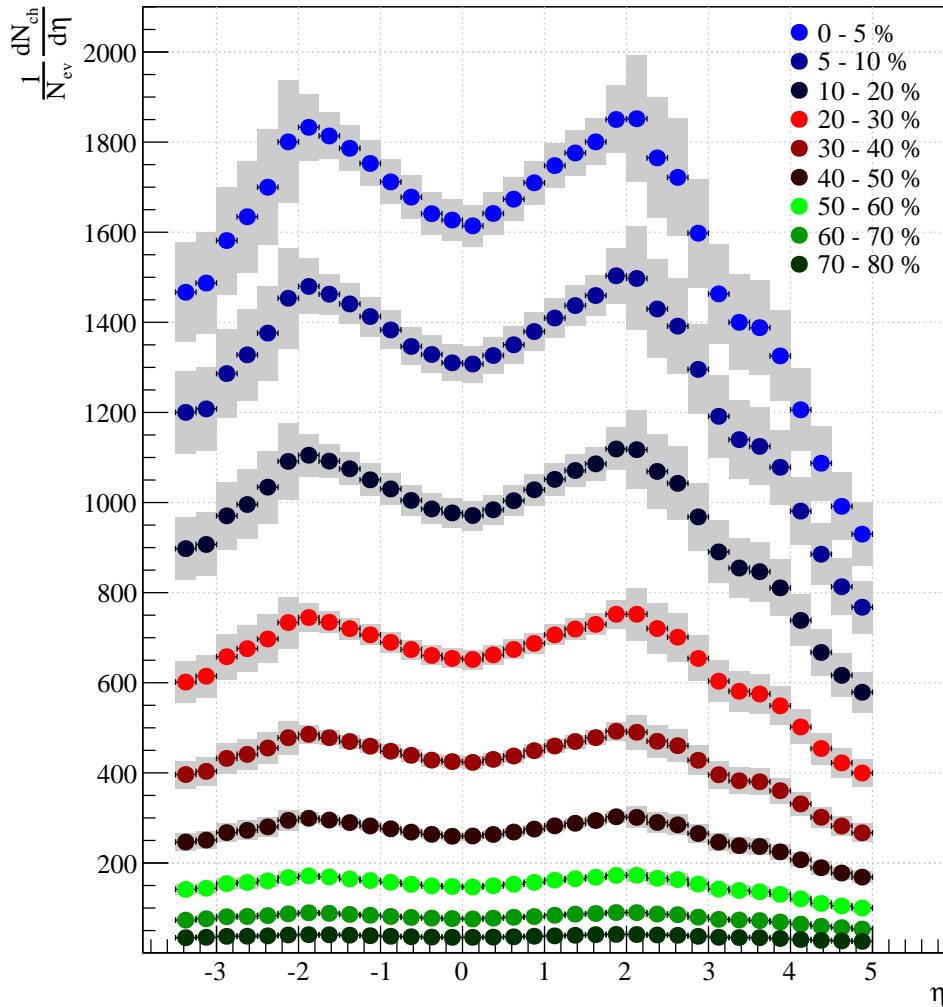


Figure 2.11: Still unpublished  $\frac{dN_{\text{ch}}}{d\eta}$  measurements over the entire  $\eta$ -range of ALICE for  $PbPb$  collisions at  $\sqrt{s_{NN}} = 2760$  GeV [87].

regions using the FMD system.

Right panel of figure 2.9 show the preliminary  $\frac{dN_{\text{ch}}}{d\eta}$  measurements in PbPb collisions at  $\sqrt{s_{NN}} = 2760$  GeV from CMS. Similarly figures 2.10 and 2.11 show preliminary PbPb results from ATLAS and ALICE respectively.

In general, it is found that the plateau in mid-rapidity increases and widens as a function of collision energy.

### 2.3.3 Mean Multiplicity Energy Dependence

In this last section results on the energy scaling of the mean multiplicity is presented. Figure 2.12 show  $\frac{dN_{\text{ch}}}{d\eta}$  at mid-rapidity published by many experiments over a wide interval of collision systems and energies. The mean multiplicity is scaled by the number of participant pairs of the collisions, to correct for different collision systems and centrality selections. It is seen that  $AA$  and  $pp$  collisions have slightly different behaviours. Both, however are proportional to  $s_{NN}^A$ .

Figure 2.13 show the theoretical predictions for the  $\frac{dN_{\text{ch}}}{d\eta}$  at mid-rapidity in  $PbPb$  collisions at  $\sqrt{s_{NN}} = 2760$  GeV, compared to the measurement from ALICE. It is obvious that

predicting this is far from trivial, as seen by the large variance in predicted values<sup>11</sup>. The reference numbers for the individual models in figure 2.13 corresponds to the references in [88], where the figure is from.

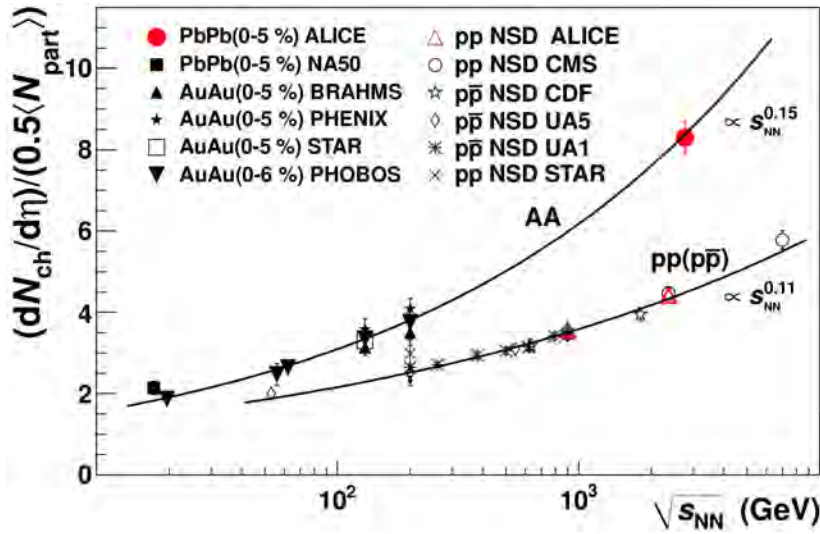


Figure 2.12: Mean multiplicity at mid-rapidity scaled with number of participant pairs, over a wide range of collision systems and energies. For both  $pp$  and  $PbPb$  collisions the mean multiplicity increases as  $s_{NN}^A$ , but with different values of  $A$ . Figure is from [88].

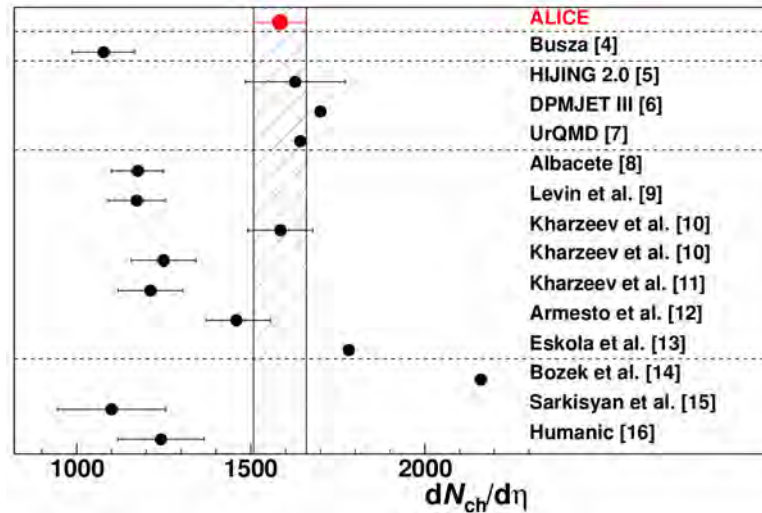


Figure 2.13: Theoretical predictions of the  $\frac{dN_{ch}}{d\eta}$  at mid-rapidity in  $PbPb$  collisions at  $\sqrt{s_{NN}} = 2760$  GeV. In the top the measured value from ALICE is indicated. The reference numbers for the individual models in the figure corresponds to the references in [88], where the figure is from.

<sup>11</sup>though these predictions at LHC energies are more in agreement with each other, than the predictions made about RHIC energies, when it started operations.



# Chapter 3

## Experimental Setup

### 3.1 The Large Hadron Collider

The Large Hadron Collider (LHC) [90] is located under the Swiss-French border near Geneva. It is CERN's latest collider, reusing the existing tunnel from the Large Electron Positron (LEP) collider. The LHC tunnel has a circumference of approximately 27km, and houses more than 1200 super-conducting dipole magnets. The LHC is designed to collide protons with up to  $\sqrt{s} = 14000$  GeV, and lead ions up to  $\sqrt{s_{NN}} = 5500$  GeV. A schematic of the CERN accelerator complex can be seen in figure 3.1.

During the very last preparations (only hours/days from the first ever collisions) in the planned September 2008 start up, the LHC encountered a serious problem. A faulty electrical connection between two super-conducting magnets sparked an electrical arc, which punctured the Helium enclosure, leading to a massive leak of liquid Helium. Once investigated it was obvious that the same construction defect existed numerous places around the ring. A conclusion of the investigation was that further safety mechanisms had to be implemented before the LHC could safely collide particles at the top design energy. Meanwhile, the LHC repaired the parts of the ring, which were deemed to have the worst electrical connections. A full year later LHC operations started again, culminating in the first collisions of protons at  $\sqrt{s} = 900$  GeV on 23<sup>rd</sup> of November 2009. The current top energy is  $\sqrt{s} = 7000$  GeV for protons and  $\sqrt{s_{NN}} = 2760$  GeV for lead ions. The schedule currently is to have a full year of shut down in 2013, where the remaining safety mechanisms are implemented, allowing the LHC to run at top design energies in 2014 and onwards.

#### 3.1.1 Colliding Protons

The protons used for p+p collisions stem from Hydrogen, being stripped of the electrons in the linear accelerator LINAC 2. They are injected from LINAC 2 into the BOOSTER at an energy of 50 MeV. The BOOSTER accelerates them to 1.4 GeV before they are sent to the Proton Synchrotron (PS), which further accelerates the protons to 25 GeV. From the PS they are sent to the Super Proton Synchrotron (SPS), where they yet again are accelerated, this time to 450 GeV. And finally they are transferred to the LHC ring. They are split into 2808 bunches travelling the ring either clockwise or counter-clockwise. The bunches of protons are then accelerated to their final energy, and made to collide at the location of the four experiments ALICE, ATLAS, CMS and LHCb.

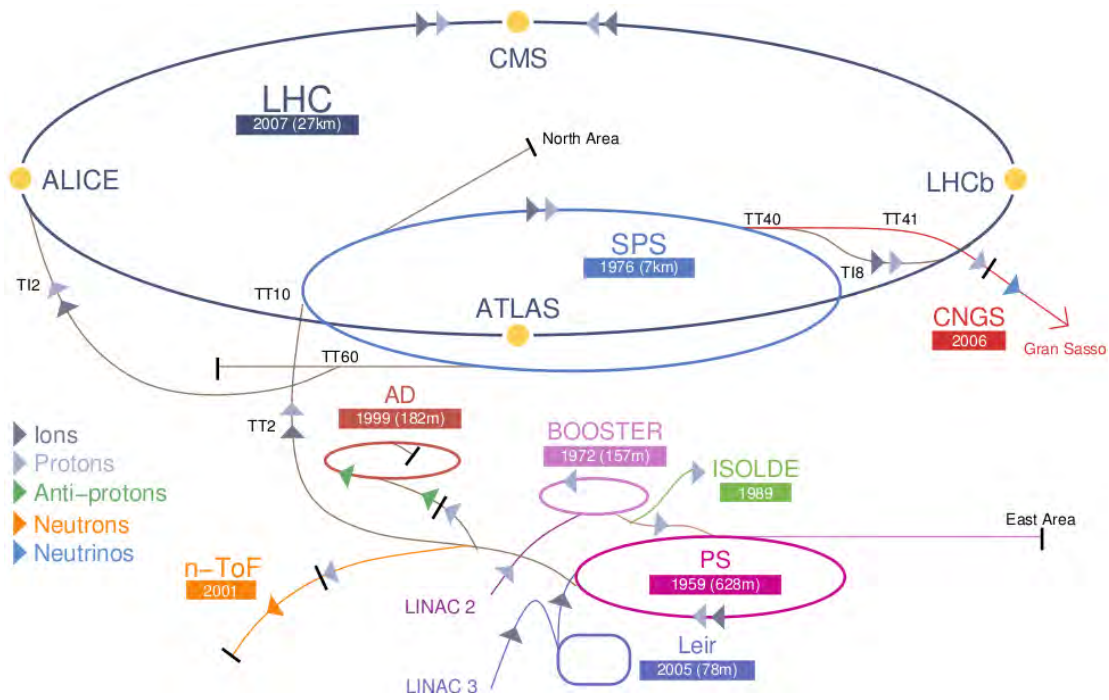


Figure 3.1: Schematic view of the CERN accelerator complex. The figure is adapted from [89].

### 3.1.2 Colliding Lead Ions

For running the LHC with lead ions the procedure is similar, but with some differences. The lead ions are produced by heating a highly purified lead sample up to around  $550^\circ$ . This lead vapour is ionised by an electron current. This creates a number of charge states, with  $Pb^{27+}$  being the dominant one. The ions are accelerated in LINAC 3 to 4.2 MeV per nucleon. Afterwards they are sent through a carbon foil, which strips most of them to  $Pb^{54+}$ . The  $Pb^{54+}$  beam is lead to the Low Energy Ion Ring (LEIR), where it is accelerated to 72 MeV per nucleon, before being transferred to the PS, where another acceleration is done bring the ions energy to 5.9 GeV per nucleon. The ions once again are sent through a foil, stripping them to  $Pb^{82+}$ , which is the final ionisation used for collisions. After the PS the now fully stripped ions arrive at the SPS, where they are accelerated to 177GeV per nucleon, before being sent into the LHC ring for acceleration to their collision energy. Like in the proton case, the ions are split into bunches, which are sent either clockwise or counter-clockwise around the ring. The collision of lead ions only occur at 3 of the experiment sites, namely ALICE, ATLAS and CMS.

Apart from the facilities mentioned, figure 3.1 also show several accelerator/detector systems at CERN not related to the LHC operation. These are the heavy isotope separator ISOLDE, the anti-matter production facility AD (Anti-proton Decelerator), the n-TOF (neutron - Time Of Flight) neutron source and last, but not least, the neutrino oscillation facility CNGS (CERN Neutrinos to Gran Sasso). CNGS has recently gotten significant attention in the media, after announcing measurements of muon neutrinos moving faster than the speed of light.

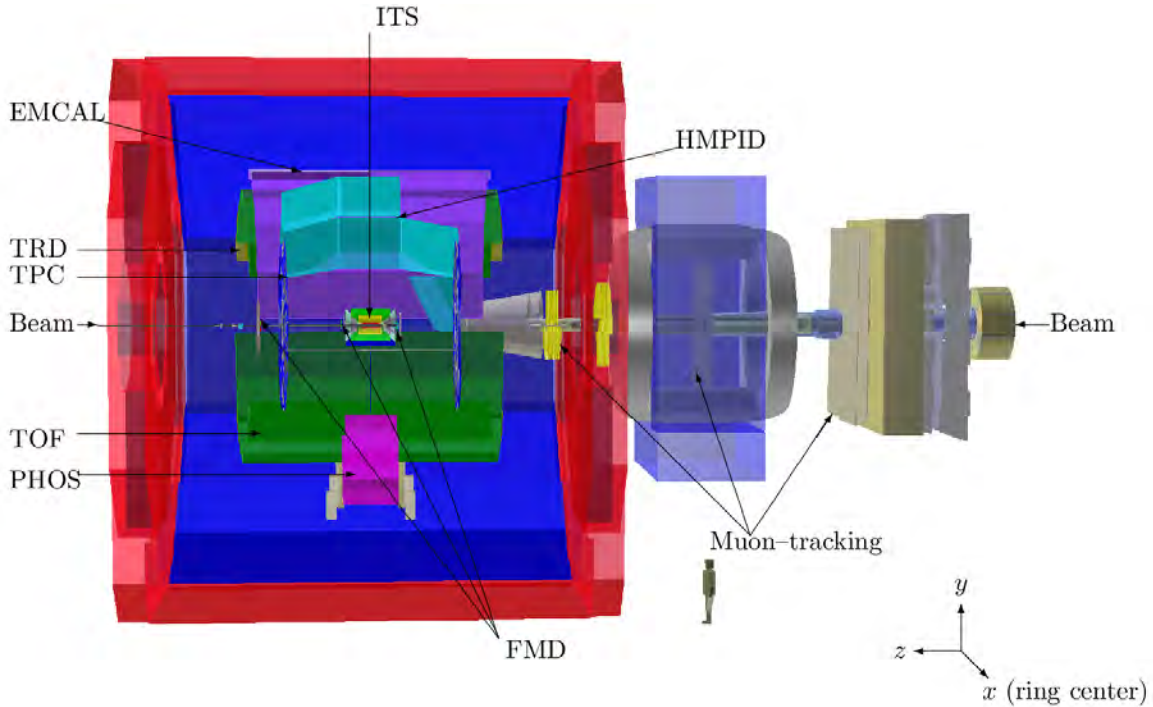


Figure 3.2: Overview of the ALICE detector. The beams are brought to collision in the very centre of the detector (just around the area marked ITS). The different sub-detector systems are shown with name and arrows. Descriptions of each are found in the text. The figure is from [91].

## 3.2 The ALICE Experiment

ALICE (A Large Ion Collider Experiment) [92] is designed as a general purpose detector, optimised for the study of high multiplicity central heavy ion collisions. The design is optimised for  $dN_{ch}/d\eta$  up to 4000, but has been designed to handle up to 8000. Even though ALICE is designed foremost as a heavy ion detector, a full physics program for  $pp$  collisions exist.

The defining abilities of ALICE is the capability of tracking and identifying charged particles over four magnitudes in particle momentum ( $10^{-2} - 10^2$  GeV/c. This allows extensive studies of topics from soft physics to jet physics, and high- $p_T$  particle production.

ALICE can be divided into three main sections; the central barrel detectors, the forward detectors and the Muon spectrometer [93]. The central barrel consists of the ITS, TPC, TRD, TOF, HMPID, EMCAL and PHOS [94–100]. The forward detectors include FMD, T0, V0, ZDC and PMD [101–103]. The individual subsystems will be discussed briefly later in this chapter. Fig. 3.2 shows an overview of the ALICE detector seen from the side.

ALICE covers a large range of pseudorapidity. The coverage of the individual subsystems is shown in fig. 3.3. For the purpose of this work we note at this time that the detectors used for analysis, the FMD and SPD, allows a  $\eta$ -coverage of  $-3.4 < \eta < 5.1$ .

## 3.3 Central Barrel Detectors

The central barrel of ALICE contains a number of sub-detector systems, covering the central region (roughly  $|\eta| < 1$ ). The main role of the central barrel is to identify charged

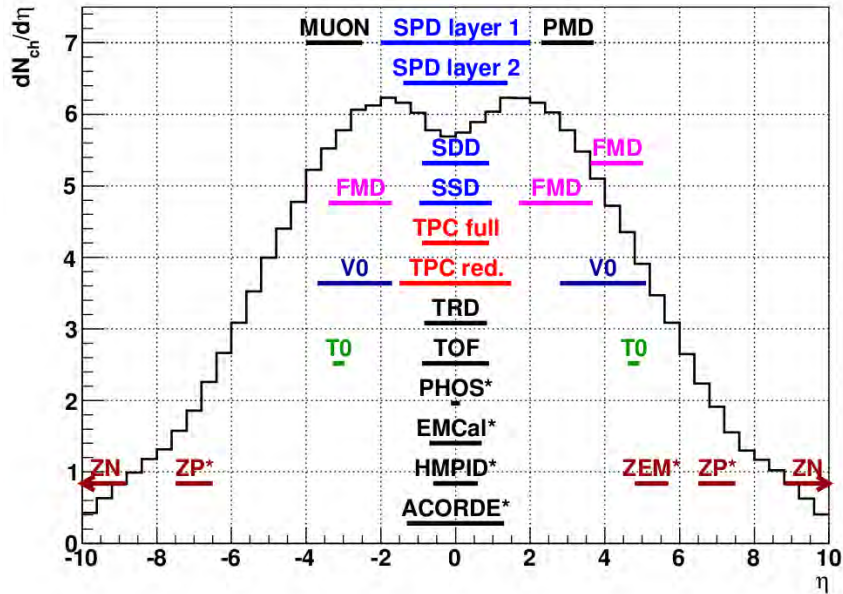


Figure 3.3: The pseudorapidity coverage of ALICE. Subsystems not having full azimuthal coverage is marked with an asterisk. The figure is from [24].

particles and their  $p_T$ , using a variety of different methods and technology. Fig. 3.4 shows the central barrel detectors.

### 3.3.1 Inner Tracking System

The Inner Tracking System (ITS) [92, 94] consist of 6 layers of Silicon. They are located at radii between 3.9 cm to 43 cm from the interaction point. This makes the innermost layer the detector closest to the interaction point.

The ITS is divided into 3 subsystems; the two innermost layers constitute the Silicon Pixel Detector (SPD), the middle two layers are named the Silicon Drift Detector (SDD) and finally the two outermost layers are the Silicon Strip Detector (SSD).

The SPD layers are based on hybrid silicon pixels consisting of silicon detector diodes with a thickness of  $200 \mu\text{m}$ . When a charged particle traverse a pixel a digital signal is read out from that pixel. The SPD does not retain any information on the energy deposition. Thus, SPD signal is binary; either there is a hit or there is not. The signals in the two SPD layers are sufficient to form so-called tracklets, which can be used to measure the charged multiplicity in  $|\eta| < 2.1$ . Due to extreme fine segmentation of the SPD, only an occupancy of around 1% is expected, making it extremely capable of multiplicity measurements. The SPD is used for analysis in this work, and will be revisited in more detail in section 4.

The SDD works as a drift chamber, where the charged particles ionise the gas when traversing the SDD volume. The created electrons drifts towards the readout, due to an electric field over the SDD. The coordinates of the particle are then directly correlated to the drift time.

The SSD utilises the energy loss from charged particles traversing strips of silicon. The SSD in this manner is quite similar to the FMD, which will be described in more detail later.

The main purposes for the ITS as a whole is:

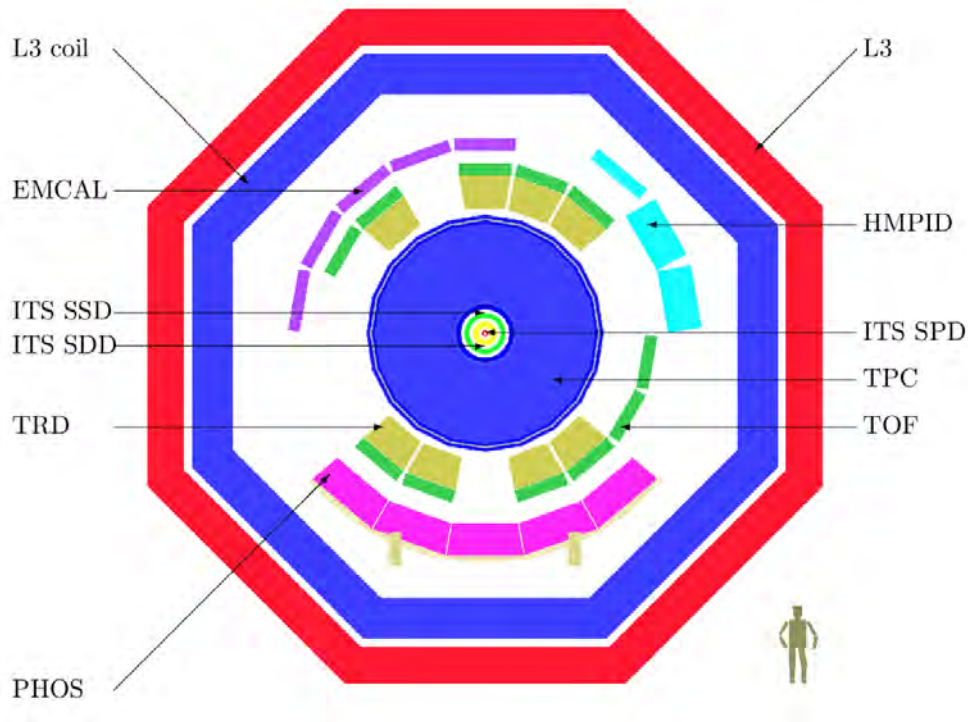


Figure 3.4: Illustration of the ALICE central barrel seen from the end. The azimuthal coverage of each of the barrel detectors is evident here. The figure is from [91].

- Act as a trigger detector.
- Determination of the primary collision vertex and the secondary vertices, necessary for the reconstruction of charm and hyperon decays.
- Particle identification and tracking of low-momentum particles.
- To improve the momentum and angle resolution in conjunction with the TPC.

### 3.3.2 Time Projection Chamber

The ALICE Time Projection Chamber (TPC) [92, 95] is the main tracking detector, and with its drift volume of  $95 \text{ m}^3$  it is the single largest sub-detector in ALICE, as well as the largest TPC in the world. The TPC's cylindrical drift volume encompasses the ITS.

The basic principle of the TPC is that charged particles traversing the gas-filled drift volume will ionise the gas, causing electrons to drift away from the central electrode towards the end-caps, where the drift time is read out and used to determine the trajectory of the original charged particle through the TPC.

The main objectives for the TPC is to provide tracking and particle identification of charged particles. Particle identification is done by using the energy loss in the gas. Tracking is done by utilising a Kalman filtering method [104, 105], which is a computational efficient recursive method of track finding.

Due to the big drift volume (and hence long drift times of up to  $90 \mu\text{s}$ ) the TPC sets an upper limit to the overall trigger rate in ALICE, since no new event should be accepted until after the read out of the previous event has passed. Thus the maximum trigger rate of ALICE (with the TPC in the read-out partition) is around 10kHz.

### 3.3.3 Transition Radiation Detector

The Transition Radiation Detector (TRD) [92,96], located radially right outside the TPC, relies on the phenomenon of transition radiation for particle identification. Transition radiation occurs when a particle crosses the boundary between two materials with different dielectric constants. The emitted radiation is linearly dependent on the  $\gamma$  factor of the particle, thereby making it very useful at distinguishing pions and electrons at high momenta.

The TRD is built up from six layers each containing a radiator, drift chamber and read out electronics. The radiator material is responsible for creating the transition radiation photons, which are then converted in the drift chamber to electrons, being detected in the read out electronics. The information of the six layers are then combined into tracklets, which are used to identify high momentum electrons. This is used as a trigger to enhance the recorded yield of  $\Upsilon$ 's and high  $p_T$   $J/\Psi$ .

The TRD does not have full azimuthal coverage. This is a design decision in order for the HMPID and PHOS detectors to also have areas without too much material in front of them. This is seen in figure 3.4.

### 3.3.4 Time Of Flight

The Time Of Flight (TOF) [92,97] detector is placed just outside the TRD, and measures the flight time of particles going from the interaction point through the TOF. The momentum information,  $p$ , and the length of the trajectory,  $l$ , of the particle is known from the tracking in the ITS, TPC, and TRD. This is used together with the flight time,  $t$ , to determine the particle mass,  $m$  :

$$m = p\sqrt{\frac{t^2}{l^2} - 1} \quad (3.1)$$

The TOF consists of Multigap Resistive Plate Chambers, which are stacks of very thin structures, featuring a gas volume with a uniform high electric field over. When a particle traverse the gas it immediately loses energy triggering an avalanche, which is detected at the anode of the detector.

As with the TRD, the TOF does not have full azimuthal coverage, due to a desire to minimise the material in front of HMPID and PHOS.

### 3.3.5 Photon Spectrometer

The PHOton Spectrometer (PHOS) [92,100] is an electromagnetic calorimeter, composed of lead-tungsten crystals. It is located in the bottom part of ALICE outside the TOF. Charged particles are rejected by multi-wire proportional chambers in front of the PHOS.

The PHOS detects photons,  $\pi^0$ , and  $\eta$  mesons. The measurements are used for analysing the initial temperature through direct single photons and/or di-photons, as well as probing deconfinement through jet quenching of high  $p_T$   $\pi^0$ 's and investigating signals of restoration of chiral symmetry<sup>12</sup>.

---

<sup>12</sup>Chiral symmetry restoration, which is the restoration of invariance under parity, is one of the truly smoking guns of a QGP.

### 3.3.6 Electro Magnetic Calorimeter

The Electro Magnetic CALorimeter (EMCAL) [92,99] was never meant to be a part of the first run period of the LHC. However due to the initial breakdown and subsequent repairs, the EMCAL was partially installed for the first runs. It is located outside the TOF.

The focus of the EMCAL is jet quenching in heavy ion collisions. Together with the tracks from the TPC and ITS, the EMCAL allows complete reconstruction of jets.

Furthermore the EMCAL functions as a trigger for hard jets, photons and electrons.

### 3.3.7 High Momentum Particle Identification Detector

The High Momentum Particle Identification Detector (HMPID) [92,98] is a Ring Imaging Cherenkov detector (RICH), which is used to identify high momentum particles. It consists of a layer of radiator material, and a Multi-Wire Proportionality Chamber behind to detect Cherenkov radiation. Any particle traversing a medium with a speed higher than the speed of light in that medium, will emit Cherenkov radiation. The radiation is emitted as a shock wave at an angle with respect to the track of the particle, defined by the speed of the particle. This Cherenkov angle,  $\theta_C$ , is given by:

$$\cos \theta_C = \frac{1}{n\beta} \quad (3.2)$$

Here  $\beta=v/c$  is the particle velocity relative to the speed of light and  $n$  is the refractive index of the medium. The emitted Cherenkov radiation is read out as a ring on the read-out plane. The ring radius is used to determine the velocity of the particle. This information is then used together with momentum information from for instance the TPC, to determine the mass of the particle.

## 3.4 Muon Spectrometer

The Muon spectrometer [92,93] is sitting in the very forward region of ALICE, with a coverage of  $-4 < \eta < -2.5$ . The purpose of the Muon spectrometer is to measure the complete spectrum of heavy quark vector-meson resonances (i.e.  $J/\Psi$ ,  $\Psi'$ ,  $\Upsilon$ ,  $\Upsilon'$ , and  $\Upsilon''$ ) and the  $\phi$  meson. All of these measurements are done in the  $\mu^+\mu^-$  decay channel. The Muon spectrometer can be seen in figure 3.5. Closest to the interaction point is the front absorber. The absorber consists of mainly carbon, concrete, and steel in order to prevent anything else but muons from passing through.

After the front absorber, tracking stations 1 and 2 are located. Tracking station 2 is located such that it determines precisely where the muons exit the solenoidal field of L3, encompassing most of ALICE. Then follows a dipole magnet, yielding the momentum of the muon by deflection. Inside the dipole magnet, tracking station 3 is placed to enhance the determination of the deflection. After the dipole magnet two more tracking stations sits, with an iron absorber in between them. In the end there are resistive plate chambers to determine the time of flight, and thus the particle mass (as in the TOF).

## 3.5 Forward detectors

The forward detectors of ALICE is comprised of the PMD, T0, V0 and the FMD. The first three will be briefly discussed in the following. A more complete description of the

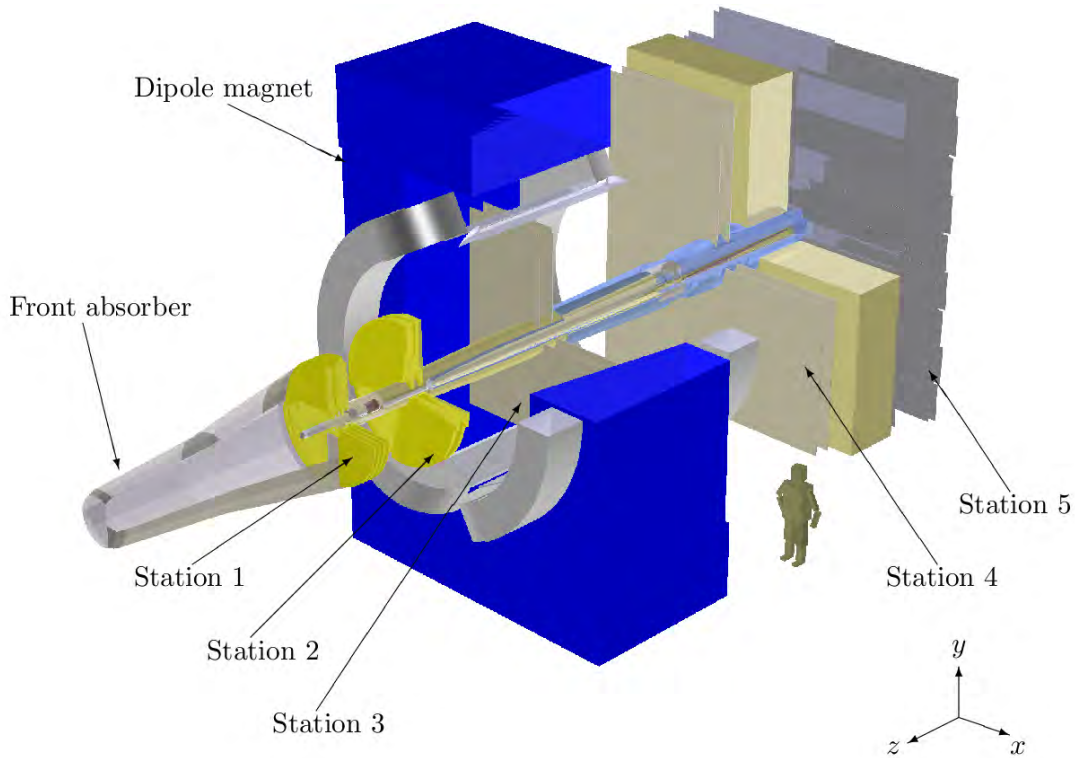


Figure 3.5: The Muon Spectrometer. The figure is from [91].

FMD system will follow in the next chapter. Figure 3.6 shows a schematic of the forward detector systems. The role of the forward detectors is to improve the  $\eta$ -range of multiplicity measurements in ALICE, as well as to determine more global event characteristics i.e., collision time, collision vertex, centrality, event plane and trigger conditions.

### 3.5.1 Photon Multiplicity Detector

The Photon Multiplicity Detector (PMD) [92, 102] measure the photon multiplicity in forward regions ( $2.3 < \eta < 3.7$  with full azimuthal coverage). It consists of two high granularity gas proportional chambers, with a three radiation length converter in between.

The first chamber acts as a veto on charged particles. The converter, consisting of lead and stainless steel, causes photons traversing it to create electromagnetic showers. These showers are detected in the second gas proportional chamber giving a signal in several cells. The thickness, and material of the converter is chosen such that there is minimum overlap between showers in the detection plane i.e., small angle showers.

### 3.5.2 T0

The T0 [92, 101] detector is designed to determine the collision time with high precision and to determine the collision vertex. T0 consists of two units, one on each side of the interaction point. It is the coincidence between signals in both sides that is used for both vertex and time determination.

Each T0 unit is comprised of quartz Cherenkov radiators glued to photo multiplier tubes. The radiator emits Cherenkov radiation, when hit, which is then detected in the photo multiplier tubes.

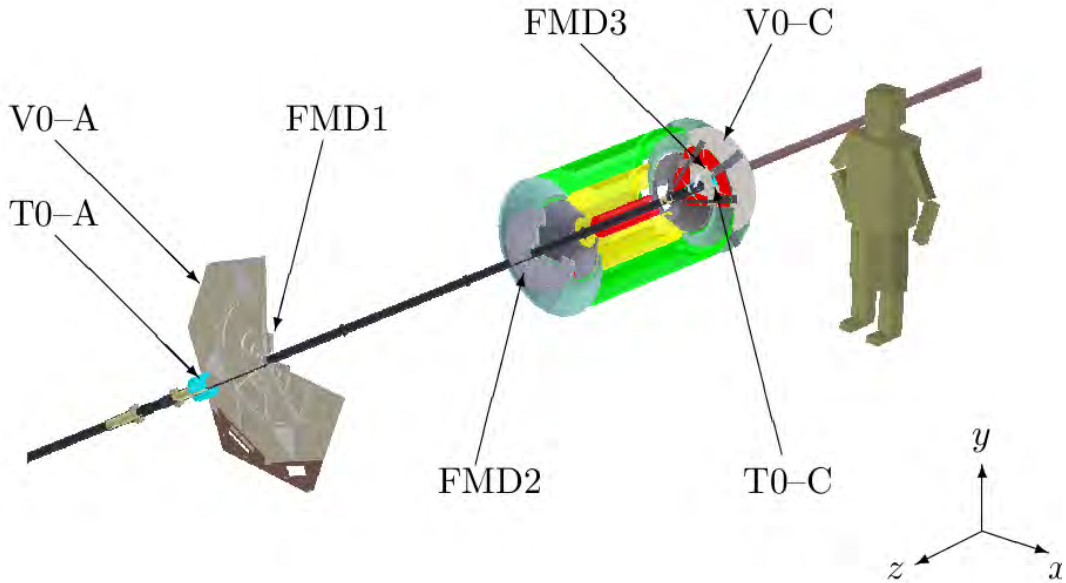


Figure 3.6: The forward detectors of ALICE. The figure is from [91].

T0 furthermore acts as a early wake-up signal to other detectors. Due to the low acceptance of T0 it is only reliable for  $AA$  collisions where the particle multiplicity is much higher than in  $pp$  collisions.

### 3.5.3 V0

Since the T0 has a low trigger efficiency in  $pp$  collisions, the V0 [92, 101] detector was designed with a much larger acceptance, in order for it to perform as a minimum bias trigger in both  $pp$  and  $AA$  collisions. Furthermore it is used to determine the event centrality and the event plane. It can also be used at studies of multiplicities at very forward angles, however with less precision than the FMD and PMD.

V0 consists of two units of scintillator counters located on each side of the interaction point.

### 3.5.4 Zero Degree Calorimeter

The Zero Degree Calorimeters (ZDC) [92, 103] are positioned at very forward angles. Their role is to measure the spectator nucleons from heavy ion collisions, in order to estimate the number of participants, and hence the centrality.

The two ZDC themselves are positioned on each side of the interaction point, 116 meters away from it. Counted as part of the ZDC system are also two electromagnetic calorimeters (ZEM). These are placed on either side of the beam pipe, but only 7 meters away from the interaction point on the opposite side of the muon absorber. The ZEM measures the photons from particles emitted at forward rapidities, which is used for determining the centrality of very central collisions where few spectators escape to the ZDCs. Similarly they are also used for very peripheral collisions. For very peripheral collisions, the spectators resemble the incoming nuclei (both in amount and direction), and thus might continue inside the beam pipe, avoiding detection in the ZDCs.

## 3.6 Data Acquisition System

This chapter ends with a brief overview of the Data Acquisition (DAQ) [92,106] in ALICE. The DAQ is responsible for collecting the signals from the various sub-detectors, and building the event. Furthermore the DAQ exports the collected events for storage.

Event building is a two step procedure. The data from the sub-detectors are transferred via Detector Data Link (DDL) optical fibers to Local Data Concentrators (LDCs). On the LDCs, the received data is gathered into sub-events, which are then shipped to Global Data Concentrators (GDCs). The GDCs collect the sub-events from all the LDCs, and assemble the final event from this.

The event is sent for immediate storage in a disc system called Transient Data Storage (TDS), before being transferred to permanent storage at magnetic tapes.

The full DAQ system of ALICE consists of 200 LDCs and 60 GDCs. [24].

When running, the DAQ can manage data taking in several partitions at the same time. A partition includes a subset of sub-detectors, that run under the same conditions. As an example of partitions, one could have separate partitions with fast or slow trigger rates respectively. Detectors that for some reason are restricted by long read-out times, like the TPC, can then run in the slow partition at one interaction rate, while the other detectors run at a higher interaction rate in the fast partition.

# Chapter 4

## The FMD and SPD

This work relies on the measurements of charged particles from the FMD, as well as from the first layer of Silicon in the SPD. Both are Silicon semi-conductor devices. The FMD is a strip detectors, where as the SPD is a pixel detector.

This chapter will start by detailing basic concepts regarding Silicon detectors in general, before moving on to presenting the two detectors.

### 4.1 Semi-conductor properties

Semi-conductors is a term denoting materials, characterised by the band-gap between the valence and conduction bands being quite small. This means that it takes little energy to excite an electron into the conduction band, leaving a hole in the valence band. Semi-conductors fall in between insulators, characterised by a large band-gap, and metals, that have no band-gap, allowing electrons to roam freely. A schematic of all three material types can be seen in figure 4.1

Semi-conductors, such as Silicon and Germanium, are popular mediums for physics detectors. The basic principle of semi-conductor detectors is analogous to gas ionisation detectors such as drift chambers etc.. The main advantage of semi-conductors is that the energy required to create electron-hole pairs are ten times smaller than for gas ionisation [107]. Thus the amount of ionisation at a given energy will be much higher, leading to a better energy loss resolution.

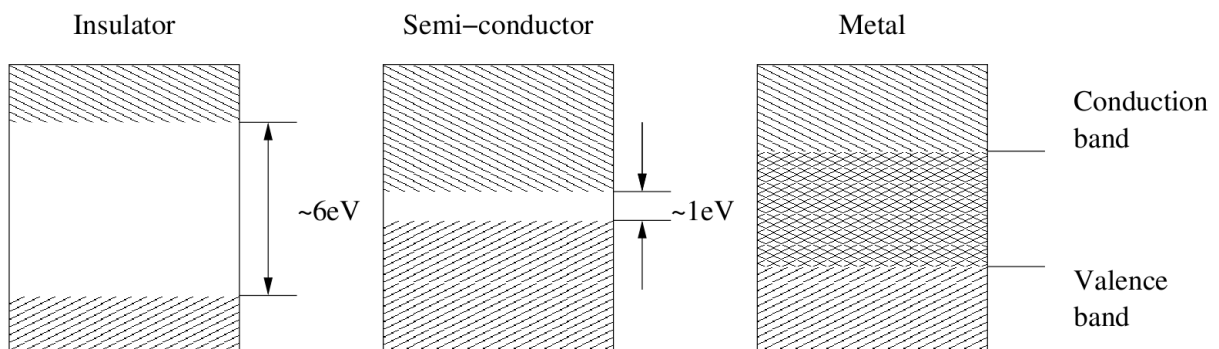


Figure 4.1: Illustration of the band-gap between the valence and conduction bands in insulators, semi-conductors and metals.

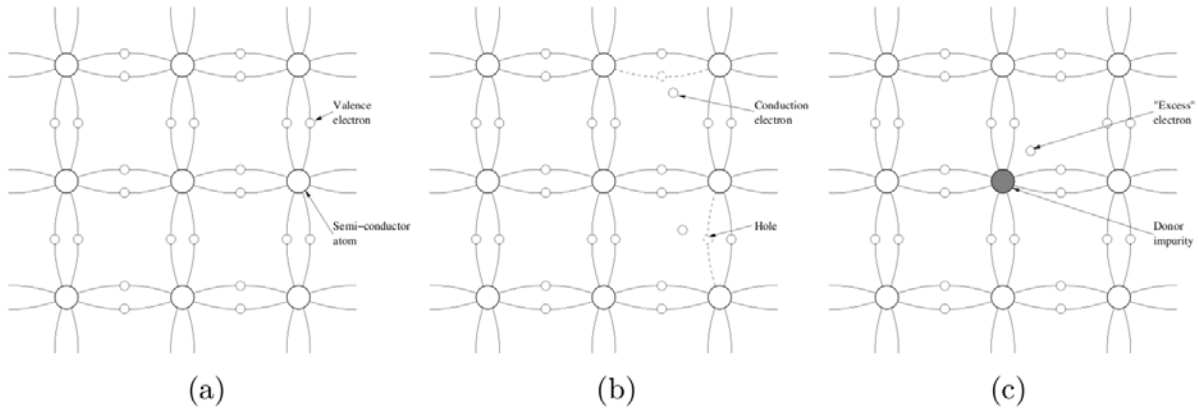


Figure 4.2: (a) At low temperatures the tetravalent Silicon crystal form four covalent bindings with neighbouring Silicon atoms. (b) At non-zero temperatures valence electrons can be thermally excited into the conduction band, leaving holes in the valence band. (c) A Silicon crystal have been doped with a pentavalent donor impurity. The excess electron create allowed energy states between the conduction and valence bands. The figure is from [91].

### 4.1.1 Doped Crystals

In pure Silicon crystals the electrons are bound covalently. The small band-gap allows even minor thermal excitation to bring the valence electrons into the conduction band, leaving an extra electron in the conduction band, as well as a hole in the valence band, both of which function as charge carriers. To increase the numbers of charge carriers the Silicon crystals are doped.

The basic idea is to introduce material with either one extra or one less valence electron than the material to be doped. Silicon is tetravalent<sup>13</sup>. Doping Silicon with pentavalent atoms thus gives one extra electron. This creates another allowed energy state in the band-gap just below the conduction band. The electron is easily excited into this state, increasing the conductivity. In figure 4.2 the covalent binding of Silicon, thermal excitation of valence electrons and a doped Silicon crystal is illustrated.

Doping with trivalent atoms on the other hand ensures that there are not enough electrons to fill the valence band. Furthermore it introduces another allowed energy state in the band gap, this time close to the valence band. Thus electrons in the valence band can easily be excited into this state, leaving even more holes in the valence band.

Semiconductors with an excess of electrons are called n-type semi-conductors, and if there is an excess of holes they are called p-type semi-conductors. Normally the concentration of the dopant impurities is very small, around  $10^{-9}$  [107].

However, heavily doped semi-conductors (usually labelled n+ and p+ respectively) are also used extensively in for instance electrical contacts. In heavily doped semi-conductors dopant concentrations can be as high as  $10^{-3}$ , leaving them highly conductive [107].

<sup>13</sup>Tetravalent atoms have four valence electrons. Similarly pentavalent and trivalent atoms have five and three valence electrons respectively.

## 4.2 Semi-conductor detectors

The basic idea behind Silicon detectors uses the fact that if a particle traverse the Silicon it excite electrons into the conduction band, leaving electron-hole pairs behind. If one applies an external electrical field over the crystal, the electrons drift to the anode, and the holes toward the cathode, thereby inducing a current over the crystal. This current can be read out.

However, just using n or p type crystals as described in the last section is not viable. Since the band-gap is sufficiently small, thermal excitations would also create a current and thus the detector would be very noisy. In the following will be described what is done to avoid this.

### 4.2.1 n-p junctions

The practical implementation in detectors is to make a junction between a n-type and a p-type semi-conductor. Due to the difference in concentration of electrons and holes between the two sides there will be an initial diffusion of electrons towards the p-side and of holes towards the n-side. Since each side was initially neutral it follows that the p-side will become negatively charged, due to the added electrons, and the n-side will become positive, due to the added holes. This creates an electrical field gradient over the junction, which eventually stops the diffusion, since the electrons and holes need to perform work to overcome the created contact potential over the junction. This leaves a region of immobile charge carriers near the junction. Any electron or hole created in this region, which is called the depletion zone, will immediately be swept away by the electric field. Thus any external particles traversing the depletion zone, will create new electron-hole pairs, that are swept away, and can be read out.

The depletion zone depth,  $d$ , in a regular n-p junction is quite small and is given by [107]:

$$d \sim \alpha_c \cdot \sqrt{\rho_c \cdot V_0} \quad (4.1)$$

where  $\alpha_c$  is a constant of the order of unity, slightly different depending on whether it is the n or p-side,  $\rho_c$  is the crystal resistivity, and  $V_0$  is the contact potential. Taking typical values for the n-side for instance ( $\alpha_n=0.53$ ,  $\rho_n \sim 5000 \Omega\text{cm}$  and  $V_0 \sim 1 \text{ V}$ ) yields a depletion depth of roughly  $35\mu\text{m}$ . This depth is very small compared to the radiation length in Silicon, making it less likely that any radiation traversing the sensor would create a significant amount of electron-hole pairs. Furthermore the noise from the sensor is proportional to the capacitance,  $C$ , of the crystal, which is connected to the depletion depth through [107]:

$$C = \epsilon \cdot \frac{A}{d} \quad (4.2)$$

Here  $\epsilon$  is the dielectric constant of Silicon,  $A$  is the crystal area and  $d$  is the depletion zone depth. Thus in order to decrease the noise, and increase the chance that a traversing particle will be detected, it is necessary to increase the depletion depth.

This is done by applying a so-called reverse bias voltage,  $V_b$ . It is a negative voltage applied to the p-side of the junction. It causes the excess holes and electrons to be drawn further away from the junction, thereby increasing the depletion depth. The depletion depth is still given by (4.1), with the substitution of  $V_0$  with  $V_b$ . There exist a maximum voltage, determined by the resistivity of the crystal, which limits the depletion depth. If the reverse bias voltage is above this maximum the n-p junction breaks down.

Ideally, the n-p junction is not conducting, even when applying a reverse bias voltage. However for various reasons this is not completely true. When the reverse bias voltage is applied a small current may flow over the sensor. This current is called the leakage current, and it contributes to the read-out noise of the sensors.

### 4.3 Energy loss in Silicon

Silicon detectors generally works through the detection of the energy lost when particles traverse the Silicon sensor. The average energy loss per unit length is called the stopping power, and is well described by the Bethe-Bloch equation [5]:

$$-\frac{dE}{dx} = 4\pi N_A r_e^2 m_e c^2 z^2 \frac{Z}{A} \frac{1}{\beta^2} \left[ \frac{1}{2} \ln \left( \frac{2m_e c^2 \gamma^2 \beta^2 T_{max}}{I^2} \right) - \beta^2 - \left\{ \frac{\delta(\beta\gamma)}{2} + \frac{C}{Z} \right\} \right] \quad , \quad (4.3)$$

where

$N_A$	Avogadro's number	$6.0221415(10) \times 10^{23} \text{ mol}^{-1}$
$r_e$	Classic electron radius	2.817940325(28) fm
$m_e$	Electron mass	0.510998918(44) MeV
$c$	Speed of light	
$z$	Charge of incident particle	e
$Z$	Atomic number of material	Si: 14
$A$	Atomic mass of material	Si: 28.0855
$\beta$	$= p/m$ of incident particle	
$\gamma$	$= 1/\sqrt{1 - \beta^2}$ of incident particle	
$T_{max}$	Maximum energy transfer in a single collision	MeV
$I$	Mean excitation energy	eV
$\delta(\beta\gamma)$	Density effect correction to ionisation energy loss	
$C$	Shell correction	

$T_{max}$  is a measure of the maximum energy transferred in a single interaction between the incident particle and the electrons in the material. It is given by:

$$T_{max} = \frac{2m_e c^2 \beta^2 \gamma^2}{1 + 2\gamma m_e/m + (m_2/m)^2} \quad (4.4)$$

with  $m$  being the mass of the incident particle. The mean excitation energy,  $I$ , is experimentally found to vary quite a bit with atomic number [5]. Its main features are parametrised by:

$$\frac{I}{Z} = \begin{cases} 12 + \frac{7}{Z} & Z < 13 \\ 9.76 + 58.8Z^{-1.19} & Z \geq 13 \end{cases} \quad , \quad (4.5)$$

Bethe and Bloch derived the main portion of (4.3) (the exception is the terms in curly brackets) from a quantum mechanical description of particles scattering softly on the electrons in dense matter.

The terms in the curly brackets were added later on as corrections for density effects ( $\delta(\beta\gamma)/2$ ) and shell effects ( $C/Z$ ). They are important at high and low energies respectively.

The density correction takes into account the fact that the electrical field of the incident particle will polarise the atoms it passes. This polarisation makes electrons contribute less to the total energy loss. The polarisation becomes bigger at higher particle velocities, as well as in denser media.

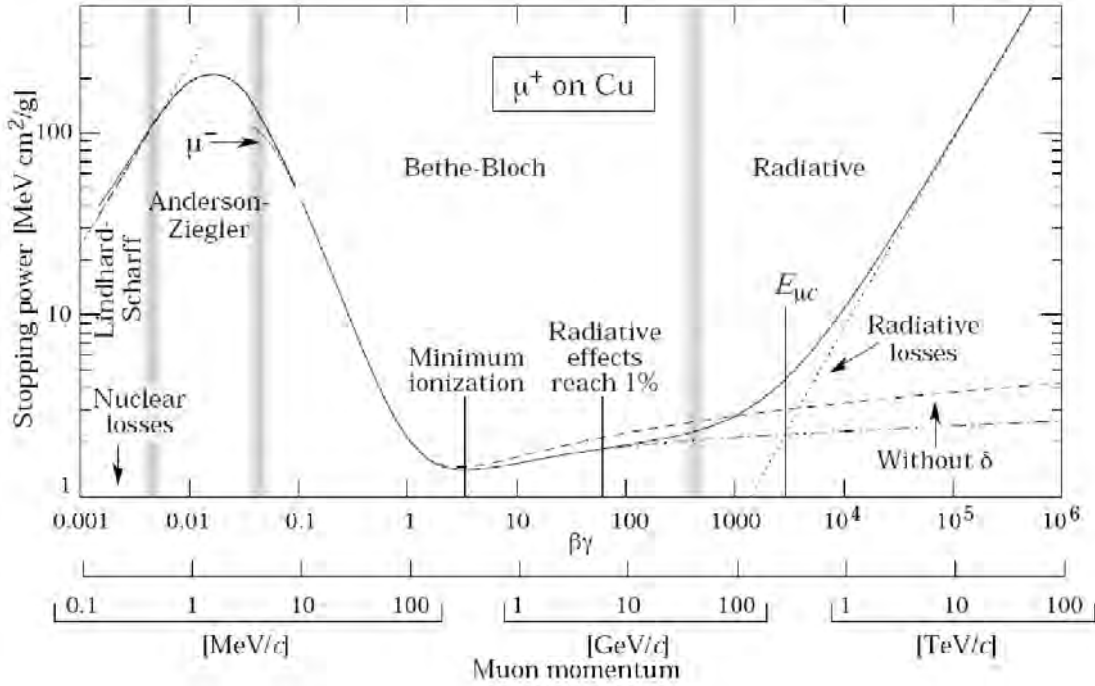


Figure 4.3: The stopper power for  $\mu$  in Copper [5]. The low and high energy loss regimes can not be described adequately by the Bethe-Bloch equation. However for medium energy losses around the minimum ionisation the Bethe-Bloch equation is a good description.

The need for the shell correction stems from the assumption by Bethe and Bloch that the electrons are at rest compared to the incident particle. However when the orbital electron velocity becomes comparable to the incident particle velocity this assumption breaks down, and the correction comes into play.

Shown in figure 4.3 is the stopping power of muons,  $\mu$ , in Copper. It is given as a function of both momentum and  $\beta\gamma = \frac{\beta}{\sqrt{1-\beta^2}}$ . In the very low regime ( $\beta\gamma < 0.1$ ) the description by (4.3) is not valid. Other models are indicated in the figure for the low end. Similarly at very high energies the Bethe-Bloch equation again becomes insufficient. In this regime radiative effects like brehmsstrahlung and Cherenkov radiation occur, requiring the description by other models.

The minimum of the Bethe-Bloch curve (around  $\beta\gamma \sim 3.5$  in figure 4.3) denote the minimum ionisation energy. A traversing particle depositing this energy is said to be a Minimum Ionising Particle (MIP).

Equation (4.3) and the full curve shown in figure 4.3 requires the thickness of the struck materials to be comparable to the mean interaction length of particles in that material. However for thin absorbers, such as the FMD and SPD this is not true.

For thin absorbers the following apply [108]:

- The incident particle will not suffer enough collisions for the central limit theorem to hold. Thus the energy loss probability distribution,  $dN/d\Delta$ , is not Gaussian (as is the case for thick absorbers).
- The incident particle does not encounter enough material for the radiative effects to build up.

- At high energy, enough energy can be transferred in order to knock out electrons, which escapes the absorber completely. These are labelled  $\delta$ -electrons. They lead to a lower average energy loss than the one in figure 4.3.

This was first treated in detail by Landau [108], who made the following assumptions:

- The maximum possible energy transfer per collision in (4.3) goes to infinity
- The energy transfers are sufficient to treat the excited target electrons in the absorber as free.
- The incident particles do not lose significant kinetic energy traversing the absorber, i.e their velocities are constant.

For thin absorbers, single large energy transfers thus have a relatively higher probability than in thick absorbers, skewing the energy loss probability distribution, and thus giving rise to a very long high energy loss tail. This distribution is called the Landau distribution, and is given by:

$$\frac{dN}{d\Delta} = \frac{1}{\xi} \frac{1}{\pi} \int_0^\infty e^{-u \log u - u\lambda} \sin(\pi u) du \quad (4.6)$$

where

$$\lambda = \frac{1}{\xi} \left[ \Delta - \xi \left( \log \xi - \log \varepsilon + 1 - C \right) \right]$$

$$\log \varepsilon = \log \left[ \frac{(1 - \beta^2)I}{2mc^2\beta^2} \right] + \beta^2$$

$C$  is Euler's number,  $\xi$  is an approximation to the mean energy loss from the Bethe-Bloch equation,  $\varepsilon$  is the minimum energy transfer to fulfil the free electron assumption above [107] and  $\Delta$  is the energy loss.

An example of the shape of a Landau distribution can be seen in figure 4.4. A consequence of the long tail of the distribution is that the mean and peak of the distribution does not coincide. Typically the distribution is thus parametrised by the energy loss value in the peak, called the Most Probable Value (MPV), which is labelled by  $\Delta_p$  and is given by:

$$\Delta_p = \xi \left[ \log \left( \frac{2mc^2\beta^2\gamma^2}{I} \right) + \log \frac{\xi}{I} + j - \beta^2 - \delta(\beta\gamma) \right] \xrightarrow{\beta\gamma \geq 100} \xi \left[ \log \left( \frac{2mc^2\xi}{(\hbar\omega_p)^2} \right) + j \right] \quad (4.7)$$

$\hbar\omega_p = 28.816 \text{ eV} \sqrt{\rho \frac{Z}{A}}$  is the plasma energy, and  $j = 0.2$  [91]. As seen by (4.7), the MPV flattens out for high  $\beta\gamma$ . Thus for thin absorbers, the energy loss can be expected to be almost constant if the incident particle has  $\beta\gamma > \beta\gamma_{MIP}$ .

Vavilov and Shulek improved the theory of Landau [109, 110] by including convolution of the Landau by a Gaussian, to account for excitations of inner shells in the atoms. But the Landau still makes a fine first order approximation.

Furthermore, occasionally the same sensor is hit several times, describable by multiple (Gauss convoluted) Landau distributions. Thus in total the energy loss can be described by [108]:

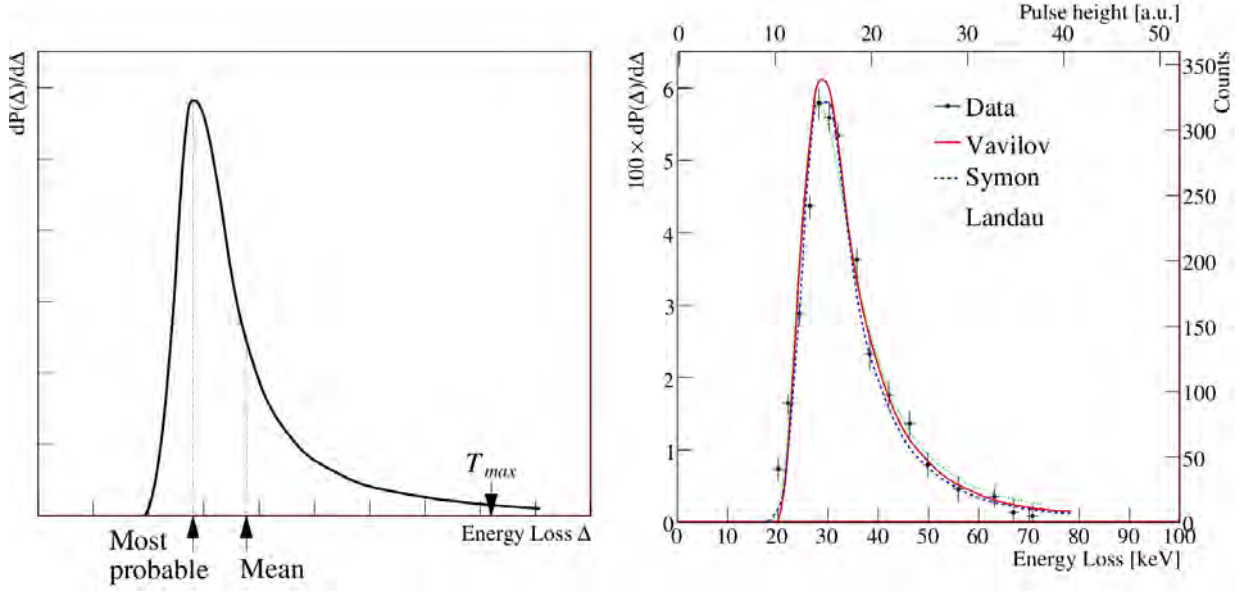


Figure 4.4: Left panel: Example of the form of a landau distribution. The most probable value and the mean differs, in contrast to a Gaussian where they are identical. Right panel: Example of the differences between the original Landau distribution, and further developments in describing the energy loss in thin absorbers. While the Landau is not the most correct of them, it remains a very good first approximation. Figure is from [91].

$$\begin{aligned}
 F(\Delta) &= \sum_{i=1}^n a_i F_n(\Delta) \\
 &= \sum_{i=1}^n a_i (L_i(\Delta) \otimes G_i(\Delta)) \\
 &= \sum_{i=1}^n a_i \int_{-\infty}^{\infty} d\Delta' L(\Delta; \Delta', \xi_i) \exp -\frac{(\Delta_{p,i} - \Delta')^2}{2\sigma^2}
 \end{aligned} \tag{4.8}$$

with  $L_i$  and  $G_i$  denoting Landau with most probable value  $\Delta_{p,i}$  and width  $\xi_i$  and Gaussian distributions for  $i$  particles depositing energy respectively. The  $a_i$ 's are the weights of each of the convoluted distributions.

It can be shown that (4.8) has  $n + 2$  free parameters [108]. Three of those stem from the Landau and Gaussian, and are the  $\sigma$  of the Gaussian component and the single particle Landau parameters  $\Delta_p$  and  $\xi$ . The remaining parameters are the  $a_i$ 's of the  $n$  individual Landau distributions.  $a_1$  is defined to be unity, which leaves  $n - 1$   $a_i$ 's as parameters.

The Landau parameters for the  $i^{th}$  distribution are connected to the single particle distribution by [111]:

$$\xi_i = i\xi \tag{4.9}$$

$$\Delta_{p,i} = i\Delta_p + \xi i \ln i \tag{4.10}$$

To sum up, the energy deposits in thin absorbers, like the FMD, can be described by multiple landau distributions, convoluted by Gaussians. From the amplitudes of the indi-

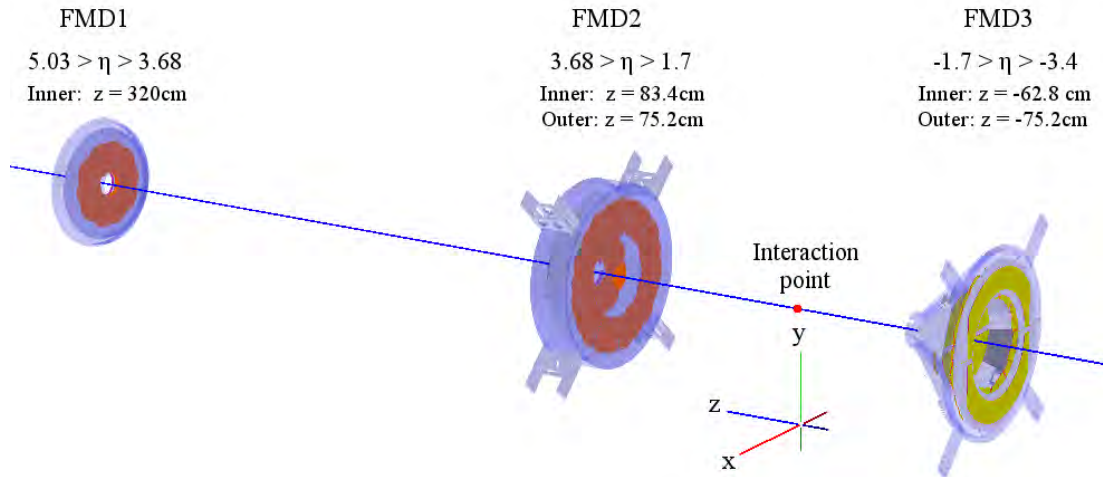


Figure 4.5: Overview of the FMD system. FMD2 and FMD 3 are placed nearly symmetrically around the interaction point, and FMD1 is located some distance away from the interaction. Ideally, one could have hoped for another FMD at around  $z = -320\text{ cm}$  (mirroring FMD1), but due to the massive Muon absorber sitting there, this is not possible.

vidual Landau distributions it can thus be inferred for a given energy deposit whether it was caused by a single or more incident particles.

## 4.4 Forward Multiplicity Detector

The Forward Multiplicity Detector (FMD) is one of the main contributions to ALICE from the Niels Bohr Institute at the University of Copenhagen. It is designed, built and tested locally before being installed in ALICE. The FMD is a Silicon strip detector, with fine  $\eta$ -segmentation, and adequate  $\phi$ -segmentation.

The FMD system consists in total of 5 Silicon rings, grouped into 3 sub-detectors named FMD1, FMD2 and FMD3. The latter two consist of 2 rings each, an inner ring and an outer ring. FMD1 only consists of an inner ring. Thus when referring to individual rings, the name will consist of the sub-detector name, with an addition of either I or O (Inner or Outer) i.e., FMD1I, FMD2I, FMD2O, FMD3I, FMD3O.

Figure 3.6 in the previous chapter showed the location of the different FMD sub-detectors with respect to the beam pipe, ITS and interaction point.

### 4.4.1 Design and Motivation

The main physics purpose of the FMD detector is to extend the charged particle coverage of ALICE into very forward rapidity regions, as seen in figure 3.3. This is essential for getting a more complete picture of particle production, as well as generally understanding the most forward regions.

Another of the main motivations for the FMD is its capability to provide independent measurements of the collision reaction plane and furthermore measurements of the various flow harmonics,  $v_n$ , in the forward region. The independence from the mid-rapidity barrel detectors in determining the reaction plane, will allow those detectors to use that measure-

ment in their determination of  $v_n$  in the mid-rapidity region (and vice versa the FMD will utilise their reaction plane measurements).

The mentioned physics goals for the FMD lead to the following design requirements:

- Broad  $\eta$  coverage.
- Fine  $\eta$  segmentation. This is important in order to have a low average detector occupancy, and thus a high measurement resolution for multiplicities. There are 512 and 256  $\eta$ -segments in inner and outer rings respectively.
- Full  $\phi$  coverage. The segmentation in  $\phi$  however is limited, with 20 and 40 segments in inner and outer rings respectively.

Ideally, tracking capabilities would be available to a detector like the FMD. However due to the very forward  $\eta$  coverage this is not possible. Particles emitted in forward regions have extremely high momentum, and thus are deflected very little in the magnetic field. Hence, in order to have a tracking detector with good momentum resolution at these pseudorapidities, the detector would need to be located very far from the interaction point.

Sub-detector	Ring	# $\varphi$ segments	# $r$ segments	$z$ [cm]	$r_{in}$ [cm]	$r_{out}$ [cm]
FMD1	I	20	512	320.0	4.2	17.2
FMD2	I	20	512	83.4	4.2	17.2
	O	40	256	75.2	15.4	28.4
FMD3	I	20	512	-62.8	4.2	17.2
	O	40	256	-75.2	15.4	28.4

Table 4.1: Overview of the segmentation and placement of the individual FMD rings.

The design requirements lead to a detector design, with rings (positioned around the beam pipe) of Silicon semi-conductor sensors. In Table 4.1 and Figure 4.5 the placement of the rings, and several characteristics are shown.

#### 4.4.2 FMD Sensors and Electronics

Each of the FMD rings consist of a number of identical base units, referred to as FMD sensors. The top part of figure 4.6 shows both an inner and outer ring, consisting of 10 and 20 sensors respectively. Each FMD sensor has two sectors on it, meaning that inner rings consist of 20 sectors and outer rings consist of 40 sectors. Each inner ring sector is radially divided into 512 Silicon detection strips, whereas the outer rings are only divided into 256 strips per sector.

In total this means that each FMD ring has 10240 channels, totalling up to 51200 individual detection channels for the entire FMD system. The bottom part of figure 4.6 shows the layout of both an outer and inner FMD sensor.

Each FMD sensor has an electronics card glued to it, which handles the pre-amplification of the incoming analog signal for the two sectors of the sensor. The amplification is taken care of by so-called  $V A1_3$  chips each responsible for 128 strips. Thus each hybrid cards has either 4 or 2  $V A1_3$  chips depending on if it is an inner or outer sensor. The electronics cards of each half-ring send the analog signal to a digitiser board, where the signal is converted to a digital signal by an Analog-to-Digital Converter (ADC). Converting from analog to

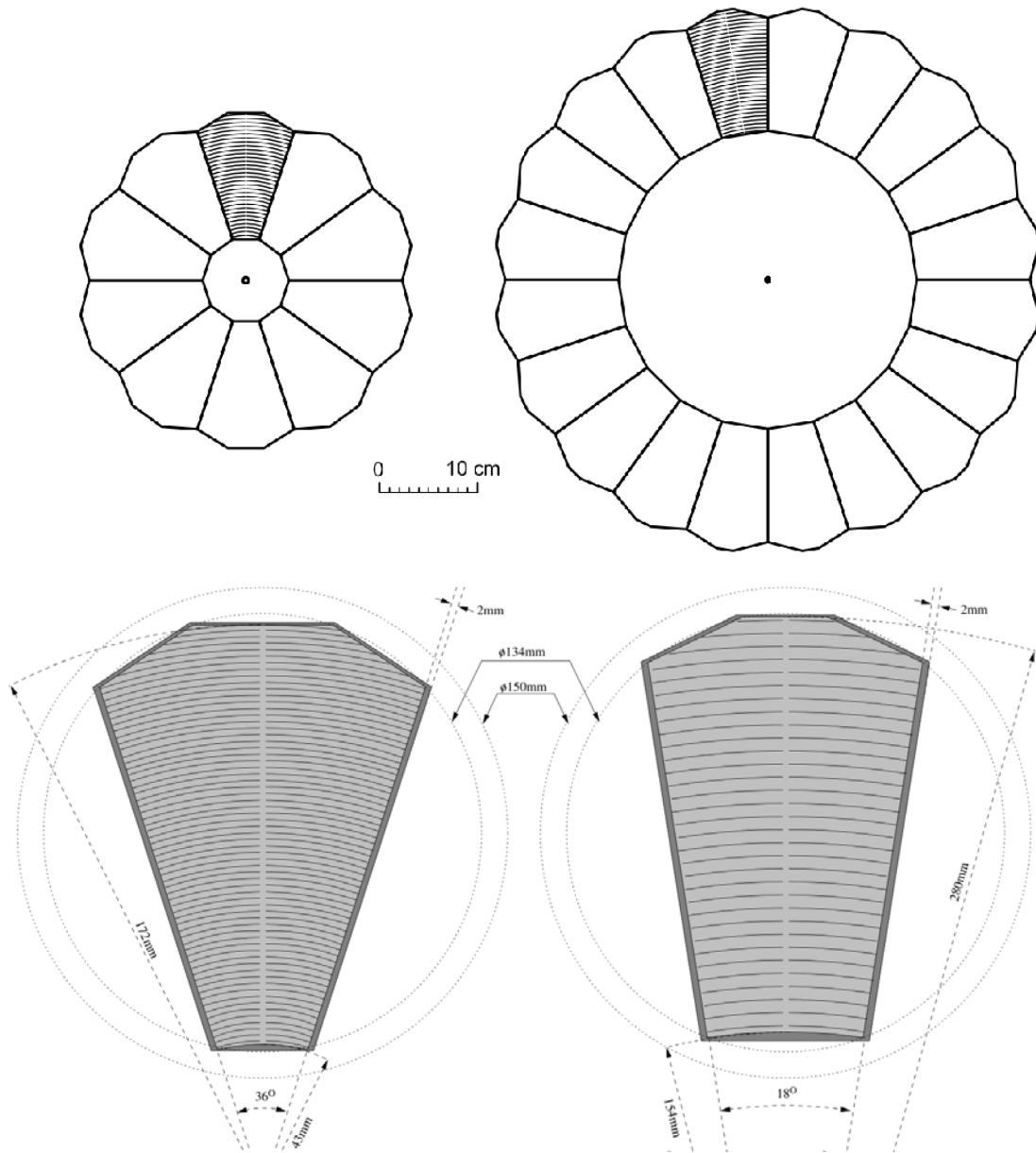


Figure 4.6: Top: The geometrical outline of the FMD rings. Left side shows an inner ring, consisting of 10 sensors. Right side shows an outer ring, consisting of 20 sensors. Bottom: Close up view of FMD sensors from an inner (left) and outer (right) ring. The sensors are cut from 6" Silicon wafers, the largest possible, in the needed quality, at the time of manufacturing. The sensors are divided radially into 512 and 256 strips respectively, depending on if it is a inner or outer sensor.

digital is done by the ALTRO chip, which is an ADC developed for the ALICE TPC<sup>14</sup>. Besides the TPC and FMD, it is also utilised by the EMCAL and PHOS.

The output of the ALTRO chip is the signal strength given in ADC counts, ranging from 0 to 1023. The digital signal is sent for the Read-out Controller Unit (RCU), which manages the readout of the ALTRO chips, as well as handling triggers, monitoring and controlling the states of the digitiser cards. Individual RCUs exist for each of the three FMDs. The RCUs used in the FMD are also originally developed for the ALICE TPC<sup>15</sup>.

From the RCU the digital signals are sent to the DAQ for read-out and storage. A schematic presentation of the front end electronics of the FMD is shown in figure 4.7.

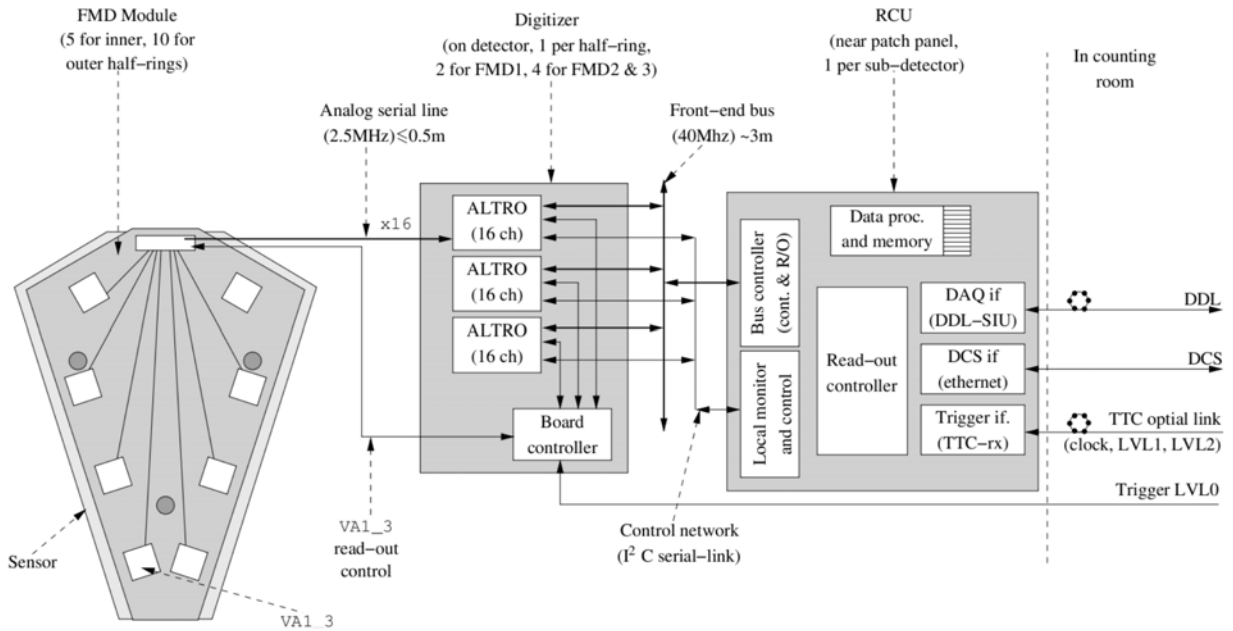


Figure 4.7: Schematic of the FMD electronics. Analog signals in the sensors are sent via the  $VA1_3$  chips to the digitiser cards, where the ALTROs convert the analog signals into digital signals. These are sent for the RCUs, which handles read-out and sending it onwards for the DAQ, where it might be stored.

The individual sensors have been extensively tested by the manufacturer, Hamamatsu. Figure 4.9 shows the capacitance, and thus noise, and leakage current of an arbitrarily chosen inner and outer sector as a function of the reverse bias voltage.

Once full depletion is reached the capacitance becomes flat. The leakage current continuously increase as a function of the bias voltage. Therefore the optimal bias voltage is set just above the point where full depletion is reached. For inner sectors this is around 70 V and for outer sectors it is around 120 V.

Next, figure 4.8 shows the test measurements of the leakage current stability over time in the same two sectors. It is found that there is little variation over time.

Additionally in figure 4.8 the depletion depth of all FMD sectors is shown. For all sectors it is  $325 \pm 3 \mu m$ .

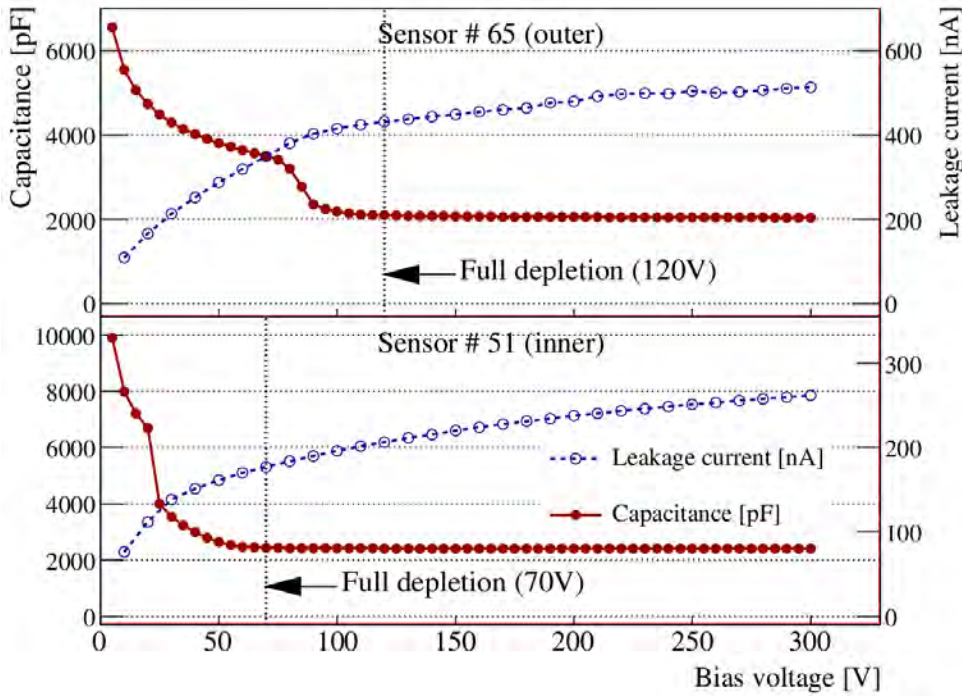


Figure 4.8: The capacitance and leakage current as a function of the reverse bias voltage for an inner and outer sector. For the outer sector a bias voltage of 120 V is chosen, whereas it is 70 V for the inner sectors. The figure is taken from [91].

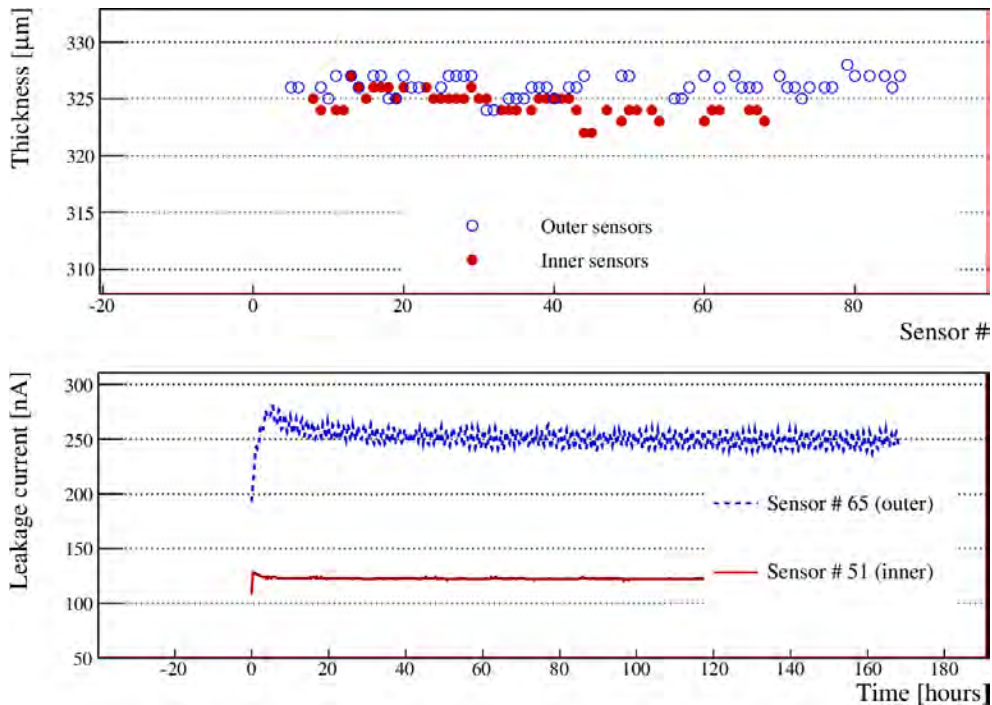


Figure 4.9: Top panel: The depletion depth of the individual sectors of the FMD. Bottom panel: The stability of the leakage current under optimal operating conditions for an arbitrarily chosen inner and outer sector. The figure is from [91].

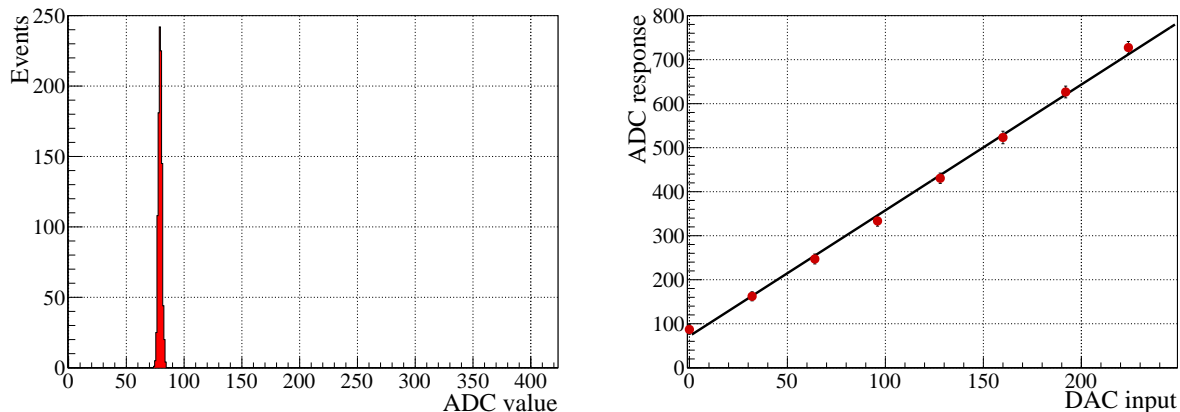


Figure 4.10: Left panel: Example of the pedestal distribution of a strip. The mean of the distribution is considered the pedestal value for that strip, whereas the standard deviation is the noise of the strip. Right Panel: Example of the concept of gain calibration of a strip. Each point corresponds to the read-out signals from a known input pulse, which is converted to an analog signal by a Digital-to-Analog Converter (DAC). The slope of the fit to the 8 points are the gain of that particular strip.

### 4.4.3 Pedestals and Gain

Due to the constant large external voltage kept over the FMD and noise from the electronics itself, there will always be signals in each strip, that are read out, regardless of whether there was a collision or not.

These signals are labelled pedestals, and must be subtracted from the data, when reconstructing the events. The pedestal calibrations are recorded in special calibration runs with no beams in the LHC. Roughly 1000 events are recorded, and all channels are read out. This yields pedestal distributions for each strip. The mean of the pedestal distribution is the pedestal value used for subtraction. The width of the pedestal distribution is labelled the noise of the strip. The left panel of figure 4.10 shows a typical example of a pedestal in a pedestal calibration run.

In the top of figure 4.11 the means of the pedestals for all strips are shown. Similarly the noise of all strips can be seen in the middle of that figure. It is seen that the pedestal means are  $\sim 100$  ADC counts, and the noise of the strips are  $\sim 2$  and  $\sim 2.5$  ADC counts for inner and outer rings respectively.

The pre-amplification of each strip can vary slightly. Thus each strip needs to be calibrated to the same gain. This is again done in a special gain calibration run, which uses a pulser with a known output voltage. The 128 strips of a  $VA1_3$  chip are calibrated sequentially, which means, that for each event the same strip on each  $VA1_3$  chip is being calibrated. For each of 8 different pulser inputs, 100 events are collected to estimate the response of the strip. Thus in total at least 102400 events are needed for the calibration. The response of each of the inputs are fitted to a straight line. The slope of this is what is labelled the gain of that strip. The right panel of figure 4.10 shows an example of the gain calibration procedure. Figure 4.11 shows the gains for all strips.

The noise and pedestal are used for subtracting the pedestals online. This dramatically

<sup>14</sup>ALTRO is an acronym for ALice Tpc ReadOut

<sup>15</sup>The choice of using the ALTRO chips dictates also using the TPC RCU

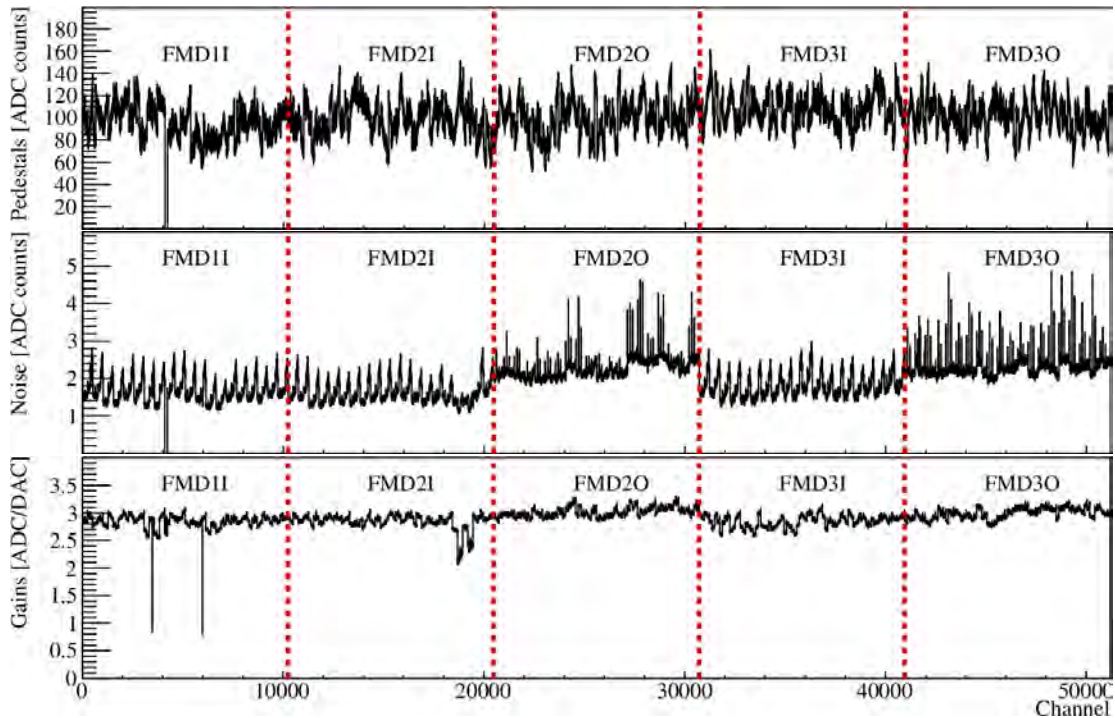


Figure 4.11: From top to bottom: Pedestal, noise, and gain values for all the 51200 channels of the FMD. In the pedestal and noise panels, one notices that an area in FMD1I ( $\sim$  channel 3500) is malfunctioning. It is an entire  $VA1_3$  chip being dead. These channels are removed during analysis.

decrease the read-out volume of the FMD, since only events with signals above the pedestal signal are read out.

## 4.5 Silicon Pixel Detector

The SPD is the innermost part of the ITS. It is the detector closest to the interaction point. As described in section 3.3.1 it consists of two concentric cylindrical layers of Silicon, enveloping the beam pipe. Figure 4.12 shows a schematic of the ITS.

The innermost layer of the SPD is located at only  $r = 3.9$  cm, just roughly 7 mm outside the beam pipe, whereas the outer layer is located at  $r = 7.6$  cm.

The SPD is grouped into base modules, labelled half-staves, each consisting of two sensor ladders and the corresponding readout electronics. Each ladder contain 40960 (=  $160 \times 256$ ) Silicon pixels. In total the SPD consists of 60 such half-staves. Thus the SPD has extremely fine segmentation with more than 2 million channels. In figure 4.13 a zoomed view of the SPD seen from the end is shown.

The individual SPD pixels do not retain the energy deposition information when a particle traverse it. Instead it solely registers if a pixel was hit with signal above a certain threshold. Due to the extremely fine segmentation of the SPD, particles traversing the detector can easily fire multiple pixels. Such a group of hits in adjacent pixels are referred to as a cluster. Using the clusters of both layers and the primary vertex information, it is possible to form so-called tracklets, pointing back to the interaction point. Since tracklets by definition points back to the interaction points, they are particles stemming directly from the collision and thus tracklets has very low contamination from particles created

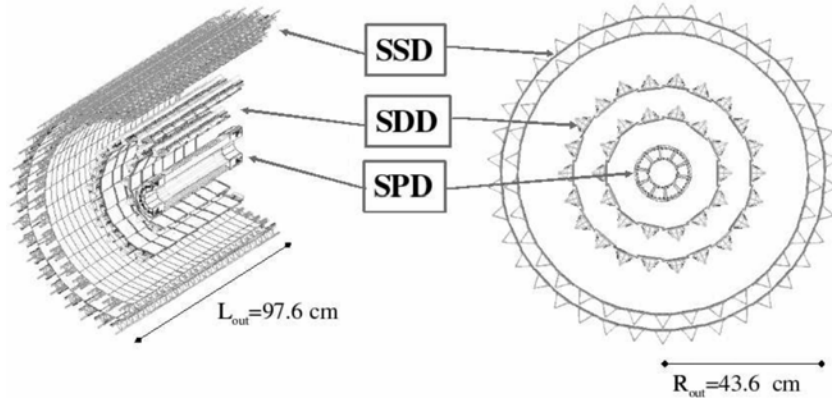


Figure 4.12: Overview of the ITS detector system. As seen the SPD is the two innermost concentric layers of the ITS.

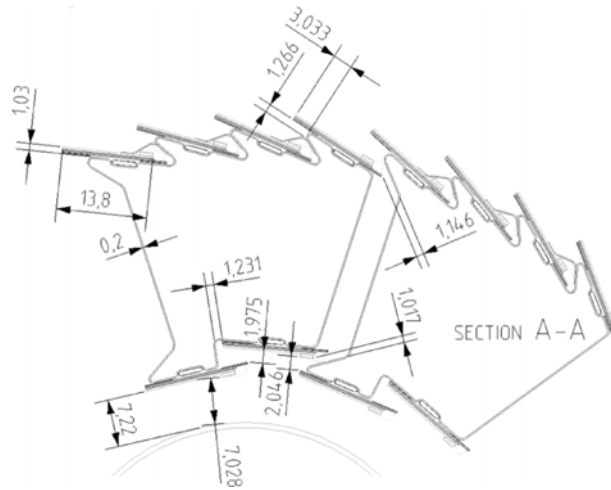


Figure 4.13: Close up view of the SPD, as seen from the end. Indicated in the bottom is the location of the beam pipe, only 7 mm from the inner layer of the SPD. The placement of the detector staves is shown.

later on in decays, material interactions etc..

Ideally, the information from the tracklets could just be used in the central region to count charged particles for this work. However since the aim is to provide multiplicity distributions for wide pseudorapidity intervals this is not possible. The tracklet coverage is limited by the coverage of the second SPD layer, which is around  $|\eta| < 1.5$  (for vertices around  $v_z \sim 0$ ). Thus, creating a continuous wide  $\eta$ -interval multiplicity distribution is not possible, but would have large gaps in it. These gaps would be different depending on the vertex position. However, the innermost layer of the SPD has a coverage of roughly  $|\eta| < 2$  for collisions around the nominal interaction point. This means that by selecting only events in a limited  $z$  vertex region there is full overlap between the inner layer of the SPD and FMD in every event. Thus in this work the inner layer of the SPD is used for analysis<sup>16</sup>.

<sup>16</sup>One might state that the inner layer of the SPD is treated as 'yet another' FMD ring, in the sense that it is treated similarly. The drawbacks of this obviously is that one can not utilise the powerful tracking capabilities of the SPD to eliminate contamination from particles away from the interaction point. But as described it allows for the analysis of a very broad continuous  $\eta$  interval.



# Chapter 5

## Off-line Data Processing

In this chapter the tools used for analysis is presented. These tools include the basic analysis programs over the specific analysis framework structure of ALICE to the simulations used.

Presented in this chapter is also information on the selected data sets being analysed in this work. The analysis itself is presented in the next chapter.

### 5.1 ROOT and AliROOT

The base tool for analysis is called ROOT<sup>17</sup> [112]. ROOT was mainly developed at CERN as a platform on which to build systems for entire experiments. ROOT contain functions for handling most analysis tasks; data storage, data management, data visualisation as well as a wealth of mathematical and statistical tools.

AliROOT (Alice ROOT) [113] is an extension to ROOT, developed specifically by the ALICE collaboration. AliROOT has implemented the detector geometry of ALICE as well as a full simulation environment. In addition to this AliROOT also contains the reconstruction code for all sub-detectors, and the analysis code.

### 5.2 Simulations

In this section an overview of the simulations used in this work is given. In general, simulated data play a crucial role in heavy ion physics. The ability to describe the physics and detector setup in high detail in simulations yield great possibilities for comparisons with theoretical predictions as well as using the simulation results for corrections on the physics data.

Simulations consist of two separate components: An event generator and a transport code. The event generator is responsible for creating simulated particles according to the theoretical understanding of collision dynamics. Event generators are typically tuned to best match physics results from earlier experiments. Quite a number of different event generators exist. They include various physics processes and theories.

In this work three different event generators are used:

**PYTHIA** This is the most widely used general-purpose generator for  $pp$  and  $p\bar{p}$  collisions. PYTHIA has a wide variety of physics implemented, including hard/soft QCD processes, Heavy-flavour production, Prompt photon production, photon-induced processes, deep inelastic scattering,  $W/Z$  production etc. Furthermore there are implementations for non-Standard Model theories such as Technicolour, SUpersYmmetry

---

<sup>17</sup>recursively short for ROOT's Object Oriented Tools.

(SUSY) and non-Standard Higgs doublet production [114]. ALICE uses PYTHIA version 6.4.

**PHOJET** This  $pp$  event generator is a implementation of the Dual Parton Model, which focuses on the description of diffractive physics by Pomeron exchanges as described in section 1.4.2 [115].

**HIJING** (Heavy Ion Jet INteraction Generator) This event generator has implementations for both  $pp$  and heavy ion collisions. However the main usage of HIJING [116] is for heavy ion collisions. HIJING uses a pQCD approach. For the description of multiple interactions in heavy ions it uses a Glauber model.

The event generator output is a stack of particles, used as input for the transport model. In this work the transport model used is GEANT 3.21 (GEometry ANd Tracking) [117]. GEANT has implementations of most interactions, such as hadronic interactions, bremsstrahlung, decays, Compton/multiple scatterings and many more.

Each particle is propagated through a virtual model of the experiment in small steps. At each step, possible interactions or decays are calculated. If new particles are created from such a process, it is placed on the stack and are subsequently propagated independently. Each time a particle enters or exits an active sub-detector volume, routines specific to that sub-detector determines which information to store as a hit. As an example, consider a particle hitting the FMD. Here the procedure is that this hit is stored with both space-time and detector coordinates ( $x, y, z, t, \text{detector, ring, sector, strip}$ ), as well as the total energy loss by the particle and the length of the trajectory through that strip. The informations about the hits are the output of the GEANT transport.

The simulated data is often referred to as Monte Carlo (MC) simulations, even though the transport models does not exclusively use Monte Carlo techniques. However, the nomenclature is heavily ingrained in the community. In this work the term MC will still be used occasionally for some concepts.

### 5.2.1 Digitisation

Creating hits in GEANT is not the end of the road for a simulation. To make the simulated data look more like physics data, it undergoes another step, known as digitisation.

In the case of the FMD the digitisation takes the integrated energy loss,  $\Delta_i$ , from all particles hitting strip  $i$  in an event, and converts this into a ADC count. This value is also referred to as a digit. The conversion from hit to digit for a given strip  $i$  is given by:

$$c_i = p_i + x + g_i \Delta_i \Omega \quad (5.1)$$

where  $p_i$  and  $g_i$  are the pedestal mean and gain of the strip respectively.  $x$  is a random value from a Gaussian with a standard deviation of the noise of the strip,  $n_i$ .  $\Omega$  is a constant factor describing the relation between gain calibrated signals and ADC counts.  $\Omega$  is dependent on the FMD electronics, and has the value  $\Omega = 29.67 \text{ MeV/DAC}$  [91].

Finally, the digits<sup>18</sup> are processed into the event format defined by the ALTRO's, ensuring that the simulation data are in the exact same raw format as the physics data. This has the advantage that both can be reconstructed from digits.

---

<sup>18</sup>The hits are also stored as summable digits (s-digits). The only difference between digits and s-digits in the FMD is the inclusion of the random noise component,  $x$ , in the digits. The s-digits are useful if looking for rare signals, where the s-digits of background events and signal events are added, before applying noise to the combined signal instead of the individual signals.

## 5.3 Reconstruction

As described, both physics data and simulated data end up in the same raw data format.

This raw data is then reconstructed using the same algorithms. The extent of operations performed during reconstruction vary a lot from sub-detector to sub-detector.

For the FMD the procedure is as follows. For each digit the reconstruction calculates the pedestal subtracted ADC counts. However this contains the noise of the pedestal distribution. Thus a noise cut is applied in the following way:

$$c'_i = \begin{cases} c_i - p_i & \text{for } c_i > p_i + fn_i \\ 0 & \text{otherwise} \end{cases} \quad (5.2)$$

where  $c'_i$  denotes the ADC value after the cut.  $f$  is how many standard deviations of the noise distribution that will be suppressed. For this work  $f = 3$  is chosen, which should cut away 99.7% of the pedestal tail, since the noise is approximately Gaussian distributed.

The pedestal subtracted ADC values are then converting into energy depositions (in units of MIP energy):

$$\frac{E'_{dep,i}}{E_{MIP}} = c'_i \frac{1}{g_i \Omega} \quad (5.3)$$

Most particles hitting the FMD do not traverse the strips perpendicularly. Thus the path length is different depending on the incident angle. The energy signal is corrected for the different path length by:

$$\frac{E_{dep,i}}{E_{MIP}} = \cos(\theta) \frac{E'_{dep,i}}{E_{MIP}} \quad (5.4)$$

where

$$\theta = \tan^{-1}\left(\frac{r_i}{z_i - v_z}\right) \quad , \text{where} \quad r_i = \sqrt{x_i^2 + y_i^2} \quad (5.5)$$

Thus  $\theta$  is the angle between the beam axis (at interaction z-vertex  $v_z$ ) and the strip being hit.

The output of the FMD reconstruction is  $\frac{E_{dep,i}}{E_{MIP}}$  as well as the  $\eta$  of strip  $i$  and the strip coordinates.

Reconstruction in the SPD (and ITS) is done in more steps, and has more output. The process will be outlined in the following.

- The digits are first run through a clusteriser, which identifies pixels that have a hit above a certain threshold. A cluster can consist of a single hit or hits in several adjacent pixels. The vast majority (around 97%) of the clusters consist of only a single pixel, or two adjacent pixels. This will be discussed further in section 6.3.
- Next, the clusters of the two layers are matched up to form so-called tracklets, whilst determining the collision vertex. It is done by matching a cluster in the inner layer with all possible clusters in the outer layer within a small azimuthal window. In this way a number of tracklets are found, and extrapolated back to the z-axis, where they are checked for distance to other tracklets. The vertex is then determined as the minimisation of distances between tracklets. The entire procedure is then run again, this time with more narrow cuts. Clusters that cannot be matched up to form tracklets are still kept, being stored as what is labelled unused clusters.
- Now the tracklets from the SPD are matched with tracklets from the SSD and SDD, forming what is labelled ITS tracks.

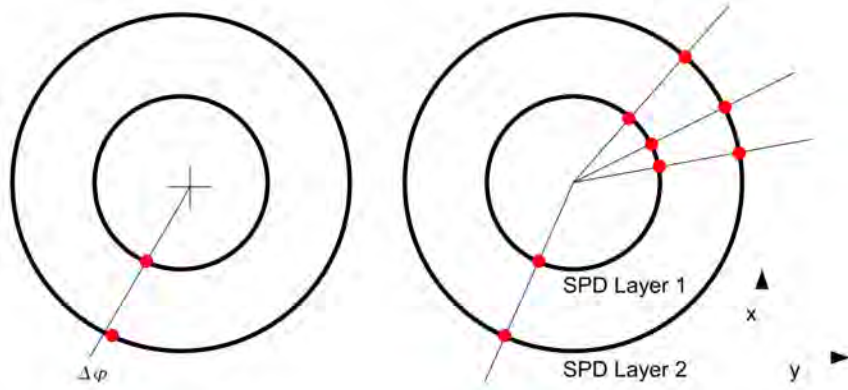


Figure 5.1: Left side shows tracklets construction. Clusters from the first layer looks for another cluster in the second layer in a narrow  $\Delta\phi$  window, in order to define a tracklet. Right hand side shows a number of tracklets all pointing back towards the interaction vertex.

Detector	Signal	Tracking	Vertex Finder
FMD	$E_{dep}/E_{MIP}$	None	None
SPD	Unused clusters	Clusters matched into tracklets	Yes
	Tracklets	Tracklets matched into ITS tracks	
	ITS tracks	ITS tracks matched into global tracks	
	Global tracks		

Table 5.1: Reconstruction in the FMD and SPD. The signal column show the various stored signals from the two detectors. The tracking column denotes the stored tracks, based on the measured signals.

- The last step is that the ITS tracks are matched to tracks in the TPC and TRD, forming global tracks.

Therefore, the output from the ITS reconstruction is the collision vertex  $(x, y, z)$  location, unused clusters, tracklets, ITS tracks and in combination with the TPC and TRD, global tracks.

The reconstruction process of the FMD and SPD is summarised in table 5.1.

## 5.4 Analysis Structure

The reconstructed data are stored in so-called Event Summary Data (ESD) files. The ESD files contain all relevant information for all sub-detectors for all analyses. This is typically trigger information, collision vertex measurements from several sub-detectors, individual particle tracks from several sub-detectors, particle identification measurements etc.

The ESD files are often stored online, and are not practical for local analysis, due to their sheer size. They are however the natural starting point for any analysis.

Instead of storing the ESDs locally Analysis Object Data (AOD) files are created. The idea behind AODs is to make a first pass over the ESDs, storing only information relevant for a more specific analysis. This makes AOD files useful for local analysis.

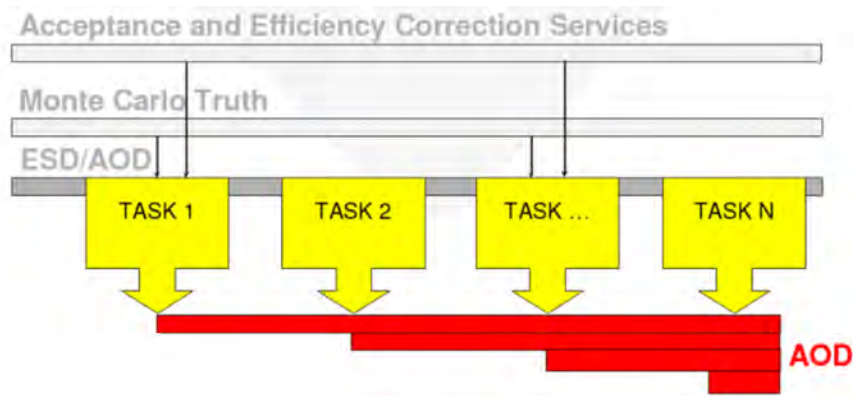


Figure 5.2: Schematic of analysis train structure. The analysis managers loops over the ESD/AOD data. The various analysis tasks can get inputs from simulated truth and/or separate acceptance and efficiency objects. Each analysis task is run on the data, storing its output in the AOD file(s).

The actual specific analysis can run with the AOD files as input. This in principle also enables one to create another AOD, with for instance stricter cuts, from an existing AOD, and use the new AOD as input.

The transition from ESDs to AODs is done by using the ALICE analysis framework. This is done by running so-called 'analysis trains' [118] over the physics or simulation data. In principle the input data can be in the form of either ESDs or AODs.

The analysis trains consist of an 'engine' called the analysis manager, which handles all input/output, and are responsible for the actual loop over the data. The engine can have any number of 'cars', called analysis tasks, attached to it. The analysis tasks are performing the main analyses. Each analysis task do one analysis, and stores the output in the AOD file(s).

The analysis presented in this work uses this framework to create AODs with mainly the relevant information from the SPD inner layer, the FMD, as well as other relevant information regarding vertices, centrality and trigger conditions.

Figure 5.2 illustrates the analysis framework.

Figure 5.3 summarises the flow of the simulation/physics data analysis. The figure shows the process of going from simulated particles in the top left corner to raw data in the bottom and then back up to reconstructed particles in the top right corner. Included is also the path for physics data, where the output from the DAQ leads to the raw data format, and from there on out through the same reconstruction as for simulations.

As a final remark on simulated data, it is useful to distinguish between two simulation concepts:

**MC Truth** This refers to the actual output information from the event generators themselves. Thus it is in no way modified by the analysis. In figure 5.3 it corresponds to the top left corner.

**MC Analysed** This refers to the result of reconstructing the digitised simulated events, and performing the same analysis as on physics data. In figure 5.3 it corresponds to the top right corner.

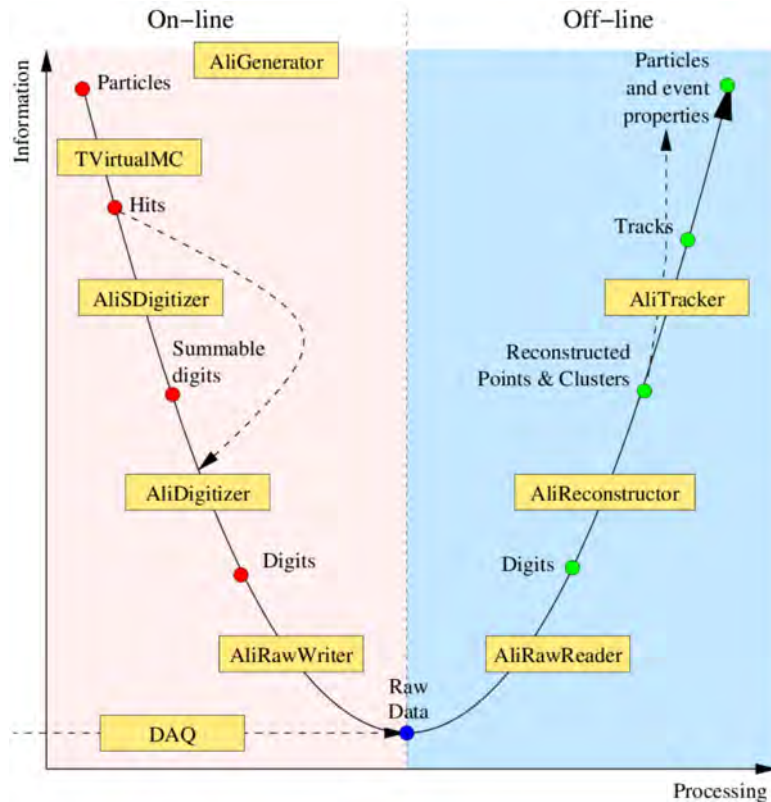


Figure 5.3: Schematic of the software chain in ALICE, going from either simulations or physics data recorded in the DAQ, through the reconstruction to ESD data.

## 5.5 GRID and AliEn

Analysing high energy physics data on local computers or computer farms is becoming increasingly difficult, due to the data volume as well as the processing power requirements increasing dramatically.

At the LHC it is estimated that roughly 15 million Gigabytes of data are stored annually [119]. Besides that data volume, significant extra space is needed for backup of the data, space for users etc. This is a task which can not be handled by a single computer facility.

This challenge is solved by parallel computing, where computer centres around the world share resources. This system is named the LHC Computing Grid (LCG), or typically The Grid for short. The name is an analogy to the electricity in our everyday lives. When turning on the TV at home, we do not care where exactly the electricity comes from, or how it was produced. And we do not need to care since we are connected to the electrical grid.

Similarly with The Grid, the main motivation is that the end user should not care exactly where their data is stored, or where it is analysed. The only thing the end user should care about is that their request of computing resources and storage is met.

The Grid currently consists of more than 150 computer centres around the world, working together as a huge virtual file system. These centres are tiered, with the biggest centre being the CERN tier 0 centre. The tier 0 stores the first copy of the raw data, as well as being responsible for the first reconstruction of data. The tier 0 furthermore distributes raw data and reconstruction output to 11 tier 1 centres. These 11 centres are major national computer centres, and are responsible for also storing raw data and



Figure 5.4: Overview of the GRID computing centres in Europe and Egypt. The coloured circles denote the live status of the centres, where read means no jobs are currently running (or possible) and green/yellow shows jobs running.

reconstruction output. They are also responsible for the distribution to a large number of tier 2 centres. A tier 2 centre could typically be the computer farm of a single university. Similarly tier 3 denote the individual user's computer.

Doing analysis on The Grid is done using a middleware software. The ALICE middleware is called AliEn (ALICE Environment), and is responsible for all the details of getting the data and assigning computing resources.

When submitting an analysis job on The Grid, AliEn splits the job into subsets of data to be analysed at the individual computer centres. The sub-jobs are run in parallel each resulting in output files, that must be merged afterwards.

The concept of The Grid means that a user could submit a job from Copenhagen, that requires data stored in Japan, to be analysed on a centre in USA, with the output being stored in Italy. This obviously put high requirements on the network capabilities of the centres. In general AliEn tries to optimise this process by allocating processing units that are close to the storage units.

Each computer centre is supposed to have identical versions of the analysis software installed. This is ensured by taking weekly tags of AliROOT and propagating them to all centres. Similarly synchronised upgrades to other softwares are performed. If a user requires newer revisions for an analysis, it is possible to send the updated code along with the job to the individual machines, recompiling the software.

Due to both network issues, individual machines crashing etc. one can never be certain that two identical jobs will end up analysing exactly the same fraction of the data. Failed sub-jobs can be re-submitted, and thus a sub-job completion rate of 95% is obtainable, without too many iterations of re-submitting.

Run Period	Collision system	Energy [GeV]	Run numbers	$\sim$ no.events [ $\times 10^6$ ]
LHC10c	pp	900	118506, 118507, 118512, 118556, 118558, 118560, 118561, 121039, 121040	10.6
LHC11a	pp	2760	146686, 146688, 146689, 146746, 146747, 146748, 146801, 146802, 146803, 146804, 146805, 146806, 146807, 146817, 146824	66.9
LHC10d	pp	7000	125085, 125097, 125101, 125847, 125848, 125849, 125850, 125851, 125855, 126097, 126351, 126352, 126359, 126404, 126406, 126407, 126408, 126409, 126422, 126424	67.3
LHC10h	PbPb	2760	138190, 138364, 138396, 138442, 138534, 138653	7.7

Table 5.2: Data samples used.

It is possible to monitor the services from AliEn through MonALISA (Monitoring A Large InfraStructure Architecture) [120]. Figure 5.4 illustrates this, showing the activity in AliEn of the computer centres in Europe and Egypt.

## 5.6 Data sets for analysis

In this section, the data sets used for analysis in the next chapter are presented. For *pp* collisions three separate energies,  $\sqrt{s} = 900$  GeV, 2760 GeV and 7000 GeV, are analysed, whereas for the *PbPb* collisions a single energy is available  $\sqrt{s_{NN}} = 2760$  GeV. For all energies the following types of data are used at some point in the analysis:

**Physics data** Not surprisingly, the main ingredients of the physics analysis is the actual physics data.

**Flat MC** This is a special simulation specifically for this type of analysis. The flat MC does not have a physical multiplicity distribution, but instead is tuned such that the probability of having  $N$  particles (inside  $|\eta| < 1$ ) is the same, up until around  $N = 100$ . This is needed for creating detector response matrices (which are detailed in section 6.6), where significant statistics are needed for high multiplicities as well.

**Normal MC** The normal simulation productions are needed for various checks, including the correction dependence on choice of event generator as well as quality measures. In principle the normal MC could be used for the creation of response matrices, but the amount of statistics needed to populated the higher multiplicities makes this unpractical.

Table 5.2 shows the physics data runs chosen for analysis. Similarly table 5.3 and table 5.4 shows the data sets used for flat multiplicity distributions as well as normal simulation runs.

Production	Description	Runs	no.events [ $\times 10^6$ ]
LHC10f1	pp, 900 GeV, PYTHIA ,Flat LHC10c anchor runs	118506- 121040	7.1
LHC11b10c	pp, 2760 GeV, PYTHIA, Flat LHC11a anchor runs	146686- 146860	1.4
LHC10h16	pp, 7000 GeV, PYTHIA, Flat LHC10d anchor runs	125186- 126437	4.2

Table 5.3: Flat multiplicity productions used to create response matrices. The concept of anchor run denotes that the simulation is run with the exact settings of the corresponding physics run period.

Production	Description	Runs	no.events [ $\times 10^6$ ]
LHC11b1a	pp, 900, PYTHIA LHC10c anchor runs	118506	2.1
LHC11c1	pp, 900 GeV, PHOJET LHC10c anchor runs	118506	2.1

Table 5.4: Normal simulation productions used.



# Chapter 6

## Analysis

This chapter is devoted to going through the details of the analysis procedure done in this work. The main headlines of the analysis are summarised here:

**Event Selection** This denotes all of the analysis pertaining the global event selections, specifically trigger, vertex, and centrality selection.

**FMD Particle Counting** The main ingredients of this section is the measurement in the FMD of energy deposition distributions, as well as presenting two methods for counting hits. Furthermore the concept of hit merging i.e., correcting for particles hitting several strips, is also covered in this part.

**SPD Particle Counting** The method of counting particles in the SPD is presented in this section.

**Secondary particles** Particles, not stemming from the initial collision, constitute a significant part of the signals, especially in the FMD. This section discuss the secondary particle contamination in ALICE, and how to correct for it.

**Strangeness Correction** In the simulations, too few secondary particles containing strange quarks are created. This must be corrected for.

**Unfolding** The measured distributions need to be corrected for detector response. This is done by unfolding the measurements with the simulated response of the detector.

**Trigger-Vertex Bias Correction** At low multiplicities, the efficiency of reconstructing a vertex and triggers drops. This is corrected for through simulations.

### 6.1 Event Selection

Event selection covers global cuts applied to the data. In the following, three selections are presented: Trigger, vertex, and centrality selection.

#### 6.1.1 Trigger Selection

Selecting only the relevantly triggered events is the very first selection criteria of the analysis. A special analysis task ensures the selection of the proper trigger words for a given configuration of the Central Trigger Processor (CTP).

System	Energy [GeV]	Name	Trigger condition
pp	900	INEL NSD	V0A or V0C or SPD pixel fired (V0A and V0C) or SPD pixels fired $\geq 5$
pp	2760	INEL NSD	V0A or V0C or SPD pixel fired (V0A and V0C) or SPD pixels fired $\geq 5$
pp	7000	INEL NSD	V0A or V0C or SPD pixel fired (V0A and V0C) or SPD pixels fired $\geq 5$
PbPb	2760	MB	Min. fulfil 2 of: a) Pixels fired in SPD outer layer $> 2$ b) V0A c) V0C

Table 6.1: Overview of the trigger conditions used in this work. *V0A* and *V0C* refers to having a single signal in the *V0* on the A- and C-side respectively. The SPD pixels fired requirement refers to having a signal in that number of pixels in the SPD.

In general one can distinguish between online and offline triggers. Online triggers designate trigger signals obtained while running. Combinations of trigger detector signals constitute different so-called trigger words. When the condition of a trigger word is fulfilled, that trigger word is sent along with the data of the event. Many trigger words can be fulfilled for a single event. After reconstruction the trigger conditions are recreated from the reconstructed trigger detector signals. Only events fulfilling both the online trigger words as well as the reconstructed trigger words are kept for analysis.

Offline triggers under one heading, are selection conditions put on the reconstructed data. The replayed online triggers are technically an offline trigger, but there are also offline triggers that have no online counterpart. These are what is typically labelled offline triggers.

For this work a few trigger words, summarised in table 6.1, are of particular interest:

**INEL** The physical motivation of the INEL trigger mask is to select actual inelastic collisions. It is an online trigger, that uses the *V0* and SPD detectors. It requires that there is a signal in either the SPD or at least one of the sides of the *V0* (labelled *V0A* and *V0C*), in conjunction with a beam bunch crossing signalled from the LHC itself.

**NSD** The purpose of the NSD trigger is to select the subset of the INEL events that are NSD events. It is an offline trigger that requires coincidence between both sides of the *V0*, or more than 5 pixels fired in the SPD, in conjunction with a bunch crossing. The NSD trigger class is the main trigger class for *pp* collisions analysed in this work.

**MB** The Minimum Bias trigger is only used for the *PbPb* collisions, and as the name implies it aims at providing a sample with minimum or virtually no bias. The condition for the MB trigger is that at least two out of three requirements are fulfilled. These requirements are a) 2 hits in the outer SPD layer, b) signal in *V0A* and c) signal in *V0C*.

**INEL>0** ALICE occasionally use this trigger condition as an alternative to the NSD trigger. As indicated by the name it selects inelastic collisions with at least one pixel fired in the SPD. If the trigger efficiency for NSD collisions is unknown INEL>0 can be used.

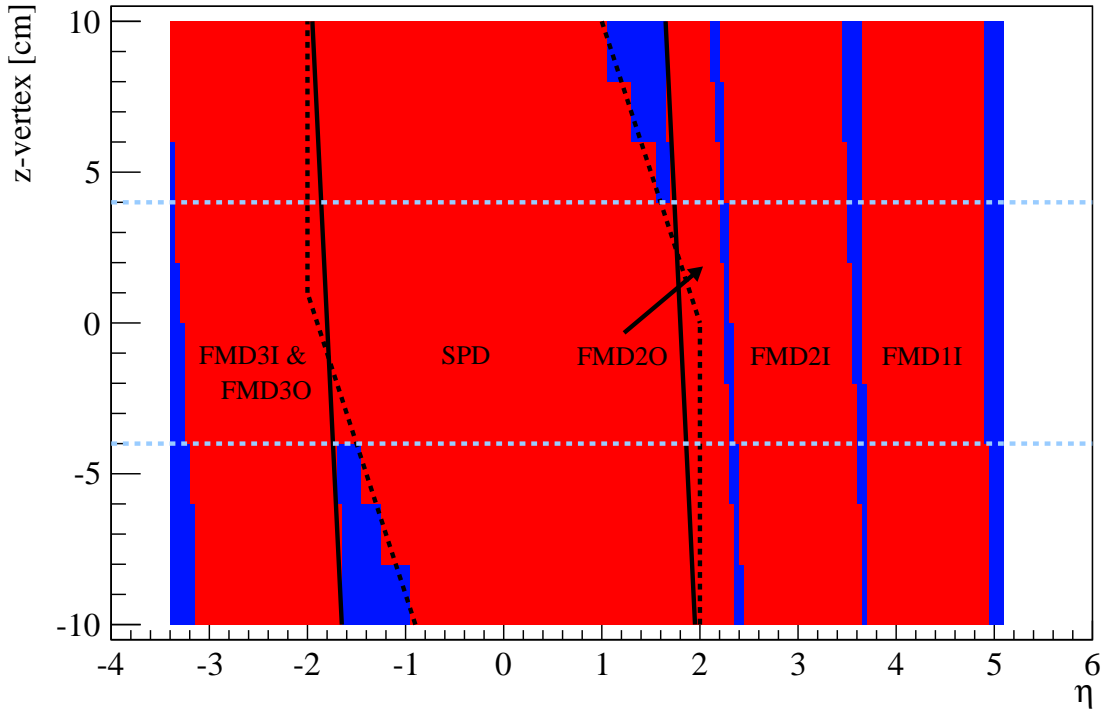


Figure 6.1:  $\eta$ -acceptance for the combination of the FMD and the SPD inner layer as a function of  $z$ -vertex. Red denotes there is acceptance, and blue denotes no acceptance. The black lines are there to guide the eye to better illustrate the extent of the SPD (dashed lines) and FMD2O/FMD3O (solid lines). There is full overlap between FMD3I and FMD3O. To minimise the acceptance gaps, only events with  $-4 < v_z < 4$  is selected. The selection is indicated by the light blue dashed lines.

**Pile Up** Occasionally, several collisions occur near the interaction point in the time window of a single event. This is referred to as a pile up event. These are flagged by the offline pile up trigger, which uses the SPD tracklets to identify the additional vertex of the second collision. The requirement for an event to be flagged as pile up is that at least three tracklets contribute to determining the second vertex, and that the two vertices are at least 0.8 cm apart. Events that are triggered as pile up events are discarded. The pile up removal is however not very efficient. It is estimated that only around half the actual pile up events are removed in this manner [121]. This is due to the requirement of the vertices being minimum 0.8 cm apart. There is currently a working group in ALICE, determining how to best correct for this. This correction is not done in this work.

### 6.1.2 Vertex Selection

The determination of the vertex position of an event is done by the SPD, as described in section 5.3. There are a few considerations regarding selecting vertex range.

The vertex  $z$ -distribution,  $v_z$ , is maximum around the nominal interaction point ( $z \sim 0$ ), falling off on either side. Assuming that the probability of having beam-gas interactions is roughly independent of  $z$ , there will from some high  $|z|$  be a point, where the amount of beam-gas events is comparable to the amount of physics events.

Thus one restricts analysis to within a certain  $v_z$ -range to avoid this. To avoid problems

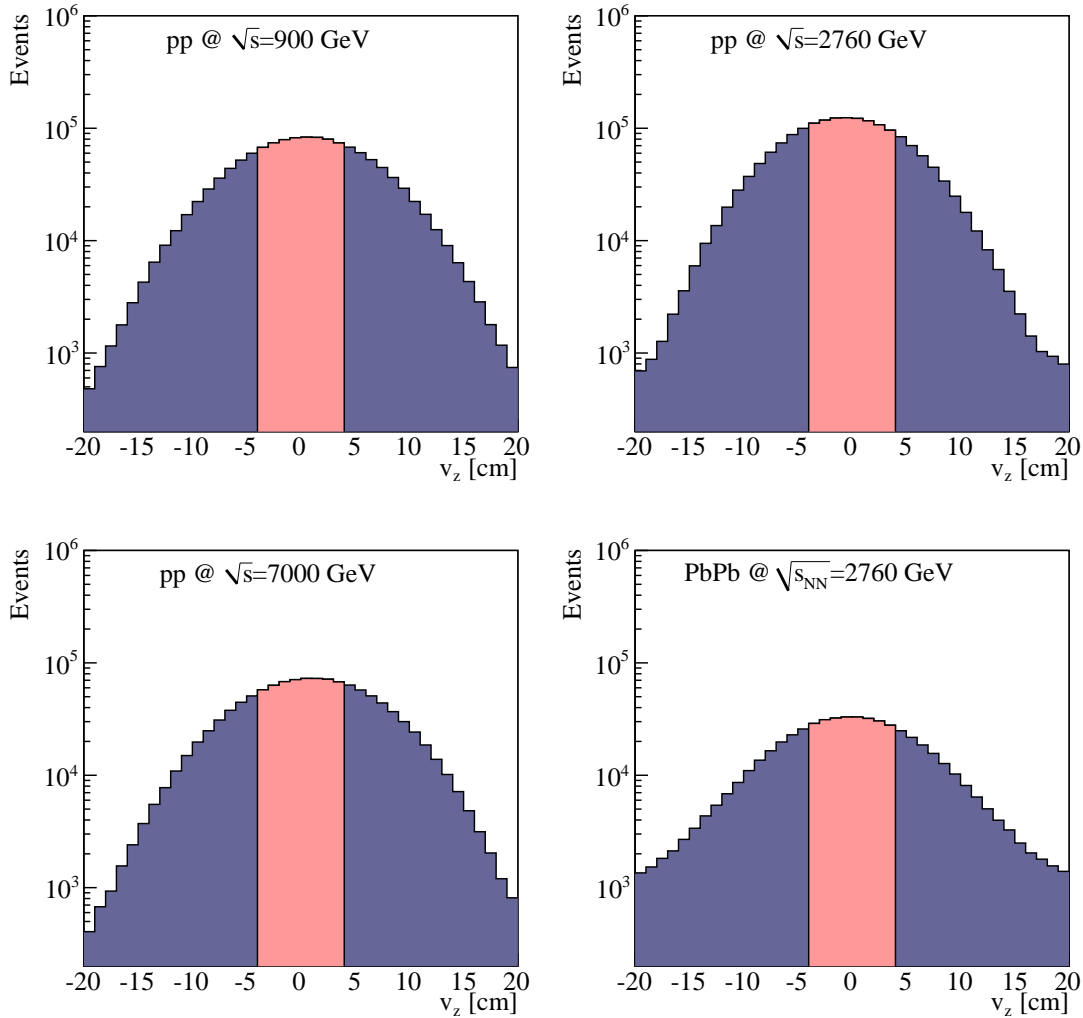


Figure 6.2: The measured  $z$ -vertex distribution for  $pp$  collisions at  $\sqrt{s} = 900$  GeV, 2760 GeV, and 7 GeV, as well as  $PbPb$  collisions at  $\sqrt{s_{NN}} = 2760$  GeV. The selected vertex interval for this analysis is indicated.

with beam-gas interaction pollution even a wide  $v_z$ -range of  $-10 < v_z < 10$  would suffice.

However for this particular analysis an extra requirement further limits the vertex selection. We require that for each event, maximum  $\eta$ -coverage must exist between the SPD inner layer and the FMD. This is illustrated in figure 6.1, where the red area denotes the acceptance of the combined SPD and FMD system. The blue area denotes areas without acceptance. On the basis of this, the selected  $z$ -vertex range used in this work is  $-4 < v_z < 4$ .

The areas without acceptance between the FMD rings is corrected for later on by unfolding (see section 6.6). In principle it is possible to also do this for the gaps between the SPD and FMD for  $|v_z| > 4$ . However it is decided best to use the biggest possible acceptance, keeping the correction to be made as small as possible. In section 6.8 comparisons with different vertex selections will be presented.

In figure 6.2 the  $z$ -vertex distribution, including the selection of this work, is shown. Figure 6.3 shows the vertex distribution in the  $xy$ -plane. It is seen that a minor offset of a few millimeters from (0,0) is found. This offset has no effect on the analysis, since it only affect the  $\eta$  of the particles minimally. When using simulations, the same off-sets are

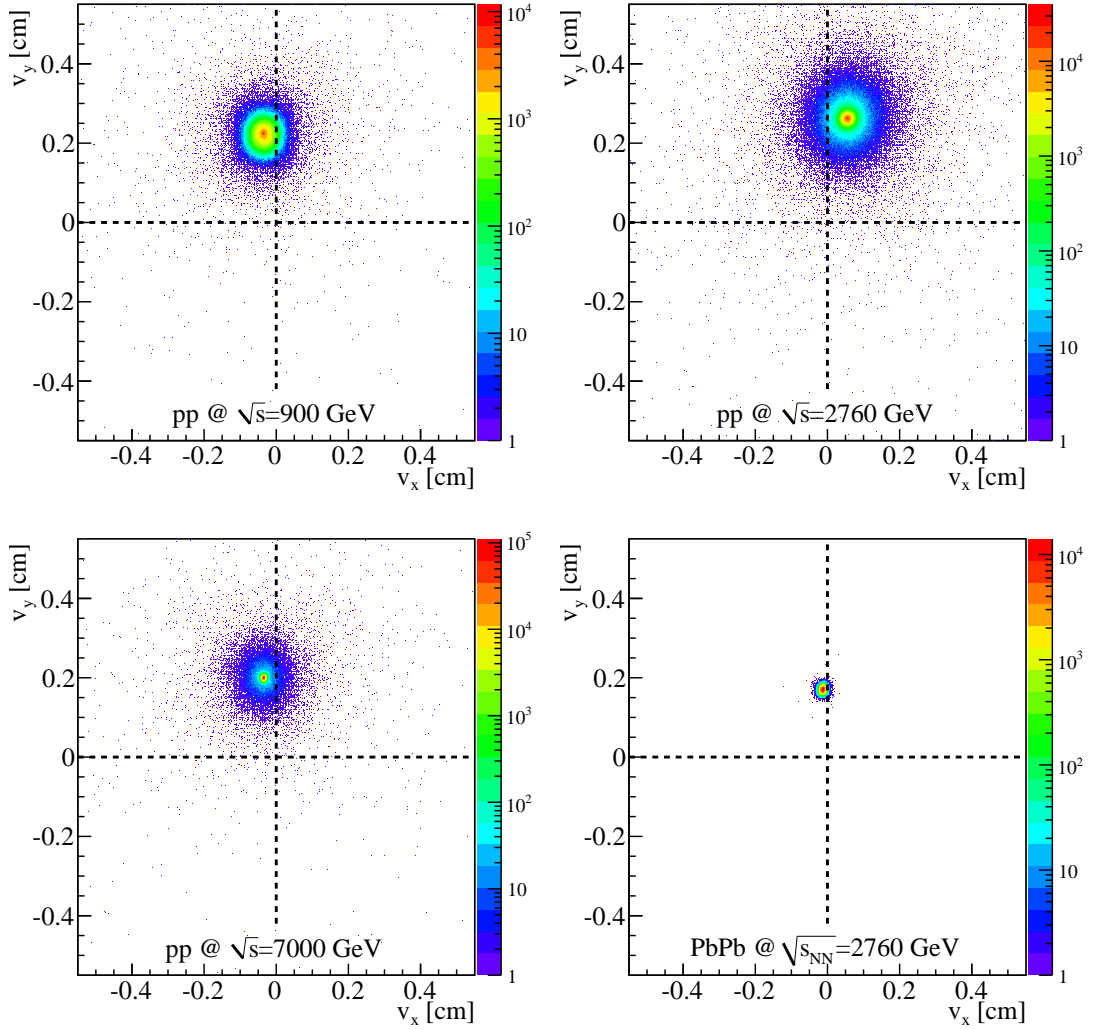


Figure 6.3: The measured  $xy$ -vertex distribution for  $pp$  collisions at  $\sqrt{s} = 900$  GeV, 2760 GeV, and 7 GeV, as well as  $PbPb$  collisions at  $\sqrt{s_{NN}} = 2760$  GeV.

however included, due to the concept of anchoring the simulations to the particular physics runs. There is no cut imposed on the  $xy$ -vertex range.

### 6.1.3 Centrality Selection

When analysing  $PbPb$  collisions an additional selection criteria is imposed on the data to only select the desired centrality classes.

The centrality selection in ALICE is done by using the  $V0$  detector. The centrality classes are determined by counting fractions of the total multiplicity from the top multiplicity. It is done by integrating the multiplicity distribution from the high end, until for instance the integral is 5% of the total number of events. This selection, the 5% events with highest multiplicities, is thus the centrality class, 0-5%. One should note that the multiplicity distributions used for centrality selection are just raw measurements with an arbitrary scale. For centrality, the absolute multiplicity value does not matter, only the fraction of the multiplicity.

Figure 6.4 show an example of the centrality determination from the  $V0$ .

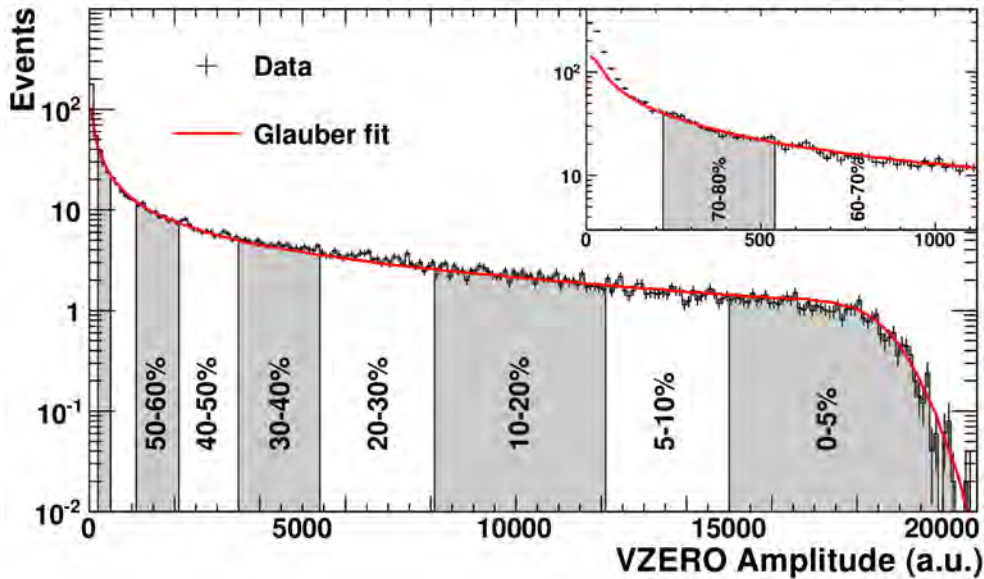


Figure 6.4: An example of the measured centrality classes by the V0 detector. The insert show the very peripheral centrality classes.

## 6.2 FMD Particle Counting

This section is devoted to the details of the particle counting methods of the FMD, describing the process of going from the initial energy deposits in the Silicon strips to calculating the final number of charged particles for that event.

### 6.2.1 Energy distributions

As described in section 4.3, particles traversing the Silicon strips of the FMD deposits energy, which to first approximation is Landau distributed. Figure 6.5 shows the measured energy distributions in FMD2I for  $pp$  collisions at  $\sqrt{s} = 900$  GeV, 2760 GeV, and 7 GeV, as well as  $PbPb$  collisions at  $\sqrt{s_{NN}} = 2760$  GeV. The Landau shape is clearly visible, with a MPV around  $0.6E_{MIP}$ . However it is immediately apparent that at the low energy deposition, other effects are at play. The sharp peak at very low energy deposition is identified as remnants of the pedestals, surviving the pedestal subtraction. Between the pedestal remnant and the Landau peak is a plateau of energy depositions. These are shared energy signals, stemming from particles traversing multiple strips. This concept is aptly labelled hit sharing, and is described in section 6.2.2.

For  $pp$  collisions at  $\sqrt{s} = 2760$  GeV it appears there is an extra peak at very low energy distributions. The data quality of  $\sqrt{s} = 2760$  GeV will be discussed later on in this chapter.

The energy distributions for simulated data show the same overall structure, but there are a few distinct differences. Firstly, the MIP peak is shifted a little downwards in energy. This is due to slight differences in how the energy deposition is calculated in data and simulations [87]. These differences give rise to a simple linear scaling between the two. Secondly, the higher order MIP peaks are significantly more broadened in data compared to simulations. This is due to the Gaussian convolution not being sufficient in the simulation. The differences in energy distributions between the used simulations and measured data is shown in figure 6.6.

Ways of tuning the simulated energy distributions to better match the measured ones

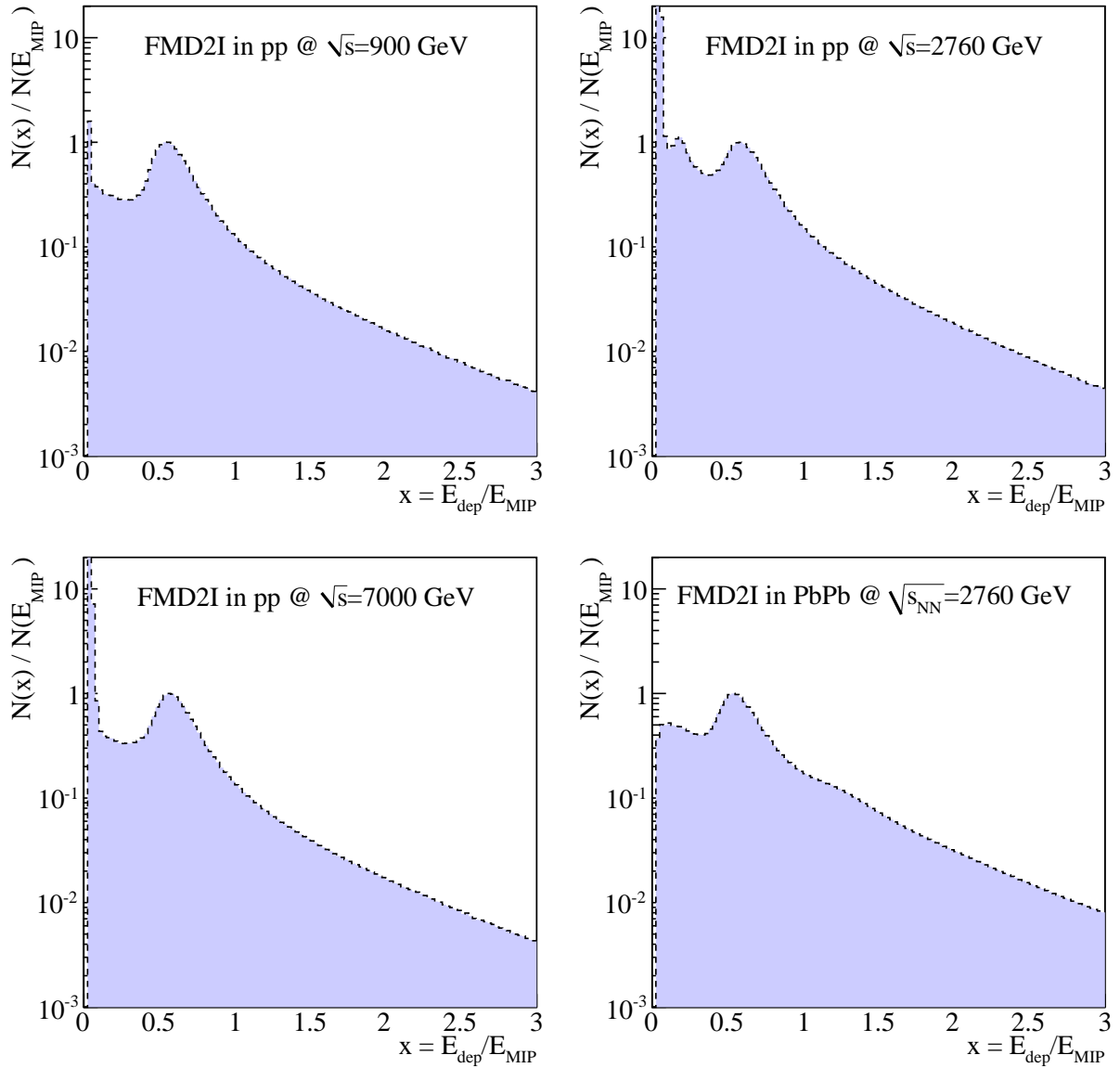


Figure 6.5: The measured energy distributions in FMD2I for  $pp$  collisions at  $\sqrt{s} = 900$  GeV, 2760 GeV, and 7 GeV, as well as  $PbPb$  collisions at  $\sqrt{s_{NN}} = 2760$  GeV. At very low energy deposits remnants of the pedestals are seen, following by a region of shared signals. At  $E_{dep}/E_{MIP} \sim 0.5$  the Landau distribution begins.

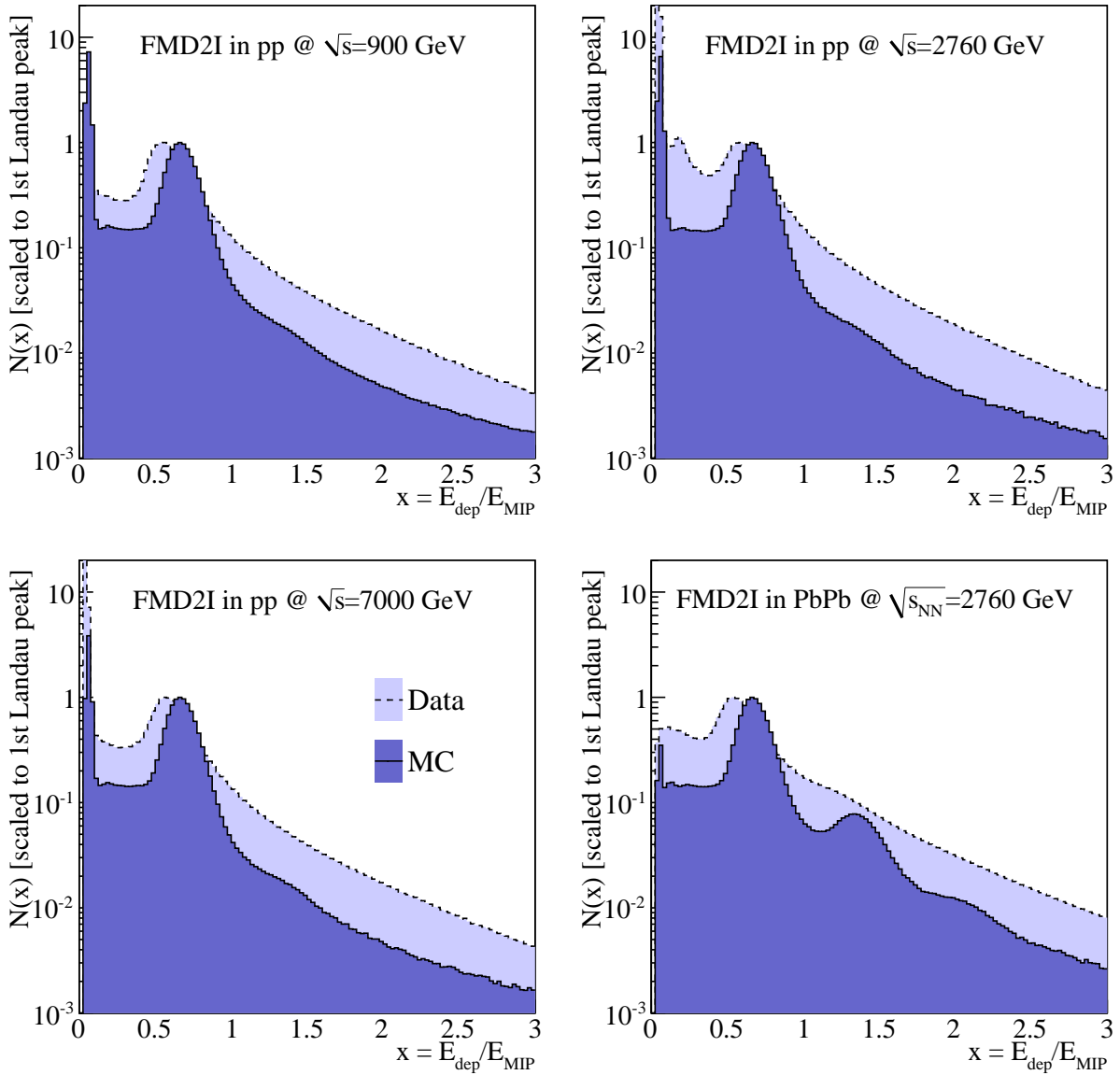


Figure 6.6: Energy distributions in the simulations compared to the measured energy distributions from figure 6.5. It is found that the peaks are shifted slightly and are smeared more in the physics data compared to the simulations.

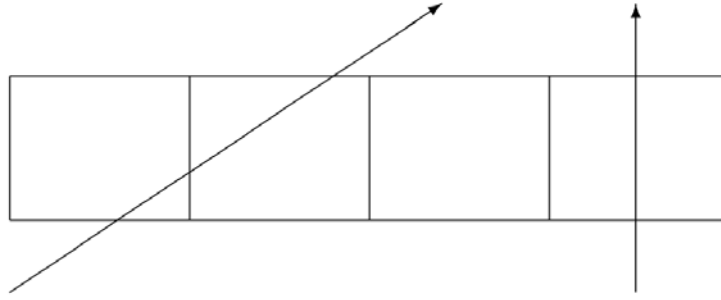


Figure 6.7: Illustration of the concept of hit sharing. The left particle hits the FMD strips at an angle, and thus deposits energy in two strips. The right particle just hits a single strip.

are being investigated. Section 8.5 discuss this more.

### 6.2.2 Hit Sharing

Occasionally, particles traversing the FMD, hit and deposit energy in more than one strip. This is called hit sharing. For particles coming directly from the interaction point it is unlikely to hit more than at most two strips going through the FMD. However, particles hitting material, thus being deflected can hit the FMD at small angles, enabling them to traverse more than two strips.

Shared signals must be merged into single signals. This is done by a algorithm, which searches for strips with energy signals in adjacent bins. Based on the energy depositions in the strips, the algorithm determines whether to merge the signals. For the sharing algorithm in this work a shared signal can at most hit three strips. Signals hitting three strips are already only an insignificant part of the hits in the FMD, why it is justified to allow at maximum three strips for a shared signal.

Figure 6.8 show the relation between neighbouring strips before and after hit merging. The anti-correlation for low energy deposits in the left panel show exactly the shared components.

The sharing algorithm has two thresholds associated with it, a lower and higher energy cut ( $E_{low}$  and  $E_{high}$  respectively).

$E_{low}$  This is the lowest energy deposition value that is accepted for a shared signal component. The main motivation for this threshold is to ensure that remnants of the pedestal are not mistaken for a shared component.  $E_{low}$  is set at approximately three times the strip noise above the pedestal mean. For inner rings this means that  $E_{low} = 0.1$  and for outer rings  $E_{low} = 0.15$ . Strips with signals below  $E_{low}$  are discarded in the analysis.

$E_{high}$  This is the highest energy deposition value that is accepted for a shared signal component. It is set at the value where the low part of the Landau peak becomes comparable with the the shared energy signals in the energy distributions. Thus two deposits above this threshold in adjacent strips are considered to be two separate particles. A hit above  $E_{high}$  can still be merged with a low energy deposit however. The threshold is set at  $E_{high} = 0.7\Delta_p$ . By defining it in terms of the MIP peak it takes into account the differences between simulations and data energy distributions<sup>19</sup>, as well as ensuring a consistent cut across all strips.

<sup>19</sup>assuming different fits are used in simulation and physics data, which is the case.

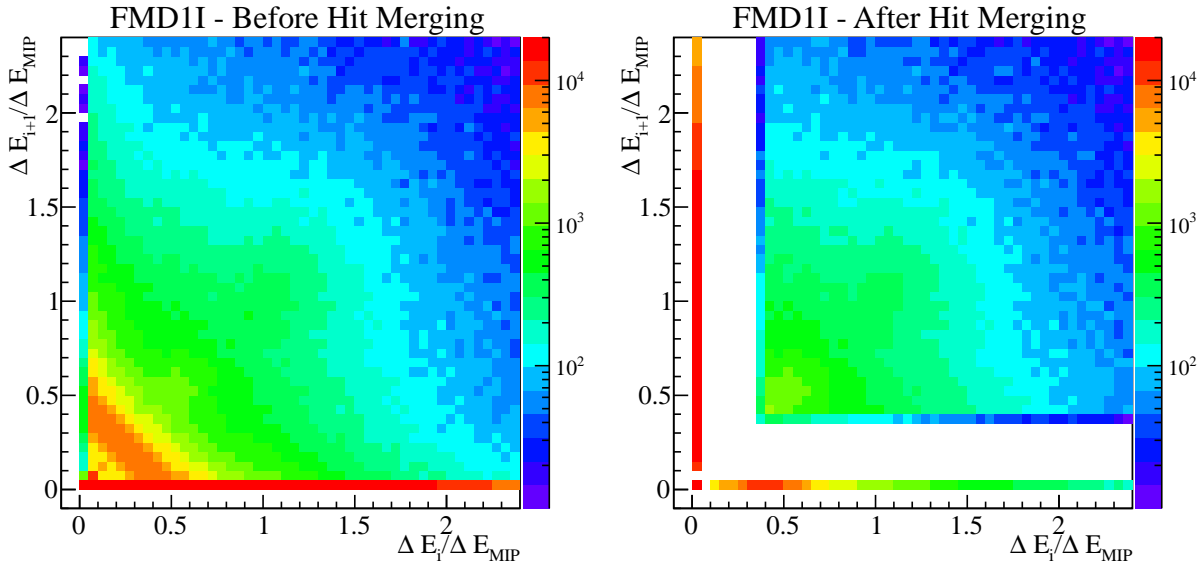


Figure 6.8: Relation between the energy deposit in neighbouring strips before and after hit merging. The anti-correlation at low energy deposits explicitly show the shared components. After the hit merging it is clear that the low energy shared signals are merged with their neighbours.

Whether or not to merge strips depends on the energy values of the strips in question. A simple example is to consider two adjacent strips both with energy deposits above the low threshold and below the high threshold. They will be merged as a single signal. If one of the strips had a energy deposition above the high threshold they would still be merged into one hit. However, if both of the strips were above the high threshold, they would not be merged, but instead considered two individual particles traversing only one strip each. In the same manner evaluations are done for all possible outcomes. For more information on the implementation of the hit merging algorithm, consult appendix C.

Figure 6.9 shows the energy distribution contribution of single signals, and merged signals from two (doubles) or three (triples) strips for physics data. The double signal, which constitute roughly 10% of the total amount of signals, resembles the single particle Landau distribution, which is a clear indication that the double signals are indeed shared components. The triple distribution however, does not resemble it, which could be an indication that the triple signals are in fact two particles hitting three strips. This can happen if it is indeed a double signal neighbored by either a single or another double signal. The contribution from triples are however insignificant, constituting only roughly 1% of the total amount of signals. The exact fractions of single, double and triple contributions can be found in appendix C.

An interesting observation in figure 6.9 for  $pp$  collisions at  $\sqrt{s} = 2760$  GeV is that the double distributions does not look at all like the single distribution. The low end of the distribution does not behave as a Landau distribution, but appears to have an extra component. This is a serious issue, that indicate that there might be significant extra 'noise' in the physics data, which is then being merged with neighbor strips, either being hit by a particle, or also having a noise signal. The latter is clearly the most problematic, since it will count as a separate particle, insted of just an existing particle with slightly higher energy deposition.

Ideally, running the sharing algorithm would remove the entire plateau before the MIP peak. However, after the sharing algorithm there are still single signals left in that very

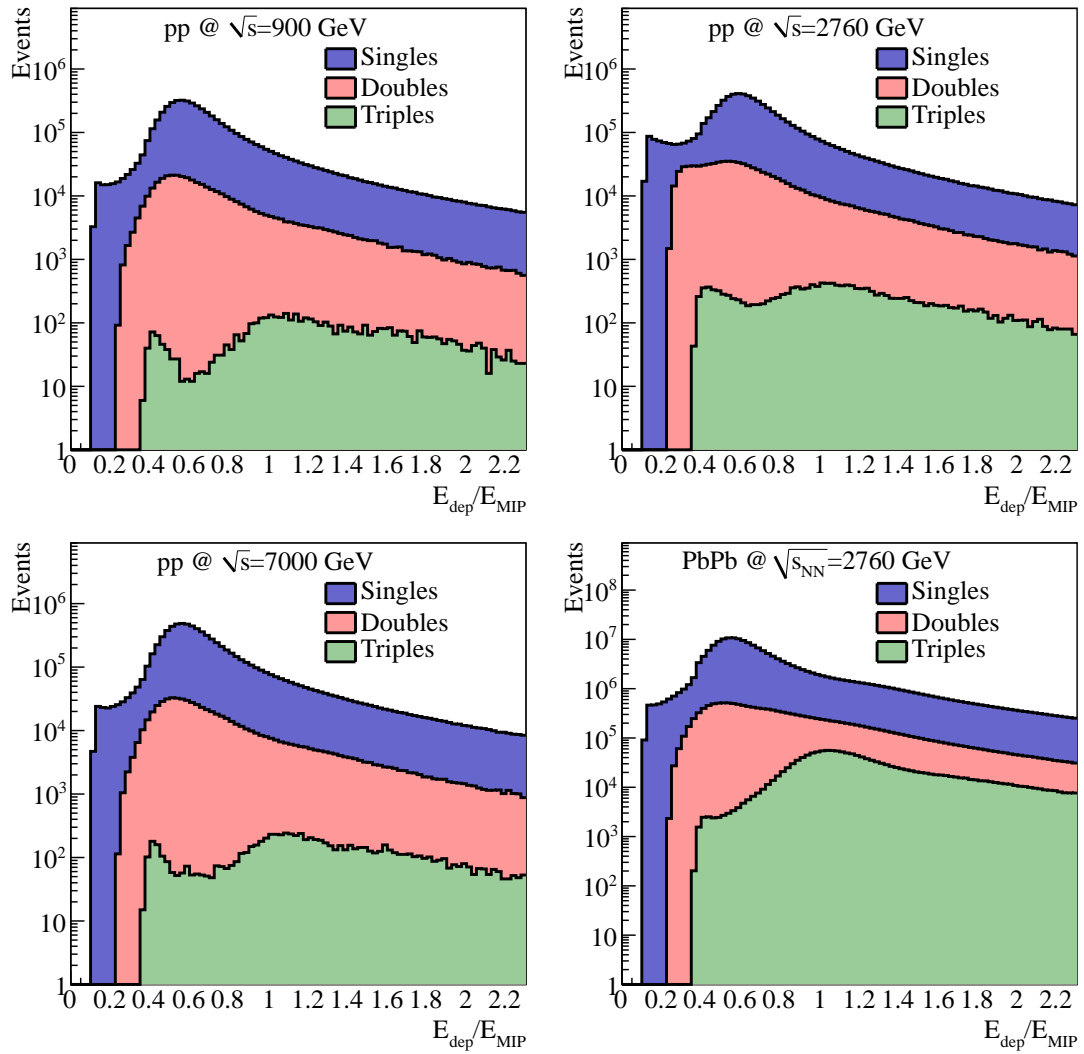


Figure 6.9: Energy distributions after hit merging for single, double and triple signals in physics data.

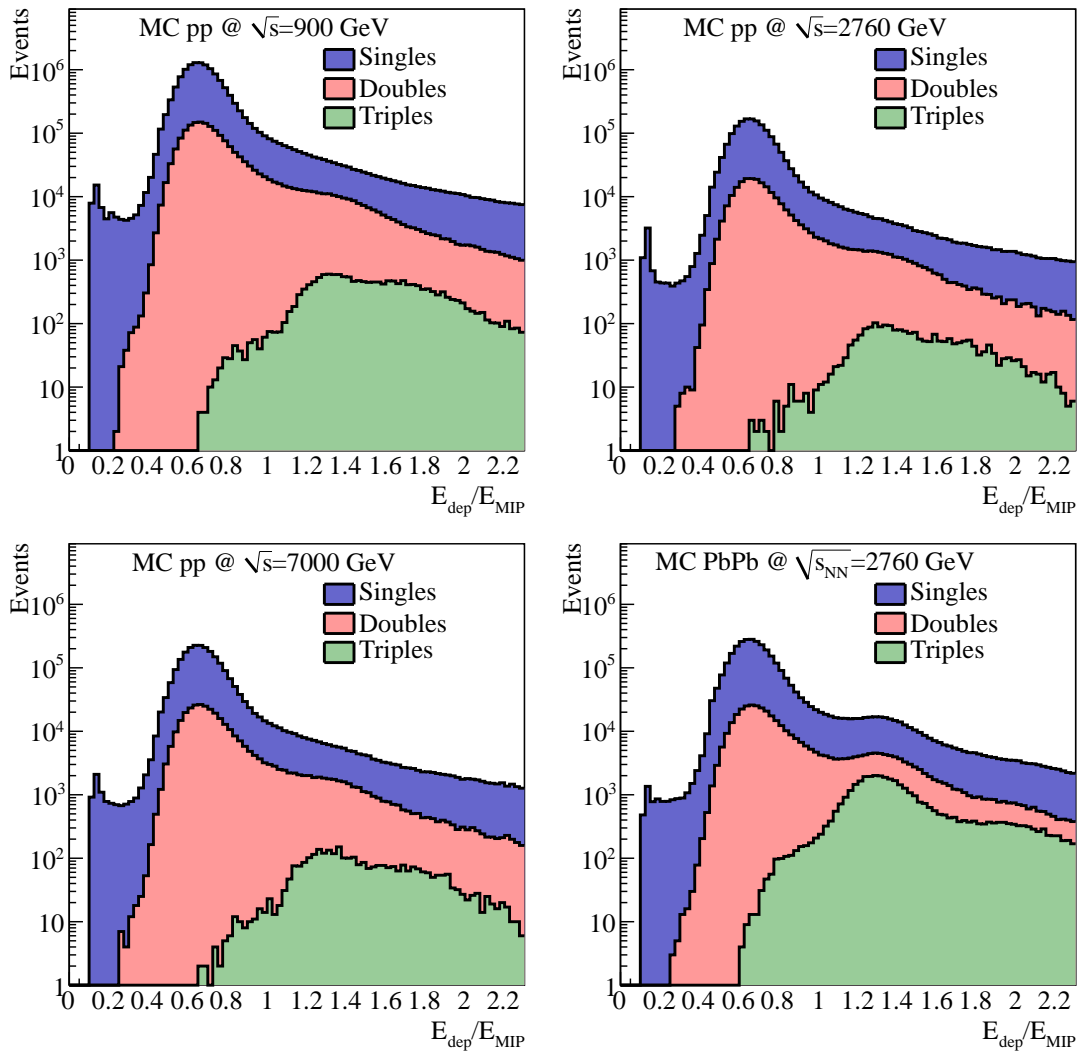


Figure 6.10: Energy distributions after hit merging for single, double and triple signals in simulated data. The low energy deposit plateau after hit merging is about an order of magnitude lower than in physics data.

region when analysing physics data at all energies. As seen in figure 6.9, after hit merging it is indeed only single signals left at those low energy deposition values. Thus we have a component of strips having small amount of energy deposited in them, without adjacent strips being hit.

This hints towards it being either shared signals, where the adjacent strip is not detecting the passing of the particle, or that the signal is not necessarily from a relevant physical particle <sup>20</sup> traversing the strip.

The former can be caused by two things; either a strip next to a strip with a hit is not working or the FMD module is not sufficiently efficient. Neither are likely though. The FMD only has very few permanently malfunctioning strips, which is discussed in section 6.2.4. Furthermore, results from the test beam facility ASTRID show that the FMD modules are more than 99.7% efficient [122].

It is worth mentioning that this low energy component after hit merging is much smaller in simulated data. For physics data the low energy deposit plateau after hit merging is about an order of magnitude below the first MIP peak. For simulation data the plateau is more than two orders of magnitude below the first MIP peak. This is seen in figure 6.10, where the single, double and triple distributions are shown for simulated data. It is generally found that fewer triple signals are present in the simulated data. The extra signals found in  $pp$  collisions at  $\sqrt{s} = 2760$  GeV, is, as expected, not found in simulated data.

Looking closer at the energy distributions as a function of strip number yield interesting information. This is presented in figure 6.11 for both physics and simulation data. The upper panels show the energy distributions of data and simulations as a function of strip number in a contour plot. One notices that the overall level of the MIP peak and high energy tail, increases going to lower strip numbers. This is expected since the lower strips cover more forward  $\eta$ -regions where the solid angle covered per strip is larger, and thus more particles hits them on average. Thus for physical particles from collisions one would expect this rising trend. However the low energy part does not experience this increase; it is constant over the entire strip range. The lower panels of figure 6.11 highlights this by grouping 32 strips together and drawing their integrated energy distributions. For the MIP peak and high energy tail the increase is clear, but it is not visible for the low energy part.

Another peculiar thing is that there are two bumps visible around strip 180 and 50 for the very low energies. The bumps are clearly visible in the lower panel as well. This behaviour is also not expected if it is particle signals.

The strip-independence of the low energy deposition part is a clear indication that the low energy component is not (at least fully) caused by charged particles traversing the detector. Thus we attribute the signals to being some sort of noise components, that are not understood. In this context noise is a very broad terms, covering everything not coming from the collision. In the light of these indications we impose another threshold,  $E_{hit}$ , which denote the lowest energy deposition accepted for analysis after the hit merging is done. Investigating and understanding this noise component fully should be a clear priority in the coming time.

Figure 6.12 summarises this section by showing the effect of the sharing algorithm, and consequent hit merging.

---

<sup>20</sup>In this regard 'relevant' refer to particles connected to the collision. Cosmic rays causing a signal in the detector is very physical, but not relevant in this context.

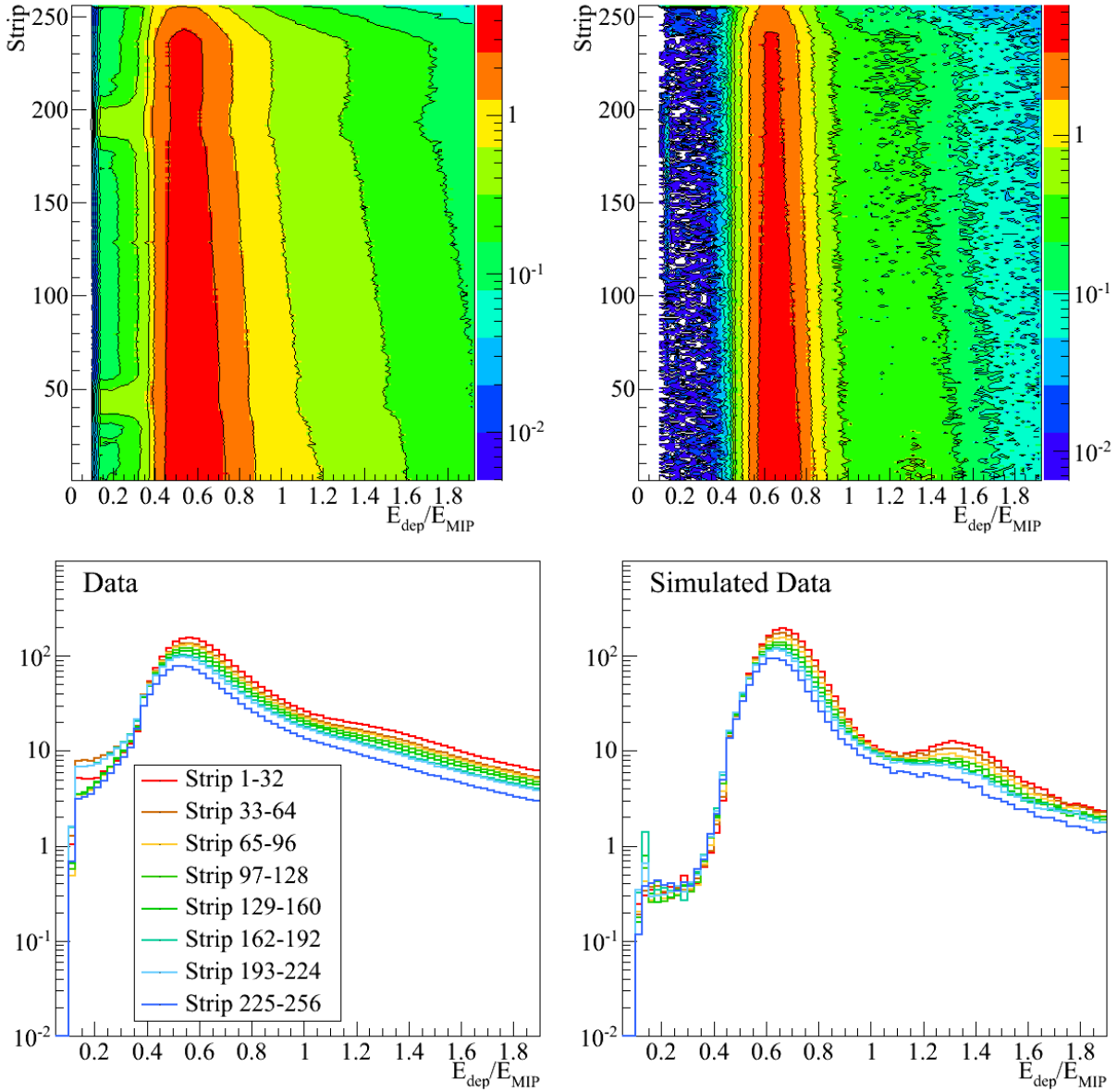


Figure 6.11: Top Panels: The single energy distributions for each strip of FMD20 for  $PbPb$  collisions at  $\sqrt{s_{NN}} = 2760$  GeV. Both physics data (left) and simulated data (right) is shown. Lower panels: The energy distributions of groups of 32 strips. It is found that there is a distinct difference at the low energy deposits, where there is many more signals in data compared to simulations. The reason for this extra component is not understood. Since it is not in the simulations a cut,  $E_{\text{hit}} \sim 0.7\delta_p$ , is imposed to cut away single strips with low energy deposits.

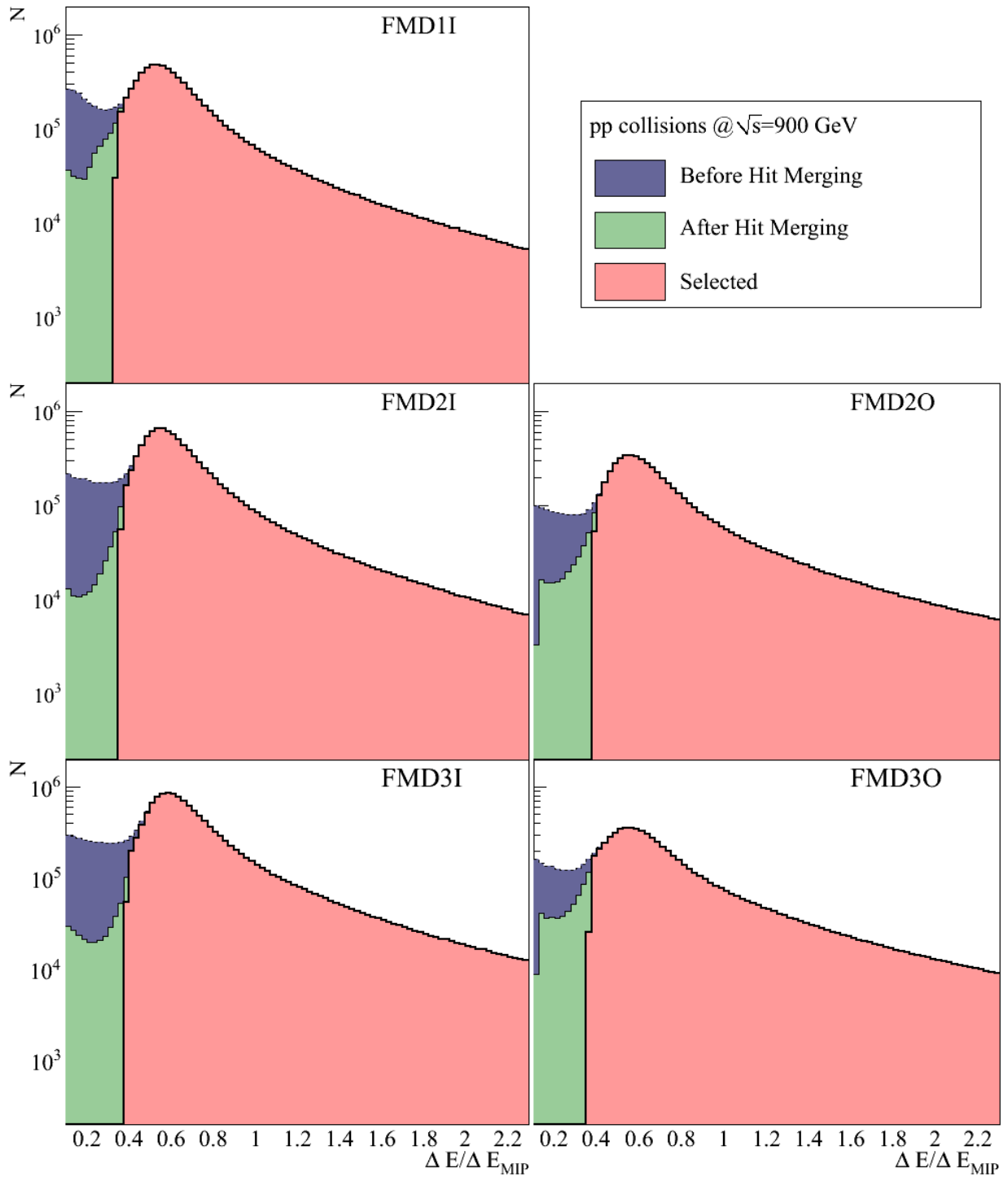


Figure 6.12: Example of the effect of merging shared signals on the energy distributions. Shown is each individual FMD ring in  $pp$  collisions at  $\sqrt{s} = 900$  GeV.

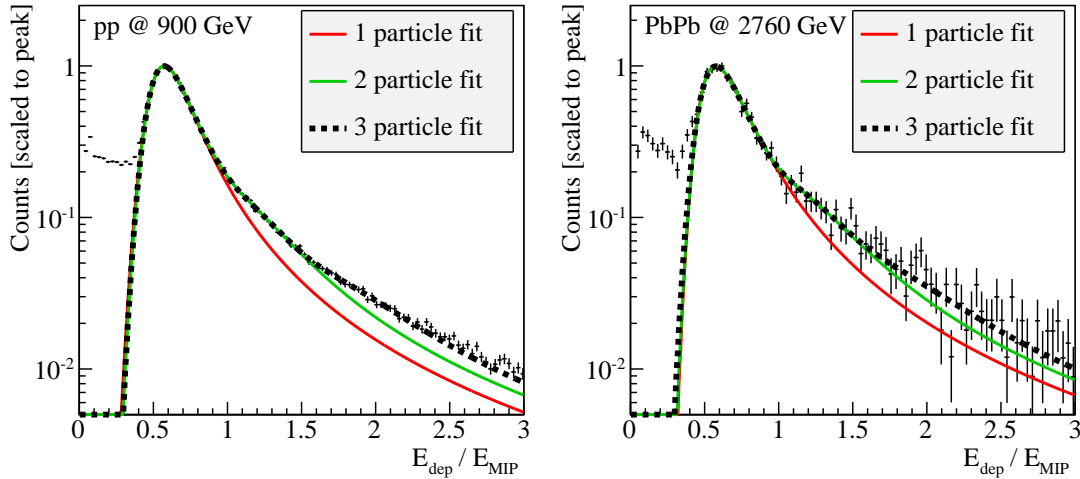


Figure 6.13: Example of a multiple (Gaussian convoluted) Landau fit to the energy distributions for  $pp$  collisions at  $\sqrt{s} = 900$  GeV and  $PbPb$  collisions at  $\sqrt{s_{NN}} = 2760$  GeV. Fits including 1-3 Landau distributions are shown.

### 6.2.3 Counting Methods

Next step in the analysis is to take into account the high occupancy i.e., cases where several particles hit the same strip<sup>21</sup>. This is what gives rise to the higher order MIP peaks, discussed previously. However, a single slow-moving particle depositing a lot of energy, and several particles depositing lower energies are indistinguishable in the FMD. Thus when counting the actual number of charged particles hitting the FMD, this must be taken into account. It has been tested using two distinct methods, which are described in this section.

#### Energy Fit Method

Multiple Landau distributions, each convoluted with a Gaussian, as described in section 4.3, are fitted to the energy distributions. Each of the fitted Landau distributions corresponds to 1, 2 or 3 MIPs depositing energy in the detection element. Figure 6.13 show the results of fitting the data with 1-3 Landau distributions respectively. The fits are shown for  $pp$  collisions at  $\sqrt{s} = 900$  GeV and  $PbPb$  collisions at  $\sqrt{s_{NN}} = 2760$  GeV. Even using only a few Landau distributions yield excellent agreement with the data. For the analysis 3 Landau distribution fits are sufficient.

The energy fit method takes high occupancy into account by directly using the fits to the energy distributions. It is done by calculating the weighted mean of the entire energy distribution, by using the weights,  $a_i$ , for the individual MIP peaks.

$$N_{ch} = \frac{\sum_{i=1}^3 i a_i F_i}{\sum_{i=1}^3 a_i F_i} \quad (6.1)$$

where the fit (and thus the sum) is restricted to include the first 3 Landau distributions.  $F_i = L_i(\Delta) \otimes G_i(\Delta)$  denotes the  $i^{th}$  Gaussian convoluted Landau distribution as described in section 1.4.1.

<sup>21</sup>Not to be confused with hit sharing as discussed in the previous section, where a single particle hit several strips.

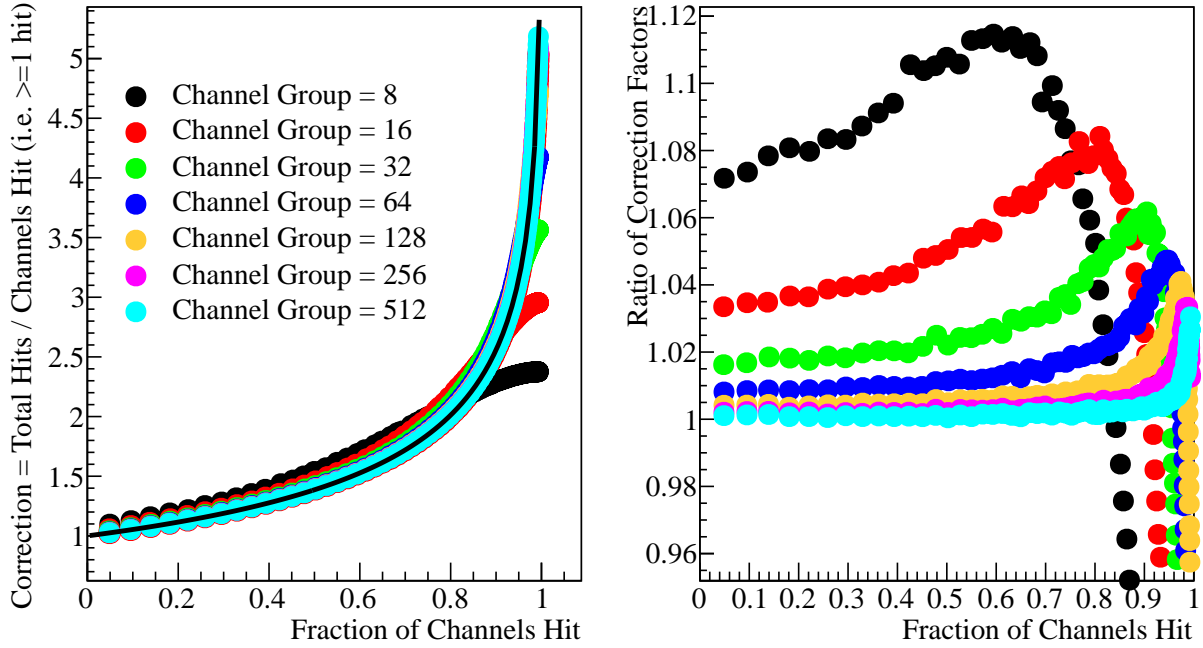


Figure 6.14: The correction for high occupancy in the Poisson counting method. Left panel shows the correction factor for different region sizes as a function of the occupancy. The analytical expression is shown as the solid black line. Right panel: The ratio between the correction factors of the different region sizes and the analytical solution. It is seen that the agreement becomes better and better for increasing region sizes.

## Poisson Method

The second method used for counting particles in the FMD takes high occupancy into account by using Poisson statistics.

To illustrate this, let us start out by defining the true occupancy for a region of the FMD as the mean number of particles per strip traversing this region.

$$\mu = N_{ch}/N_{channels} \quad (6.2)$$

Similarly the measured occupancy of a single event is given by:

$$\mu_{meas} = N_{hits}/N_{channels} \quad (6.3)$$

where  $N_{hits}$  is the number of strips with a hit above  $E_{hit}$ . If the assumption is made that the distribution of particles hitting a region of the FMD is uniform, then the number of particles hitting that region is described by Poisson statistics i.e., the probability of finding  $N_{ch} = n$  particles in the region is:

$$P(n) = \frac{\mu^n e^{-\mu}}{n!} \quad (6.4)$$

The measured occupancy, which is the probability of having any number of hits in the region, can then be related to the true occupancy:

$$\mu_{meas} = P(n > 0) = 1 - P(0) = 1 - e^{-\mu} \quad (6.5)$$

Now, for a strip being hit the average number of particles hitting it will be:

$$\begin{aligned}
C &= \frac{\sum_{n>0} nP(n)}{\sum_{n>0} P(n)} \\
&= \frac{e^{-\mu}}{1 - e^{-\mu}} \sum_{n>0} \frac{n\mu^n}{n!} \\
&= \frac{e^{-\mu}}{1 - e^{-\mu}} \mu \sum_{n>0} \frac{\mu^{n-1}}{(n-1)!} \\
&= \frac{e^{-\mu}}{1 - e^{-\mu}} \mu \sum_{k=n-1} \frac{\mu^k}{k!} = \frac{e^{-\mu}}{1 - e^{-\mu}} \mu e^{\mu} \\
&= \frac{\mu}{1 - e^{-\mu}} \tag{6.6}
\end{aligned}$$

$\mu$  can in principle be calculated analytically, but can also be found by inverting (6.5), yielding

$$\mu = \frac{1}{\ln(1 - \mu_{meas})} \tag{6.7}$$

This is done in regions of the FMD each containing 256 strips. Thus each strip being hit in this region takes high occupancy into account by scaling with  $C$  for that region.

Figure 6.14 shows the motivation for using at least 256 strips as a region. The left panel shows the correction factor as a function of the occupancy for several choices of region size. Also included is the analytical calculation plotted on top as a solid black line. The right panel shows the ratio of the correction of the various region sizes compared to the analytical curve. It is clear that for our selection of 256 strips there is great agreement with the analytical curve to very high occupancies. The regions used, consists of 64 strips in 4 adjacent sectors.

Even better agreement could be reached by using 512 strips, but it comes at a cost in the sense that it would mean larger regions in either  $\eta$  or  $\phi$ . Having too large regions can cause problems due to the number of particles varying over the region. Thus, we aim at having regions with sufficient strips to ensure agreement with the analytical calculation without washing out changes in number of particles over a region. The difference between 256 and 512 strips in figure 6.14 is around 0.1%.

As seen regions of 256 strips has good agreement until the highest occupancies. Figure 6.15 show the distribution of region occupancies for one of the FMD rings for  $pp$  collisions at  $\sqrt{s} = 900$  GeV and  $PbPb$  collisions at  $\sqrt{s_{NN}} = 2760$  GeV. As is evident, even in  $PbPb$  collisions the mean region occupancy of the FMD system is low enough to ensure that the chosen regions of 256 strips are in accordance with the analytical curve.

## Comparison between Poisson and Energy Fit counting

Both methods of counting are viable. Figure 6.16 show the comparison between the two methods for each FMD ring in  $pp$  collisions at  $\sqrt{s} = 900$  GeV. The comparison for  $pp$  collisions at  $\sqrt{s} = 2760$  GeV and 7000 GeV and  $PbPb$  collisions at  $\sqrt{s_{NN}} = 2760$  GeV can be found in appendix D.

In both cases good agreement is found between the two methods, with the regression slope close to unity. The agreement is better for the inner rings, compared to outer rings. The reason for this is not understood and must be studied more. For the results presented in chapter 8 the Poisson method is used, since it is the simpler of the two methods. The minor disagreements between the two methods are included as a systematic uncertainty.

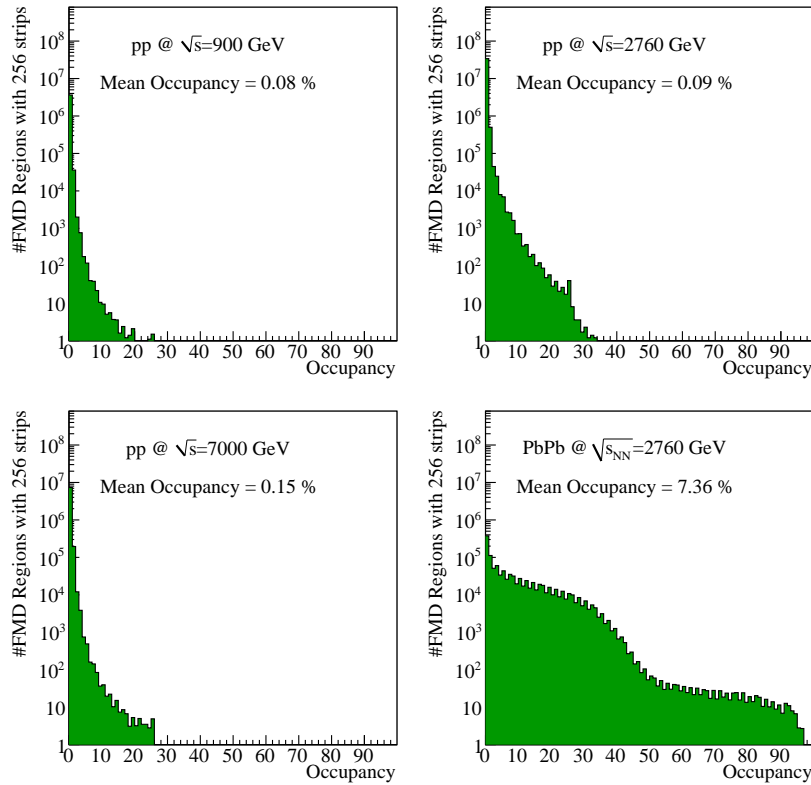


Figure 6.15: Occupancy distribution in regions of 256 strips in FMD2I for  $pp$  collisions at  $\sqrt{s} = 900$  GeV, 2760 GeV, and 7000 GeV, as well as  $PbPb$  collisions at  $\sqrt{s_{NN}} = 2760$  GeV.

### 6.2.4 FMD Acceptance

As any other detector, the FMD does not have perfect acceptance. The issues with acceptance can be grouped into three types of acceptances, that will be corrected for separately:

**$\eta$  acceptance** The edge of the outermost  $\eta$  bins in each ring might not coincide with the actual  $\eta$  value of the outermost strip. This means that the outermost bin might be only partially full, and thus consist of fewer strips. This can cause corrections in those bins to blow up, as well as general edge effects from rapidly changing acceptance compared to limited resolution. Thus a cut is imposed to cut away the outer partial bin. In section 6.8 comparisons between the analysis with 0,1 or 2 bins cut away will be discussed.

**$\phi$  acceptance** The FMD is in principle built as a detector with full  $\phi$ -coverage. However, at the time of construction, it was not possible to manufacture silicon wafers at the quality required for the FMD, in sizes bigger than 6". To maximise the  $\eta$  coverage it was decided to cut away the corners of the individual sensors (as seen in figure 4.6). Thus the outermost strips span a shorter arc length than the rest, and therefore does not have full  $\phi$  acceptance. This is solved by geometrically calculating the ratio between the length of the actual strip and the length of the strip if the corners had been there, and correcting the signal by this ratio. An example of this correction is shown in figure 6.17.

**Dead Channels** Over time individual strips will permanently malfunction. Typically, what will happen, is that individual strips become completely unresponsive. But

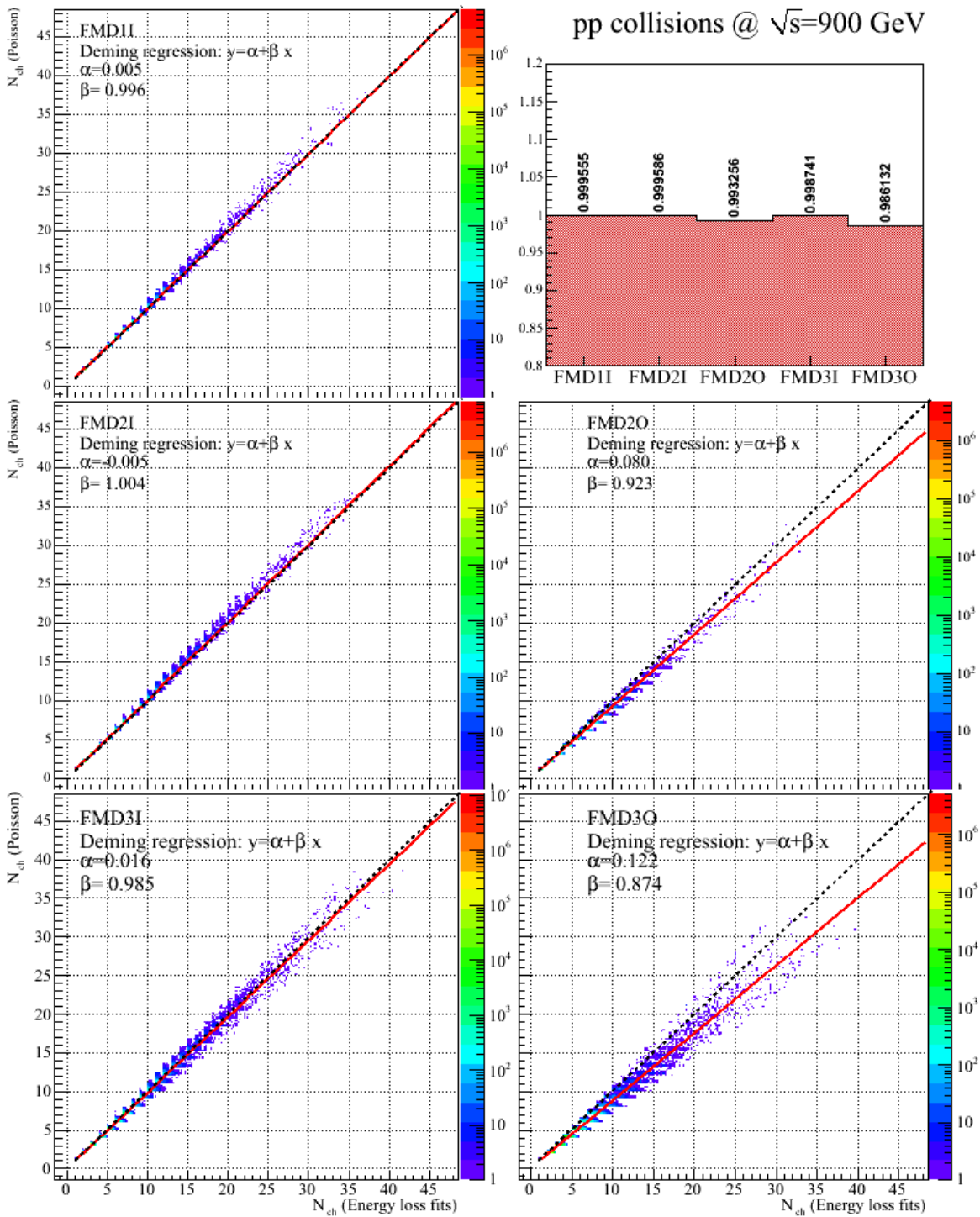


Figure 6.16: Comparison between the Poisson and Energy fit counting methods for  $pp$  collisions at  $\sqrt{s} = 900$  GeV. Overall good agreement is found between the two methods in the inner rings.

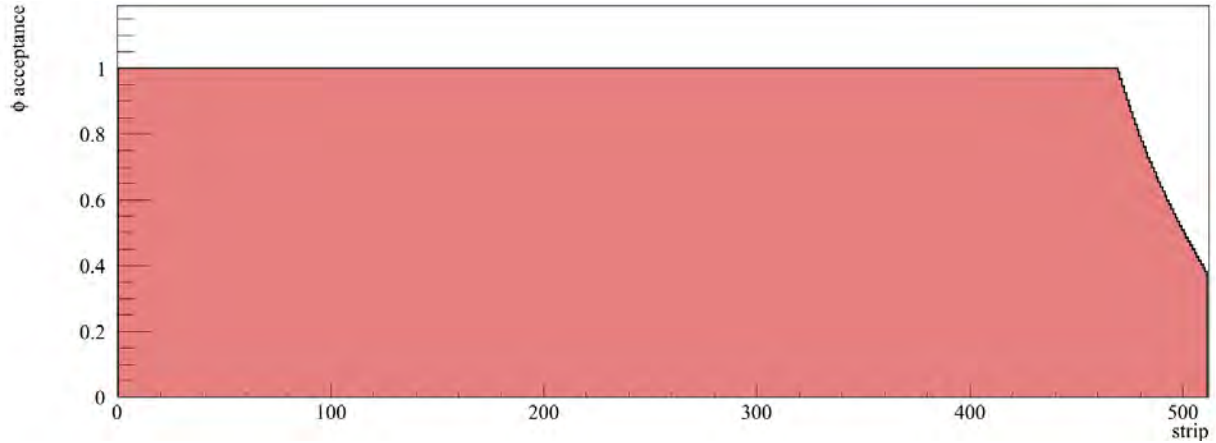


Figure 6.17: Example of the  $\phi$ -acceptance of an inner ring. There is full azimuthal coverage until the outermost strips, where the acceptance drops due to the corners being cut off on the FMD silicon wafers.

in principle one could also have strips malfunction such that they are giving a high signal every event, regardless of whether or not there is a hit. This latter effect has not been observed yet however.

The dead strips must be taken out of the analysis, and a correction for the missing strips must be made. A channel in the FMD is considered active and well if it fulfils

$$\begin{aligned} 0.5 < g_i < 5 \\ 0 < n_i < 10 \end{aligned} \quad (6.8)$$

where  $g_i$  and  $n_i$  corresponds to the gain and noise of strip  $i$  respectively.

For the initial run period at  $\sqrt{s} = 900$  GeV the fraction of dead channels amount to 0.93%. Due to a better implementation of the software on the front-end electronics, the amount of dead channels decreased to 0.25% after the initial run period.

It is found that the 0.25% stems almost solely of a single  $VA1_3$  chip in FMD1I being entirely faulty. This particular dead region was also pointed out in in the figures 4.11, 4.11 and 4.11.

The correction factor for a given  $(\eta, \phi)$ -bin is given by calculating the ratio of working strips to the total number of strips in that bin.

## 6.3 SPD Particle Counting

Counting particles in the SPD inner layer is simpler than in the FMD case.

The analysis procedure does not make use of the tracklets, but instead only uses the clusters from the inner layer. In some sense the analysis procedure is very similar to the one used for the FMD rings i.e., the inner layer is seen as a silicon layer with no tracking information.

In the reconstruction of the SPD data, both the tracklets and unused clusters were saved as described in section 5.3. Thus the number of particles in the SPD in a given  $\eta$  range is simply given by:

$$N_{ch} = \sum_t 1 + \sum_c 1 \quad (6.9)$$

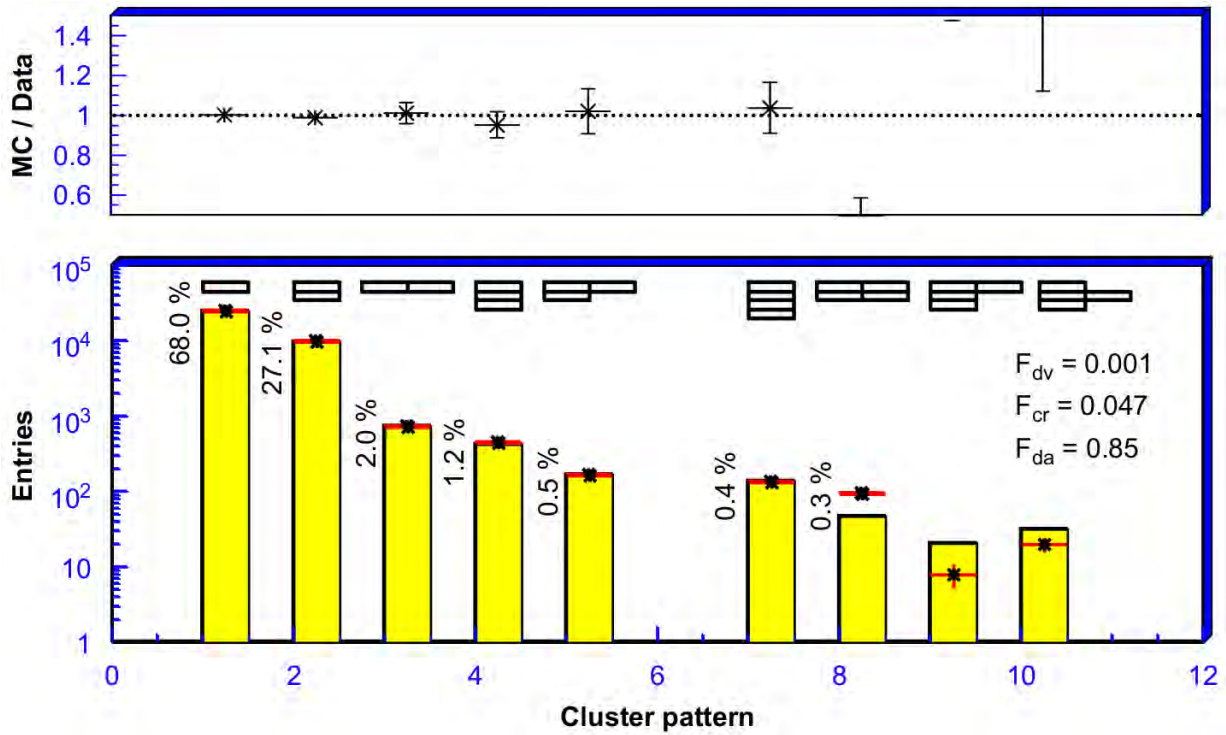


Figure 6.18: The frequency of various cluster patterns in the SPD [123]. The yellow bars are for physics data and the black points are for simulations. It is seen that 68% of hits in the SPD are single pixels being hit. Less than 3% of hits consist of more than two adjacent pixels firing.

Here the sum is over  $c$  and  $t$ , which are the unused clusters and the tracklets in the first layer respectively.

The big challenges in the FMD with hit sharing and high occupancy are not present in the SPD. Due to the very fine segmentation in  $\eta$  it is very unlikely to have multiple signals in the same pixel, which removes the need for taking high occupancy into account.

The individual clusters can consist of signals in several adjacent pixels. But again, due to the fine resolution, it is unlikely that two particles would hit adjacent pixels.

Therefore even multi-pixel signals are very likely to be just a single particle. Furthermore, since the SPD is a pixel threshold detector, the deposited amount of energy is not available, and thus no hit merging could be done if needed.

Figure 6.18 show the frequency of the various cluster signatures in the SPD, both for physics data and from simulated data [123]. 97% of all cluster are either single pixel clusters or clusters made up of two adjacent pixels.

### 6.3.1 SPD Acceptance

As in the case of the FMD there are similar acceptance issues regarding the SPD inner layer.

**$\eta$  acceptance** In the same manner as in the FMD, the first  $\eta$  bin is cut away, since it might be partly filled with pixels only.

**$\phi$  acceptance** The SPD is designed with full  $2\pi$   $\phi$ -coverage.

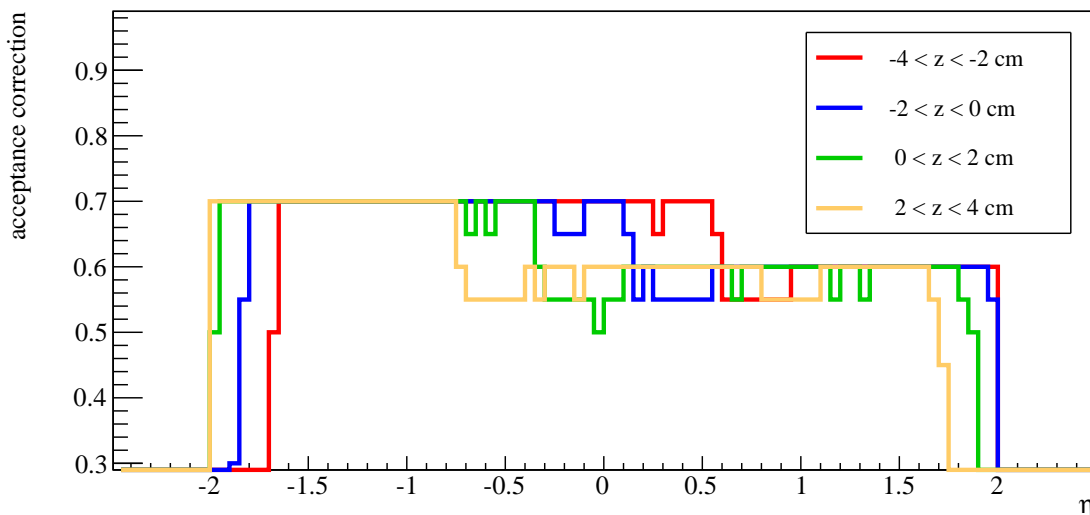


Figure 6.19: The actual  $\phi$ -acceptance of the SPD as a function of  $\eta$ . As discussed in the text, cooling issues has meant that parts of the SPD is turned off. This leaves large holes in the acceptance.

**Dead channels** The SPD have two contributions to dead channels. The first is malfunctioning pixels, connectors, etc., analogous to the malfunctioning strips in the FMD. This type of dead channels only amount to less than 1 % of the number of pixels [123].

The second contribution is much bigger. The cooling requirements for the SPD are very large. And so far the cooling capabilities of the SPD has not been sufficient. The unfortunate consequence is that parts of the SPD has been turned off for data taking to avoid overheating. Thus while the SPD is designed with full  $\phi$ -coverage, it does not have it, due to turned off channels. Figure 6.19 shows the acceptance correction as a function of  $\eta$  for the running conditions, and later on, figure 6.26 shows the large holes in the  $(\eta, \phi)$  acceptance of the SPD.

## 6.4 Secondary particles

Particles can be grouped as either primary particles or secondary particles. For this work all particles stemming directly from the initial collision are considered primary particles. On the other hand, particles created by decays, interaction with materials on the way to the SPD or FMD is labelled secondary particles.

This section will discuss the secondary contamination in both detectors, as well as describe how to correct for secondary particles.

We start out by looking at the amount of secondary particles hitting each detector, as well as where they were created. This is done using simulated data. If the implemented virtual model of the experiment, as well as the physics processes in the transport model, is accurate, then the simulation describes the actual physics collisions well. Figure 6.20 show an example of the origin of all secondary particles in the central  $(z, r)$  region. It is immediately possible to identify sub-detectors, support structures etc., by the secondary particles created in their material. Figure 6.21 shows a similar example, but this time only the the origin of the secondary particles eventually hitting one of the FMD rings.

What is apparent is that there is a vast difference in the amount of material in front of the SPD and FMD respectively. The SPD, sitting just outside the beam-pipe, has very little material in front of it, and thus a low secondary particle contamination. The FMD

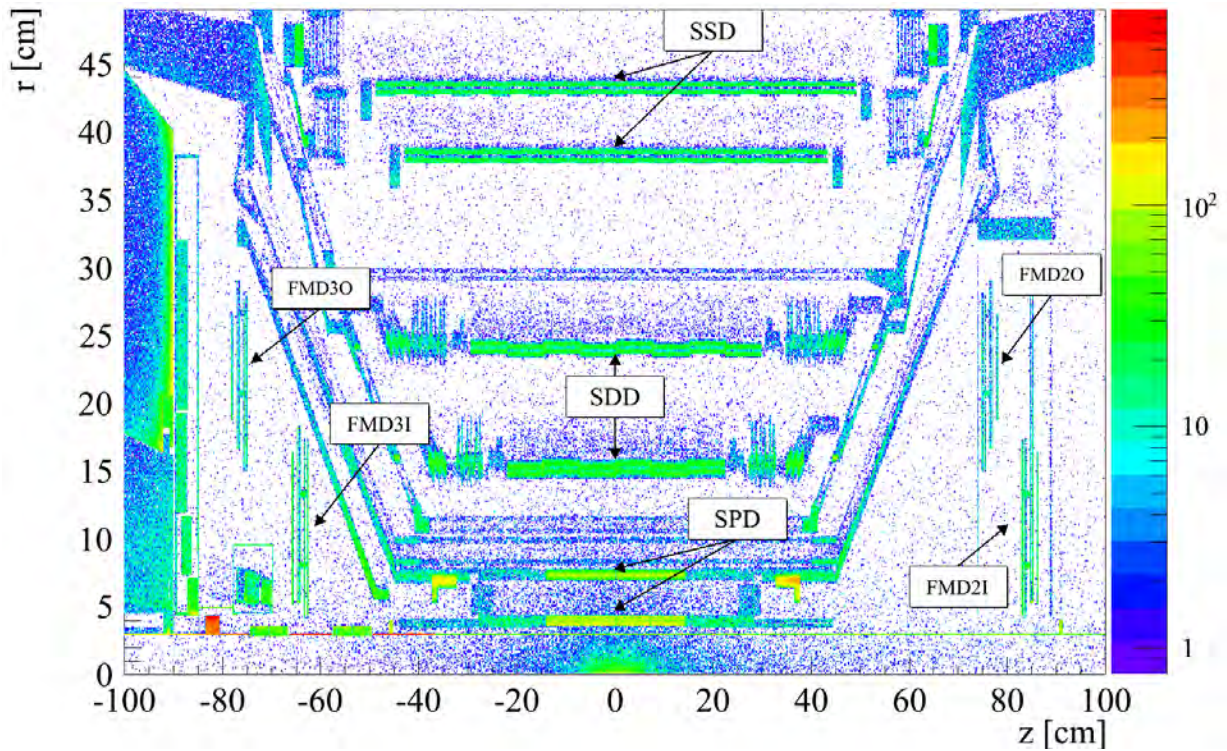


Figure 6.20: The origin of secondary particles within the central region of ALICE. Secondary particles created by interaction with the detector material immediately show the detailed structure of the individual detectors, and their support structures.

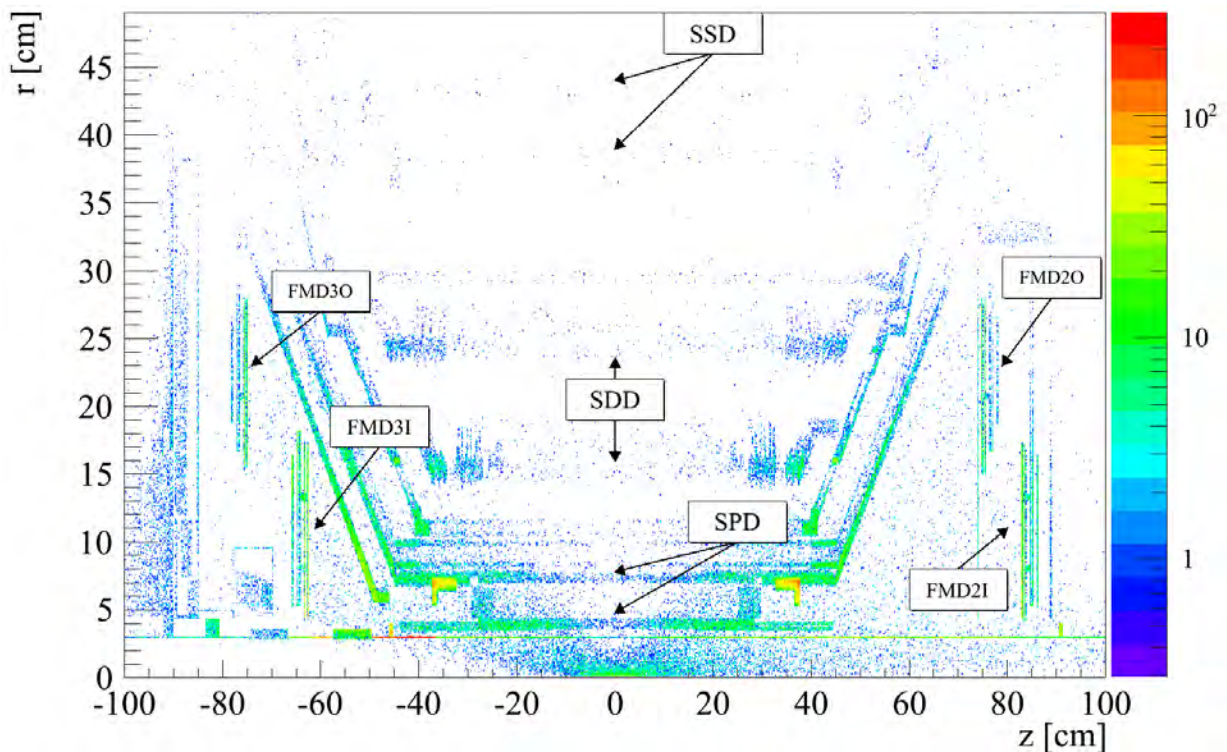


Figure 6.21: The origin of the secondary particles, which eventually hit the FMD system.

on the other hand has a considerable amount of material in front of it.

Another point worth bringing up is that secondary particles hitting a detector element in a certain region in  $\eta$  is quite likely to originate from that same  $\eta$  region. Thus, most secondary particles created continues in a similar direction as their primary ancestor. This is illustrated in figure 6.22, which show the origin of secondary particles hitting each of the individual FMD rings.

Using figure 6.20 as a reference it is possible to define geometrical shapes in  $(z, r)$ , that correspond to certain detectors. Summing up everything inside these shapes will thus yield the secondary particles contribution from that selection. For this study, five different selections are sufficient to get a clear picture of the origin of the secondary particles hitting the SPD or FMD. These are:

**Early Decay** This is used as a common name for all secondary particles created inside the beam pipe.

**Beam Pipe** These are the secondary particles created in the beam pipe material, as the primary (or early decay secondary) particles traverse it.

**ITS** These secondaries are created inside the ITS volume.

**FMD** These secondaries are created inside the FMD volume.

**OTHER** All the rest of the secondary particles are grouped together. This is viable, since the vast majority of secondary particles hitting either the FMD or SPD falls into one of the four other categories.

In figure 6.23 the total contamination of secondary particles for both the FMD and SPD region is shown. In the region of  $\eta$ -overlap between FMD3I and FMD3O i.e., around  $\eta \sim -2$ , contributions from each sub-detector is added together, giving a peak structure. In figure 6.24 the same information is shown per sub-detector. It is seen that the secondary particles hitting the FMD stems mainly from itself and the ITS. Going more and more forward in  $\eta$  yields a bigger and bigger contribution from the beam pipe, since the effective path length through the beam pipe becomes longer and longer<sup>22</sup>. The amount of secondary particles hitting the FMD is in some areas almost twice as big as the amount of primaries hitting it. In the SPD the amount of secondaries is in the order of 10% of the amount of primaries.

It is necessary to correct for the secondary particles, in order to retrieve the primary distribution. This can either be done in a separate step, which we label the secondary correction, or be done later on during the unfolding process, described in section 6.6.

The secondary correction is done by using simulations, to determine the amount of secondary particles compared to the total number of particles in each  $(\eta, \phi)$  bin. Thus, the correction factor for a given  $(\eta, \phi)$  bin is:

$$C_{sec}(\eta, \varphi) = \frac{\sum_i N_{ch, \text{prim}}^i(\eta, \varphi)}{\sum_i N_{ch, \text{sec} + \text{prim}}^i(\eta, \varphi)} \quad (6.10)$$

The sums run over the simulated data sample, having a valid vertex and trigger. The total number of charged particles hitting the chosen FMD bin in event  $i$  is denoted  $N_{ch, \text{sec} + \text{prim}}^i$ . Similarly  $N_{ch, \text{prim}}^i$  is the number of primary charged particles as given immediately after

<sup>22</sup>This is not the only reason though. At  $z \sim -35$  cm, the Beryllium beam pipe stops, replaced by steel, which create many more beam pipe secondary particles in FMD3I, compared to the other rings.

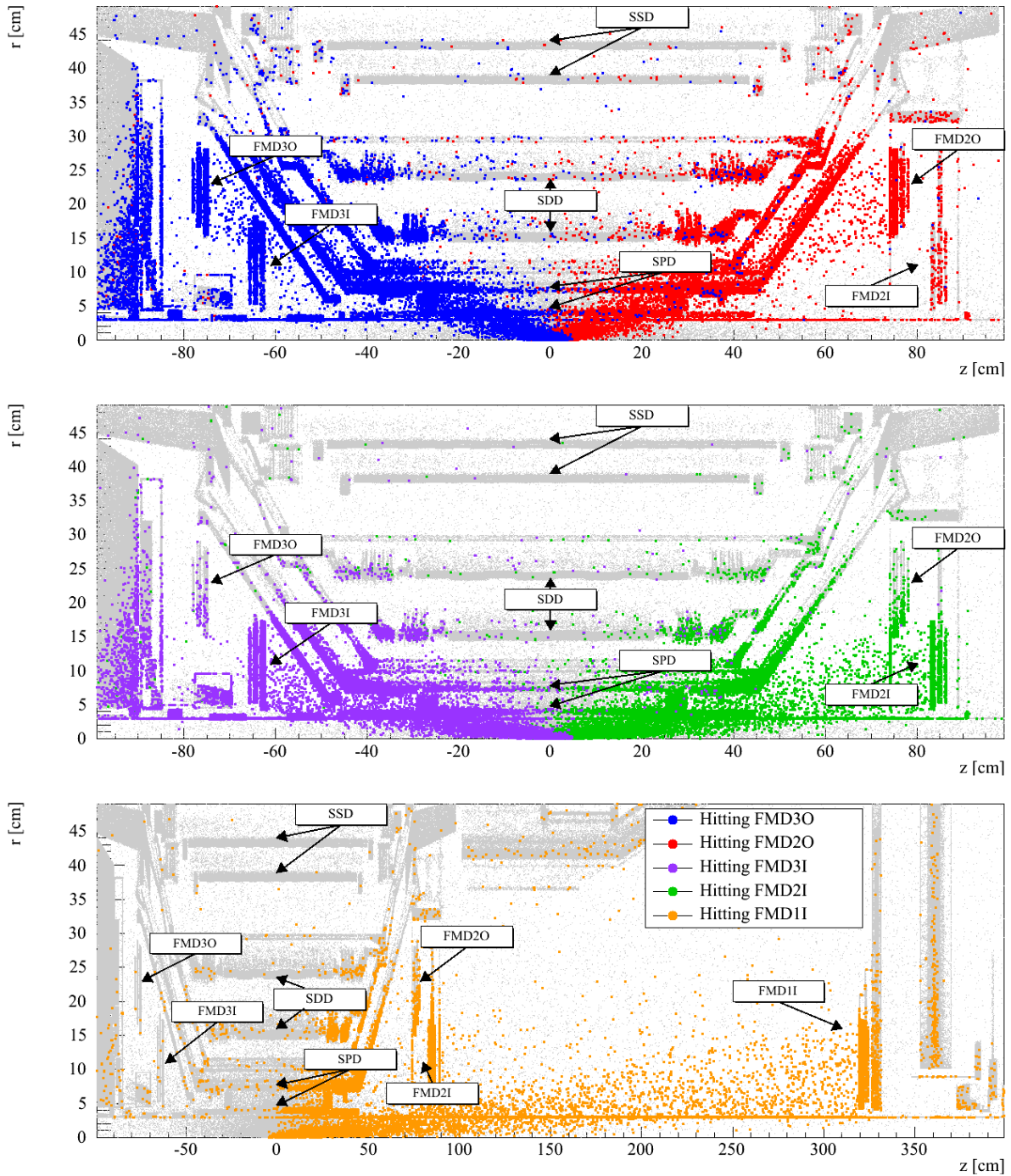


Figure 6.22: The origin of secondary particles hitting each individual FMD ring. The top panel show the two outer rings, and the middle panel show the inner rings of FMD2 and 3. The lower panel shows FMD1, where the scale on the  $x$ -axis is different. It is seen that the majority of secondary particles continue in roughly the same direction as their primary ancestor particle.

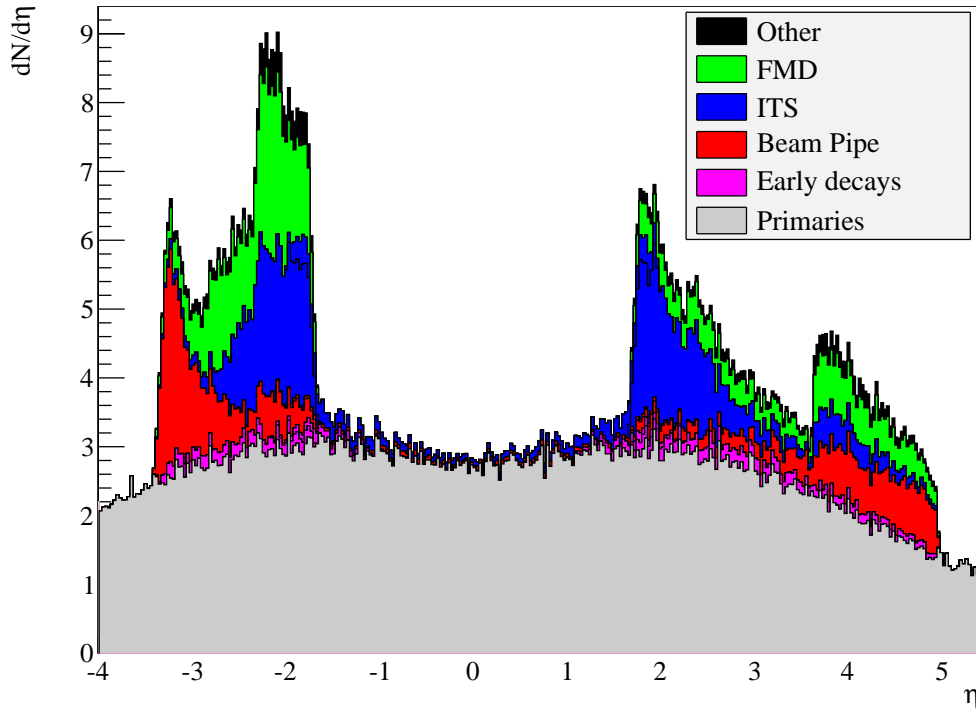


Figure 6.23: The origin of secondary particles hitting either the FMD or SPD inner layer as a function of  $\eta$ . In regions of detector overlap the contributions are summed for each detector, which explains for instance the 'peak' in the overlap between FMD3I and FMD3O at  $\eta \sim -2$ . The grey area show the primary particle distribution.

the collision. Thus the secondary correction yields a  $(\eta, \phi)$  map of the average number of primaries compared to total number of particles. The secondary maps varies slightly with  $v_z$ , and thus the secondary correction is performed independently in  $v_z$  bins of 2 cm.

Left panel of figure 6.25 shows an example of a secondary map from FMD31. The right panel shows the same map, with the edges cut away (as described in section 6.2.4), and with data superimposed as black boxes. This serve as a good test that the simulation and data actually do cover the same region.

Figure 6.26 shows the same for the SPD. The distinct holes in acceptance, due to lack of cooling, are clearly seen.

Comparison of the effects of doing the secondary correction or letting the unfolding handle the secondaries follows in section 6.8.

As a closing remark on secondary corrections, it is useful to keep in mind that any analysis using the approach of correcting for secondary contamination by the secondary maps is said to be secondary corrected. Analyses that handle the secondary contamination in the unfolding is in this terminology not said to be secondary corrected. Thus in essence the term secondary correction only refer to the separate correction procedure, even though secondary particles are removed using both methods.

## Material budget overhaul

The very studies of the origin of secondaries presented in the previous section, concluded at a early time that the description of the ITS material budget in particularly the forward region was not accurately enough described in the simulation. Thus it prompted a complete overhaul of the ITS geometry implementation from the spring of 2010 and throughout that

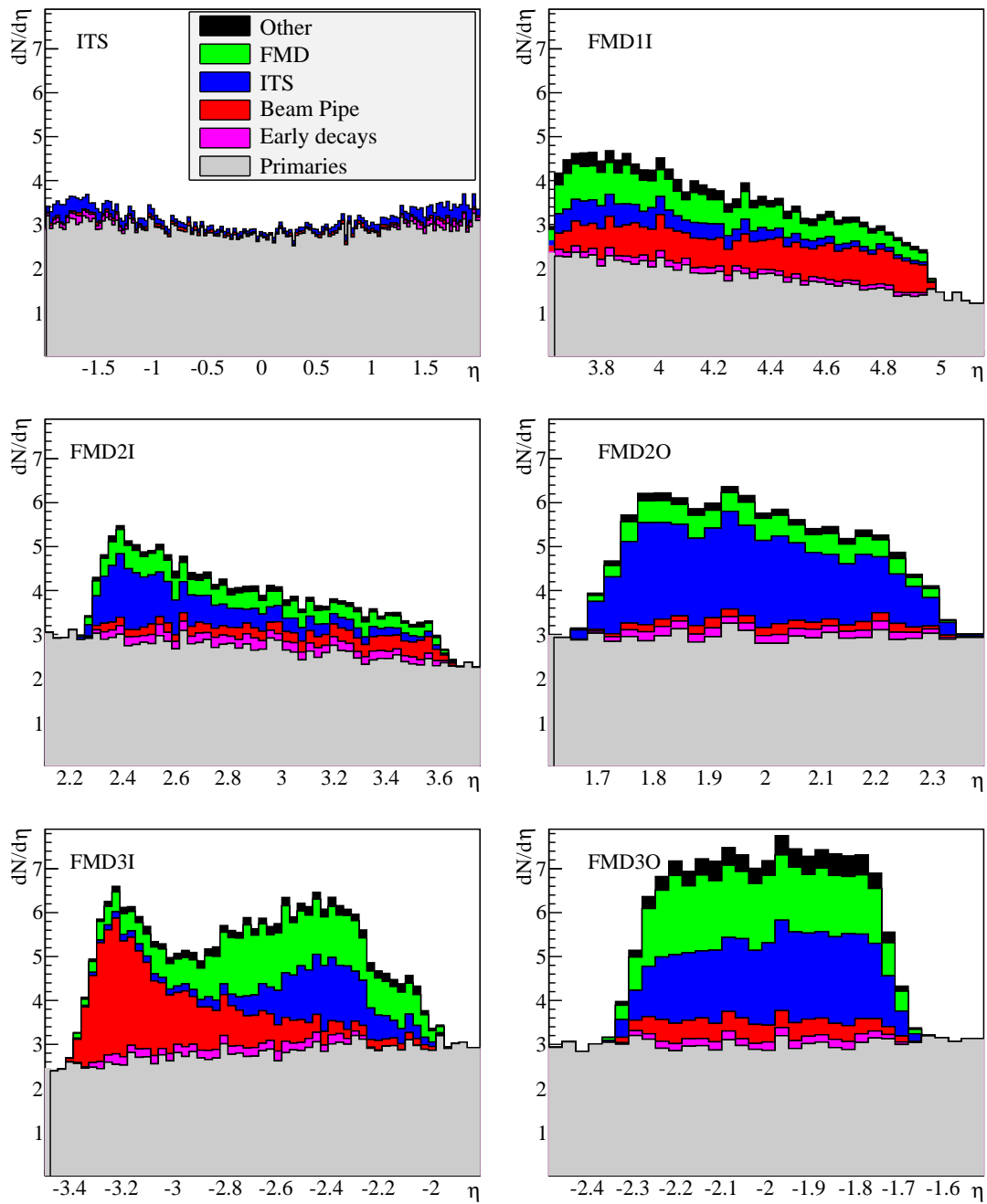


Figure 6.24: The origin of secondary particles hitting the various FMD rings and the inner layer of the SPD respectively. It is clear that that pollution of secondary particles is much higher in the FMD rings compared to the SPD. This reflects the amount of material sitting in front of each of the detectors. As seen, in some areas (FMD3I) there can be almost two times the number of secondary particles, compared to primary particles, hitting the detector.

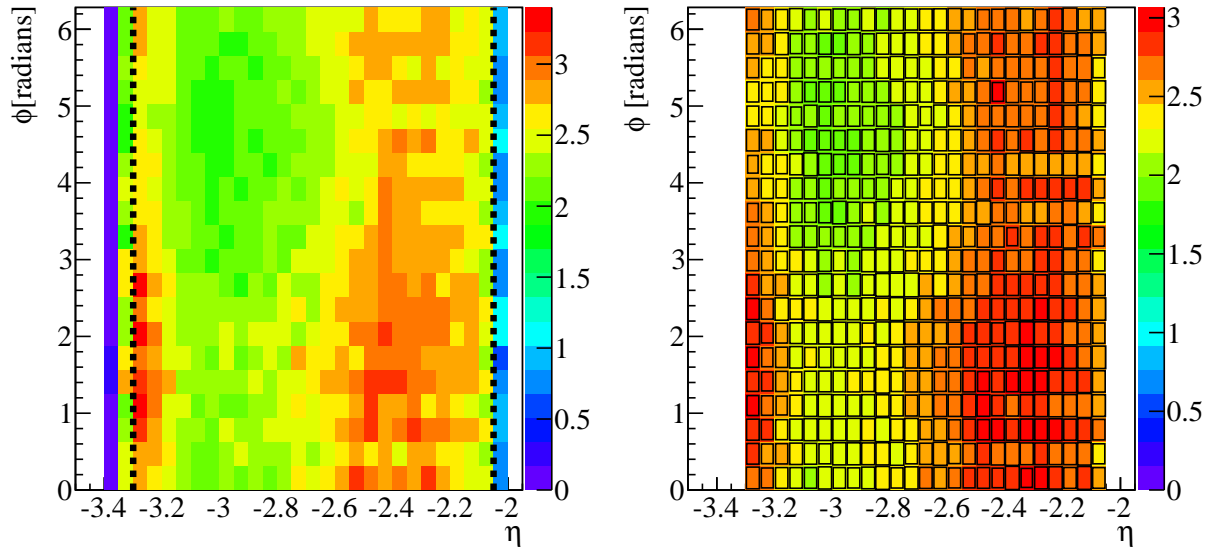


Figure 6.25: Left panel: An example from FMD3I of a secondary correction map. The dashed line shows the bins that are cut away at the edges. Right panel: Data superimposed on top of the secondary map as boxes.

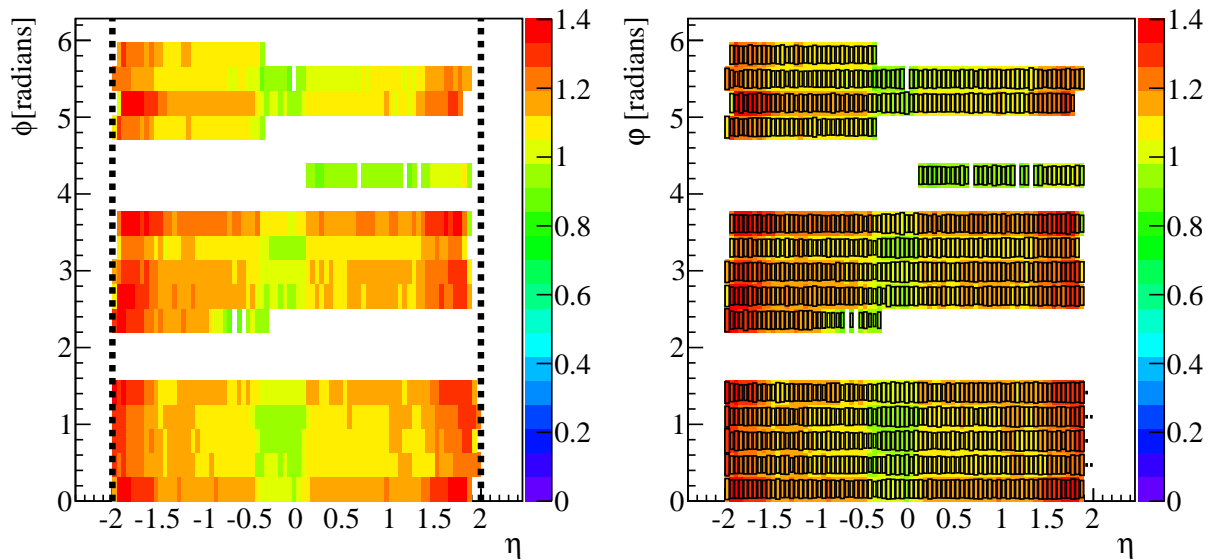


Figure 6.26: Left panel: Example of a SPD secondary correction map. The shut off parts of the SPD are clearly visible. Right panel: Data superimposed on top of the secondary map as boxes.

Range	Correction factor
$0.00 < p_T < 0.17$	1.00
$0.17 < p_T < 0.40$	$1.00 + 0.3(p_T - 0.17)$
$0.40 < p_T < 0.60$	$1.07 + 0.9(p_T - 0.4)$
$0.60 < p_T < 1.20$	$1.25 + 0.42(p_T - 0.6)$
$1.20 < p_T$	1.50

Table 6.2: Strangeness correction parametrisation.

year. This was crucial to particularly the FMD analysis effort, due to the large secondary particle contamination, as well as the lack of any tracking capabilities (since tracking detectors can immediately cut away secondary particles, not pointing back to the nominal interaction point.)

The changes made was a great leap forward for the analysis efforts of the forward detectors. The case of the material budget is still not closed however. There are still suspicions that there might still be minor inaccuracies in the material description in the forward regions. There are plans in place to hopefully once and for determine this. These will be discussed in section 8.5

## 6.5 Strangeness Correction

In the central ( $|\eta| < 0.5$ ) region, there is found a discrepancy between simulations and data in the amount of secondary particles, containing strange quarks [124]. Thus too few strange secondary particles are included in the simulations, and this must be corrected for.

The excess of strange secondary particles in data is found to be dependent on  $p_T$ . The correction factor parametrisation as a function of  $p_T$  is found in table 6.2.

This parametrisation is applied to each secondary particle in a special simulation run, and then compared to a reference simulation. The strangeness correction factor is thus

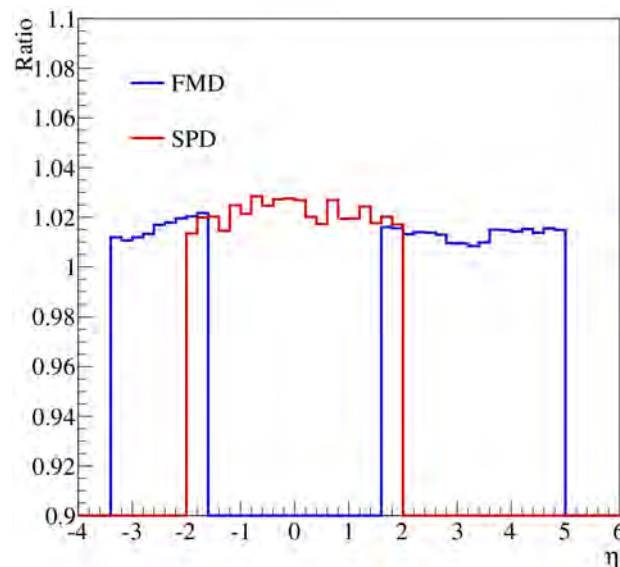


Figure 6.27: The strangeness correction factor as a function of  $\eta$ , given as the ratio between a special simulation, where each secondary particle is weighted in accordance to data, and a reference simulation.

given as the ratio between the two. The correction factor as a function of  $\eta$  is seen in figure 6.27. It is found to be roughly a 2% correction over all  $\eta$ .

However it must be stressed that this is a quite ill-determined correction. It assumes that all conditions in the midrapidity region holds for the forward region as well. However strangeness production could in principle easily depend on  $\eta$ ,  $\langle p_T \rangle$  or other quantities changing when moving to forward regions. To illustrate this we assign a relative error of 100% to the correction such that the correction becomes  $2 \pm 2\%$ .

## 6.6 Unfolding

If one had ideal detectors, the measured distribution of a quantity would by definition also be the ‘true’ distribution of that quantity. However detectors are not ideal systems. Thus in real detectors the actual ‘true’ measurement of a quantity can be complicated by the following effects [125]:

**Limited acceptance** The detector acceptance is generally less than unity, as described in sections 6.2.4 and 6.3.1.

**Transformation** Often, the desired quantity is not measured directly. Instead another related quantity is measured. The transformation from one to the other can have non-linear terms in some detector components. An example on such a transformation is the measurement in the FMD system, where the energy deposited in the Silicon strips are measured, and then transformed into a number of particles.

**Finite resolution** Measurements conducted will be smeared, due to finite resolution of the detector.

All these effects can be corrected by unfolding the measured distribution. Unfolding is a term mostly used in heavy ion physics. The concept of unfolding however is also known in mathematics in general as inverse problems, and in other areas of application it is known as deconvolution or unsmearing.

The basic idea behind all unfolding techniques is to construct the detector response in the form of a response matrix. The response matrix connects the true signal to the measured signal in the detector. The correlation given by the response matrix is then used to recover the true signal.

The relation between the measured distribution  $\bar{m}$ , and the truth distribution  $\bar{t}$  is thus given by:

$$\bar{m} = \hat{R}\bar{t} \quad (6.11)$$

where  $\hat{R}$  is the response matrix.

Unfolding aims to find the truth distribution by matrix inversion, either directly or by some approximation i.e.,:

$$\bar{t} = \hat{R}^{-1}\bar{m} \quad (6.12)$$

There exists several methods of unfolding. This work concentrates on two methods, namely the so-called Bayesian iterative unfolding and Single Value Decomposition (SVD) unfolding.

As discussed in section 5.6 the response matrices used in this work are constructed using special flat multiplicity simulations. This is necessary, since it is imperative that the very high multiplicity part of the response matrix is well populated. Figure 6.28 shows an example of a response matrix.

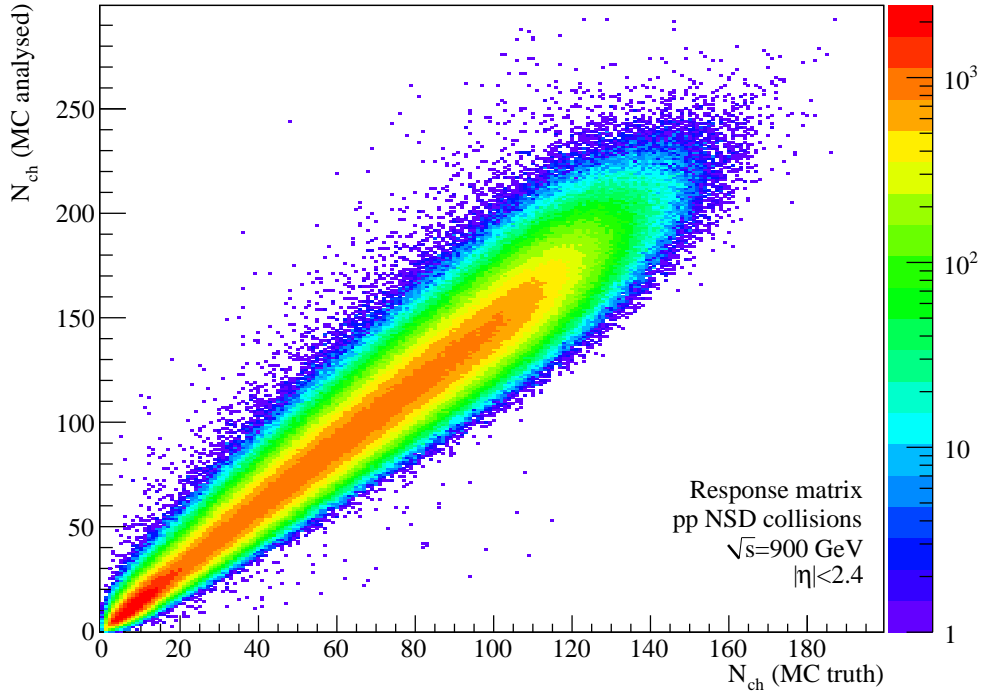


Figure 6.28: Example of a response matrix for  $|\eta| < 2.4$  in  $\sqrt{s} = 900$  GeV  $pp$  collisions. Each generated true multiplicity is propagated through the detector simulation and analysis code, resulting in a distribution of measured multiplicities.

### 6.6.1 Bayesian Iterative Unfolding

One way of doing the unfolding is using a technique known as Bayesian iterative unfolding. The starting point is Bayes' Theorem

$$P(A|B) = \frac{P(B|A)P(A)}{P(B)} \quad (6.13)$$

where  $P(A)$  and  $P(B)$  are probabilities of two outcomes  $A$  and  $B$ , and  $P(A|B)$  is the conditional probability of having  $A$  under the condition of  $B$  being true (and vice versa for  $P(B|A)$ ).

Let  $A$  denote a collision with a given true multiplicity, and  $B$  is collision with a given measured multiplicity in the detector.  $P(B)$  is then the measured multiplicity distribution, and  $P(A)$  is the true distribution, we aim to determine through unfolding. Similarly  $P(B|A)$  is identified as the response matrix.

The two unknown quantities of (6.13) is the true distribution,  $P(A)$  and  $P(A|B)$ , which is sometimes referred to as the smearing matrix. Determining these is the main ingredient of the Bayesian iterative unfolding method.

It can be done by following a iterative procedure by D'Agostini [126, 127]. Equation (6.13) is rewritten as:

$$S_{tm} = \frac{R_{mt}P_t}{\sum_{t'} R_{mt'}P_{t'}} \quad (6.14)$$

$S_{tm}$  denotes the smearing matrix entry  $(t, m)$  and  $R_{mt}$  is the response matrix.  $P_t$  is an a priori guess of the true distribution. The denominator in (6.14) comes from the concept of the detector response i.e., that the true distribution folded with the response matrix will yield the measured distribution.

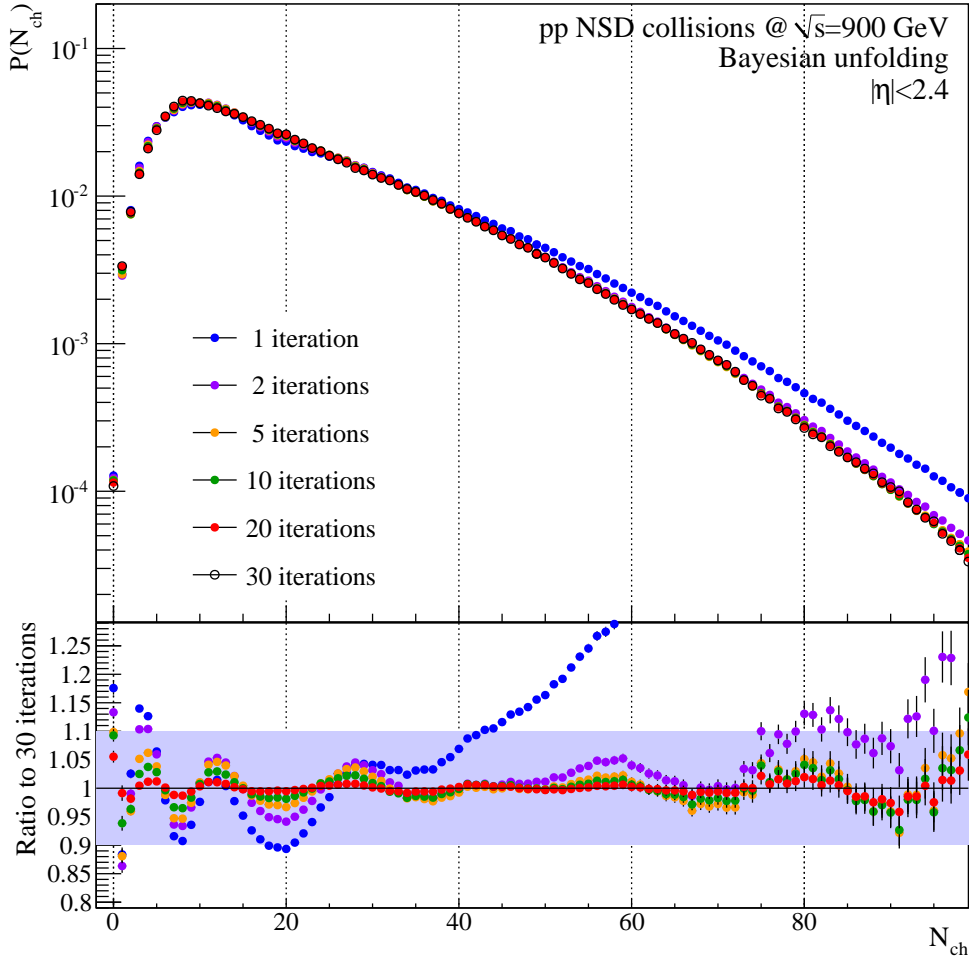


Figure 6.29: The unfolded solution from Bayesian unfolding, stopping the unfolding after different numbers of iterations. It is seen that few iterations are needed. For this work 20 iterations is used for the Bayesian method. The lower panel shows the ratio of the different solutions to the solution involving 30 iterations. It is found that going from 20 to 30 iterations changes to solution with at maximum 1-2% locally.

The choice of prior distribution  $P_t$  is somewhat arbitrary. One can choose for instance the measured distribution as prior, or even a flat distribution if no previous knowledge of the distribution is available. The choice of prior has very little effect on the solution, but mainly on the number of iterations needed for the unfolding [128].

Having found the smearing matrix,  $S_{tm}$  from (6.14) one can determine the unfolded solution:

$$P_t^\dagger = \sum_m S_{tm} M_m \quad (6.15)$$

Here  $M_m$  is the  $m^{\text{th}}$  value of the measured distribution. If  $P_t^\dagger = P_t$ , then  $P_t$  is the exact true unfolded distribution. If not  $P_t^\dagger$  will be between  $P_t$  and the true distribution [126]. The iterative part of the method is that  $P_t^\dagger$  is used as the next prior for the next iteration. In general the number of iterations can be decided on beforehand, or one can set up a convergence criteria for when the difference between  $P_t^\dagger$  and  $P_t$  is within a predefined tolerance.

For this work the Bayesian unfolding is stopped after a predetermined number of itera-

tions. Figure 6.29 show several Bayesian unfolding with different number of iterations for  $pp$  NSD collisions at  $\sqrt{s} = 900$  GeV for  $|\eta| < 2.4$ . It is found that the unfolded solutions changes only slightly after just 5 iterations. Going from 20 to 30 iterations changes the solution less than a percent. For this work 20 iterations are used whenever the Bayesian method is used.

### 6.6.2 Single Value Decomposition Unfolding

The SVD unfolding is also occasionally referred to as  $\chi^2$  minimisation unfolding. The basic principle behind SVD unfolding is to construct a quantity reminiscent to a normal statistical  $\chi^2$ , and through iterations minimise this quantity.

The  $\chi^2$  definition used in this work and others [24, 129], consists of a sum of the square of residuals and a so-called regularisation choice penalty factor,  $\beta F(\bar{d})$ :

$$\begin{aligned}\chi^2(\bar{d}) &= (\bar{m} - \hat{R}\bar{d})^T \hat{C}(\bar{m} - \hat{R}\bar{d}) + \beta F(\bar{d}) \\ &= \sum_o \left( \frac{m_o - \sum_t R_{ot} d_t}{e_o} \right)^2 + \beta F(\bar{d})\end{aligned}\quad (6.16)$$

Here  $\hat{R}$  denotes the response matrix and  $\bar{m}$  is the measured raw multiplicity distribution vector.  $\hat{C}$  is the covariance matrix of  $\bar{m}$ . The only non-zero terms of  $\hat{C}$  are in the diagonal, and are given by the inverse of the statistical errors squared for a given multiplicity. The variable  $\bar{d}$  is the unfolded guessed solution vector.  $\chi^2$  is minimised once the guessed distribution multiplied with the response matrix is equal to the measured one<sup>23</sup>.  $\beta$  and  $F(\bar{d})$  deals with the concept of regularised solutions. Solving (6.16) without the last term will often give rise to highly oscillating (unphysical) solutions. By imposing a regularisation one imposes both a smoothness requirement and a functional bias on the solution.

Equation (6.16) presents  $\chi^2$  both in matrix and sum notation. In the latter  $m_o$  denotes the  $o$ 'th entry of  $\bar{m}$ , i.e the value in observed multiplicity bin  $m$ . In the same fashion  $d_t$  denotes the value in the unfolded (true) multiplicity bin  $t$ .  $e_o$  is the statistical error on the observed multiplicity.

Various functional forms  $F(d)$  can be used for regularisation. For this work the following are used:

$$F(\bar{d}) = \sum_t \left( \frac{d_t - d_{t-1}}{d_t} \right)^2, \text{ pol0 : Favours constant function} \quad (6.17)$$

$$F(\bar{d}) = \sum_t \left( \frac{d_{t-1} - 2d_t + d_{t+1}}{d_t} \right)^2, \text{ pol1 : Favours linear function} \quad (6.18)$$

$$F(\bar{d}) = \sum_t \left( \frac{\ln d_{t-1} - 2 \ln d_t + \ln d_{t+1}}{d_t} \right)^2, \text{ log : Favours exponential function} \quad (6.19)$$

Equation (6.17) is minimised for guessed distributions with small variations from bin to bin. Similarly (6.18) favours distributions where the slope difference between adjacent bins is minimal and finally (6.19) favours distributions where the logarithmic slope differences between adjacent bins are minimal i.e., exponential distributions. They will be referred to throughout the text as *pol0*, *pol1* and *log*<sup>24</sup> regularisation functions.

The main objective when using this particular unfolding method is to determine the best choice of regularisation function and weight. If  $\beta$  is too small the solution could

<sup>23</sup>And thus the guessed distribution is equal to the true distribution.

<sup>24</sup>The best name for this regularisation function can be discussed. Depending if one prefers to focus on the favoured solution, or the form of the regularisation function it can be labelled *exp* or *log* respectively. In this work the latter is used.

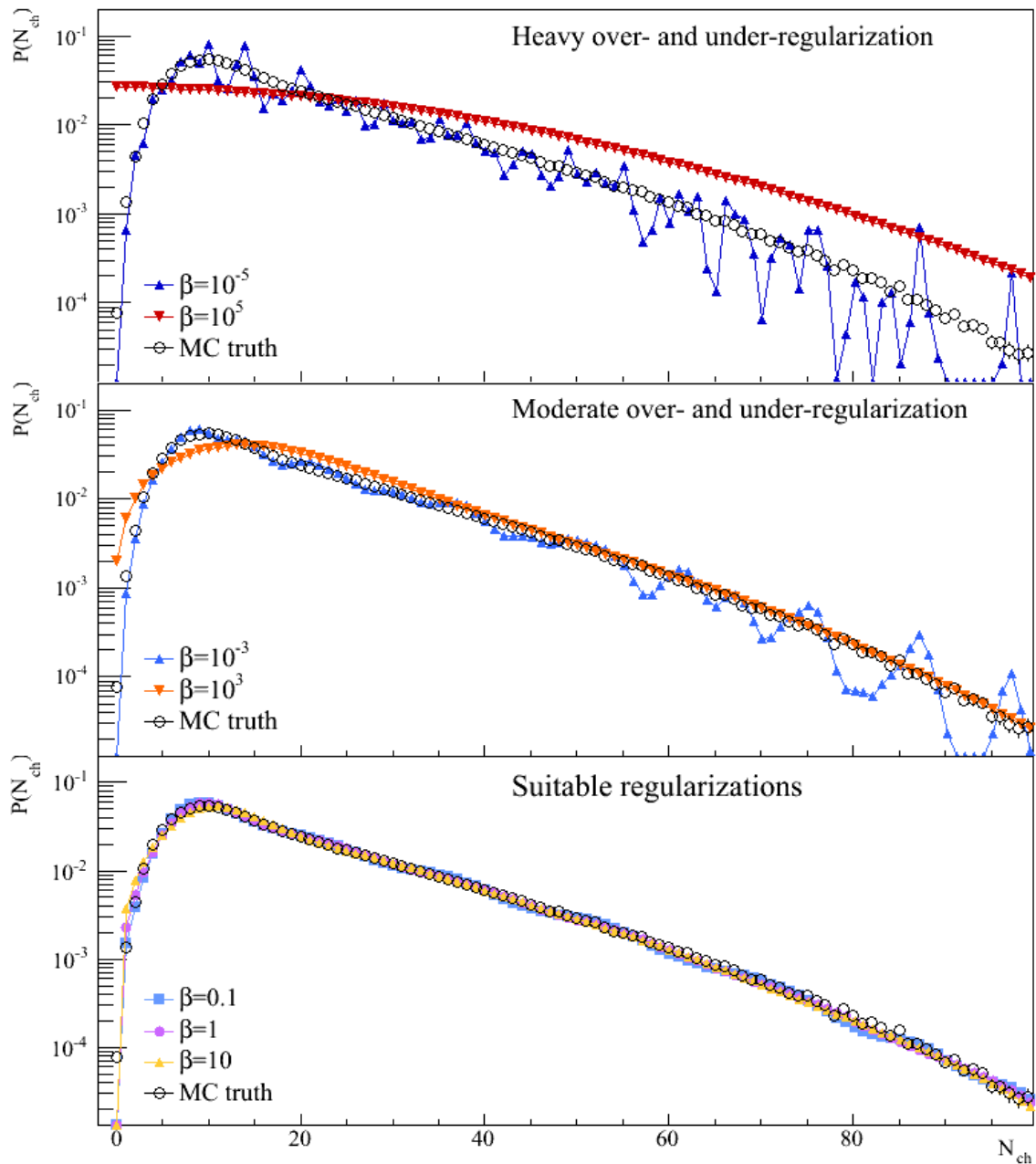


Figure 6.30: Example of the effects of the choice of regularisation weight. All unfoldings are done by using a *pol1* regularisation function. Top panel: Extreme  $\beta$  values yields either highly oscillating under-regularised solutions, or over-regularised solutions. Middle panel: Less extreme values of  $\beta$ . Still the solutions are over- and under-regularised. Bottom panel:  $\beta$  values that yields sensible regularisations. These are obviously the desired regularisation weights for this regularisation.

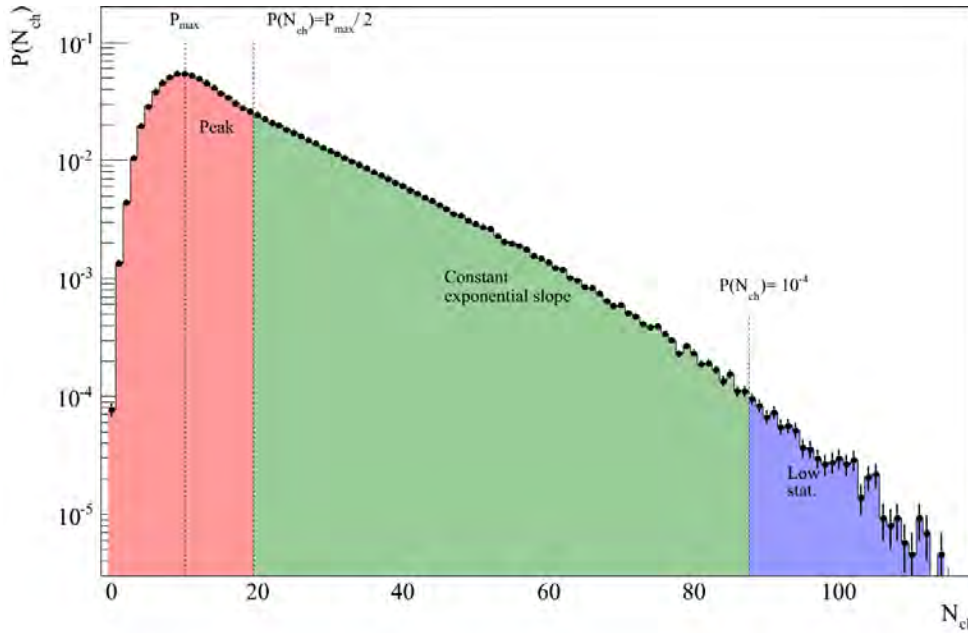


Figure 6.31: Illustration of the various characteristic regions of a multiplicity distribution. The quality of the unfoldings are assessed in each region independently. The criteria used for the boundaries between regions are indicated.

be wildly oscillating; if  $\beta$  is too large the solution will be measurement-independent, and the solution will just describe the choice of regularisation function. Oscillating solutions are said to be under-regularised, and solutions that are measurement independent are said to be over-regularised. These concepts are illustrated in figure 6.30, where a single simulated distribution is unfolded using a wide range of regularisation weights. The MC truth distribution is included for comparisons with the individual unfolding solutions.

### 6.6.3 Unfolding Quality Measure

Determining the success of the unfolding by visually comparing the unfolded distribution to the truth distribution is not enough. Therefore some way of quantifying the quality of the unfolding is needed.

We start by defining three characteristic regions of multiplicity distributions:

**The peak** This is the region where the multiplicity distribution rises, reach a maximum, and then starts decreasing again. Characteristics of the peak is that the slope of the distribution changes rapidly.

**Constant exponential slope** After the peak follows a region where the exponential slope of the distribution is fairly constant.

**Low statistics** At high multiplicities the data sample runs low in statistics. This is considered a region for itself, since the limited statistics could have a significant influence on the quality assessment of the constant slope region.

For each of these it is possible that a given unfolding would be more or less successful. Thus it makes sense to gauge the quality of the unfolding of each of these regions separately. In the ideal case the best choice of unfolding would be the same in each region, but this is not necessarily the case.

Where to exactly make the distinction between each region (especially when analysing various  $\eta$  intervals) is not predetermined. For this work the limits are chosen such that the constant exponential slope start when the distribution has fallen to 50% of the maximum value of the peak. Similarly the onset of the low statistics region is defined as when the probability of a given multiplicity falls below  $10^{-4}$ . Figure 6.31 illustrates the various regions. Variations of the limits between the regions have been tested. The conclusions presented in the following have been the same for these variations.

The quality of a given unfolding can be assessed by the following quality parameter:

$$Q_1 = \frac{1}{t_2 - t_1 + 1} \sum_{t=t_1}^{t_2} \left| \frac{T_t - U_t}{e_t} \right| \quad (6.20)$$

$T_t$  and  $U_t$  denote the value of the the  $t^{\text{th}}$  multiplicity bin of the truth and unfolded distributions respectively, and  $e_t$  is the error on  $U_t$ .

$Q_1$  is normalised to be independent of the region (going from  $t_1$  to  $t_2$ ) by the terms in front of the sum in (6.20). It was decided not to let the sum be in quadrature (like in in a traditional  $\chi^2$ ), in order to not give too much importance to possible massive single-bin deviations. Like for a traditional  $\chi^2$  the ideal unfolding should have a  $Q_1$  around unity. If  $Q_1$  is less than unity, the errors are overestimated. If it is above unity, it is not the perfect unfolding.

The best choice of unfolding can thus be decided upon, by examining  $Q_1$  of the various regions. The solution that globally best minimises  $Q_1$  is the best unfolding. The  $Q_1$  of the individual regions are additive, by weighting with the region sizes and renormalising. However, by keeping  $Q_1$  separated into regions, it is possible to put particular emphasis on a specific region. In one analysis, it might be crucial to retrieve the high multiplicity tails accurately, while in another analysis it might be the peak region, which is of most importance. Thus it is possible to fine-tune the unfolding parameters to fit each analysis.

To test the unfolding quality, simulated data is used. The following discussion is based on PHOJET simulations used as data distributions, with the flat PYTHIA simulations used for response matrices. Using normal PYTHIA simulations as data distributions have also been tested, and the conclusions are the same.

Figure 6.32 show  $Q_1$  for multiplicity distributions in  $|\eta| < 2.4$  using SVD unfolding with *pol0*, *pol1* and *log* regularisations for a wide range of regularisation weights. Included in the plot is also  $Q_1$  for the Bayesian unfolding method. Since it does not have any regularisation parameters it is represented as a horizontal line. Similar plots for a more narrow  $\eta$ -interval,  $|\eta| < 1.0$ , can be found in appendix E.

Evaluating figure 6.32 yield:

**Peak** For the peak region it is found that best SVD solution is *pol1* regularisation with  $\beta$  in the order of  $10^{-2} - 1$ . *pol0* and *log* has minimas in  $\beta$  around 1-10 and  $10^2 - 10^3$  respectively, but are not as good a solution as *pol1*. However, the best match for the peak region is the Bayesian unfolding, which has a lower  $Q_1$  than any SVD solution.

**Constant exponential slope** For the constant exponential slope region all three SVD regularisation functions does very well at various  $\beta$  values. The minima of the three SVD regularisations are for  $\beta$  around 10 (*pol0*), 10 (*pol1*) and  $10^5$  (*log*). The Bayesian unfolding is marginally worse than the three SVD solutions for this region.

**Low statistics** For the high multiplicity region the best of the SVD regularisations are *pol0* and *pol1* at  $\beta = 10^3$ . As in the case of the constant exponential region *log* is

continuously falling having its minimum at the high limit of the survey. Bayesian unfolding does equally well as *pol0* and *pol1* for this region.

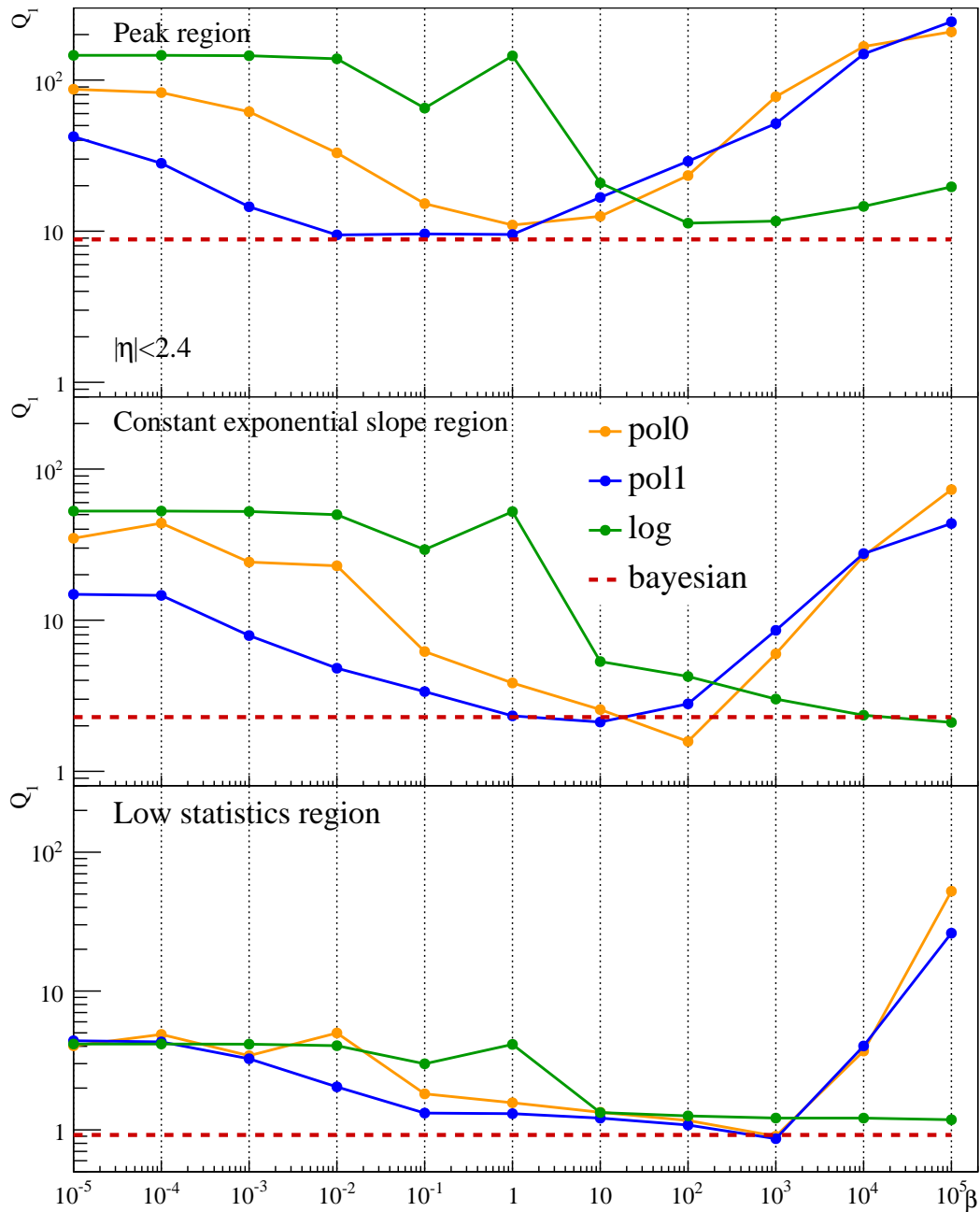


Figure 6.32: The unfolding quality parameter,  $Q_1$ , for the three distinct multiplicity distribution regions for  $|\eta| < 2.4$ . SVD unfolding with three regularisation functions are checked over a large range of  $\beta$  weight parameters. Included is also the Bayesian unfolding as the horizontal dashed red line. The Bayesian unfolding is found to be the best solution.

As discussed, the *log* regularisation is falling continuously in both the constant exponential and low statistics regions. However for the Peak, *log* regularisation rapidly becomes worse for very high  $\beta$ . Thus, even though the minima is perhaps not reached for the regions besides the peak, there is found no reason to expand the  $\beta$  range surveyed. This is due to

the peak region becoming worse and worse at higher regularisation weights, and thus the overall solution will never become the best.

Figure 6.33 shows a comparison of the best SVD and Bayesian unfolding for  $|\eta| < 2.4$ . Overall it is found that the Bayesian unfolding is the best solution for unfolding. Of the SVD regularisations it is found that *pol1* is the best choice with a  $\beta$  around 1. The next best choices for *pol1* are also included in figure 6.33. These illustrate an issue with the SVD method at broader  $\eta$ -intervals. Lowering the  $\beta$  value increases the accuracy of the very first bins. But doing so, causes oscillations in the higher multiplicities. This is not seen for the narrow  $\eta$ -intervals, the oscillations set in at lower  $\beta$ -values. Thus for the narrow  $\eta$ -intervals the SVD unfolding is a reasonable option, and has been used by ALICE previously [73, 74].

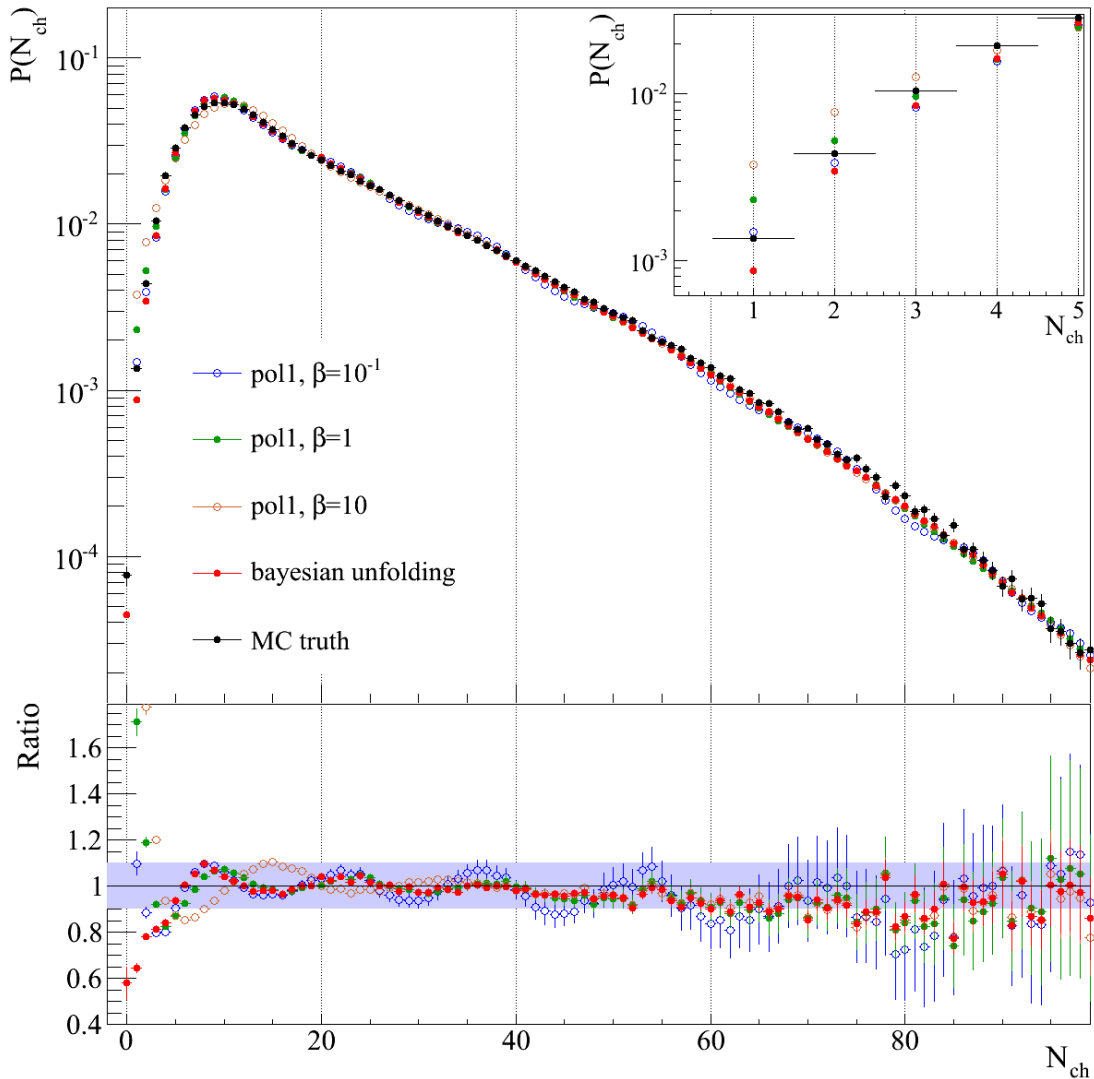


Figure 6.33: The best unfolding solutions for  $|\eta| < 2.4$ . It is found that Bayesian unfolding overall show best agreement with MC truth. SVD unfolding with *pol1* and  $\beta = 1$  is the best SVD solution. The insert show the very first multiplicity bins. It is found that  $\beta = 10^{-1}$  gives better agreement in the very low bins, but the oscillations start appearing at higher multiplicities. The lower panel show the ratio to MC truth for the various solutions. The oscillations of the under-regularised solutions are seen.

## 6.7 Trigger-Vertex Bias Correction

After unfolding the measured distributions, they need to be corrected for trigger and vertex inefficiency. This is referred to as the trigger–vertex bias correction.

At very low multiplicities, few particles hit the detectors, which makes reconstruction of a vertex increasingly difficult, and thus the vertex efficiency decreases. Similarly few particles makes it difficult for the trigger algorithms to recognise a given collision trigger.

The trigger–vertex bias correction is done by simulations, and is given by:

$$C = \frac{P(N_{ch,MCNSD})}{P(N_{ch,ESDNSD})} \quad (6.21)$$

The subscript MCNSD denote events that have a vertex between  $-4 < v_z < 4$ , and are NSD events according to the simulation truth. Similarly the subscript ESDNSD denote events, where a vertex is reconstructed within  $-4 < v_z < 4$ , and that are triggered as a NSD event in the analysis.

The correction for  $pp$  collisions at  $\sqrt{s} = 900$  GeV is shown in 6.34. As seen the main part of the correction is in the very low multiplicity region. A thing worth mentioning is that the correction becomes slightly less than unity in some range before ending at unity for higher multiplicities. This drop below unity is caused by the triggering algorithm misidentifying SD events as NSD events. This is not clearly visible in figure 6.34.

For the very broad  $\eta$ -intervals the limited statistics becomes an issue. This is due to the extremely low probability of having a triggered NSD event with a vertex but with no particles over 8 units of  $\eta$ . As an example, the first point ( $N_{ch} = 0$ ) of the  $-3.4 < \eta < 5.1$  curve in figure 6.34, stems from only 3 ESDNSD events, and 5400 MCNSD events out of the roughly 3 millions events of the simulation. This obviously means that there will be a huge error assigned to the correction (which is already very large) in this point. This error can in theory be reduced drastically by running over many times more simulated data. For this work, this has not been possible.

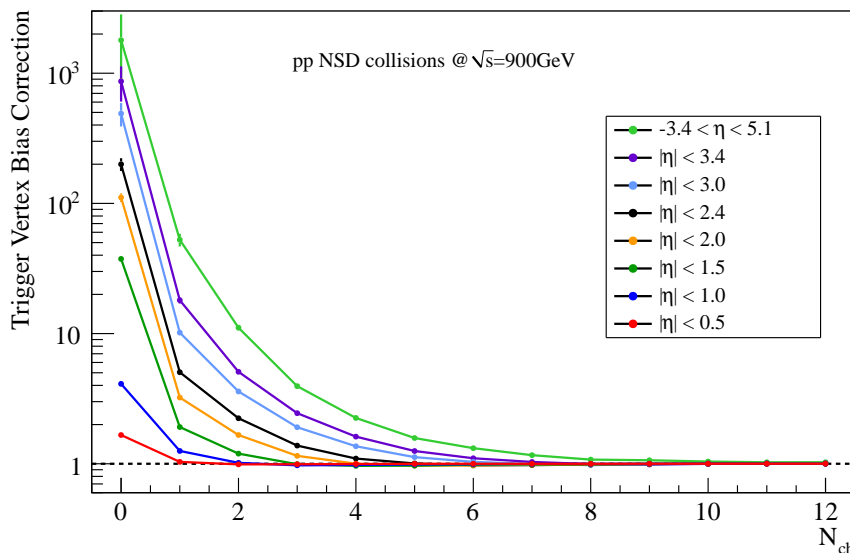


Figure 6.34: Trigger–Vertex bias correction factor for various  $\eta$ -intervals for  $pp$  NSD collisions at  $\sqrt{s} = 900$  GeV. It is seen that it only affects the very low multiplicity bins. For the broader  $\eta$ -intervals, the uncertainty on the correction becomes quite large for the first few multiplicity bins, due to lack of statistics.

## 6.8 Defining Analysis Parameters

This section is devoted to presenting some of the choices of analysis parameters, used for the final analysis results presented in chapter 8.

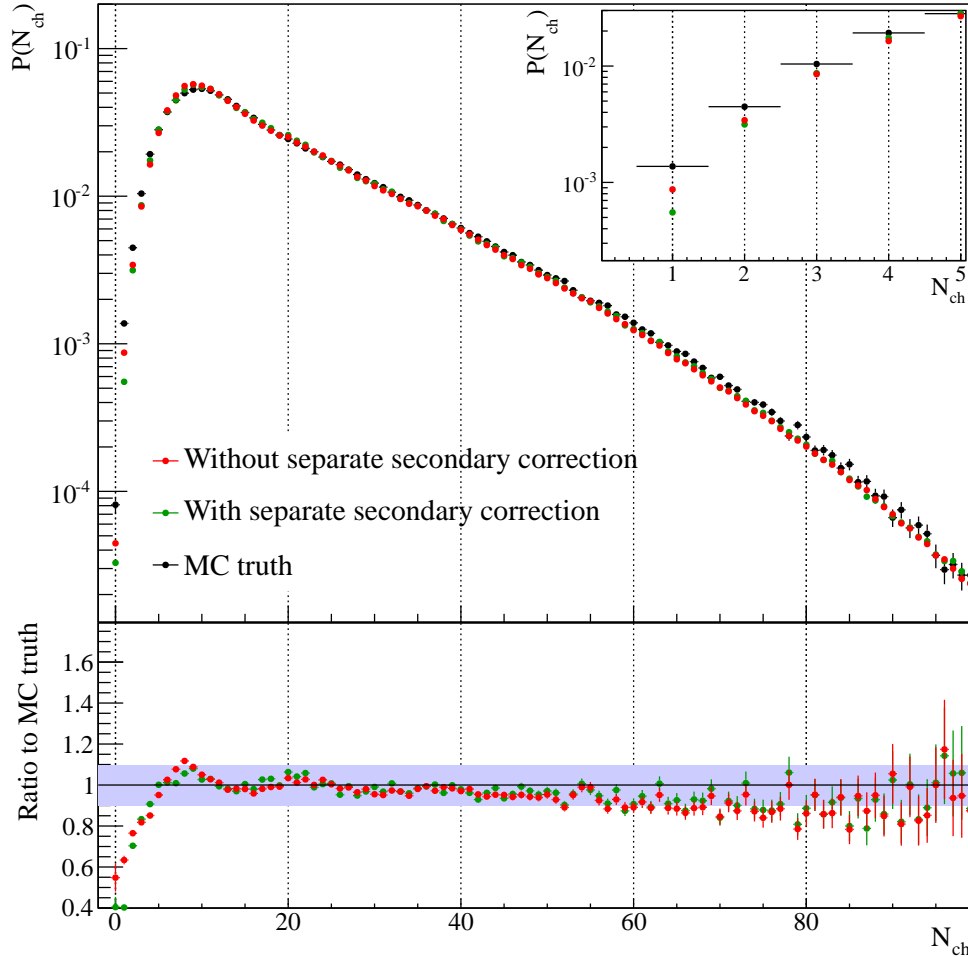


Figure 6.35: The analysis effect of letting the response matrix correct for secondary particle contamination, or having a separate statistical secondary correction. As can be seen there is no significant difference. The figure is from  $|\eta| < 2.4$  PHOJET simulations using flat multiplicity simulations for response matrices.

**Unfolding method** The first topic covered is the choice of unfolding method. This choice picks up the discussion from section 6.6.3. There it was found that overall the Bayesian unfolding is better than any of the regularisations of the SVD unfolding. Particularly it was found that for wide  $\eta$ -intervals, it is not possible for the best SVD regularisation, *pol1*, to obtain a great solution for the very low multiplicities, while avoiding the oscillating behaviour of a under-regularised solution at higher multiplicities. The best SVD solution thus overcounts at the very low multiplicities.

When this is coupled with the very high trigger–vertex bias correction factors at very low multiplicities for wide  $\eta$ -intervals, as well as the huge errors, it is clear that this pose a problem.

Correcting a unfolded distribution, that is already too high, with a factor in the order of  $10^3$ , having a relative error above 50%, obviously is not desirable. It can give complications

with the zero bin being much too high, when renormalising the multiplicity distribution, and thus pushing the overall distribution significantly downwards.

The Bayesian unfolding does a better job at the zero bin, and thus is not as affected by this. However also in this case, one should keep the massive uncertainty of the first bin in mind.

Thus the choice is made to use the Bayesian unfolding method. The performance of the SVD unfolding will be used to estimate the uncertainty on the results due to the unfolding. This is discussed in the next chapter.

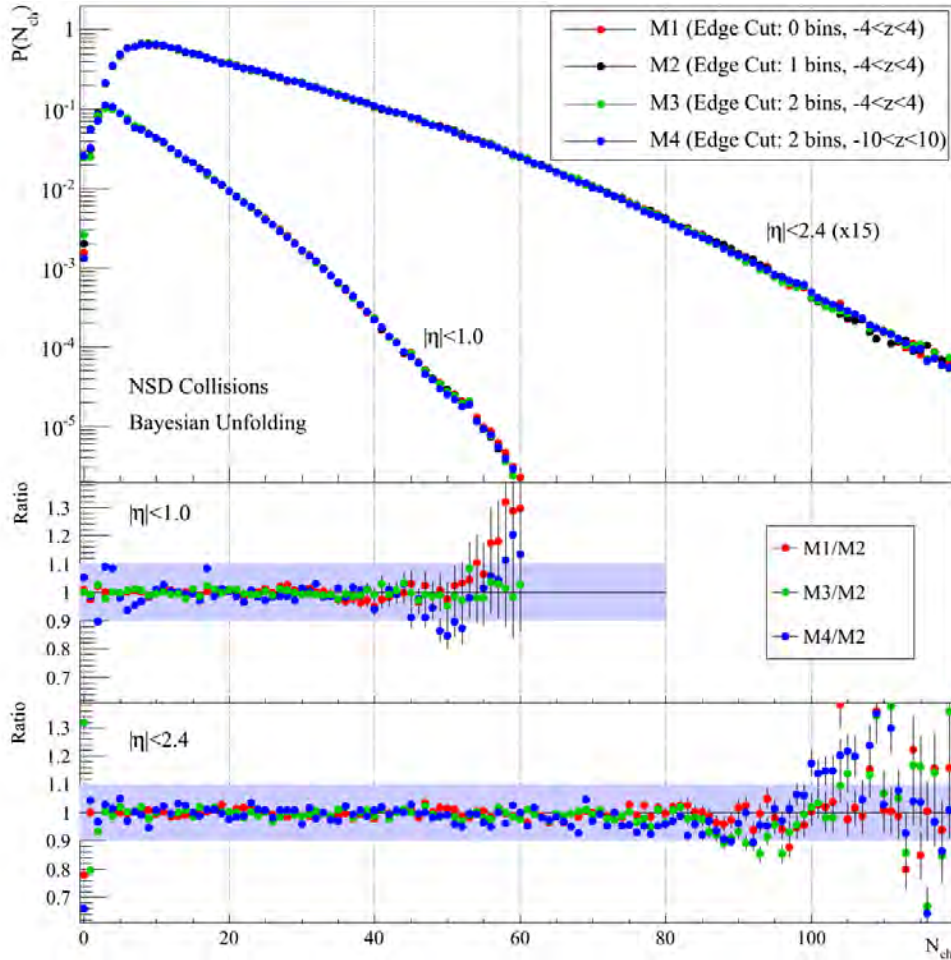


Figure 6.36: Comparisons of the analysis effect of changing the amount of acceptance gaps allowed. It is decided to use the setting, where a single edge bin in each FMD ring and the SPD is but away.

**Secondary particle contamination** The next test presented revolves around using the correction maps for secondary particle correction as described in section 6.4, or letting the unfolding handle it. The result is shown in 6.35.

It is found that it makes very little difference which approach is used. At the very low multiplicities, letting the unfolding handle the secondary contamination is closer to the simulation truth, whereas the multiplicity tail show very slightly better agreement for the separate secondary correction approach.

For the analysis, it is decided to use the method of removing the secondaries as part of the unfolding in  $pp$  collisions.

For  $PbPb$  collisions the separate secondary correction is used, due to the very high multiplicities of very central collisions. Including secondary particles, a very central collisions can create more than 30000 particles in the detector acceptance, which means the response matrix would be at least  $30000 \times 30000$ , and thus computer intensive.

**Acceptance gaps** For the remainder of this section the focus is on some of the tests performed on physics data to see the differences in the unfolded multiplicity distributions depending on various choices of parameters. Common for the plots is that they show multiplicity distributions for a narrow central  $\eta$ -interval ( $|\eta| < 1.0$ ) and a wider  $\eta$ -interval ( $|\eta| < 2.4$ ).

Figure 6.36 shows the result of changing the size of the acceptance gaps in the FMD/SPD system. This is tested by removing 0,1 or 2  $\eta$ -bins on the edges of each FMD ring in separate analyses. Furthermore another test is run where the chosen vertex- $z$  range is  $-10 < v_z < 10$ , and 2 bins are cut away. Of the four setting it is the one with clearly the biggest acceptance gaps.

Included in figure 6.36 is the ratio of the settings to the chosen setting (1 bin cut away,  $-4 < v_z < 4$ ). It is found that for the setting where the vertex range is enlarged point to point oscillations occur compared to the others. For the three remaining settings little variation is found.

**Response matrix event generator** Now we turn to looking at the generator used for the response matrix. There are three possibilities in ALICE as discussed in section 5.6: PYTHIA, PHOJET and the special flat multiplicity PYTHIA productions. The results are shown in figure 6.37. Each of the test simulations are run as anchored in run 118506, such that the number of events are comparable. It is clearly seen that using the flat multiplicity runs as response matrix greatly enhances the multiplicity range (for a limited number of events). Overall there is good agreement between all three in the range where all three has adequate statistics. In the very low multiplicities deviations are seen. There, the ratios differ significantly. However, since the distribution is very steeply rising in that region, a small uncertainty in the particle multiplicity (x-axis) will translate into a very big difference in the probability (y-axis).

**Vertex range** Next test elaborate on the selection of vertex range. Figure 6.38 show the unfolded multiplicity distributions using four different vertex selections. The selections are:

- $-10 < v_z < -4$  and  $4 < v_z < 10$ , which both has big acceptance gaps between the FMD and SPD.
- $-4 < v_z < 4$ , which is the chosen vertex selection which has no acceptance gap between the FMD and SPD.
- $-10 < v_z < 10$ . This setting contains the previous three settings.

It is found that the vertex selections with big acceptance gaps between the FMD and SPD causes the results to oscillate. For the combined setting oscillations are still present, but to a smaller degree. This is a consequence of combining regions with big acceptance gaps ( $-10 < v_z < -4$  and  $4 < v_z < 10$ ), with a region of almost no gaps ( $-4 < v_z < 4$ ), thereby lowering the relative amount of gaps over the entire range. From figure 6.38 it is clear that the best choice for analysis is to use events inside  $-4 < v_z < 4$ .

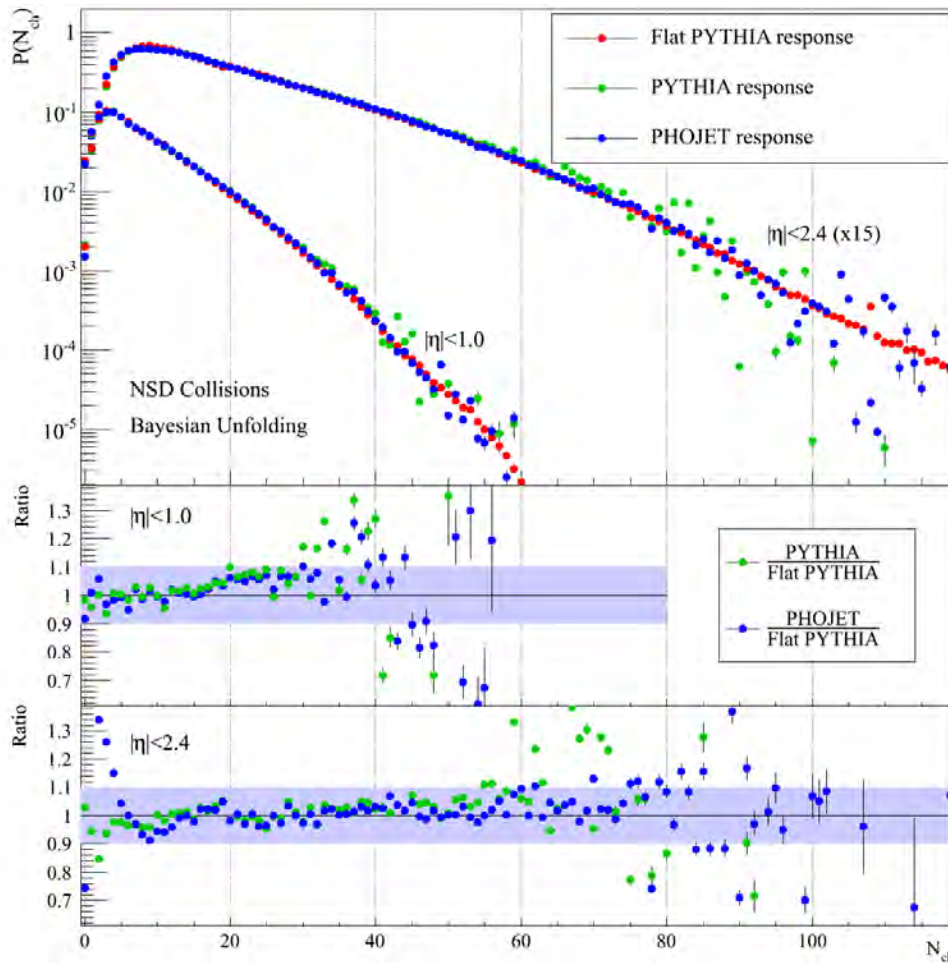


Figure 6.37: Effect on the analysis of changing the event generator used for the response matrix. Each sample is run over the same amount of events. It is found that the flat PYTHIA production has a far superior multiplicity range.

**Summary of parameter choices** To summarise, in this section the best analysis parameters have been determined. Thus the final analysis is done for events in the range  $-4 < v_z < 4$  cm, where we cut away the first edge bin of the  $\eta$ -acceptance for both FMD rings, and the SPD. Furthermore it has been illustrated that the flat multiplicity distributions are best suited as the input for the response matrices. It is also found that letting the response matrices deal with the secondary particle contamination or performing the statistical secondary correction makes little difference. For  $pp$  the former approach is used, where as the latter is used for  $PbPb$  collisions.

For unfolding method the Bayesian method yield better agreement to simulated truth, and is therefore used.

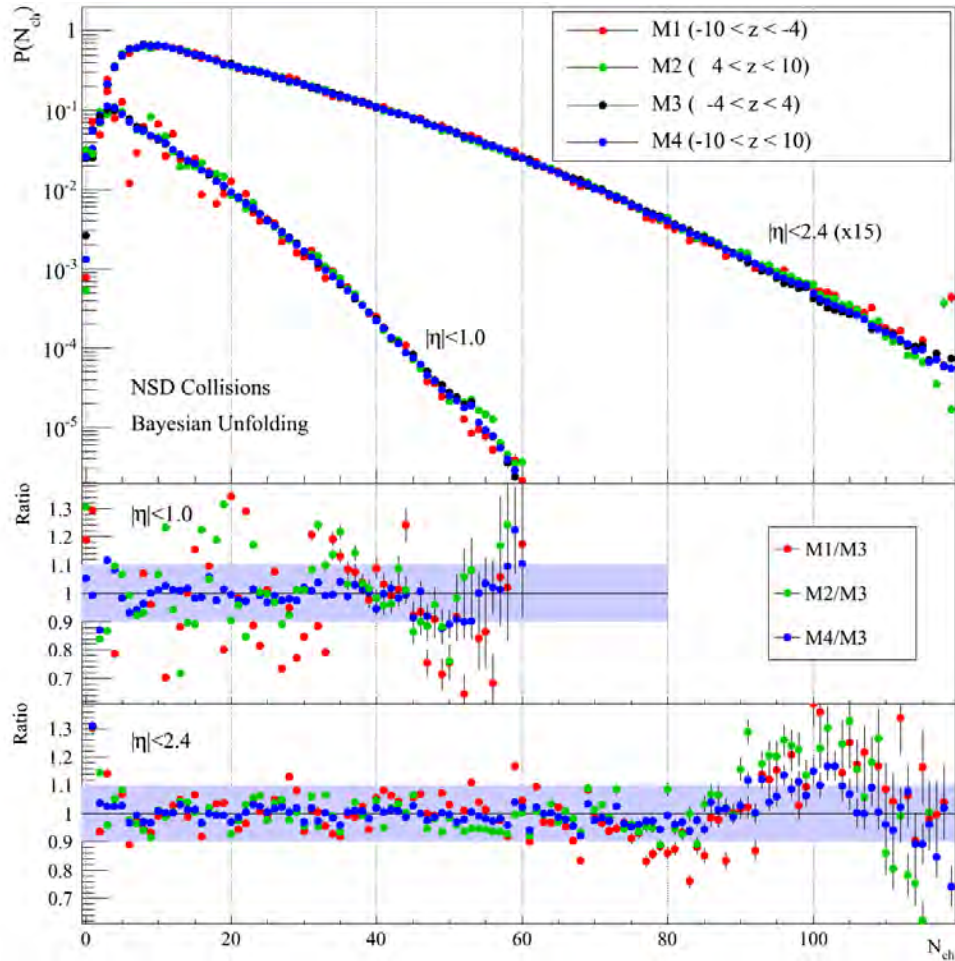


Figure 6.38: Comparisons of the analysis effect when using different  $z$ -vertex ranges. The setting with the minimum acceptance gaps ( $-4 < v_z < 4$ ) is chosen.



# Chapter 7

## Systematic Errors

This chapter is devoted to the treatment of systematic errors for multiplicity distributions. The systematic errors are composed of three parts; the systematic error on the number of measured particles in a given event, a contribution from the trigger–vertex bias correction, as well as a contribution from the choice of unfolding method.

### 7.1 Uncertainty on event multiplicity

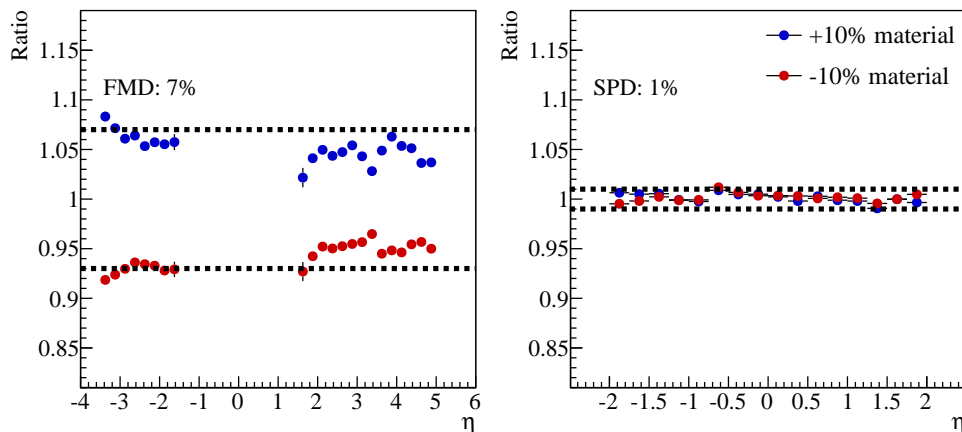


Figure 7.1: Effect of scaling the material density of all of ALICE up and down by 10%. The left panel shows the ratio of the changed material simulations to the reference simulations. The change in material yields a 7% difference. The right panel shows the same for the SPD. The effect of adding and removing material is only around 1%.

The following effects are considered for determining the systematic error on the event multiplicity.

**Material budget** The accuracy of the description of the material budget is by far the biggest contribution to the systematic error in the FMD, and also constitute a significant part for the SPD. The accuracy of the material description directly effect the response matrix, and thus the unfolded solution.

The systematic error from the material budget is estimated by using special simulations, where the material density of every single component in ALICE is scaled up and down by 10%. These special runs are then compared to a reference simulation.

For the FMD this yields an estimate of the systematic error of  $\sim 7\%$  on the measured multiplicity. Since the amount of material in front of the SPD is much less, the effect is smaller there. The estimate of the systematic error in the SPD is  $\sim 2\%$ . For both detectors the estimate can be seen in figure 7.1.

While it is quite unlikely that there are global inaccuracies in the material description of this magnitude, it could however occur locally. This might especially be true in forward regions, which do not only house the forward detectors. The service structures of the central barrel detectors are also located in this region. These include large amounts of bundled cables, which can not be modelled individually, but instead are modelled as effective volumes.

Section 8.5 will discuss how to determine how accurate the current description is.

**Event generator** The implemented physics of different input generators leads to differences in the production of secondary particles, and thus yields a systematic uncertainty. This contribution is estimated by testing PHOJET and PYTHIA, and using the ratio of secondary particles produced as the uncertainty estimate. The effect amounts to  $\sim 2\%$  in both the FMD and SPD. Illustrations of this are shown in figures 7.2 and 7.3 for the FMD and SPD respectively.

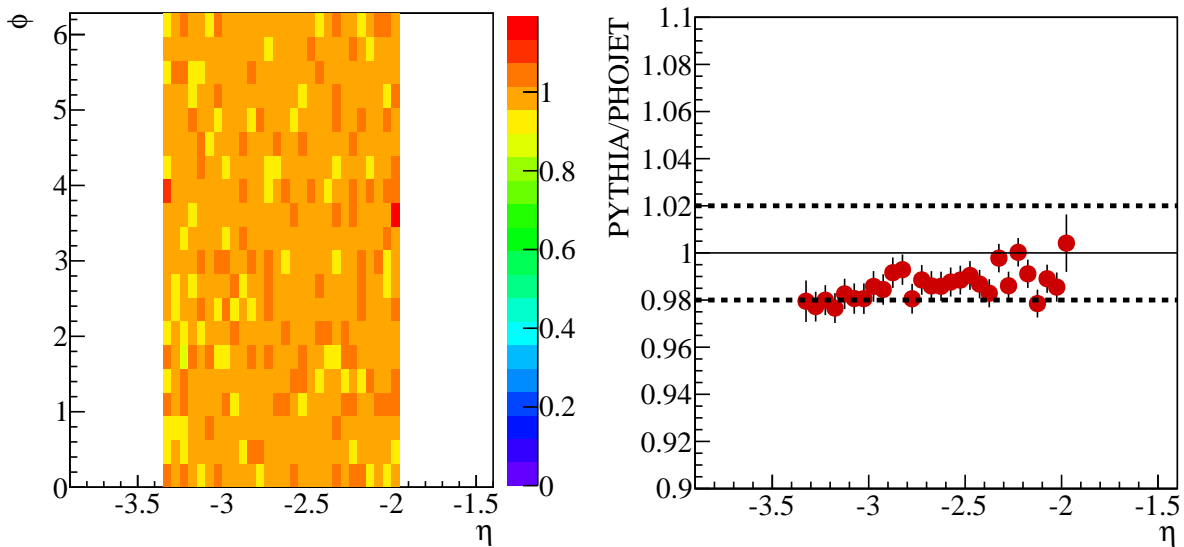


Figure 7.2: Effect of the choice of event generator in FMD3I. The left panel shows PYTHIA/PHOJET ratio as a function of  $(\eta, \phi)$ . The right panel shows the projection onto the  $\eta$ -axis. The choice of event generator yields a 2% difference.

**Strangeness Correction** The strangeness correction is not well determined as described in section 6.5. Thus it was decided to impose a large systematic uncertainty of 2% (= 100% relative error) to it for both the SPD and FMD.

**Sharing cuts** Variation of  $E_{hit}$  and  $E_{high}$ , discussed in section 6.2.2, yields a  $\sim 2\%$  uncertainty in PbPb collisions, and  $\sim 3\%$  in pp collisions. Concretely, this estimate is gotten by changing  $E_{high}$  and  $E_{hit}$  up and down with  $0.1E_{MPV}$ , and comparing the results to the reference analysis. This systematic effect only applies to the FMD analysis.

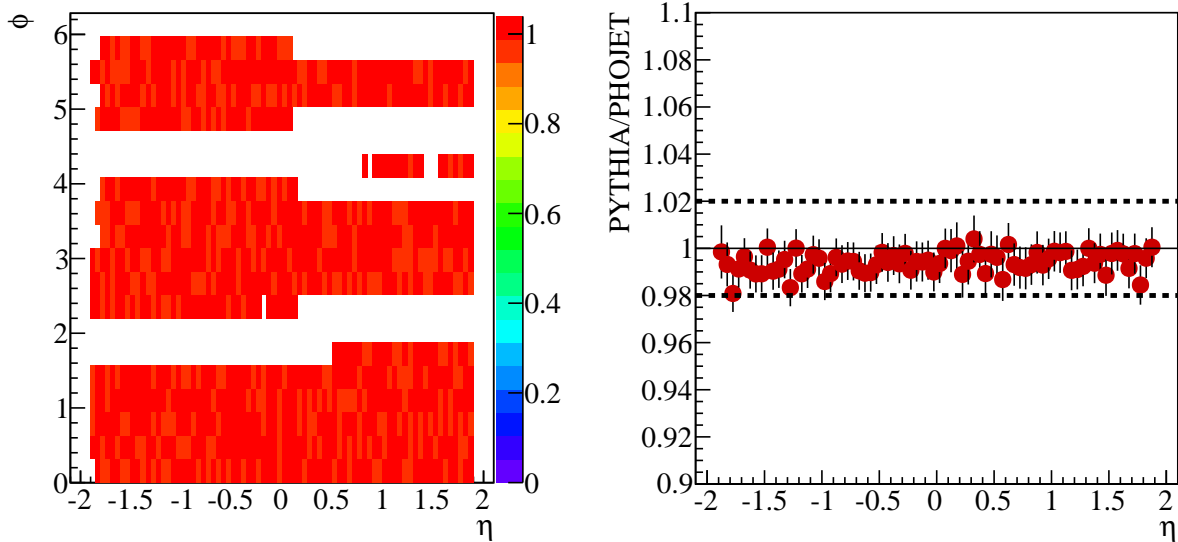


Figure 7.3: Effect of the choice of event generator in the SPD. The left panel shows PYTHIA/PHOJET ratio as a function of  $(\eta, \phi)$ . The right panel shows the projection onto the  $\eta$ -axis. The choice of event generator yields a 2% difference.

**Counting methods** Two counting methods have been tested, the Poisson method, and the Energy Fits method. The uncertainty on the event multiplicity due to the choice of counting method is estimated to be  $\sim 4\%$  for  $pp$  collisions and  $\sim 2\%$  for  $PbPb$  collisions [87].

**Centrality** There is an uncertainty on the centrality determination. This yields a systematic uncertainty on the event multiplicity from  $< 1\%$  in the most central collisions (0-5%) up to  $\sim 6\%$  for peripheral collisions (70-80%) [130].

The individual contributions are added in quadrature, yielding the total systematic uncertainty on the number of charged particles in each of the detectors. Table 7.1 summarises this information for both  $pp$  and  $PbPb$  collisions.

	$pp$ coll.		$PbPb$ coll.	
	FMD	SPD	FMD	SPD
	$\delta_{FMD}$	$\delta_{SPD}$	$\delta_{FMD}$	$\delta_{SPD}$
$E_{hit}$ and $E_{high}$ variation	3%	N/A	2%	N/A
Material budget variation	7%	1%	7%	1%
Event Generator	2%	2%	2%	2%
Strangeness Correction	2%	2%	2%	2%
Counting Method	4%	N/A	2%	N/A
Centrality	N/A	N/A	1 - 6%	1 - 6%
Total	9.1%	3%	8.1 - 10.0%	3.2 - 6.7%

Table 7.1: Systematic uncertainties on the number of charged particles measured in the FMD and SPD in  $pp$  and  $PbPb$  collisions.

Depending on which  $\eta$ -interval is analysed different fractions of the measurements are performed by either sub-detector. Thus the total systematic error on the event multiplicity

Range	Systematic Error ( $\delta_{mult}$ )	
	<i>pp coll.</i>	<i>PbPb coll.</i>
-0.5 < $\eta$ < 0.5	3.0%	3.2 - 6.7%
-1.0 < $\eta$ < 1.0	3.0%	3.2 - 6.7%
-1.5 < $\eta$ < 1.5	3.0%	3.2 - 6.7%
-2.0 < $\eta$ < 2.0	3.9%	3.9 - 7.1%
-2.4 < $\eta$ < 2.4	5.1%	4.8 - 7.6%
-3.0 < $\eta$ < 3.0	6.1%	5.6 - 8.1%
-3.4 < $\eta$ < 3.4	6.5%	5.9 - 8.4%
-3.4 < $\eta$ < 5.1	7.0%	6.4 - 8.7%

Table 7.2: Overview of the systematic error on the event multiplicity in the different  $\eta$ -intervals. The line denote the change from SPD-only  $\eta$  – intervals to combined SPD and FMD  $\eta$ -intervals.

must reflect this.

This is done by weighting the systematic error for each of the sub-detectors by the fraction in  $\eta$  covered by that detector in the specific measurement. Three areas are considered: the FMD only region, the SPD only region and the region of overlap between the two sub-detectors. Each region gets the weights

$$\begin{aligned}
\alpha_{FMD} &= \frac{N_{bins,FMD}}{N_{bins}} \\
\alpha_{SPD} &= \frac{N_{bins,SPD}}{N_{bins}} \\
\alpha_{overlap} &= \frac{N_{bins,overlaps}}{N_{bins}}
\end{aligned} \tag{7.1}$$

The overlap region is treated as if half of it is governed by the FMD error, and the other half by the SPD error.

Thus the total systematic error is given by:

$$\delta_{mult}^2 = \alpha_{FMD}\delta_{FMD}^2 + \alpha_{SPD}\delta_{SPD}^2 + 0.5\alpha_{overlap}(\delta_{FMD}^2 + \delta_{SPD}^2) \tag{7.2}$$

where by definition

$$\alpha_{FMD} + \alpha_{SPD} + \alpha_{overlap} = 1 \tag{7.3}$$

The total systematic error on the event multiplicity are summarised in table 7.2, for the  $\eta$ -intervals used for analysis.

The error on the event multiplicity corresponds to an error on the x-axis of the multiplicity distribution. This is translated into an error on the y-axis, by doing the following.

- The measured distribution is scaled up and down with the systematic error,  $\delta_{mult}$ .
- The up and down scaled distributions are unfolded using the response matrix used for the data distribution<sup>25</sup>
- The resulting distributions are used as the error boundaries i.e., the lower limit is evaluated as the minimum of the two distributions, and similarly the upper limit is given by the maximum of the two distributions.

<sup>25</sup>An alternative test has been performed, where instead the same data distribution has been unfolded with different (scaled) response matrices. The results of the two methods are consistent.

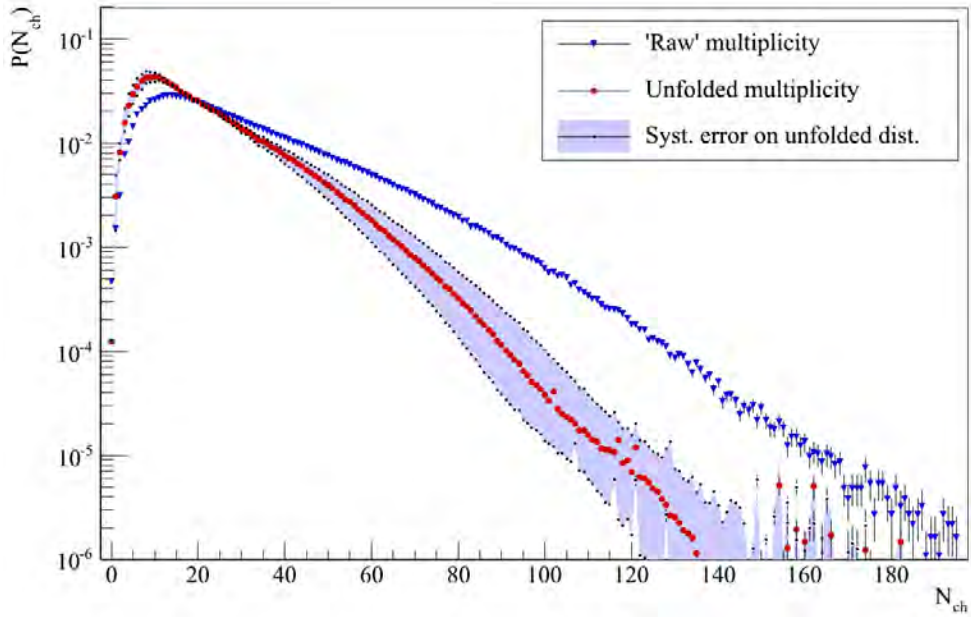


Figure 7.4: Example of the systematic uncertainty on the event multiplicity for  $|\eta| < 2.4$  in  $\sqrt{s} = 900$  GeV collisions. The raw multiplicity distribution is unfolded by the detector response, yielding the unfolded distribution. The systematic error bands are estimated by scaling the raw distribution upwards and downwards with the uncertainty on counting particles, and then unfolding these distributions with the same response matrix.

- The errors are now translated to the y-axis, yielding a band around the unfolded distribution.

## 7.2 Uncertainty on trigger–vertex bias correction and unfolding method

Besides the uncertainty on event multiplicity, error contributions from both the trigger bias vertex correction and unfolding method has to be taken into account. Both are treated in this section.

We start by considering the trigger–vertex bias correction. As discussed in section 6.7, the trigger–vertex bias correction require a large amount of statistics, especially for the broadest  $\eta$ -intervals. Thus any error assigned to it, can be decreased by having a larger simulated sample.

The systematic uncertainty on the correction is given by:

$$\delta_{bias}^2 = \epsilon_{MCNSD}^2 + \epsilon_{ESDNSD}^2 \quad (7.4)$$

$\epsilon_{MCNSD}$  is the error on the number of events labelled NSD by the simulation, and  $\epsilon_{ESDNSD}$  is similarly the number of events found by the analysis as NSD events. These errors are given as  $\epsilon_x = 1/\sqrt{N_x}$ , where  $x$  is either MCNSD or ESDNSD.

Thus (7.4) reduces to:

$$\delta_{bias} = \sqrt{\frac{1}{N_{MCNSD}} + \frac{1}{N_{ESDNSD}}} \quad (7.5)$$

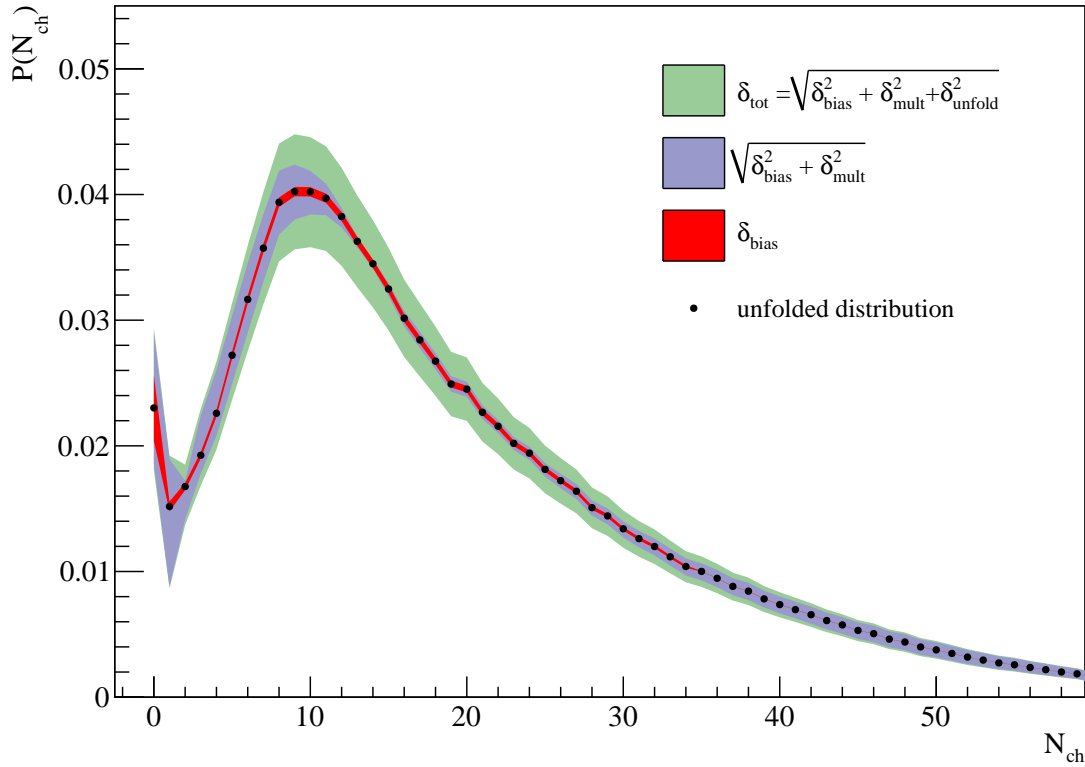


Figure 7.5: Example of the various contributions to the systematic uncertainty for  $|\eta| < 2.4$  in  $\sqrt{s} = 900$  GeV collisions.  $\delta_{bias}$  includes the statistical error added in quadrature with trigger–vertex bias uncertainty. For clarity the distribution is shown on a linear scale, and the tail is not shown. In the tail region the total uncertainty is fully dominated by  $\delta_{mult}$ .

The error contribution from the trigger–vertex bias correction is only significant in the very lowest multiplicity bins.

The last contribution is from the unfolding method itself. Figure 6.33 presented the best unfolding solutions for both the Bayesian method and the SVD method. In that figure it was found that there was generally good agreement between the unfoldings and the simulated truth. Over the entire multiplicity range it is estimated that the deviations from simulated truth are of the order of 10 %. This will be used as a systematic uncertainty of the unfolding method,  $\delta_{unfold}$ .

The systematic uncertainty of the hit merging i.e., the variation of  $E_{high}$  and  $E_{hit}$  could be a component in both  $\delta_{mult}$  as well as  $\delta_{unfold}$ . How much it factors into  $\delta_{unfold}$  is not known.

However in comparison to some of the other errors its contribution is not dominant, and thus it has little effect on the final error. Therefore it is assumed that it does not factor into  $\delta_{unfold}$ .

## 7.3 Total systematic error

The total systematic uncertainty is thus constructed by adding the three contributions in quadrature bin-by-bin:

$$\delta_{tot}^2 = \delta_{unfold}^2 + \delta_{bias}^2 + \delta_{mult}^2 \quad (7.6)$$

In figure 7.5 an example of the total systematic uncertainty is shown.

For  $PbPb$  collisions the uncertainties become much simpler, since trigger and vertex efficiency is unity [87]. Furthermore, as discussed in the previous chapter,  $PbPb$  collisions are not unfolded. Thus the only systematic uncertainty is given by the event multiplicity uncertainty,  $\delta_{tot} = \delta_{mult}$ .



# Chapter 8

## Results

In this chapter the results of this thesis are presented. The chapter is divided into four sections: Multiplicity distribution results, KNO scaling results,  $\frac{dN_{ch}}{d\eta}$  results, and mean multiplicity energy dependence results. The first three have separate subsections for  $pp$  and  $PbPb$  collisions, whereas the fourth section treats them simultaneously.

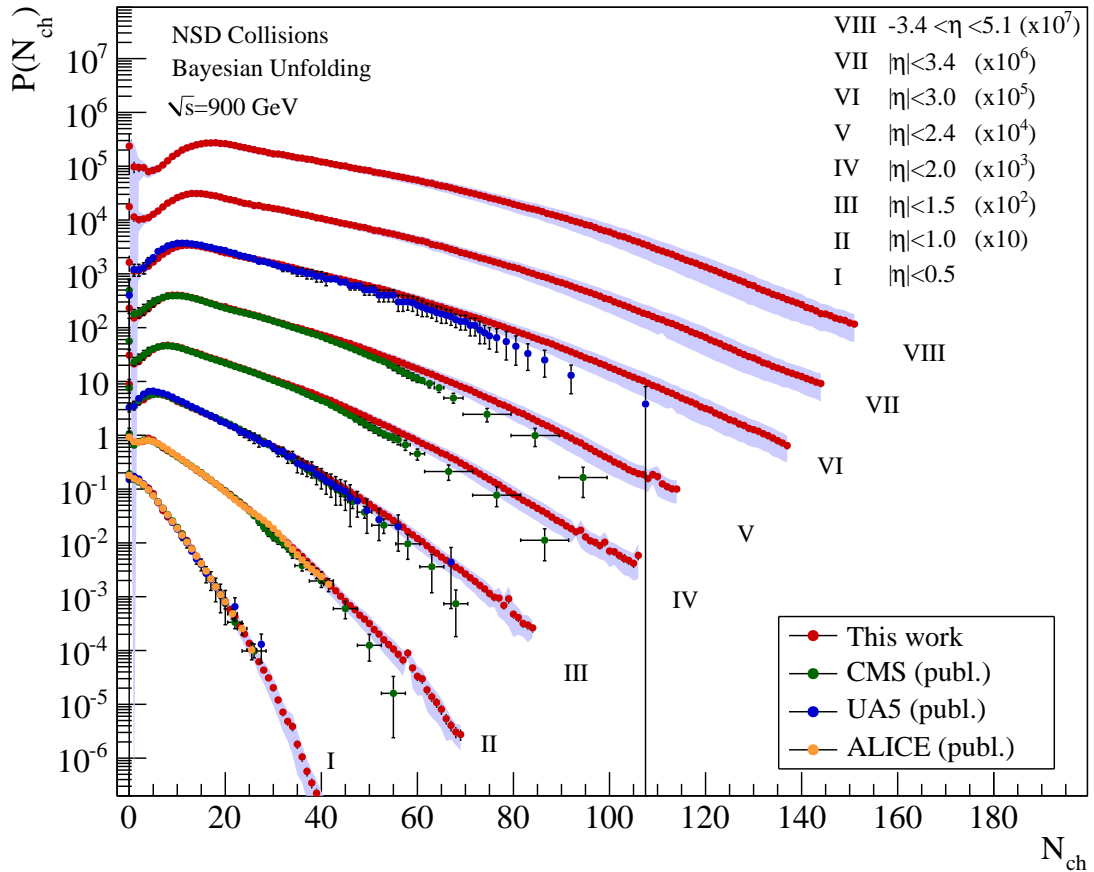


Figure 8.1: Charged particle multiplicity distributions for NSD  $pp$  collisions at  $\sqrt{s} = 900$  GeV. Included in the plot are previously published results from CMS, UA5 and ALICE.

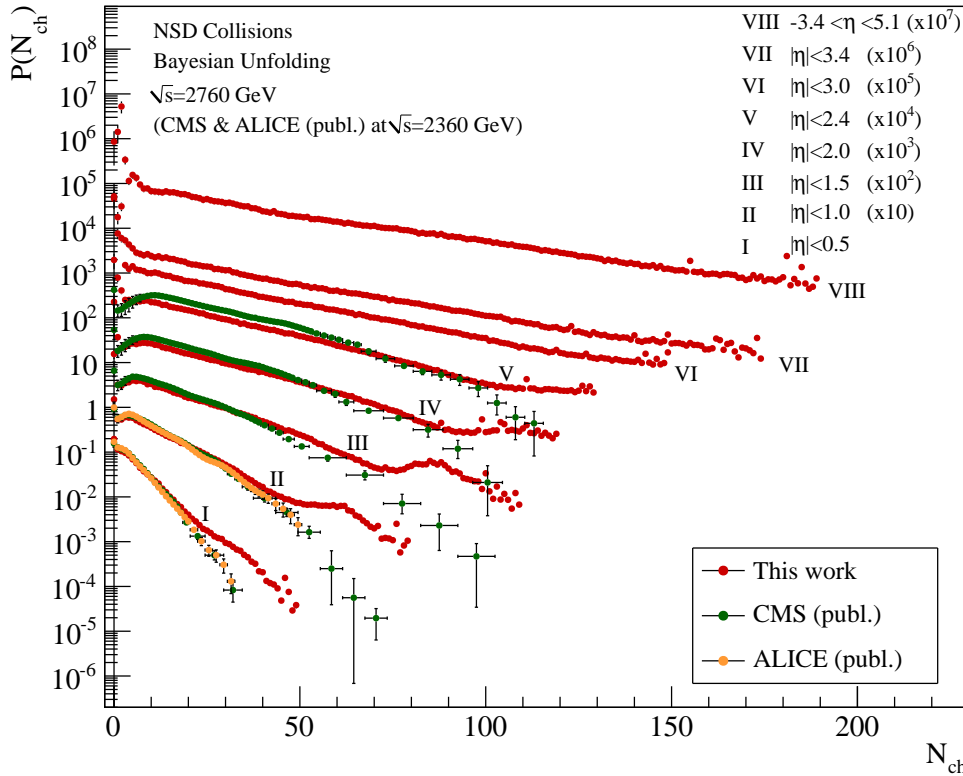


Figure 8.2: Charged particle multiplicity distributions for NSD  $pp$  collisions at  $\sqrt{s} = 2760$  GeV. As discussed in the text there are clear indications that the data quality of this run period is bad.

## 8.1 Multiplicity Distributions

### 8.1.1 $pp$ collisions

The first results presented in this section are considered the main measurement of this work, namely the multiplicity distributions for  $pp$  NSD collisions at the available energies. Figures 8.1, 8.2 and 8.3 show these at the three energies  $\sqrt{s} = 900$  GeV, 2760 GeV and 7000 GeV respectively.

For both  $\sqrt{s} = 900$  GeV and 7000 GeV it is found that there are good agreement between the results in this analysis, and the published results from other experiments. This is particularly true for the more narrow  $\eta$ -intervals. For the very broad intervals the tails are systematically higher in this analysis, compared to CMS and UA5. However they are still consistent within the uncertainties. The cause of this systematic deviation is currently unknown, but a likely explanation is that the implementation of the geometry in the forward region is not accurate enough, as described in section 6.4.

The published ALICE results are made using SPD tracklets, which restricts that analysis to the very central region. One of the ambitions of this work is to expand the already existing ALICE measurements.

It is found that the collisions at  $\sqrt{s} = 2760$  GeV has serious problems. The bump at very high multiplicities is clearly unphysical. It is present already in the raw multiplicity distributions. It is not present in simulations, and thus the unfolding can not handle it.

It is the culmination of the trend seen from various of the plots in the analysis chapter, where the  $\sqrt{s} = 2760$  GeV behaves abnormally. All seems to indicate that these data are heavily polluted, compared to the other energies, with some form of background signals.

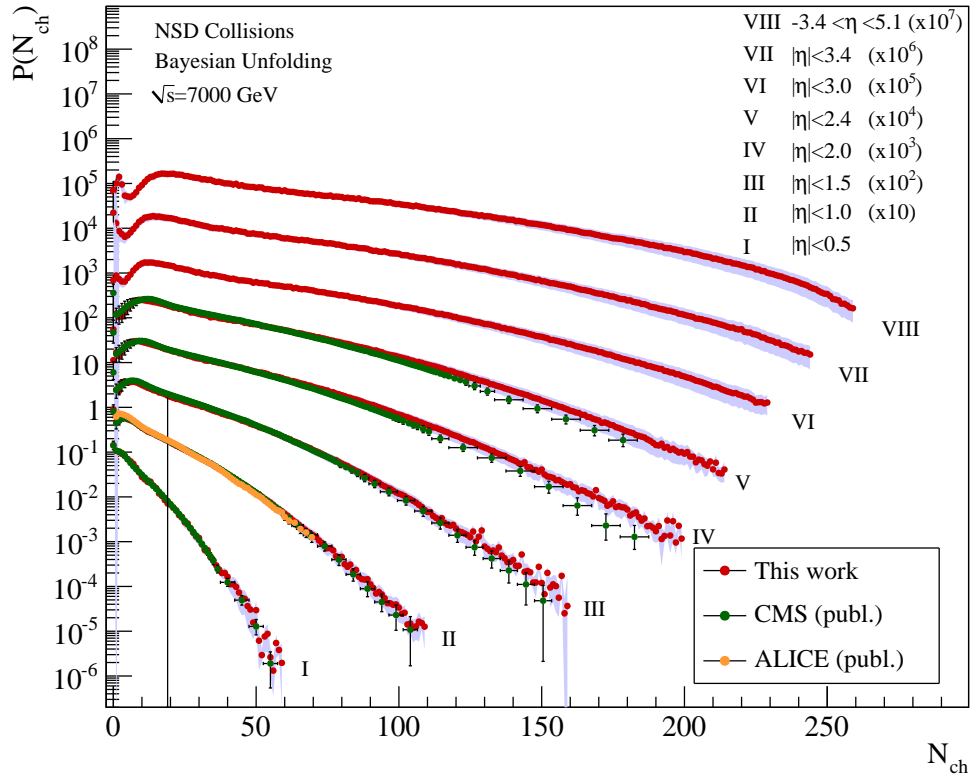


Figure 8.3: Charged particle multiplicity distributions for NSD  $pp$  collisions at  $\sqrt{s} = 7000$  GeV. Included in the plot are previously published results from CMS and ALICE.

The data at  $\sqrt{s} = 2760$  GeV is recorded in 2011, compared to the other energies, which were recorded in 2010. There are other indications that both the FMD in particular and ALICE in general might have problems with the data quality in the latter run periods<sup>26</sup>.

While the results for  $\sqrt{s} = 2760$  GeV are presented here alongside the results for the other two energies, they will not be used further in derived results. Understanding and hopefully improving the data quality for  $\sqrt{s} = 2760$  GeV is a high priority issue in the coming time.

While figures like 8.1, 8.2 and 8.3 are good for an overview, they are not very useful for detailed comparison. Figures 8.4 and 8.5 show two examples of detailed comparisons between the individual measurements for  $|\eta| < 0.5$  at  $\sqrt{s} = 900$  GeV and for  $|\eta| < 1.0$  at  $\sqrt{s} = 7000$  GeV. In appendix F the comparisons for the remaining multiplicity distributions can be found.

In both figures good agreement between measurements of this work and the previously published values is found. For the  $\sqrt{s} = 7000$  GeV comparison it is found that there is better agreement with the CMS measurement than with the ALICE measurement. This is attributed to the fact that the CMS measurements also use the Bayesian unfolding method, whereas the published ALICE measurements use the SVD method.

<sup>26</sup>This seem to be a problem which has gotten progressively worse over time. On a ALICE level it has gotten so bad, that ALICE currently does not start taking data immediately when the LHC declare stable beams. Instead they wait until the background levels are tolerable. This is a new practise, and was not implemented during the  $\sqrt{s} = 2760$  GeV runs. The cause and precise extent of the background is not fully understood.

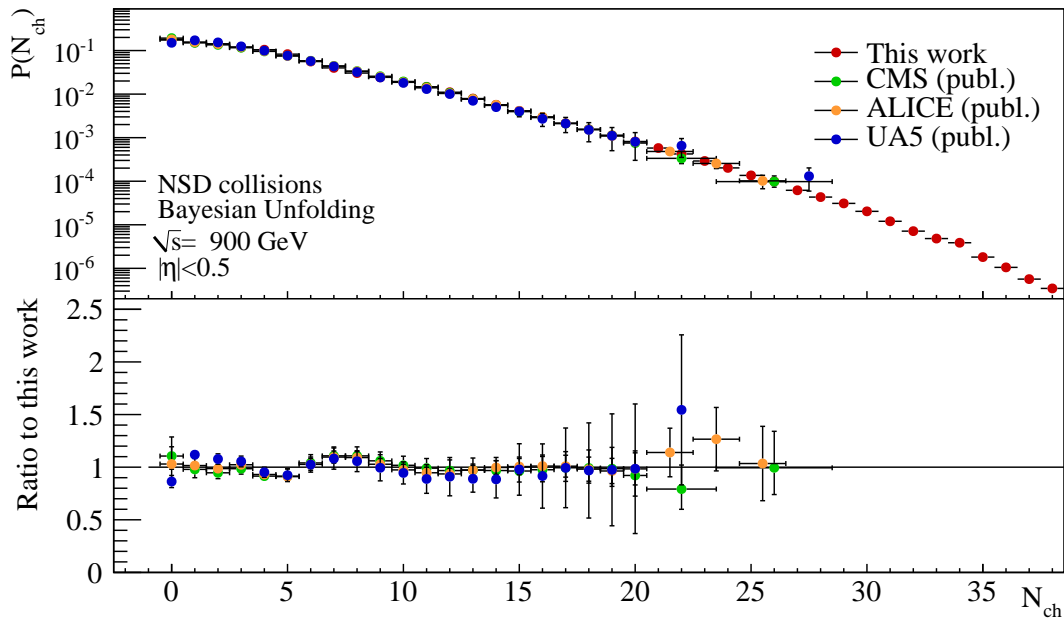


Figure 8.4: Detailed comparisons of the measured multiplicity distributions for NSD  $pp$  collisions at  $\sqrt{s} = 900$  GeV in the  $\eta$ -interval,  $|\eta| < 0.5$ . There is excellent agreement over the entire multiplicity range.

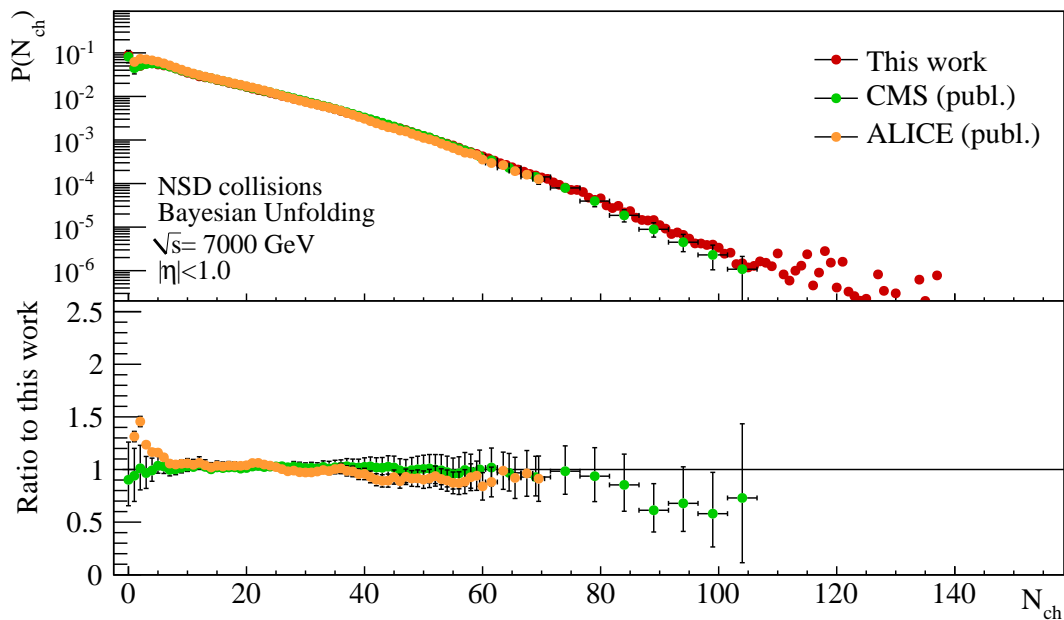


Figure 8.5: Detailed comparisons of the measured multiplicity distributions for NSD  $pp$  collisions at  $\sqrt{s} = 7000$  GeV in the  $\eta$ -interval,  $|\eta| < 1.0$ . There is good agreement over the most of the multiplicity range. At low multiplicities the agreement with CMS is better than with the tracklets in ALICE. At high multiplicities this analysis measures an excess of events compared to CMS.

### 8.1.2 PbPb collisions

For PbPb collisions at  $\sqrt{s_{NN}} = 2760$  GeV the multiplicity distribution have also been measured. In figure 8.6 the multiplicity distribution is presented for 0-5% centrality using the same  $\eta$ -intervals as in the  $pp$  case.

In figure 8.7 the multiplicity distribution for  $-3.4 < \eta < 5.1$  for a number of centrality bins is seen. As expected the distributions for the individual centrality bins add up to the black 0-100% centrality distribution.

The dashed lines denote the centrality bin regions if they were determined by the FMD distribution. This is similar to what was presented for the V0 centrality in figure 6.4. Thus the first dashed line from the right show the limit between 0-5% centrality and 5-10% centrality and henceforth.

While the measurement of centrality using the FMD and SPD combination is still quite preliminary it is clear that further development of the method can yield another measure of collision centrality, either as an independent measurement or as an internal cross check.

This method has the advantage of using a very wide range in  $\eta$ , which means that a large fraction of the total event multiplicity is actually measured. This lessens the risk of putting events into a wrong centrality class, due to the measured part of the event not being representative of the total event. The more of the total multiplicity that is actually measured, the lower that risk.

Potentially, the resolution of centrality determination for very peripheral collisions are better determined by the SPD and FMD combination, than for the V0.

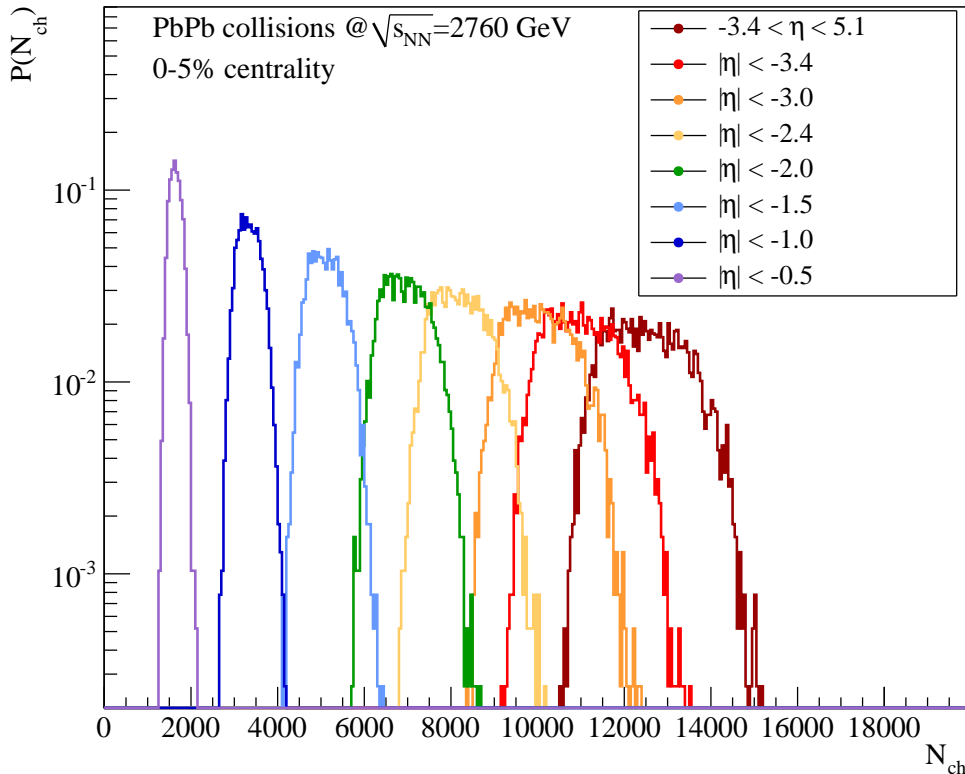


Figure 8.6: The charged particle multiplicity distribution for 0-5% central  $PbPb$  collisions at  $\sqrt{s_{NN}} = 2760$  GeV for the same  $\eta$ -intervals used in the analysis of  $pp$  collisions.

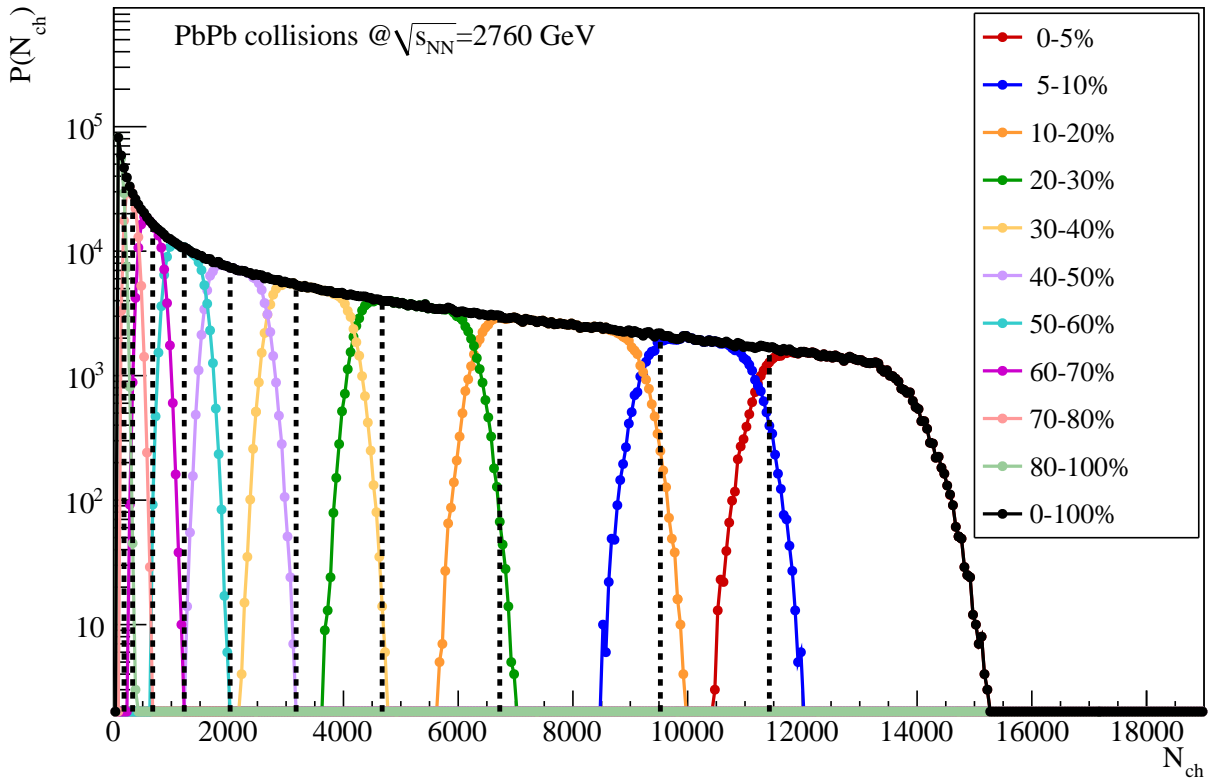


Figure 8.7: The charged particle multiplicity distribution in  $-3.4 < \eta < 5.1$  for  $PbPb$  collisions at  $\sqrt{s_{NN}} = 2760$  GeV. The different centrality classes, determined by the V0 detector, are shown. The vertical dashed lines show the centrality selections as it would be if centrality was determined by the multiplicity distributions of this work.

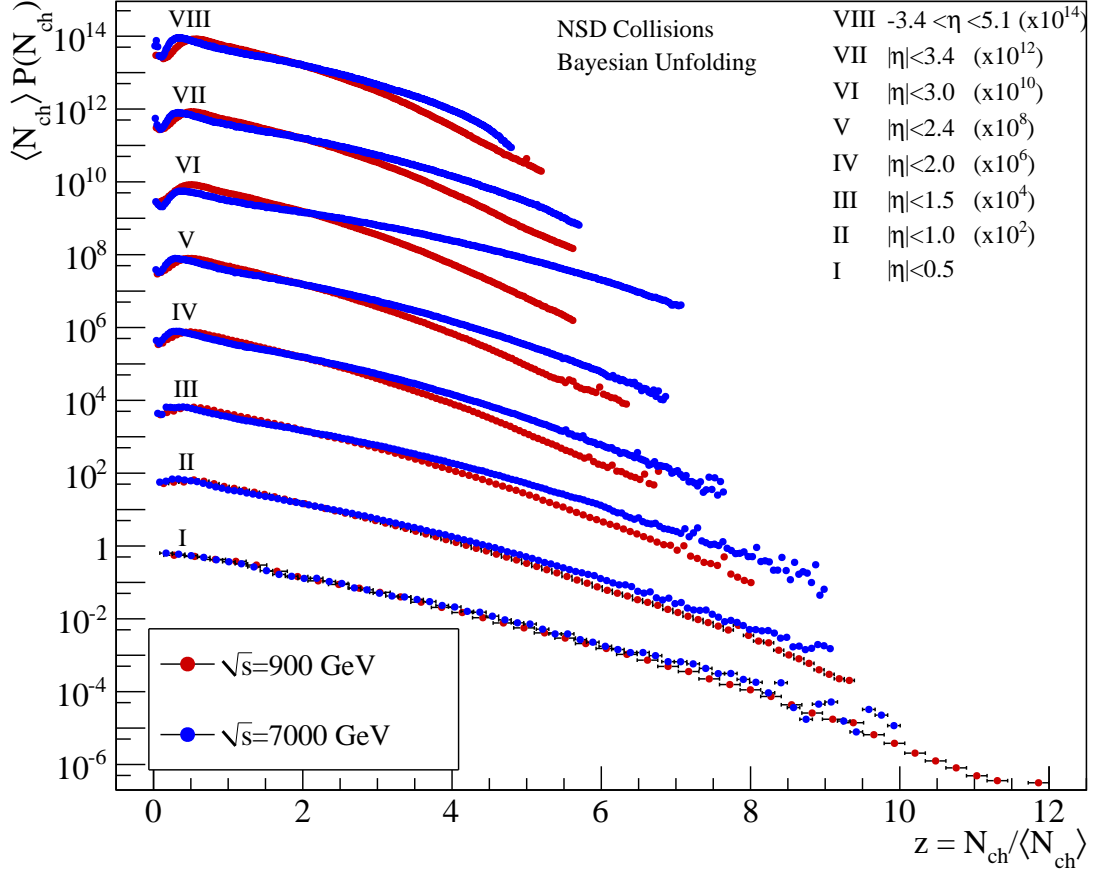


Figure 8.8: pp NSD collisions in KNO variables at  $\sqrt{s} = 900 \text{ GeV}$  and  $7000 \text{ GeV}$ . It is found that KNO scaling is violated in all  $\eta$ -intervals, except perhaps the most central  $\eta$ -region.

## 8.2 KNO

The next group of results revolves around KNO scaling. The first results presented will be for  $pp$  collisions, and in the next subsection the results from  $PbPb$  collisions are shown.

### 8.2.1 pp collisions

Figure 8.8 show  $pp$  NSD collisions at  $\sqrt{s} = 900 \text{ GeV}$  and  $7000 \text{ GeV}$  in KNO variables. It is found that the broader the observed  $\eta$ -interval, the more KNO scaling is violated when moving from  $\sqrt{s} = 900 \text{ GeV}$  to  $\sqrt{s} = 7000 \text{ GeV}$ . For the most narrow  $\eta$ -interval,  $|\eta| < 0.5$ , it is difficult to conclude whether KNO scaling is also violated, but any violation is at best very small. CMS concludes that KNO scaling holds for  $|\eta| < 0.5$  [75].

Figure 8.9 show comparisons between this work and CMS for  $|\eta| < 0.5$  and  $|\eta| < 2.4$ . It is seen that there is good agreement in both intervals. The ratio between  $\sqrt{s} = 900 \text{ GeV}$  and  $7000 \text{ GeV}$  for both set of measurements is included in figure 8.9.

It is interesting to notice that the shape of the ratio-distribution is the same for both  $|\eta| < 0.5$  and  $|\eta| < 2.4$ . For the latter this is a clear sign that the KNO multiplicity distributions are distinctly different, and thus KNO scaling is violated. For  $|\eta| < 0.5$  the shape is similar, but the magnitude of the effect is clearly smaller. However it appears as if the overall picture is the same, namely that KNO scaling is possibly violated also for the  $|\eta| < 0.5$  interval. In order to reach a firm conclusion on this, better control of the

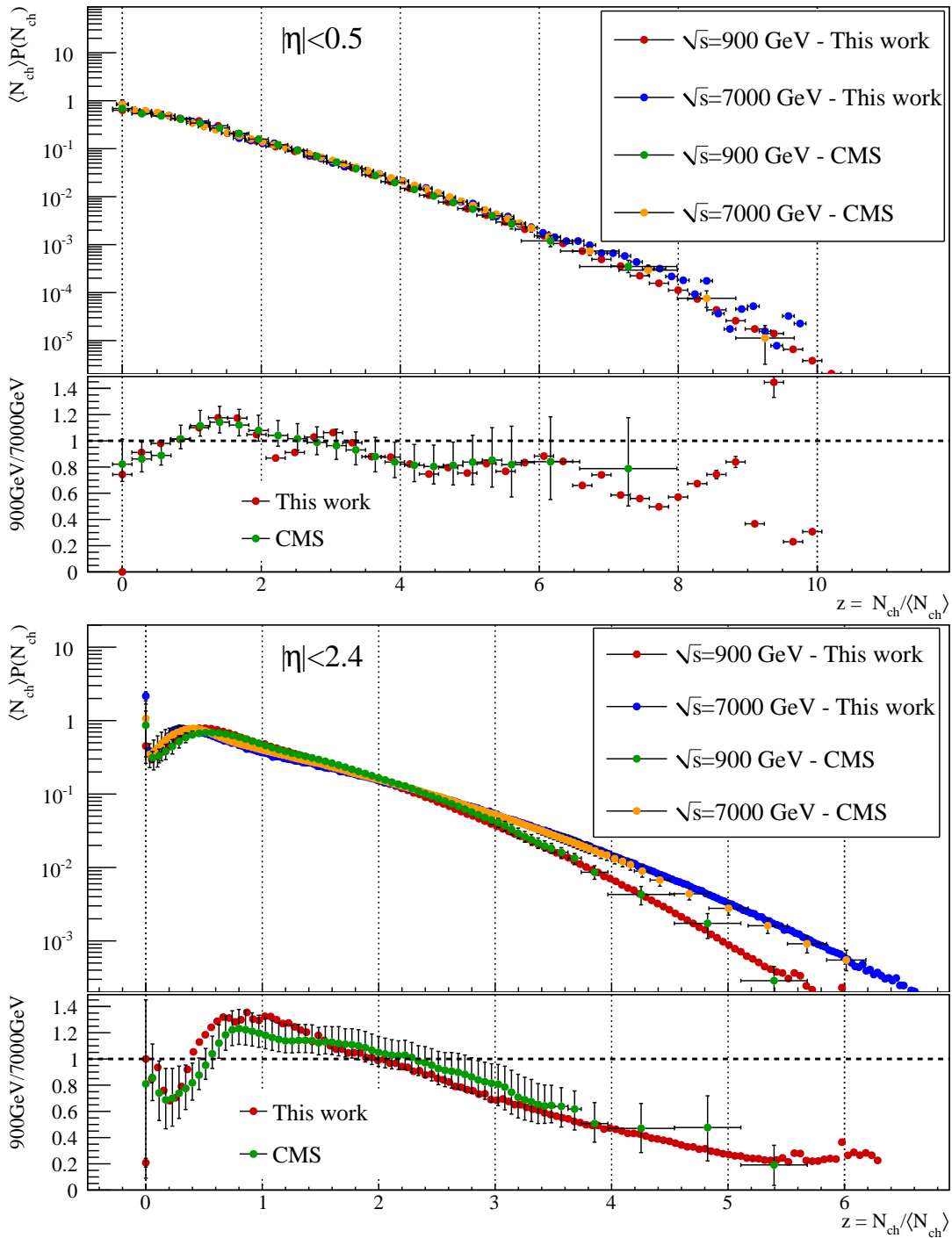


Figure 8.9: Detailed comparison of KNO scaling in  $|\eta| < 0.5$  and  $|\eta| < 2.4$  between CMS and this work. Good agreement is found between the experiments for the multiplicity distributions in KNO variables. The shape of the ratio between  $\sqrt{s} = 900$  GeV and 7000 GeV is similar for both  $\eta$  intervals, however the scale of the deviations from unity is less in the  $|\eta| < 0.5$  case. This might indicate that KNO scaling is also violated for  $|\eta| < 0.5$ , however very slightly.

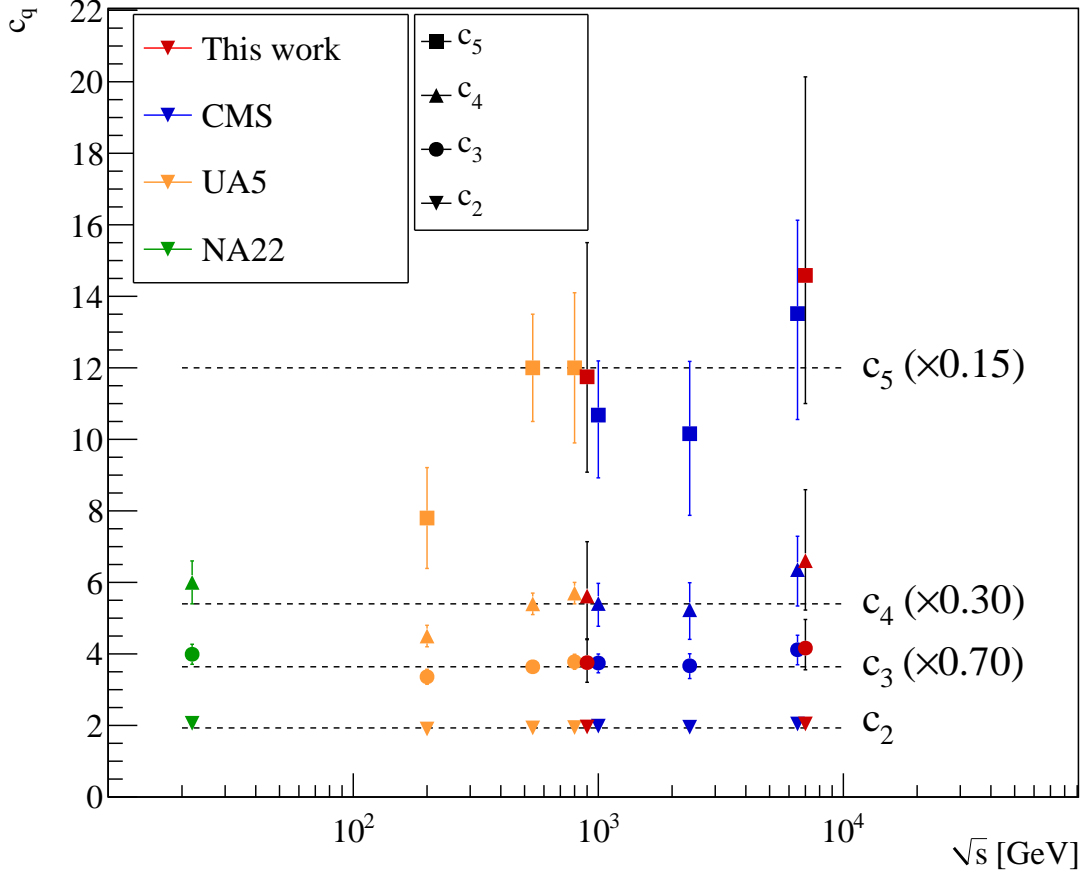


Figure 8.10: Statistical moments  $c_2$ - $c_5$  for  $|\eta| < 0.5$  multiplicity distributions over a large range of collision energies. The dashed horizontal lines are meant to guide the eye. The CMS points have been slightly shifted horizontally for clarity.

experimental uncertainties is needed.

Another interesting feature of figure 8.9 is that the tails of the KNO distributions are not higher in the analysis of this work, compared to CMS. This is an indication that the deviations seen in the multiplicity distributions can be explained by a minor scale factor; i.e. that the measurements of this work are consistently a few % higher (the ratio of the mean between CMS and this work is around  $\mu_{ALICE} \sim 1.02\mu_{CMS}$ ). This might be a clue to better understanding the differences between the two measurements. An inaccuracy in the material description could for instance have this effect, due to too few secondaries being produced in the simulations.

We return to the concept of KNO violation. To further investigate it we turn to the statistical moments,  $c_2 - c_5$ , as given by (2.29). Figures 8.10 and 8.11 show the moments as a function of collision energy for  $|\eta| < 0.5$  and  $|\eta| < 2.4$  respectively. In the latter interval, all the moments increase as a function of collision energy. By definition the moments must be constant as a function of collision energy for KNO scaling to remain valid. For  $|\eta| < 0.5$  the moments  $c_2$ ,  $c_3$  and  $c_4$  are all constant over all collision energies.  $c_5$  has large errors associated with it, and it becomes increasingly difficult to determine if it is constant or increasing slightly. Both a constant or a line could be fitted to the data points with a good agreement.

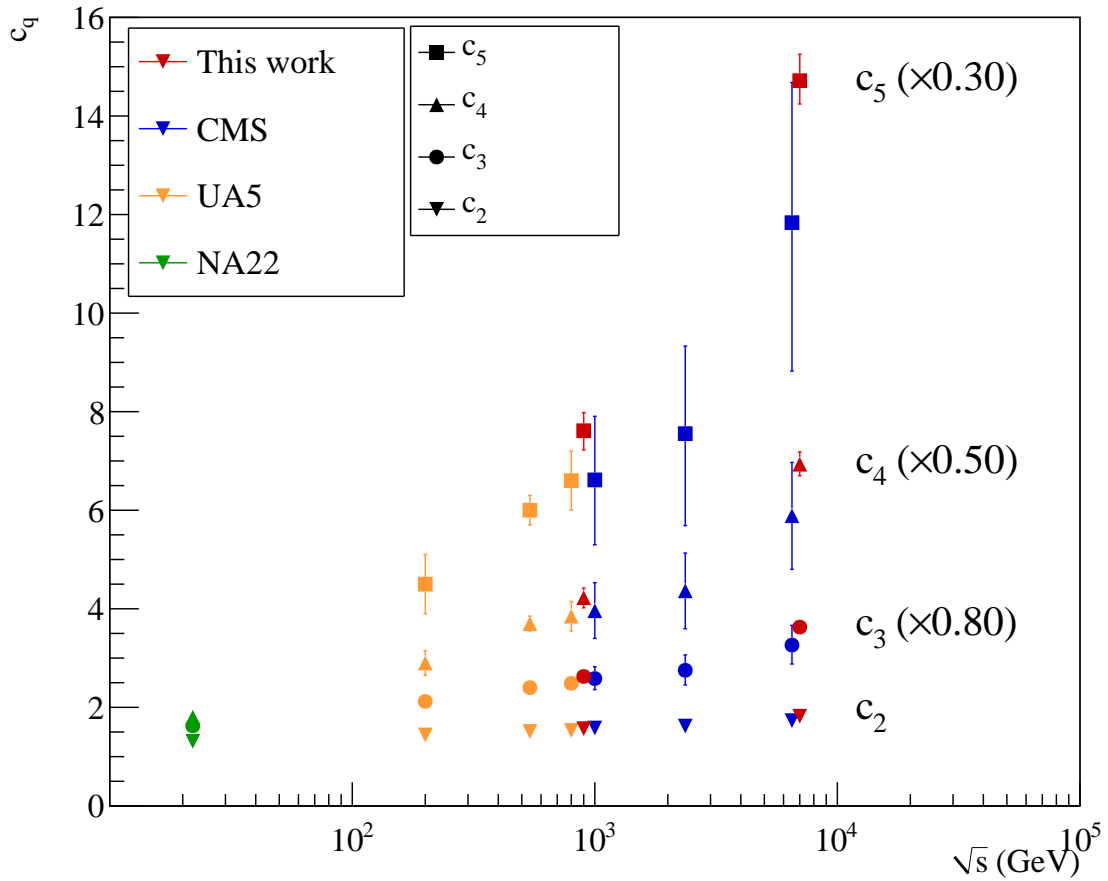


Figure 8.11: Statistical moments  $c_2$ - $c_5$  for  $|\eta| < 2.4$  multiplicity distributions over a large range of collision energies. The moments increase as a function of the collision energy, which is equivalent to KNO scaling being violated. The CMS points have been slightly shifted horizontally for clarity.

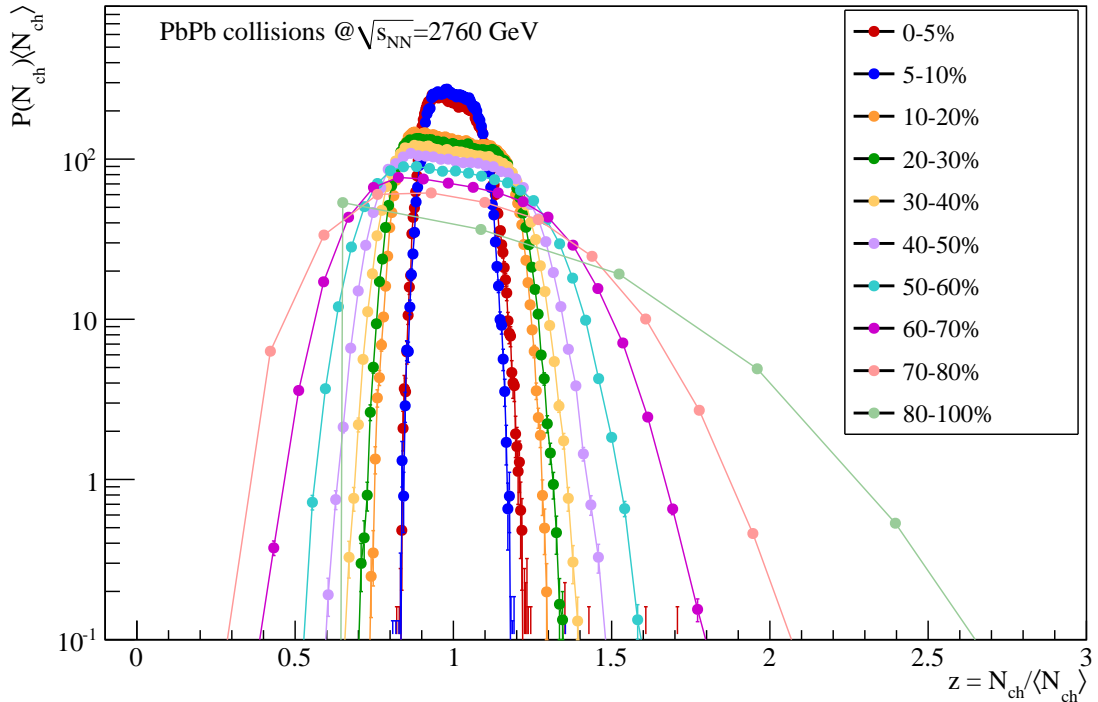


Figure 8.12: Multiplicity distributions of various centrality classes in  $PbPb$  collisions in KNO variables. No scaling with respect to the mean multiplicity is apparent.

### 8.2.2 PbPb collisions

For  $PbPb$  collisions the multiplicity distributions have also been studied in KNO variables. In figure 8.12 they are shown for a number of centrality classes. It is seen that there is no apparent scaling with respect to the mean multiplicity. It does however look as if normalising to the mean multiplicity is not the best choice. Looking at the two most central distribution, which only span 5% centrality each, it is found that they are significantly different than the rest, which span 10% centrality each.

Thus the distributions are not independent of the choice of centrality bins, which obviously makes it a sub-optimal choice. For further studies it could be interesting to see if it is possible to find another way to scale the distributions. Letting the scaling involve the mean number of participants springs to mind as a place to start. This avenue has not been pursued further in this work.

However, another study has been performed. Figure 8.13 shows the multiplicity distributions in KNO variables for various  $\eta$ -intervals. The top panel includes the same  $\eta$ -intervals as for  $pp$  collisions. It is seen that there is a clear scaling with respect to the mean multiplicity that persists over even the broadest  $\eta$ -interval. The origin of this scaling is currently not understood. Going forward in  $\eta$ , each interval includes the previous one. If there is any changes going to forward regions, this could be washed out by the inclusion of the more central region. To rule this out, the KNO multiplicity distributions are also measured for narrow  $\eta$ -intervals of  $\Delta\eta = 0.5$ . These are presented in the lower panel of figure 8.13. There is clear scaling with respect to the mean multiplicity visible for all the  $\eta$ -intervals. Quite surprisingly there are two intervals which deviate slightly from the rest, namely  $2.0 < \eta < 2.5$  and  $3.5 < \eta < 4.0$ . The reason for this is not understood.

The scaling itself is also not understood at this time. It is entirely possible that it is a mundane effect, or could perhaps hint at interesting physics.

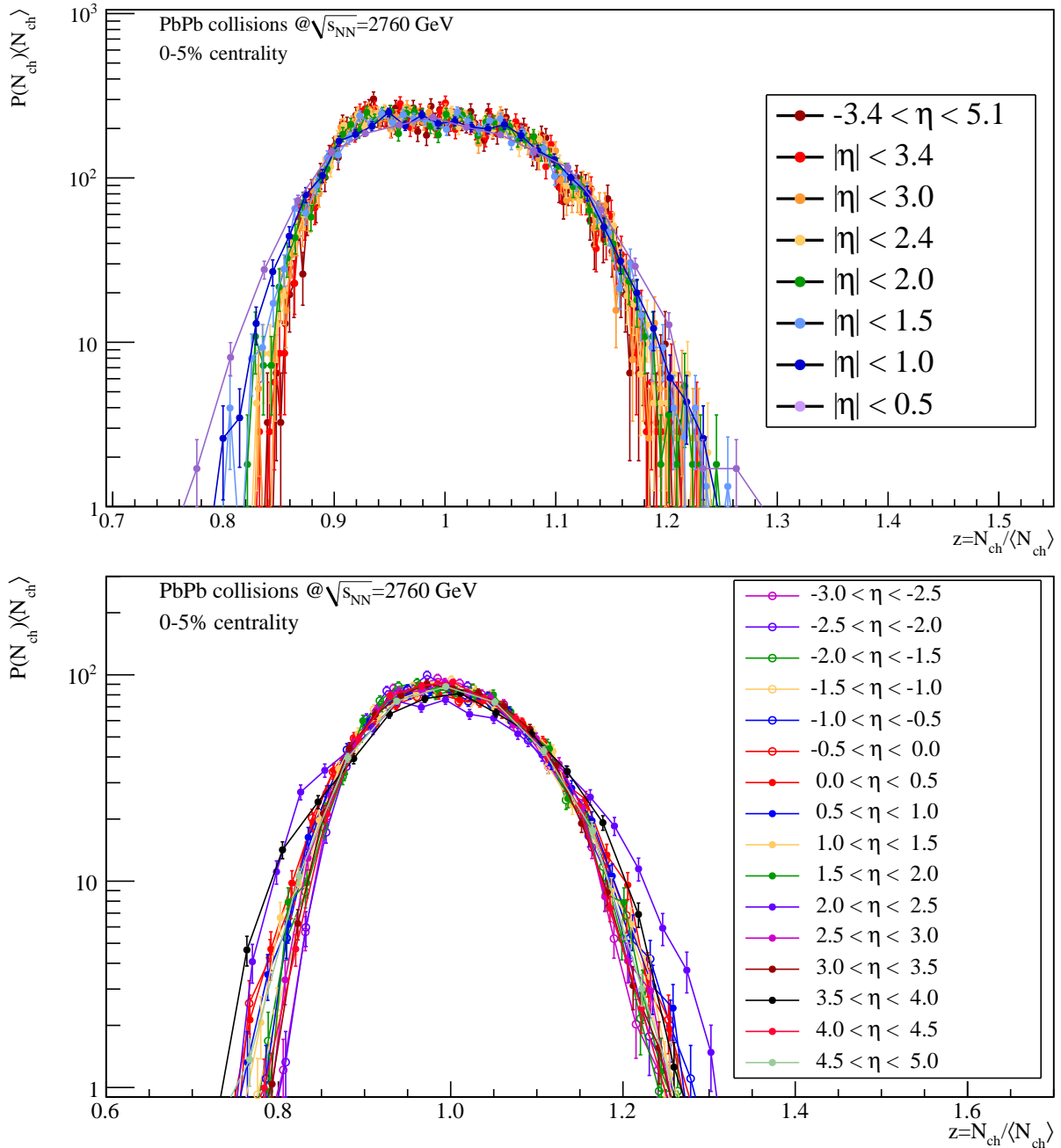


Figure 8.13: An attempt at looking at KNO scaling in  $PbPb$  collisions for the centrality class 0-5%. The upper panel shows the the multiplicity distributions for the same  $\eta$ -intervals used for analysis of  $pp$  collisions. The lower panel show small  $\Delta\eta = 0.5$  intervals. For both representations, a clear scaling with respect to the mean multiplicity is seen.

### 8.3 $\frac{dN_{\text{ch}}}{d\eta}$

Next up are the derived measurements of  $\frac{dN_{\text{ch}}}{d\eta}$ . These are created by running the analysis for very narrow pseudorapidity intervals,  $\Delta\eta = 0.5$ , as described in the previous section. The mean value of these distributions each give a point in the  $\frac{dN_{\text{ch}}}{d\eta}$  distributions.

#### 8.3.1 pp collisions

Figure 8.14 show  $\frac{dN_{\text{ch}}}{d\eta}$  for  $pp$  NSD collisions at  $\sqrt{s} = 900$  GeV and 7000 GeV. It is found that for the mid-rapidity region, there is good agreement between this method and the published data from other experiments. For the forward region in  $\sqrt{s} = 900$  GeV the agreement is not very good. For  $\sqrt{s} = 7000$  GeV there is no published data at forward angles, and the ALICE comparison is done to the trigger class INEL $>0$ .

The cause of the disagreement at forward angles is not fully understood, but it is likely that it is due to problems unfolding the very narrow  $\eta$ -intervals. At especially  $\sqrt{s} = 900$  GeV the raw multiplicity distribution for a narrow  $\eta$ -interval does not extend to very high multiplicities. In the forward region the secondary contamination is very large, and thus the unfolding changes the shape of the multiplicity distribution dramatically.

When the multiplicity distribution only spans few multiplicity values, this can cause problems with the unfolding precision. This can give unfolded distributions, which are

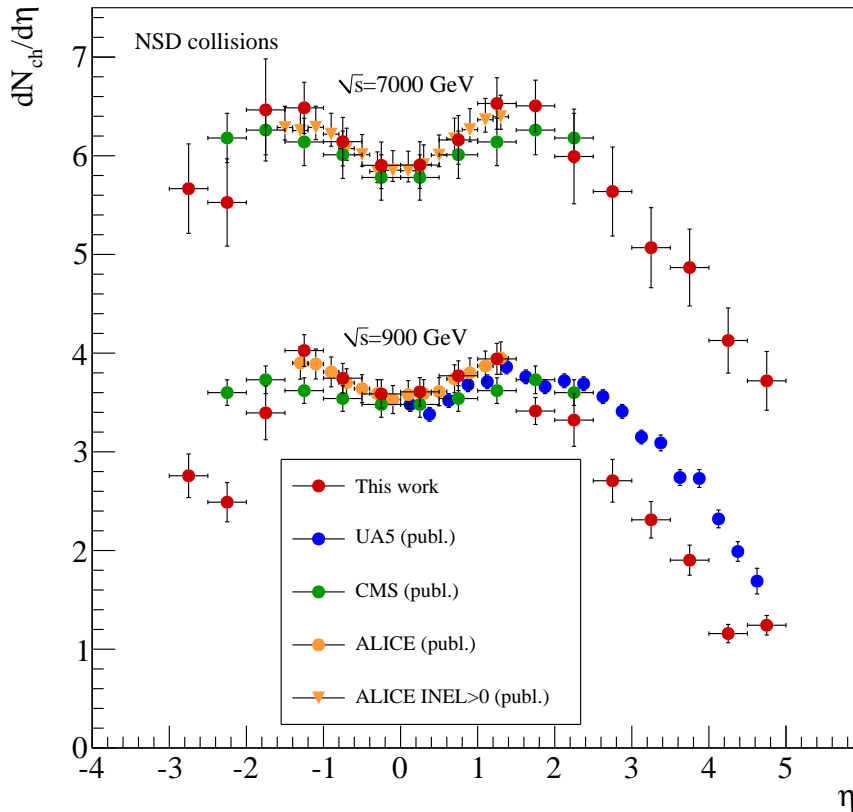


Figure 8.14:  $\frac{dN_{\text{ch}}}{d\eta}$  in  $pp$  NSD collisions measured as the mean of narrow unfolded multiplicity distributions. Included are measurements from CMS, UA5 and ALICE for reference. In the mid-rapidity region good agreement is seen. For forward regions there are significant deviations.

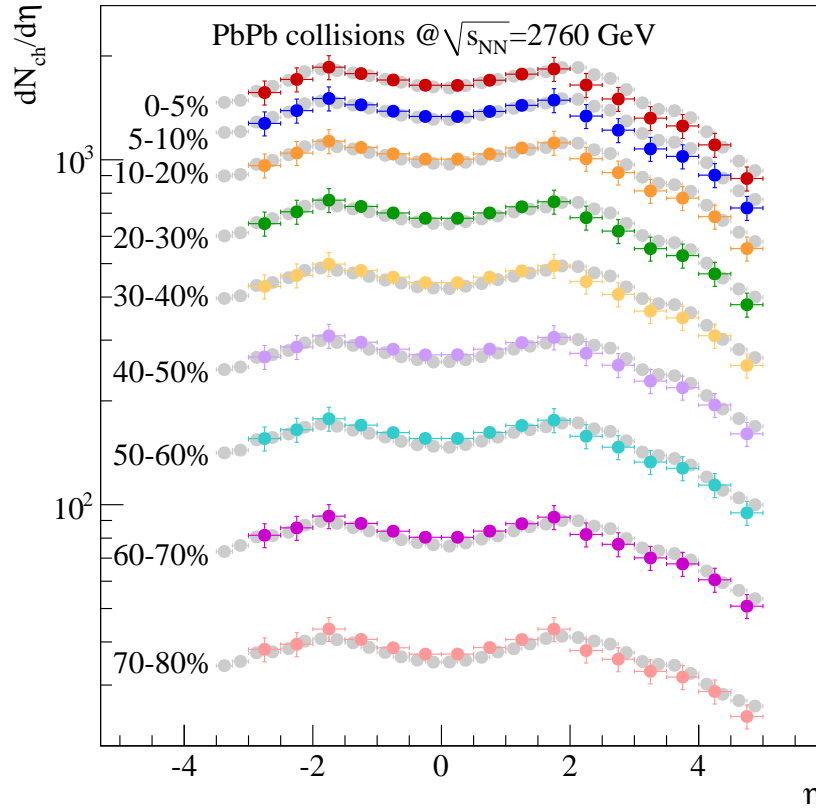


Figure 8.15:  $\frac{dN_{\text{ch}}}{d\eta}$  in  $PbPb$  collisions at  $\sqrt{s_{NN}} = 2760$  GeV, measured as the mean of narrow unfolded multiplicity distributions. Included is a reference measurement from another preliminary ALICE analysis [87]. Overall reasonable agreement is found between the two methods.

not reminiscent to the true distribution, and thus the mean value determination will be inaccurate <sup>27</sup>.

However, for the mid-rapidity region, the contamination of secondaries are very low, and thus the response matrix is almost diagonal. Thus the unfolding does not dramatically change the shape.

This can explain why good agreement is seen for the SPD range, where there are few secondaries, compared to the poor agreement in the secondary rich forward regions.

### 8.3.2 PbPb collisions

Figure 8.15 shows the  $\frac{dN_{\text{ch}}}{d\eta}$  for  $PbPb$  collisions at  $\sqrt{s_{NN}} = 2760$  GeV. Included as grey points are also the preliminary measurements of another current analysis by ALICE [87]. It is found that there overall seem to be reasonable agreement between the two methods.

Making  $\frac{dN_{\text{ch}}}{d\eta}$  measurements in this way, was never a main ambition of this work. Instead it is meant as a simple, and fun exercise. Given more time it is possible to further enhance the method, thereby providing a real alternative for  $\frac{dN_{\text{ch}}}{d\eta}$  measurements.

<sup>27</sup>for  $\eta$ -bins of size  $\Delta\eta = 0.2$  the unfolding has been tested, and regularly breaks down completely, yielding very unphysical solutions.

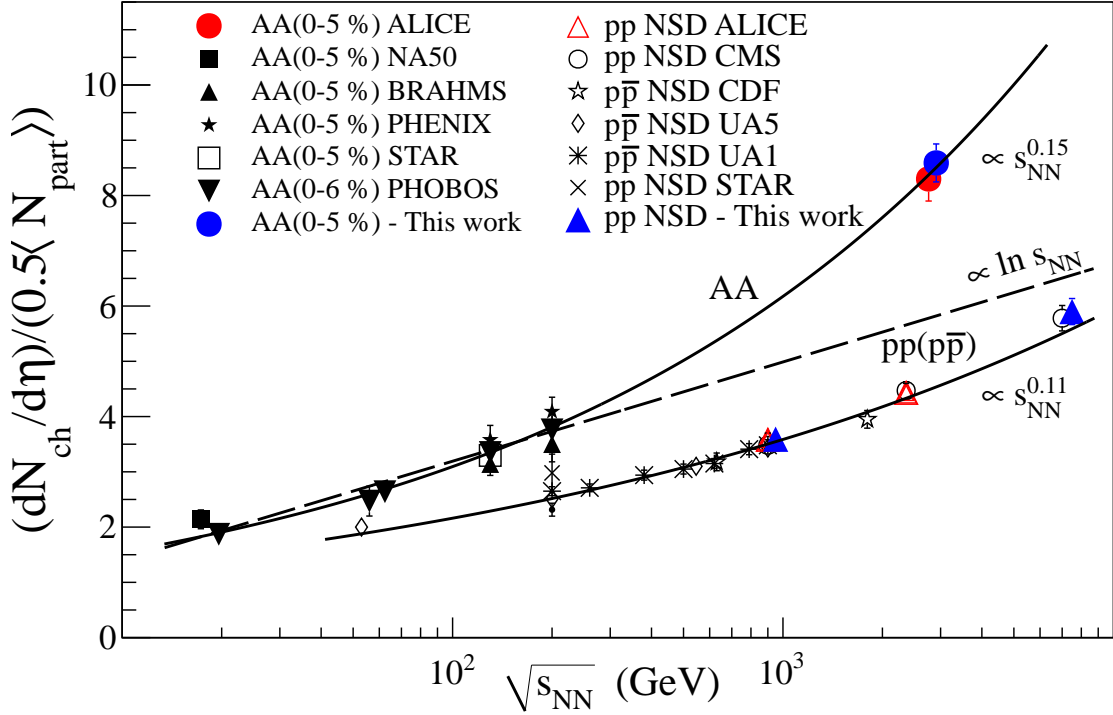


Figure 8.16: Mean multiplicity per participant pair scaling with collision energy. Good agreement is found with previous measurements. The measurements of this work is shifted upwards in energy for clarity. Figure is adapted from [88].

## 8.4 Mean Multiplicity Energy dependence

The last result presented is the collision energy scaling of the mean multiplicity in mid-rapidity per participant pair. In this context mid-rapidity is the  $\eta$ -interval  $|\eta| < 0.5$ . The results for  $pp$  NSD collisions at  $\sqrt{s} = 900$  GeV and 7000 GeV, as well as  $PbPb$  collisions at  $\sqrt{s_{NN}} = 2760$  GeV are shown in figure 8.16.

The measurements are consistent with the published values from ALICE, as well as for the CMS measurement for  $pp$  NSD collisions at  $\sqrt{s} = 7000$  GeV.

Thus, the conclusions from those experiments, that the mean multiplicity in mid-rapidity scales in both  $pp$  and  $PbPb$  collisions as a function of  $s^a$  [88] is supported by these measurements. The scaling is different for the two collision systems. It is found that:

$$\frac{1}{0.5 \langle N_{part} \rangle} \frac{dN_{ch}}{d\eta} \propto s^{0.11}, \text{ for } pp \text{ collisions} \quad (8.1)$$

$$\frac{1}{0.5 \langle N_{part} \rangle} \frac{dN_{ch}}{d\eta} \propto s_{NN}^{0.15}, \text{ for } PbPb \text{ collisions} \quad (8.2)$$

## 8.5 Outlook

While the FMD is fairly well understood, as demonstrated throughout this thesis, there are still numerous issues where a better understanding is needed. Improving upon these areas is paramount to increasing the accuracy of measurements of the FMD.

### Material budget of ALICE

The largest uncertainty in the FMD measurements is the accuracy of the virtual model of the experiment. While the major geometry revision in 2010 definitely was a great leap forward, there could be inaccuracies still in the geometry description.

There are immediately plans for starting a study, that can once and for all put this issue to rest. This study is similar to how the TPC has mapped their geometry very precisely in the mid-rapidity region.

Their method revolves around photons interacting with material, thus creating electron-positron pairs, that are eventually tracked in the TPC. By extrapolating the tracks back it is possible to determine exactly where the photon conversions happened. By doing so it is possible to get very detailed information of the material distribution in ALICE. In some sense it is reminiscent to the secondary particles origin plots presented in section 6.4. However the main advantage of the TPC method is that the actual physics data are used, and can be directly compared to the simulations. By using this method the TPC group was able to discover, amongst other things, a thin layer of glue missing in the material description.

The TPC only covers the mid-rapidity region, for collisions around the nominal interaction point. However if collisions with vertices at high  $|v_z|$ , are used, particles stemming from conversions in the forward regions are possible to be measured by the TPC.

Getting this study underway in collaboration with the TPC group has highest priority.

### FMD energy distributions

Another issue which was touched upon in section 6.2.1 is the differences between the energy distributions in physics data and simulated data. The energy distributions of simulations have much less smeared Landau peaks than in physics data.

A way to tune the simulations to better match the physics data is outlined in the following. First, it is assumed that the underlying energy loss signal is described by a Landau distribution, given by the variable  $(\Delta - \Delta_p)/\xi$  where  $\Delta_p$  is the MPV energy loss,  $\Delta$  is the energy loss and  $\xi$  denotes the spread of the Landau distribution. The energy distribution we are looking for after tuning is similarly given by  $(\Delta' - \Delta'_p)/\xi'$ . For now, focus is only on changing the width of the distributions, not the peak location, and therefore we set  $\Delta'_p = \Delta_p$ . Thus the relation between the two distributions are given by:

$$\frac{\Delta - \Delta_p}{\xi} = \frac{\Delta' - \Delta'_p}{\xi'} \quad , \text{ and thus} \quad \Delta' = \frac{\xi'}{\xi} \Delta + \left(1 - \frac{\xi'}{\xi}\right) \Delta_p \quad (8.3)$$

Retrieving  $\xi/\xi'$  from fits of the physics data and simulations respectively, it is possible to recalculate the tuned energy distribution from the original one.

Two examples of this are shown in figure 8.17. As seen the simulated energy distributions changes to better resemble the physics data energy distributions after tuning. In the same manner it is possible to also shift the Landau peaks of the simulated energy distributions.

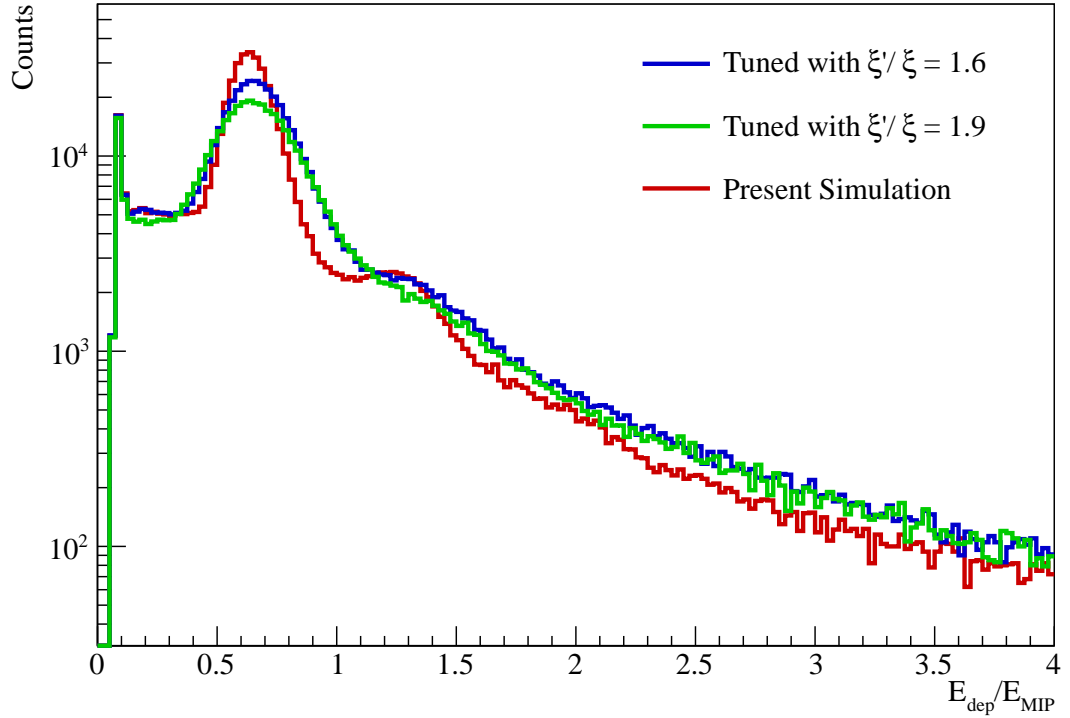


Figure 8.17: Preliminary tests of tuning the simulated energy distributions. Further tests will help ensuring that the energy distributions in simulations matches energy simulations in physics data as closely as possible

It is worth mentioning that the fraction of singles, doubles and triples in simulations compared to physics data is seemingly unaffected by the tuning of the energy distributions. Similarly the tuning will not have any effect on the appearance of very low energy deposition signals in physics data. These are issues which has to be dealt with separately.

Once the energy distributions for simulations matches the physics data, it needs to be included in new official ALICE simulation productions.

### *pPb* collisions

The LHC has so-far successfully provided both *pp* and *PbPb* collisions. At the end of 2011 they will attempt to setup and make the first *pPb* collisions.

As briefly discussed in section 1.4 this asymmetric collision systems is very interesting, since it is hoped that it will yield major insights into the initial conditions of the collisions.

In particular it will be exciting to study whether the gluon density is saturated, which would be clearly indicative of a Colour Glass Condensate state of matter. Colour Glass Condensate is theorised to be the state of matter of the nuclei just before they collide.

The existence of a Colour Glass Condensate can explain some of the unsolved problems of how exactly particles are produced in relativistic collisions as well as the distribution of matter inside particles themselves [131].

The FMD is perfect to look for signs of gluon saturation by examining how the multiplicity scales in *pPb* collisions as opposed to either *pp* or *PbPb* collisions.



# Chapter 9

## Conclusion

When the LHC succeeded providing  $pp$  collisions at  $\sqrt{s} = 900$  GeV on 23<sup>rd</sup> of November 2009, it was the culmination of 25 years of planning and extraordinary experimental ingenuity. Since then the LHC has provided  $pp$  collisions at higher energies, as well as  $PbPb$  collisions at  $\sqrt{s_{NN}} = 2760$  GeV. This work has presented analysis of these initial run periods.

The analysis framework and capabilities of the FMD has been discussed in detail. A method of using the FMD together with the inner layer of the SPD has been presented. This method have enabled ALICE to perform multiplicity analysis over a very large range in pseudorapidity.

With this method the charged particle multiplicities for  $pp$  NSD collisions at three collision energies have been measured for many  $\eta$ -intervals, the largest covering more than 8 units of  $\eta$ . It has been found that the measurements in this work are consistent with previous measurements from CMS and UA5. Even though they fall within the uncertainties, the multiplicity tails are systematically, if only slightly, higher in this analysis.

For  $\sqrt{s} = 2760$  GeV collisions the conclusion is that the data quality is too poor, that reliable analysis is not a possibility at this time. The exact extent of this is being investigated extensively in ALICE. Hopefully a focused effort can help improve the data quality.

Going from  $\sqrt{s} = 900$  GeV to 7000 GeV it is concluded that KNO scaling is strongly violated for at least all  $\eta$ -intervals except perhaps  $|\eta| < 0.5$ , where no clear conclusion can be drawn from the available data. This was further investigated in the presentation of the statistical moments for  $|\eta| < 0.5$  and  $|\eta| < 2.4$ . Smaller systematic uncertainties are needed to conclude definitively whether KNO scaling is violated at  $|\eta| < 0.5$ .

For  $PbPb$  collisions scaling in KNO variables has also been investigated; both as a function of centrality and  $\eta$ -interval. In the former case, no scaling is seen. For the latter there is clear scaling over all  $\eta$ -ranges. The multiplicity distributions are very similar in KNO variables from mid-rapidity to the most forward regions. The origin of this scaling is not understood, and must be investigated further.

It has furthermore been demonstrated that it is possible to make  $\frac{dN_{ch}}{d\eta}$  distributions by taking the mean value of multiplicity distributions from very narrow  $\eta$ -intervals. Particularly in  $pp$  collisions there are however unsolved issues in the forward regions, but good agreement with previous experiments in the mid-rapidity region.

The last result presented was the mean multiplicity per participant pair in  $|\eta| < 0.5$  for both  $pp$  and  $PbPb$  collisions. It is found that there is good agreement with previous measurements from CMS and ALICE.

Summing up, a variety of the first LHC results of analysis using the FMD has been

presented in this work. There are however still much room for improvement in the detailed understanding of the FMD system. This continued effort of reducing the systematic uncertainties is very important for both the analyses presented in this work, but also for subsequent analysis, that might be even more susceptible to the remaining issues.

Gaining a better understanding of the FMD, and solving the remaining issues, will leave the FMD in great shape when the LHC finally starts colliding particles at the design top energy in 2014.

Casper Nygaard, October 2011

# Appendix A

## Lorentz Invariance of $dy$

The Lorentz transformation is given by:

$$\begin{aligned} E^* &= \gamma E - \gamma\beta p_z \\ p_z^* &= -\gamma\beta E + \gamma p_z \end{aligned} \tag{A.1}$$

Here  $\beta$  velocity of the frame from which we view the collision and  $\gamma$  is defined as  $\gamma = \frac{1}{\sqrt{1-\beta^2}}$

The transformation is done by inserting the transformations of  $E$  and  $p_z$  into the definition of the rapidity:

$$\begin{aligned} y^* &= \frac{1}{2} \ln \frac{E^* + p_z^*}{E^* - p_z^*} \\ &= \frac{1}{2} \ln \frac{\gamma E - \gamma\beta p_z - \gamma\beta E + \gamma p_z}{\gamma E - \gamma\beta p_z + \gamma\beta E - \gamma p_z} \\ &= \frac{1}{2} \ln \frac{E + p_z}{E - p_z} + \frac{1}{2} \ln \frac{\gamma - \gamma\beta}{\gamma + \gamma\beta} \\ &= y + \frac{1}{2} \ln \frac{\gamma - \gamma\beta}{\gamma + \gamma\beta} \end{aligned} \tag{A.2}$$

$$\tag{A.3}$$

This means that:

$$dy^* = y^*_{*2} - y^*_{*1} = y_2 - y_1 = dy \tag{A.4}$$

Thus rapidity differences are Lorentz invariant.



# Appendix B

## The Glauber Model

In the Glauber model three assumptions are made [132]:

1. Nucleons are distributed according to a density function (e.g. Woods Saxon).
2. Nucleons travel in straight lines and are not deflected by interactions.
3. Nucleons interact with the inelastic cross section  $\sigma_{NN}$  measured in  $pp$  collisions at the same initial energy even after multiple interactions.

Presented in fig. B.1 is the correlation between  $N_{part}$  and  $b$  in  $AuAu$  collisions, based on the Glauber model.

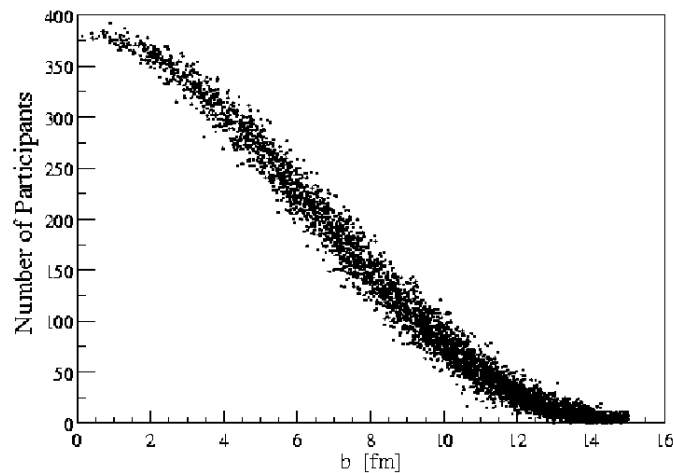


Figure B.1:  $N_{part}$  versus impact parameter using the Glauber model. Picture taken from [133].



# Appendix C

## Sharing algorithm

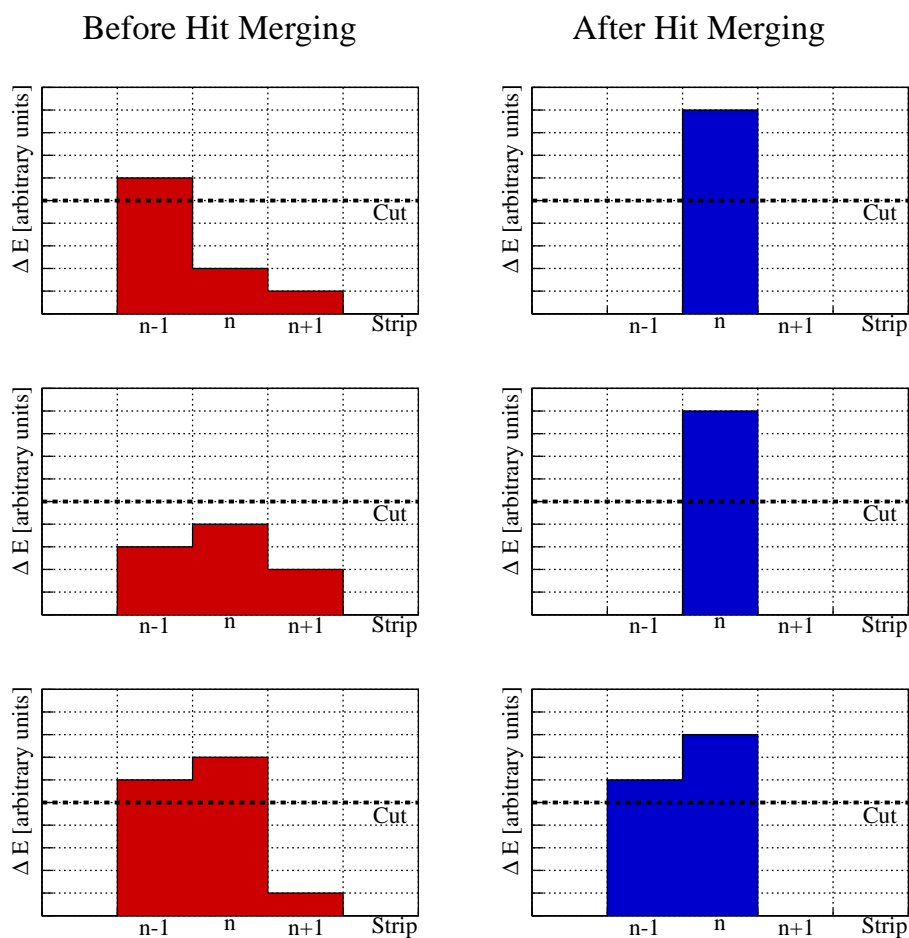


Figure C.1: Illustration of the concept of hit sharing. Incoming particles can traverse multiple strips, depositing energy in all of them. A hit sharing algorithm searches for neighboring strips with energy signals above the low threshold. The shared energy signals are merged into one signal.

In figure C.1 a few examples of hit merging with 3 strips hit are illustrated. In figure C.2 the flow chart of the sharing algorithm is shown.

In the case of merging two strips, the merged signal is always placed in the strip with the highest energy deposition. For three strips being merged, the signal is placed in the middle strip. There are arguments for/against placing it in the middle strip compared to placing it in the highest deposit strip like for the two-strip case. The difference however is

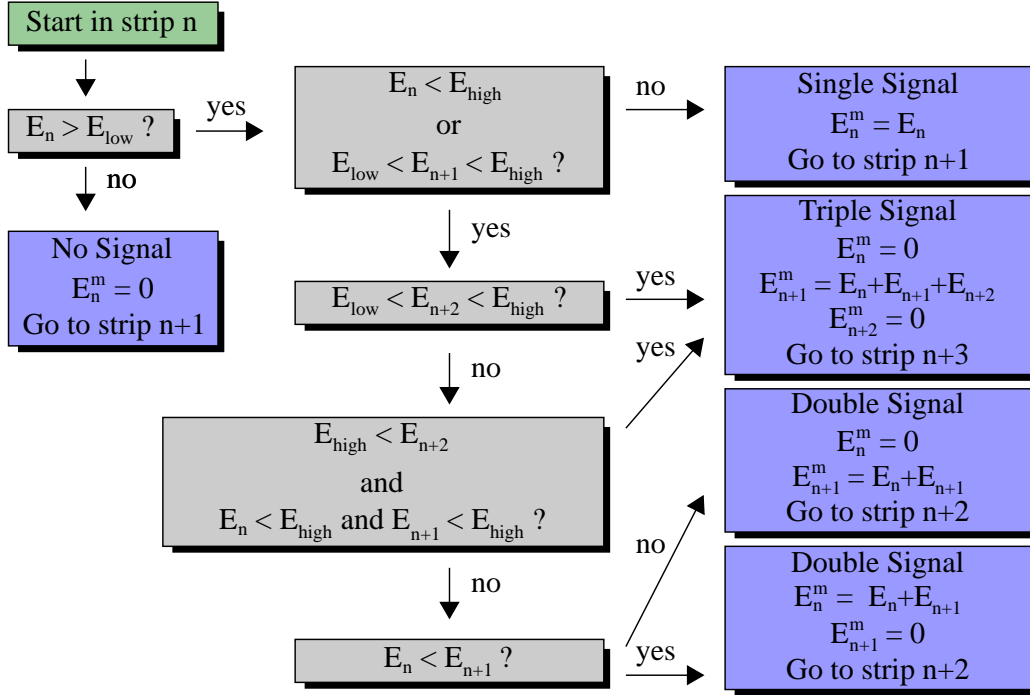


Figure C.2: Flow chart of the sharing algorithm. Up to three adjacent strip are searched through and their deposited energy merged depending on the energy deposits in each of the strips.

completely negligible due to the tiny  $\eta$  difference between two adjacent strips, as well as the fact that having merged signals from three strips are quite rare.

pp @ $\sqrt{s} = 900\text{GeV}$					
Signal	FMD1I	FMD2I	FMD2O	FMD3I	FMD3O
Single	86.99 %	87.07 %	92.26 %	85.65 %	91.96 %
Double	12.71 %	12.67 %	7.64 %	13.99 %	7.86 %
Triple	0.30 %	0.26 %	0.10 %	0.36 %	0.18 %
PbPb @ $\sqrt{s} = 2760\text{GeV}$					
Signal	FMD1I	FMD2I	FMD2O	FMD3I	FMD3O
Single	88.95%	88.48%	91.22 %	88.24 %	91.79 %
Double	9.67 %	9.95%	7.91 %	10.17 %	7.37 %
Triple	1.38 %	1.58 %	0.87 %	1.59 %	0.84 %

Table C.1: Overview over the amount of single, double and triple signals in each of the FMD rings.

# Appendix D

## Comparison between Poisson and Energy Fits counting

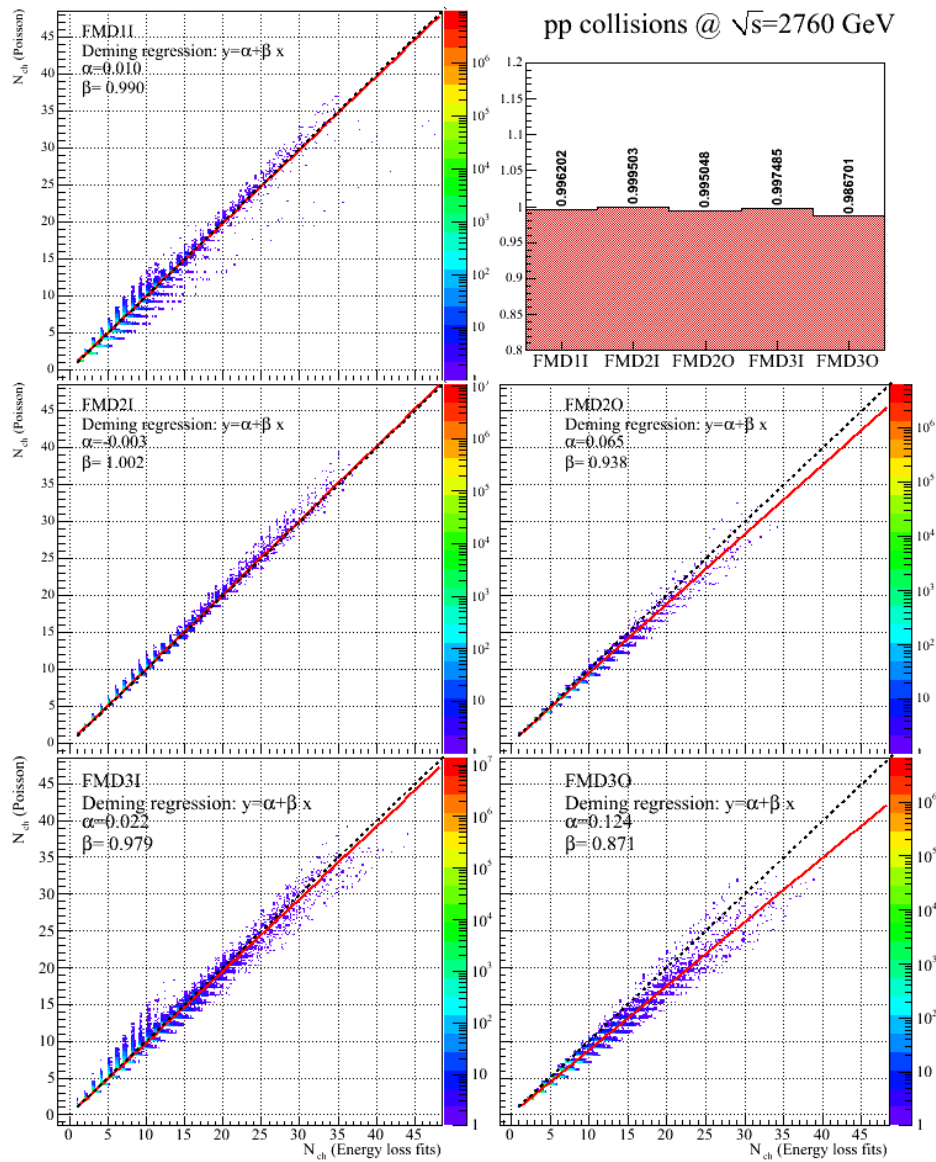


Figure D.1: Comparison between the Poisson and Energy fit counting methods for  $pp$  collisions at  $\sqrt{s} = 2760$  GeV.

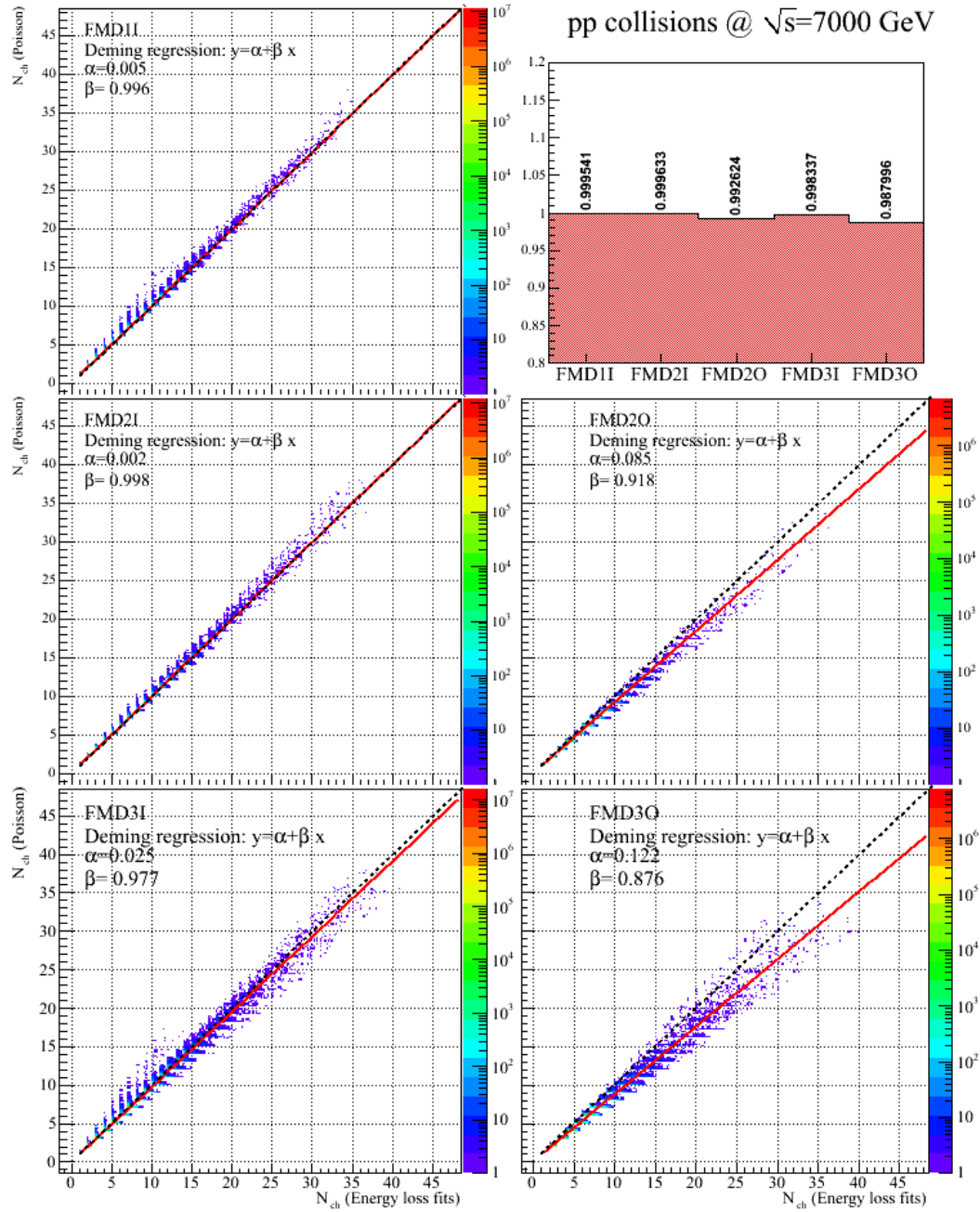


Figure D.2: Comparison between the Poisson and Energy fit counting methods for  $pp$  collisions at  $\sqrt{s} = 7000$  GeV.

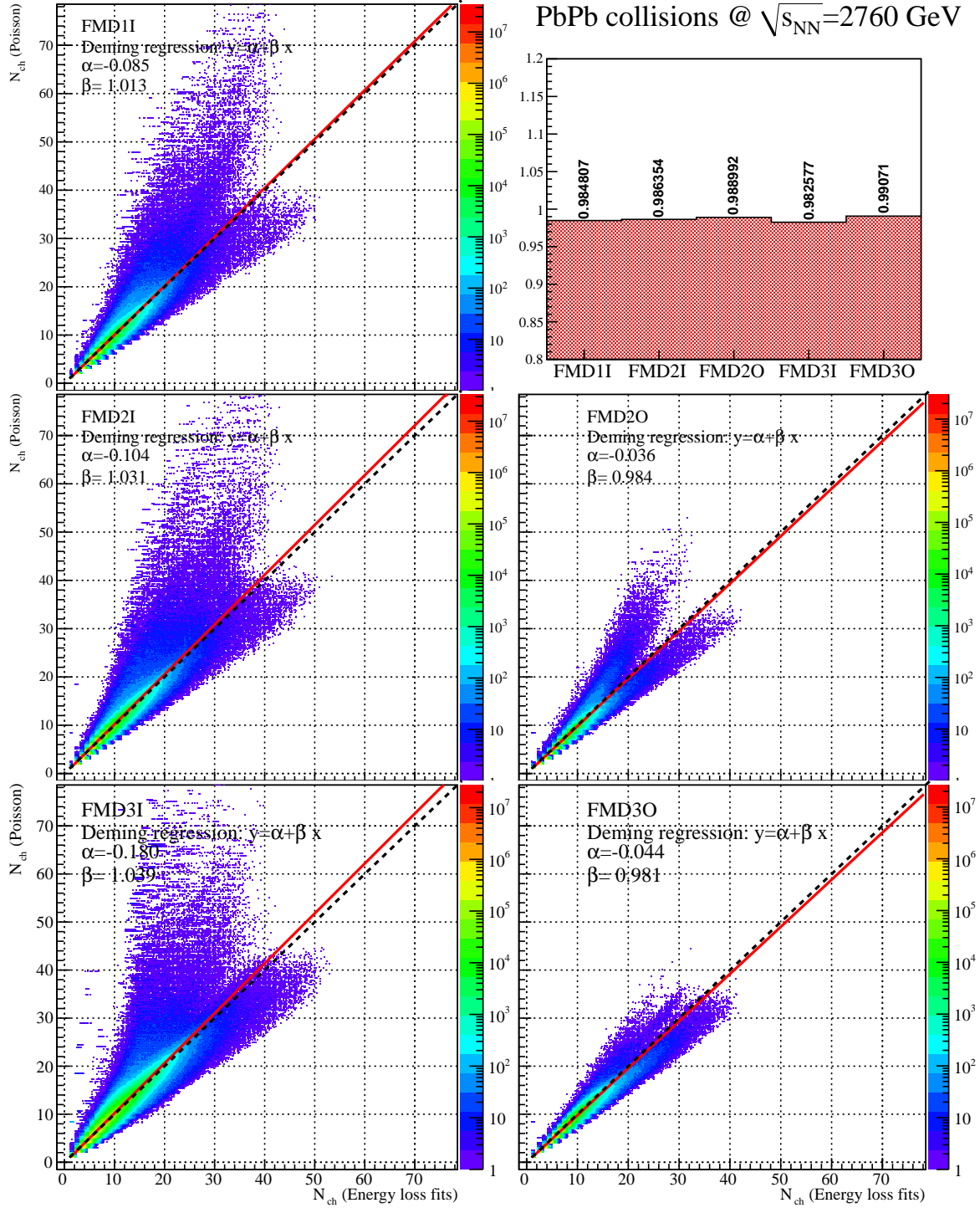


Figure D.3: Comparison between the Poisson and Energy fit counting methods for  $PbPb$  collisions at  $\sqrt{s_{NN}} = 2760$  GeV.



# Appendix E

## $Q_1$ in central $\eta$ -interval

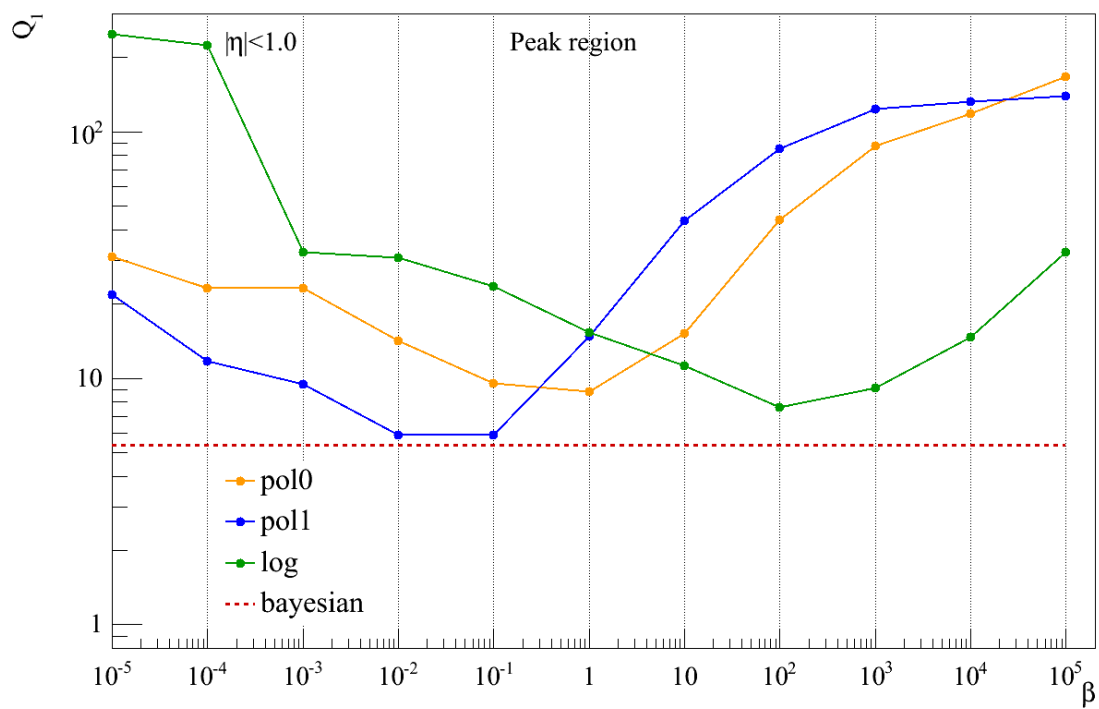


Figure E.1: The unfolding quality parameter,  $Q_1$ , for the peak region for  $|\eta| < 1.0$ .

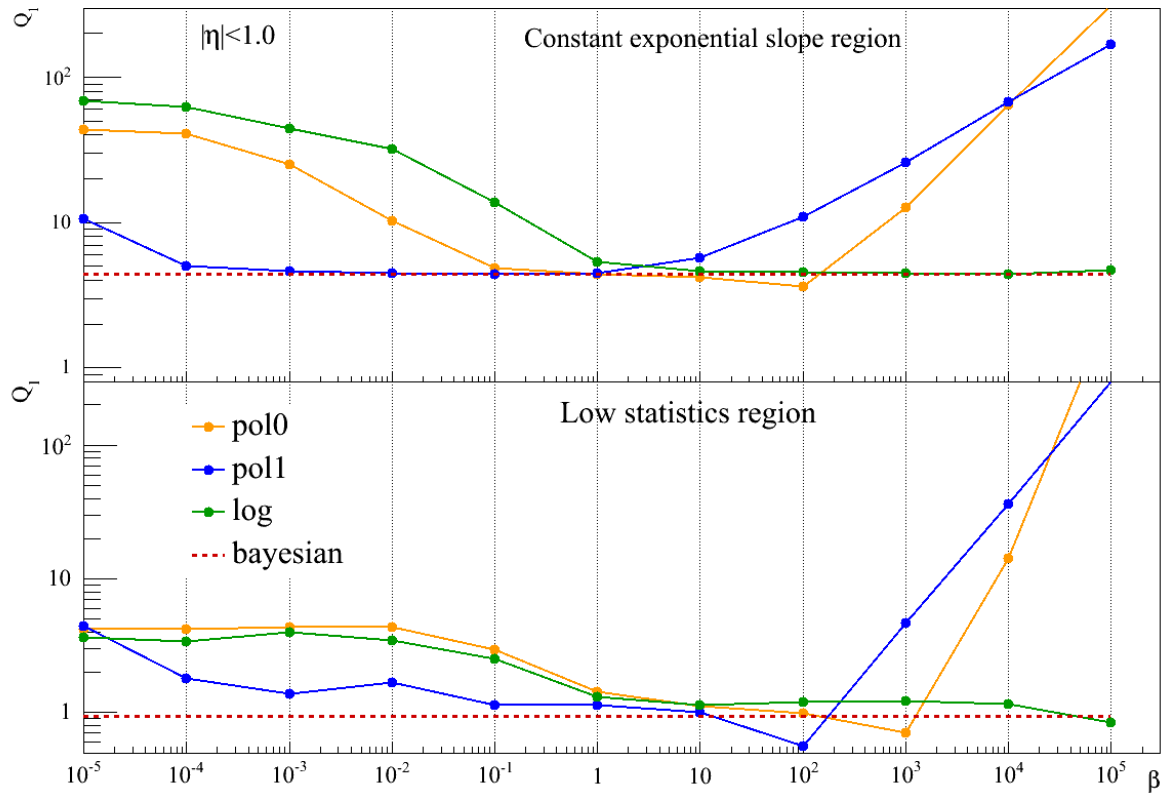


Figure E.2:  $Q_1$  for the constant exponential slope region and the low statistics region for  $|\eta| < 1.0$ .

# Appendix F

## Detailed comparisons of multiplicity distributions

pp NSD collisions at  $\sqrt{s} = 900\text{GeV}$

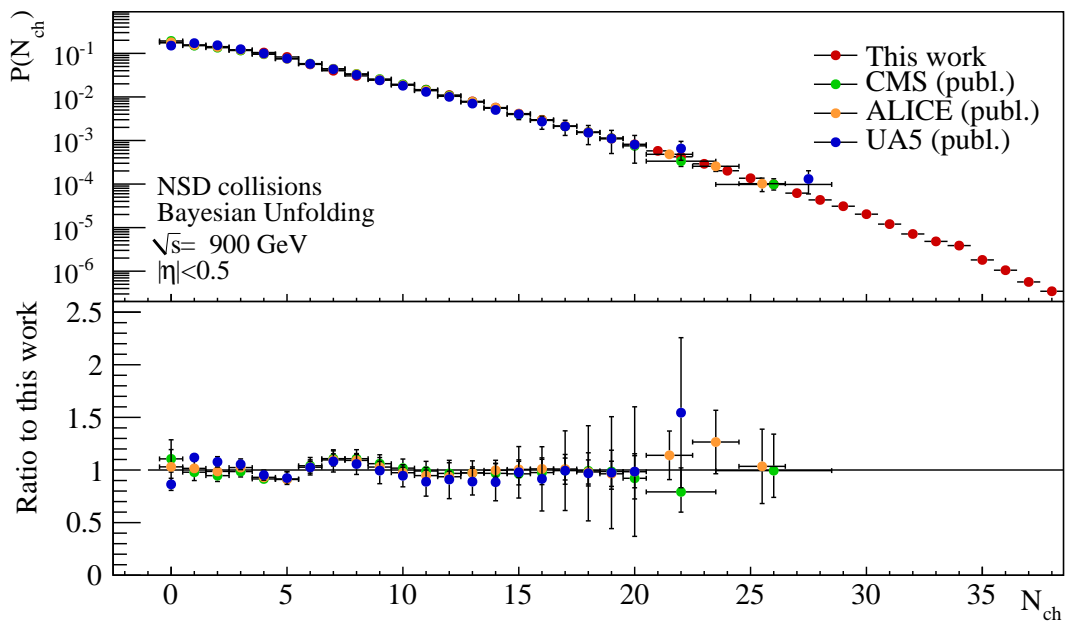


Figure F.1: Detailed comparisons of the measured multiplicity distributions for NSD  $pp$  collisions at  $\sqrt{s} = 900\text{ GeV}$  in the  $\eta$ -interval,  $|\eta| < 0.5$ .

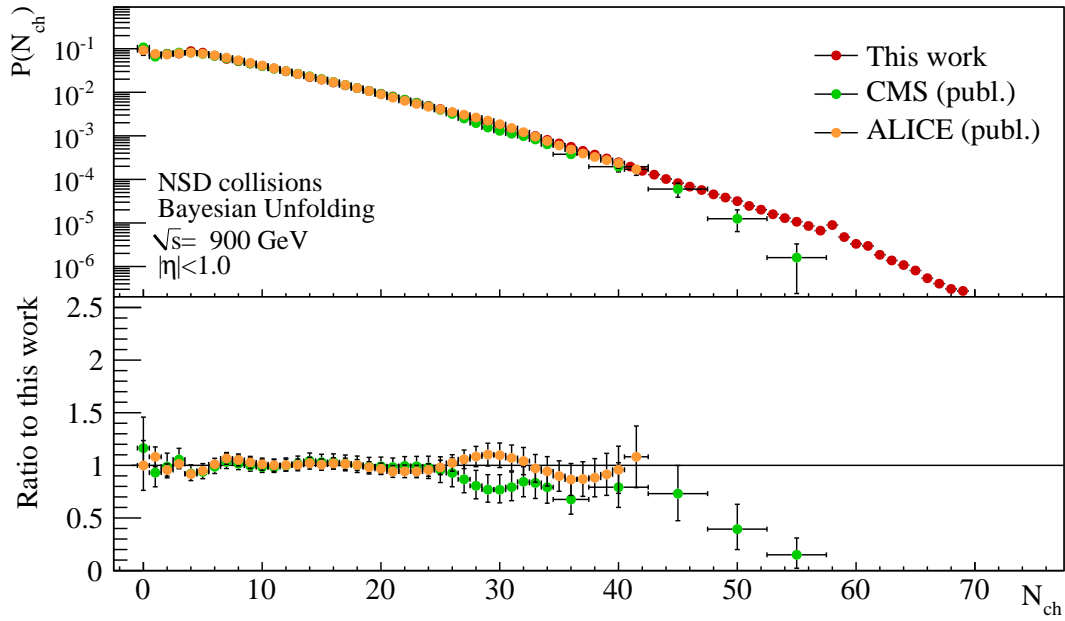


Figure F.2: Detailed comparisons of the measured multiplicity distributions for NSD  $pp$  collisions at  $\sqrt{s} = 900$  GeV in the  $\eta$ -interval,  $|\eta| < 1.0$ .

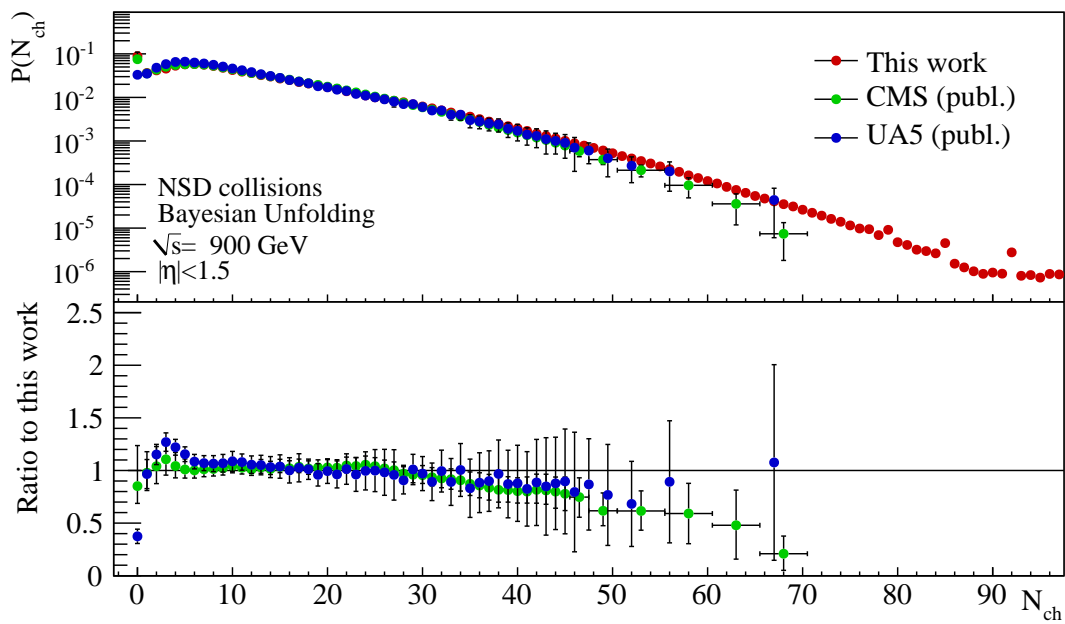


Figure F.3: Detailed comparisons of the measured multiplicity distributions for NSD  $pp$  collisions at  $\sqrt{s} = 900$  GeV in the  $\eta$ -interval,  $|\eta| < 1.5$ .

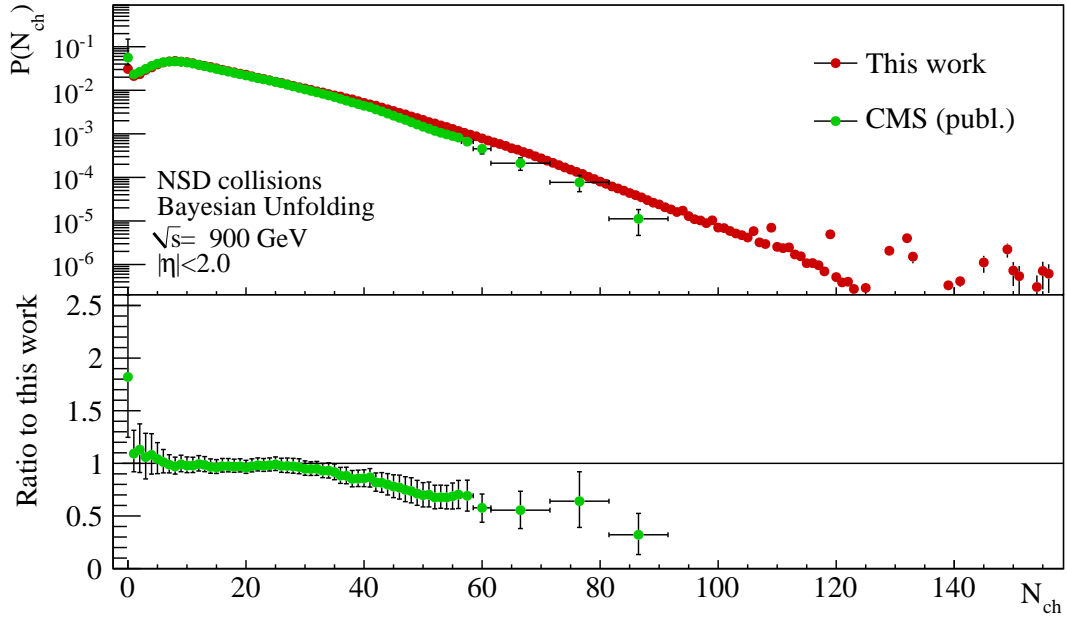


Figure F.4: Detailed comparisons of the measured multiplicity distributions for NSD  $pp$  collisions at  $\sqrt{s} = 900$  GeV in the  $\eta$ -interval,  $|\eta| < 2.0$ .

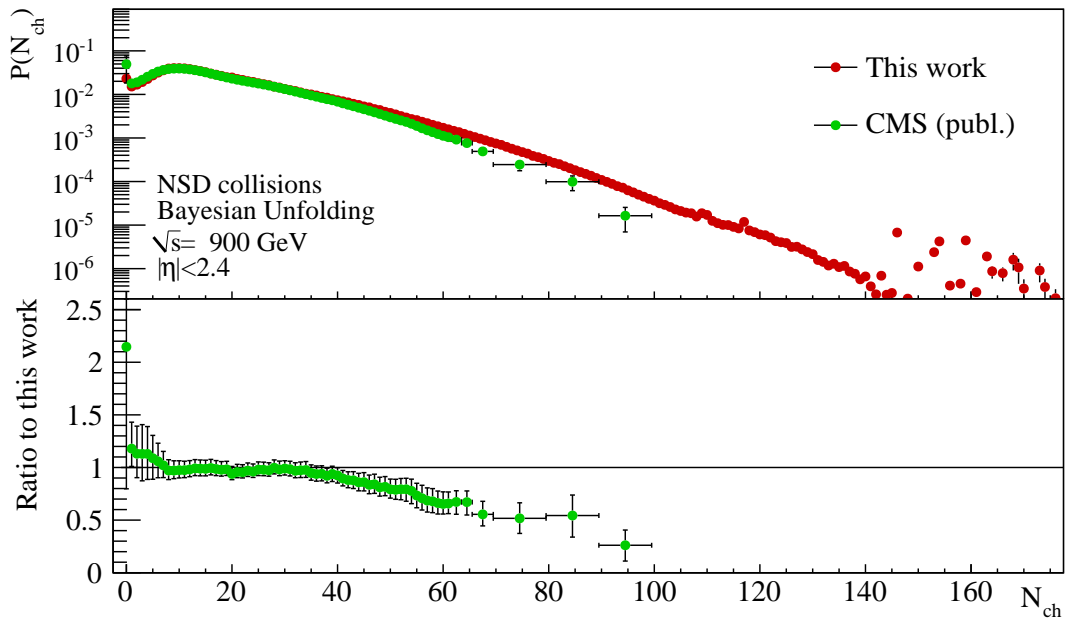


Figure F.5: Detailed comparisons of the measured multiplicity distributions for NSD  $pp$  collisions at  $\sqrt{s} = 900$  GeV in the  $\eta$ -interval,  $|\eta| < 2.4$ .

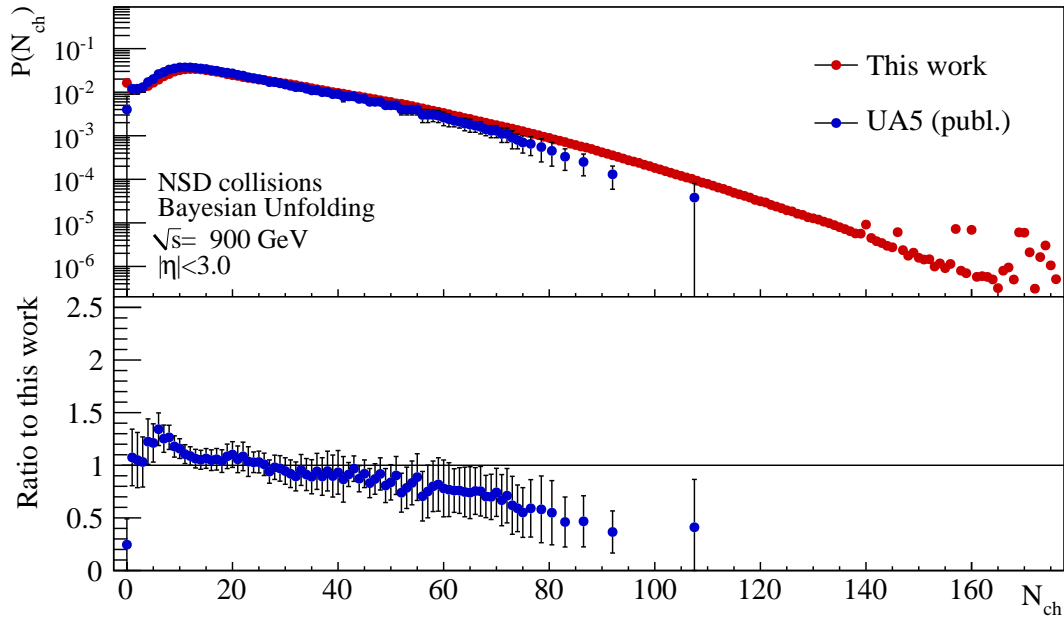


Figure F.6: Detailed comparisons of the measured multiplicity distributions for NSD  $pp$  collisions at  $\sqrt{s} = 900$  GeV in the  $\eta$ -interval,  $|\eta| < 3.0$ .

### $pp$ NSD collisions at $\sqrt{s} = 7000$ GeV

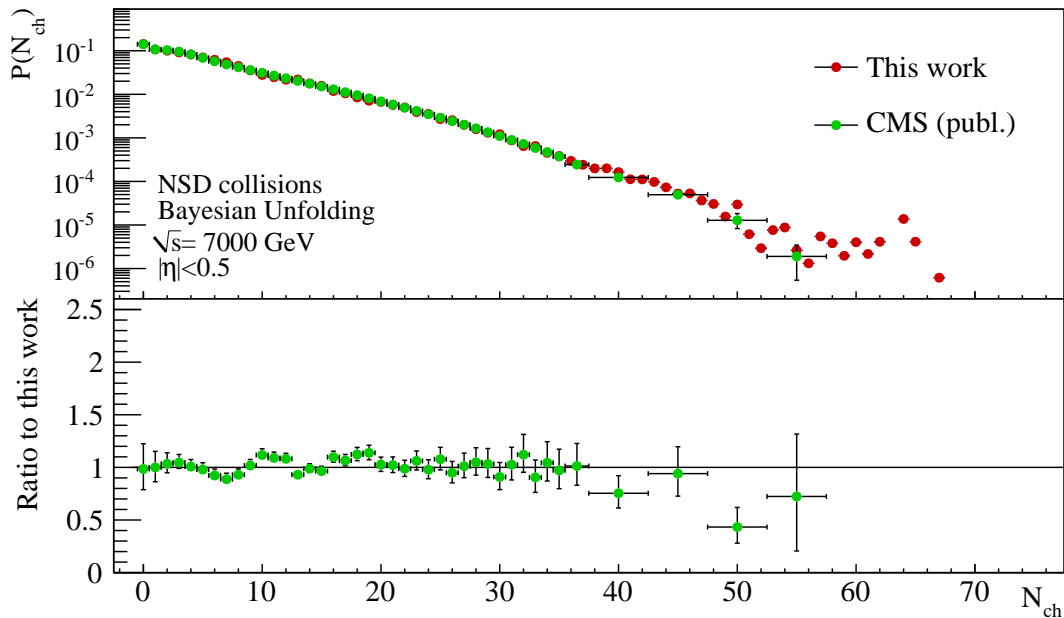


Figure F.7: Detailed comparisons of the measured multiplicity distributions for NSD  $pp$  collisions at  $\sqrt{s} = 7000$  GeV in the  $\eta$ -interval,  $|\eta| < 0.5$ .

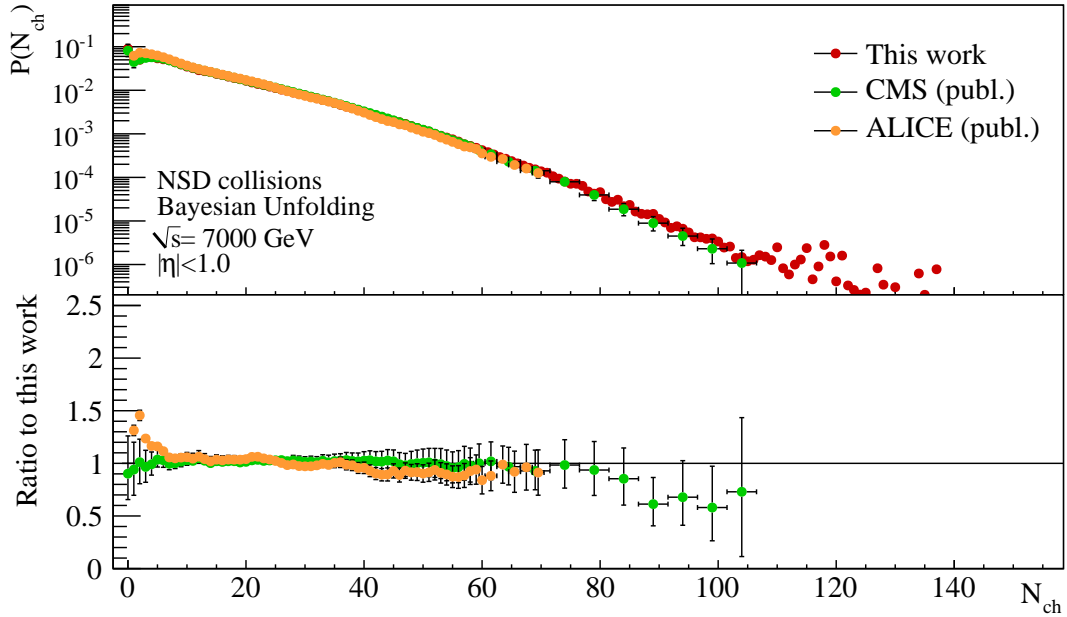


Figure F.8: Detailed comparisons of the measured multiplicity distributions for NSD  $pp$  collisions at  $\sqrt{s} = 7000$  GeV in the  $\eta$ -interval,  $|\eta| < 1.0$ .

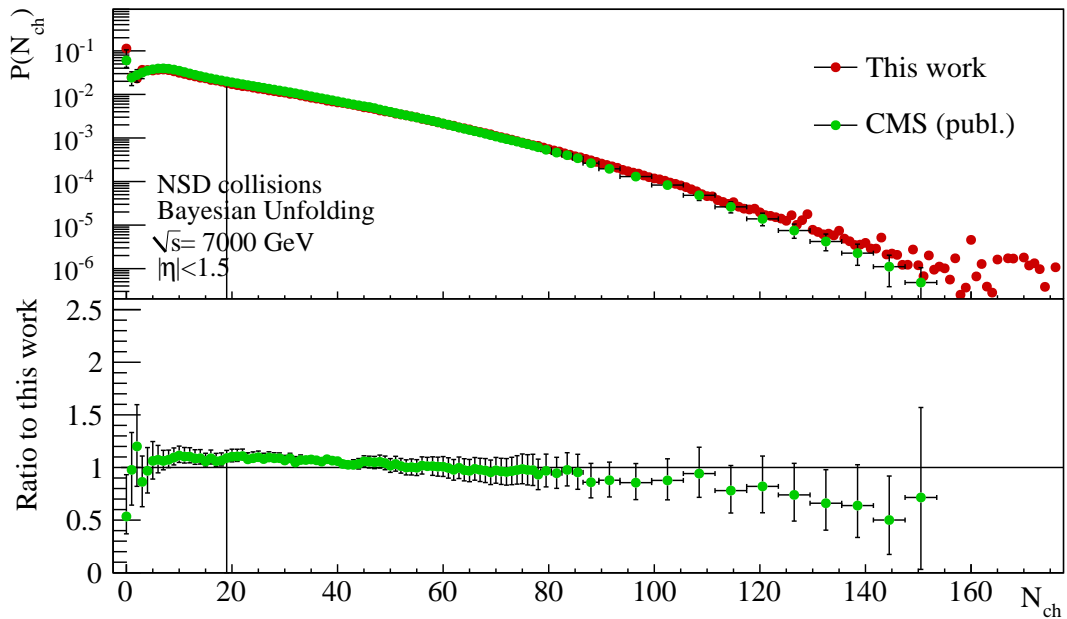


Figure F.9: Detailed comparisons of the measured multiplicity distributions for NSD  $pp$  collisions at  $\sqrt{s} = 7000$  GeV in the  $\eta$ -interval,  $|\eta| < 1.5$ .

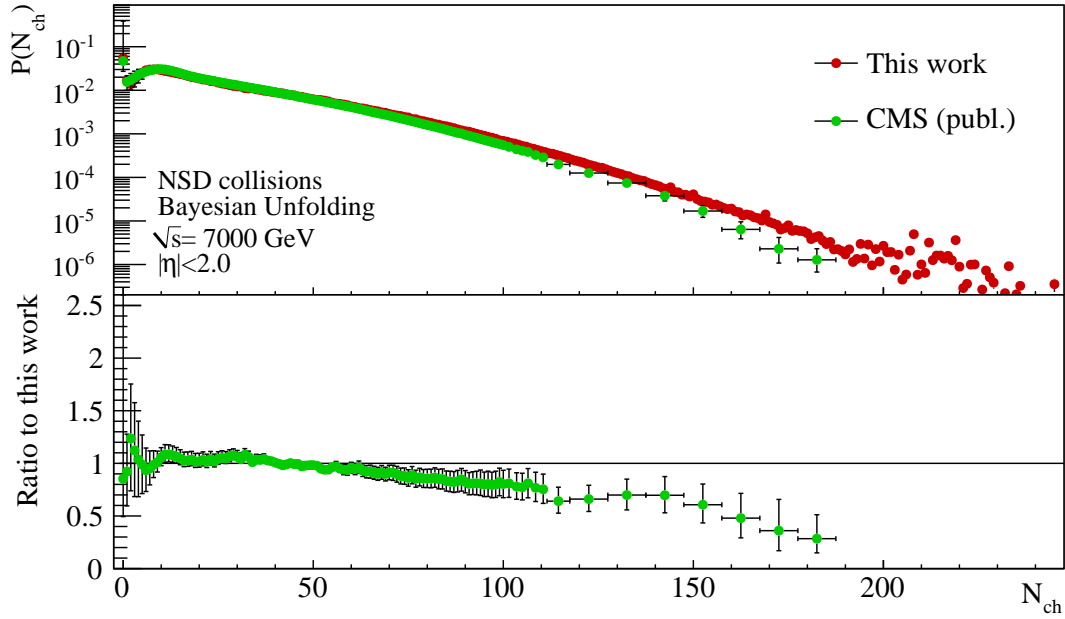


Figure F.10: Detailed comparisons of the measured multiplicity distributions for NSD  $pp$  collisions at  $\sqrt{s} = 7000$  GeV in the  $\eta$ -interval,  $|\eta| < 2.0$ .

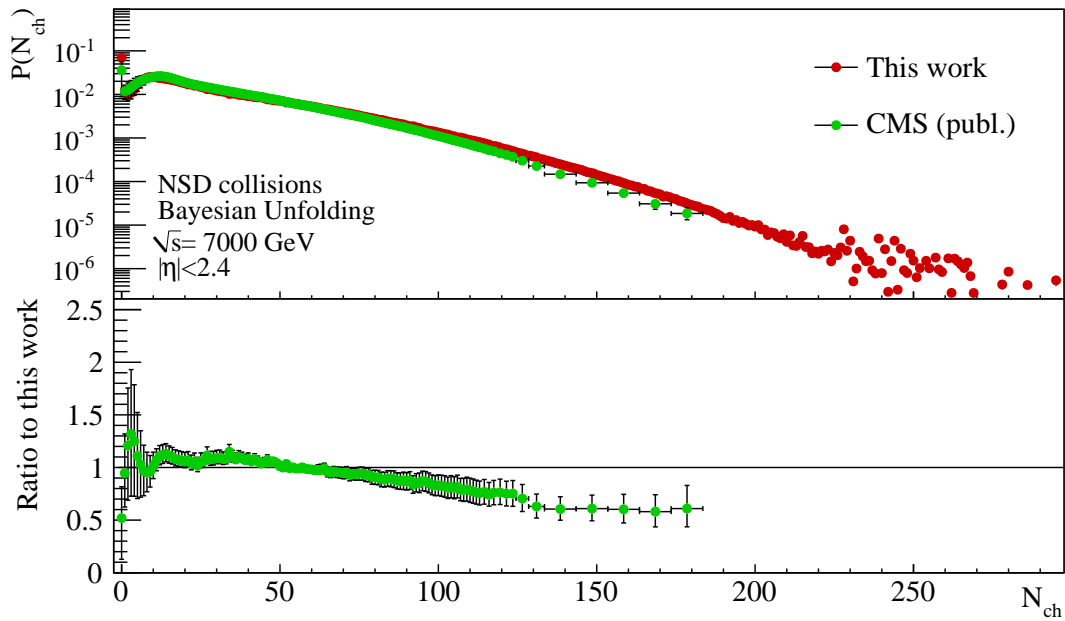


Figure F.11: Detailed comparisons of the measured multiplicity distributions for NSD  $pp$  collisions at  $\sqrt{s} = 7000$  GeV in the  $\eta$ -interval,  $|\eta| < 2.4$ .

# Bibliography

- [1] BRAHMS Collaboration, I. Arsene *et al.*, ‘Nuclear stopping and rapidity loss in Au+Au collisions at  $\sqrt{s_{NN}} = 62.4$ -GeV,’ *Phys.Lett.*, **B677** (2009) 267–271.
- [2] BRAHMS Collaboration, I. Arsene *et al.*, ‘Rapidity dependence of deuteron production in Au+Au collisions at  $\sqrt{s_{NN}} = 200$  GeV,’ *Phys.Rev.*, **C83** (2011) 044906.
- [3] M. Kaku, *Hyperspace*. Oxford University Press, 1995.
- [4] ALEPH Collaboration, D. Decamp *et al.*, ‘A Precise Determination of the Number of Families with Light Neutrinos and of the Z Boson Partial Widths,’ *Phys. Lett.* **B235**, (1990) 399–411.
- [5] Particle Data Group Collaboration, K. Nakamura *et al.*, ‘The Review of Particle Physics,’ *J. Phys.*, **G37** (2010).
- [6] F. Halzen and A. D. Martin, *Quarks and Leptons: An Introductory Course in Modern Particle Physics*. John Wiley & Sons, Inc., 1984.
- [7] J. Schwinger, ed., *Selected Papers on Quantum Electrodynamics*. Dover Publications, 1958.
- [8] M. E. Peskin and D. V. Schroeder, *An Introduction to Quantum Field Theory*. Westview Press, 1995.
- [9] C. S. B. Povh, K. Rith and F. Zetsche, *Particles and Nuclei*. Springer-Verlag, 4th edition ed., 2003.
- [10] T. R. Klassen, ‘QCD (lattice) potential and coupling: How to accurately interpolate between multiloop QCD and the string picture,’ *Phys. Rev.*, **D51** (1995) 5130.
- [11] M. L. Perl, E. R. Lee, and D. Loomba, ‘A Brief Review of the Search for Isolatable Fractional Charge Elementary Particles,’ *Mod. Phys. Lett.*, **A19** (2004) 2595–2610.
- [12] C. O. E. Jørgensen, ‘Charged Particle Production in Au+Au Collisions at,’ Master’s thesis, University of Copenhagen, 2001.
- [13] BRAHMS Collaboration, I. Arsene *et al.*, ‘Quark Gluon Plasma and Color Glass Condensate at RHIC? The perspective from the BRAHMS experiment,’ *Nucl.Phys.*, **A757** (2005).
- [14] Z.Fodor and S. Katz, ‘Lattice determination of the critical point of QCD at finite T and  $\mu$ ,’ *JHEP* *0203*, **014** (2002).

- [15] J. Letessier and J. Rafelski, *Hadrons and Quark–Gluon Plasma*, vol. 18 of *Cambridge Monographs on Particle Physics, Nuclear Physics and Cosmology*. Cambridge University Press, 2005.
- [16] P. Kovtun, D. Son, and A. Starinets, ‘Viscosity in strongly interacting quantum field theories from black hole physics,’ *Phys.Rev.Lett.*, **94** (2005) 111601. An Essay submitted to 2004 Gravity Research Foundation competition.
- [17] R. Karabowicz, ‘Study of Nuclear Modification Factors in Au+Au collisions at  $\sqrt{s_{NN}} = 200$  GeV,’. PhD thesis, Jagellonian University, 2006.
- [18] F.-M. Liu and K. Werner, ‘Direct photons at low transverse momentum – a QGP signal in pp collisions at LHC,’.
- [19] M. L. Miller, K. Reygers, S. J. Sanders, and P. Steinberg, ‘Glauber modeling in high energy nuclear collisions,’ *Ann. Rev. Nucl. Part. Sci.*, **57** (2007) 205–243.
- [20] J. Jia, ‘High- $p_T$  Charged Hadron Suppression in *Au – Au* Collisions at  $\sqrt{s_{NN}} = 200$  GeV,’. PhD thesis, State University of New York at Stony Brook, 2003.
- [21] J. Bjorken, ‘Highly Relativistic Nucleus-Nucleus Collisions: The Central Rapidity Region,’ *Phys. Rev.*, **D27** (1983) 140.
- [22] L. D. Landau, ‘On the multiparticle production in high-energy collisions (In Russian),’ *Izv. Akad. Nauk. SSSR Ser. Fiz.*, **17** (1953) 51–54. [English translation in: *Collected Papers of L. D. Landau*, D. Ter Haar (ed.), Intl Pub Distributor Inc, 1965].
- [23] BRAHMS Collaboration, I. G. Bearden *et al.*, ‘Nuclear stopping in Au + Au collisions at  $s(NN)^{1/2} = 200$ -GeV,’ *Phys.Rev.Lett.*, **93** (2004) 102301.
- [24] J. F. Große-Oetringhaus, ‘Measurement of the Charged-Particle Multiplicity in Proton–Proton Collisions with the ALICE Detector,’. PhD thesis, University of Münster, 2009.
- [25] A. Kaidalov, ‘Regge poles in QCD,’ (2001).
- [26] P. D. B. Collins, *An Introduction to Regge Theory and High Energy Physics*. Cambridge University Press, 1977.
- [27] E. Predazzi, ‘Diffraction: Past, present and future,’ (1998).
- [28] M. Poghosyan, *Diffraction dissociation of protons in proton-proton collisions at  $\sqrt{s} = 0.9$  TeV, 2.76 TeV and 7 TeV with ALICE at the LHC* Quark Matter 2011 parallel talk.
- [29] BRAHMS Collaboration, I. Arsene *et al.*, ‘Phys. Rev. Lett.,’ *Transverse momentum spectra in Au+Au and d+Au collisions at  $\sqrt{s_{NN}} = 200$  GeV and the pseudorapidity dependence of high  $p_T$  suppression.*, **91** (2003), no. 072305,.
- [30] H. Appelhaeuser, *Particle Production at Large Transverse Momentum with ALICE* Quark Matter 2011 plenary talk.

- [31] PHENIX Collaboration, A. Adare *et al.*, ‘Suppression Pattern of Neutral Pions at High Transverse Momentum in Au + Au Collisions at  $s_{NN} = 200\text{GeV}$  and Constraints on Medium Transport Coefficients,’ *Phys. Rev. Lett.*, **101** (Dec, 2008) 232301.
- [32] PHENIX Collaboration, A. Adare *et al.*, ‘Transverse momentum dependence of meson suppression  $\eta$  suppression in Au+Au collisions at  $\sqrt{s_{NN}} = 200\text{ GeV}$ ,’ *Phys.Rev.*, **C82** (2010) 011902.
- [33] Y. J. Lee, *Nuclear Modification Factors From the CMS Experiment* Quark Matter 2011 plenary talk.
- [34] M. Gyulassy, P. Levai, and I. Vitev, ‘Reaction operator approach to nonAbelian energy loss,’ *Nucl.Phys.*, **B594** (2001) 371–419. nucl-th/0006010.
- [35] M. L. Porschke, *R<sub>AA</sub> Measurements in PHENIX* Quark Matter 2011 plenary talk.
- [36] STAR Collaboration, C. Adler *et al.*, ‘Disappearance of back-to-back high  $p_T$  hadron correlations in central Au+Au collisions at  $\sqrt{s_{NN}} = 200\text{-GeV}$ ,’ *Phys.Rev.Lett.*, **90** (2003) 082302.
- [37] STAR Collaboration, J. Adams *et al.*, ‘Evidence from d + Au measurements for final state suppression of high p(T) hadrons in Au+Au collisions at RHIC,’ *Phys.Rev.Lett.*, **91** (2003) 072304.
- [38] C. Roland, *Jet Measurements by the CMS experiment in pp and PbPb collisions* Quark Matter 2011 plenary talk.
- [39] ATLAS Collaboration, G. Aad *et al.*, ‘Observation of a Centrality-Dependent Dijet Asymmetry in Lead-Lead Collisions at  $\sqrt{s_{NN}} = 2.76\text{ TeV}$  with the ATLAS Detector at the LHC,’ *Phys.Rev.Lett.*, **105** (2010) 252303.
- [40] B. A. Cole, *Jet Probes of  $\sqrt{s_{NN}} = 27600\text{ GeV}$  Pb+Pb Collisions with the ATLAS detector* Quark Matter 2011 plenary talk.
- [41] CMS Collaboration, S. Chatrchyan *et al.*, ‘Observation and studies of jet quenching in PbPb collisions at nucleon-nucleon center-of-mass energy = 2.76 TeV,’.
- [42] ALICE Collaboration, K. Aamodt *et al.*, ‘Elliptic flow of charged particles in Pb-Pb collisions at 2.76 TeV,’ *Phys.Rev.Lett.*, **105** (2010).
- [43] ALICE Collaboration, K. Aamodt *et al.*, ‘Higher harmonic anisotropic flow measurements of charged particles in Pb-Pb collisions at 2.76 TeV,’ *Phys.Rev.Lett.*, **107** (2011) 032301.
- [44] R. Snellings, *Anisotropic flow measurements from ALICE* Quark Matter 2011 plenary talk.
- [45] S. A. Voloshin and Z. Y., ‘Flow study in relativistic nuclear collisions by Fourier expansion of azimuthal particle distributions,’ *Z. Phys.*, **C70** (1996) 665–672.
- [46] A. M. Poskanzer and S. A. Voloshin, ‘Methods for analyzing anisotropic flow in relativistic nuclear collisions,’ *Phys. Rev.*, **C58** (1998) 1671–1678.
- [47] R. Snellings, ‘Elliptic Flow: A Brief Review,’ *New J.Phys.*, **13** (2011) 055008.

- [48] G.-Y. Qin, H. Petersen, S. A. Bass, and B. Muller, ‘Translation of collision geometry fluctuations into momentum anisotropies in relativistic heavy-ion collisions,’ *Phys.Rev.*, **C82** (2010) 064903.
- [49] J. Velkovska, *Flow Measurements from CMS* Quark Matter 2011 plenary talk.
- [50] J. Jia, *ATLAS  $v_n$  results* Quark Matter 2011 plenary talk.
- [51] S. Esumi, *Collective Flow Measurements from the PHENIX Experiment* Quark Matter 2011 plenary talk.
- [52] PHOBOS Collaboration, B. B. Back *et al.*, ‘The PHOBOS Perspective on Discoveries at RHIC,’ *Nucl. Phys.*, **A757** (2005) 28–101.
- [53] P. F. Kolb and U. W. Heinz, ‘Hydrodynamic description of ultrarelativistic heavy-ion collisions,’ *Quark-Gluon Plasma*, (2003) 634.
- [54] UA5 Collaboration, G. J. Alner *et al.*, ‘An Investigation of Multiplicity Distributions in Different Pseudorapidity Intervals in p+p Reactions at a CMS Energy of 540 GeV,’ *Phys. Lett. B*, **160** (1985) 193.
- [55] D. Ghosh, A. Deb, and S. Dutta, ‘Nonmonotonic target excitation dependence of pion clans in relativistic nucleus-nucleus collisions,’ *Int. J. Mod. Phys.*, **A25** (2010) 1507–1518.
- [56] A. Giovannini and L. Van Hove, ‘Negative binomial multiplicity distributions in high energy hadron collisions,’ *Z. Phys.*, **C30** (1986) 391.
- [57] A. Giovannini and L. Van Hove, ‘Negative binomial properties and clan structure in multiplicity distributions,’ *Acta Phys. Polon.*, **B19** (1988) 495.
- [58] J. Benecke and J. Kühn, ‘How to See Independent Emission in Hadronic Production,’ *Nucl. Phys.*, **B140** (1978) 179–188.
- [59] R. P. Feynman, ‘Very high-energy collisions of hadrons,’ *Phys. Rev. Lett.*, **23** (1969) 1415–1417.
- [60] Z. Koba, H. B. Nielsen, and P. Olesen, ‘Scaling of multiplicity distributions in high-energy hadron collisions,’ *Nucl. Phys.*, **B40** (1972) 317–334.
- [61] CERN-College de France-Heidelberg-Karlsruhe Collaboration, M. Della Negra *et al.*, ‘Observation of Jet Structure in High  $p_T$  Events at the ISR and the Importance of Parton Transverse Momentum,’ *Nucl.Phys.*, **B127** (1977) 1.
- [62] Ames-Bologna-CERN-Dortmund-Heidelberg-Warsaw Collaboration, A. Breakstone *et al.*, ‘Charged Multiplicity Distribution in p p Interactions at ISR Energies,’ *Phys.Rev.*, **D30** (1984) 528.
- [63] UA5 Collaboration, G. Alner *et al.*, ‘An Investigation of Multiplicity Distributions in Different Pseudorapidity Intervals in anti-p p Reactions at a CMS Energy of 540-GeV,’ *Phys.Lett.*, **B160** (1985) 193.
- [64] UA5 Collaboration, G. Alner *et al.*, ‘Scaling Violations in Multiplicity Distributions at 200-GeV and 900-GeV,’ *Phys.Lett.*, **B167** (1986) 476–480.

- [65] UA5 Collaboration, R. Ansorge *et al.*, ‘Charged Particle Multiplicity Distributions at 200-GeV and 900-GeV Center-Of-Mass Energy,’ *Z.Phys.*, **C43** (1989) 357.
- [66] UA5 Collaboration, G. Alner *et al.*, ‘Scaling Violation Favoring High Multiplicity Events at 540-GeV CMS Energy,’ *Phys.Lett.*, **B138** (1984) 304.
- [67] UA1 Collaboration, C. Albajar *et al.*, ‘A Study of the General Characteristics of  $p\bar{p}$  Collisions at  $\sqrt{s} = 0.2\text{-TeV}$  to  $0.9\text{-TeV}$ ,’ *Nucl.Phys.*, **B335** (1990) 261.
- [68] UA1 Collaboration, G. Arnison *et al.*, ‘Charged Particle Multiplicity Distributions in Proton Anti-Proton Collisions at 540-GeV Center-of-Mass Energy,’ *Phys.Lett.*, **B123** (1983) 108. Revised version.
- [69] UA1 Collaboration, A. Astbury *et al.*, *A  $4\pi$  solid angle detector for the SPS used as a proton-antiproton collider at a centre of mass energy of 540 GeV* Tech. Rep. CERN-SPSC-78-6. CERN-SPSC-78-06, CERN, Geneva, Jan, 1978.
- [70] Bonn-Brussels-Cambridge-CERN-Stockholm Collaboration, J. G. Rushbrooke *et al.*, ‘The UA5 Streamer Chamber Experiment at the SPS p anti-p Collider,’ *Phys.Scripta*, **23** (1981) 642–648.
- [71] CDF Collaboration, F. Rimondi, ‘Multiplicity distributions in  $\bar{p}p$  interactions at  $\sqrt{s} = 1800\text{-GeV}$ ,’ *Aspen Multipart. Dyn.*, (1993).
- [72] CDF Collaboration, F. Abe *et al.*, ‘The CDF Detector: An Overview,’ *Nucl.Instrum.Meth.*, **A271** (1988) 387–403.
- [73] ALICE Collaboration, K. Aamodt *et al.*, ‘Charged-particle multiplicity measurement in proton-proton collisions at  $\sqrt{s} = 0.9$  and  $2.36$  TeV with ALICE at LHC,’ *Eur.Phys.J.*, **C68** (2010) 89–108.
- [74] ALICE Collaboration, K. Aamodt *et al.*, ‘Charged-particle multiplicity measurement in proton-proton collisions at  $\sqrt{s} = 7$  TeV with ALICE at LHC,’ *Eur.Phys.J.*, **C68** (2010) 345–354.
- [75] CMS Collaboration, V. Khachatryan *et al.*, ‘Charged particle multiplicities in pp interactions at  $\sqrt{s} = 0.9, 2.36,$  and  $7$  TeV,’ *JHEP*, **1101** (2011) 079.
- [76] C. Fuglesang, ‘UA5 Multiplicity Distributions and Fits of Various Functions,’ Presented at Festschrift Leon Van Hove.
- [77] A. Giovannini and R. Ugoccioni, ‘Possible scenarios for soft and semihard components structure in central hadron hadron collisions in the TeV region: Pseudorapidity intervals,’ *Phys.Rev.*, **D60** (1999) 074027.
- [78] A. Giovannini and R. Ugoccioni, ‘On signals of new physics in global event properties in  $pp$  collisions in the TeV energy domain,’ *Phys.Rev.*, **D68** (2003) 034009.
- [79] T. Alexopoulos, E. Anderson, N. Biswas, A. Bujak, D. Carmony, *et al.*, ‘The role of double parton collisions in soft hadron interactions,’ *Phys.Lett.*, **B435** (1998) 453–457.
- [80] W. D. Walker, ‘Multiparton interactions and hadron structure,’ *Phys.Rev.*, **D69** (2004) 034007.

- [81] R. Harr, C. Liapis, P. Karchin, C. Biino, S. Erhan, *et al.*, ‘Pseudorapidity distribution of charged particles in  $\bar{p}p$  collisions at  $\sqrt{s} = 630\text{-GeV}$ ,’ *Phys.Lett.*, **B401** (1997) 176–180.
- [82] CDF Collaboration, F. Abe *et al.*, ‘Pseudorapidity distributions of charged particles produced in  $\bar{p}p$  interactions at  $\sqrt{s} = 630\text{ GeV}$  and  $1800\text{ GeV}$ ,’ *Phys.Rev.*, **D41** (1990) 2330.
- [83] Aachen-CERN-Heidelberg-Munich Collaboration, W. Thome *et al.*, ‘Charged Particle Multiplicity Distributions in p p Collisions at ISR Energies,’ *Nucl.Phys.*, **B129** (1977) 365.
- [84] CMS Collaboration, V. Khachatryan *et al.*, ‘Transverse-momentum and pseudorapidity distributions of charged hadrons in pp collisions at  $\sqrt{s} = 7\text{ TeV}$ ,’ *Phys.Rev.Lett.*, **105** (2010) 022002.
- [85] K. Krajczár, *Charged hadron multiplicity and transverse energy densities in PbPb collisions from CMS* Quark Matter 2011 parallel talk.
- [86] Y. Chen, *Measurement of charged particle pseudorapidity density in Pb+Pb collisions at  $\sqrt{s_{NN}} = 2.76\text{TeV}$  with the ATLAS detector* Quark Matter 2011 parallel talk.
- [87] H. H. Dalsgaard, ‘Pseudorapidity densities in p+p and Pb+Pb collisions at the LHC measured with the ALICE experiment,’. PhD thesis, University of Copenhagen, 2011.
- [88] The ALICE Collaboration, K. Aamodt *et al.*, ‘Charged-particle multiplicity density at mid-rapidity in central Pb-Pb collisions at  $\sqrt{s_{NN}} = 2.76\text{ TeV}$ ,’ *Phys.Rev.Lett.*, **105** (2010) 252301.
- [89] C. Vanoli, ‘CERN accelerator complex,’ 2006. <http://documents.cern.ch/cgi-bin/setlink?base=PH0&categ=photo-di&id=0606052>.
- [90] O. S. Brüning, P. Collier, P. Lebrun, S. Myers, R. Ostojic, J. Poole, and P. Proudlock, ‘Lhc design report vol. i-iii.’ CERN-2004-003-V-1.
- [91] C. H. Christensen, ‘ALICE Forward Multiplicity Detector - From Design to Installation,’. PhD thesis, University of Copenhagen, 2007.
- [92] ALICE Collaboration, K. Aamodt *et al.*, ‘The ALICE experiment at the CERN LHC,’ *JINST*, **3** (2008) S08002.
- [93] ALICE Collaboration, ‘Technical design report of the muon spectrometer.’ ALICE-DOC-2004-004 v.1.
- [94] ALICE Collaboration, ‘Technical design report of the inner tracking system.’ ALICE-DOC-2005-002 v.1.
- [95] ALICE Collaboration, ‘Technical design report of the time projection chamber.’ ALICE-DOC-2004-006 v.1.
- [96] ALICE Collaboration, ‘Technical design report of the transition radiation detector.’ ALICE-DOC-2004-009 v.1.

- [97] ALICE Collaboration, ‘Technical design report of the time of flight system.’ ALICE-DOC-2004-002.
- [98] ALICE Collaboration, ‘Technical design report of the high momentum particle identification detector.’ ALICE-DOC-1998-01 v.1.
- [99] ALICE Collaboration, ‘Technical design report of the electromagnetic calorimeter.’ ALICE-TDR-014.
- [100] ALICE Collaboration, ‘Technical design report of the photon spectrometer.’ ALICE-DOC-2004-008 v.1.
- [101] ALICE Collaboration, ‘Technical design report on forward detectors: Fmd, t0, v0.’ ALICE-DOC-2004-010 v.1.
- [102] ALICE Collaboration, ‘Technical design report of the photon multiplicity detector.’ ALICE-DOC-2004-007 v.1.
- [103] ALICE Collaboration, ‘Technical design report of the zero degree calorimeter.’ ALICE-DOC-2004-003 v.1.
- [104] P. Billoir and S. Qian, ‘Simultaneous pattern recognition and track fitting by the Kalman filtering method,’ *Nucl.Instrum.Meth.*, **A294** (1990) 219–228.
- [105] R. Fruhwirth, ‘Application of Kalman filtering to track and vertex fitting,’ *Nucl.Instrum.Meth.*, **A262** (1987) 444–450.
- [106] ALICE Collaboration, ‘Technical design report of the trigger, data acquisition, high-level trigger, and control system.’ ALICE-DOC-2004-001 v.2.
- [107] W. R. Leo, *Techniques for Nuclear and Particle Physics Experiments: A How-to Approach*. Springer-Verlag, Berlin, Germany, 1987.
- [108] L. Landau, ‘On the energy loss of fast particles by ionization,’ *J.Phys.(USSR)*, **8** (1944) 201–205.
- [109] S. Hancock, F. James, J. Movchet, P. Rancoita, and L. Van Rossum, ‘Energy Loss Distributions for Single Particles and Several Particles in a Thin Silicon Absorber,’ *Nucl.Instrum.Meth.*, **B1** (1984) 16.
- [110] S. Hancock, F. James, J. Movchet, P. Rancoita, and L. Van Rossum, ‘Energy Loss and Energy Straggling of Protons and Pions in the Momentum Range 0.7-GeV/c to 115-GeV/c,’ *Phys.Rev.*, **A28** (1983) 615.
- [111] P. Sarin, ‘Measurement of Charged Particle Multiplicity Distributions in Au+Au Collisions up 200 GeV,’. PhD thesis, Massachusetts Institute of Technology, 2003.
- [112] <http://root.cern.ch> - ROOT webpage.
- [113] <http://aliceinfo.cern.ch/Offline/> - ALICE offline webpage.
- [114] T. Sjostrand, S. Mrenna, and P. Z. Skands, ‘PYTHIA 6.4 Physics and Manual,’ *JHEP*, **0605** (2006) 026.

- [115] F. W. Bopp, R. Engel, and J. Ranft, ‘Rapidity gaps and the PHOJET Monte Carlo,’ in *LAFEX International School On High-Energy Physics (LISHEP 98) Session A: Particle Physics For High School Teachers - Session B: Advanced School In HEP - Session C: Workshop On Diffractive Physics*, pp. 729–741. 1998.
- [116] <http://www-nsdth.lbl.gov/~xnwang/hijing/doc.html> - HIJING webpage.
- [117] <http://wwwasd.web.cern.ch/wwwasd/geant/> - GEANT webpage.
- [118] <http://aliceinfo.cern.ch/Offline/Activities/Analysis/AnalysisFramework/index.html> - ALICE analysis framework webpage.
- [119] <http://public.web.cern.ch/public/en/lhc/Computing-en.html> - CERN LHC computing webpage.
- [120] <http://alimonitor.cern.ch/map.jsp> - MonALISA webpage.
- [121] L. Barnby, ‘Private communication.’
- [122] C. Søgaard, ‘ALICE Forward Multiplicity Detector - Test Beam,’ Master’s thesis, University of Copenhagen, 2007.
- [123] ALICE Collaboration, R. Santoro, ‘Status of the ALICE silicon pixel detector,’ *Nucl.Instrum.Meth.*, **A581** (2007) 330–334.
- [124] A. Dainese, *ITS Tracking: Rejection of secondaries for  $p_T$  paper* ALICE Internal Presentation.
- [125] V. Blobel, *An Unfolding method for high-energy physics experiments* hep-ex/0208022, 2002.
- [126] G. D’Agostini, ‘A Multidimensional unfolding method based on Bayes’ theorem,’ *Nucl. Instrum. Meth.*, **A362** (1995) 487.
- [127] G. D’Agostini, ‘Bayesian reasoning in high-energy physics: Principles and applications,’ *CERN Yellow Report*, (1999). CERN-YELLOW-99-03.
- [128] G. D’Agostini, *Improved iterative Bayesian unfolding* Alliance Workshop on Unfolding and Data Correction, 2010.
- [129] A. Hocker and V. Kartvelishvili, ‘SVD Approach to Data Unfolding,’ *Nucl. Instrum. Meth.*, **A372** (1996) 469–481.
- [130] ALICE collaboration, ‘Analysis note for Pb+Pb multiplicity papers’, Internal note, 2011.
- [131] E. Iancu and R. Venugopalan, ‘The Color glass condensate and high-energy scattering in QCD,’ (2003).
- [132] P. H. L. Christiansen, ‘Stopping in central  $\sqrt{s_{NN}} = 200$  GeV Au+Au Collisions at RHIC,’. PhD thesis, University of Copenhagen, 2003.
- [133] D. Ouerdane, ‘Charged Pion and Kaon Production in Central Au+Au Collisions at  $\sqrt{s_{NN}} = 200$  GeV,’. PhD thesis, University of Copenhagen, 2003.